

Aeroacoustic sources in internal flows

Citation for published version (APA):

Peters, M. C. A. M. (1993). *Aeroacoustic sources in internal flows*. [Phd Thesis 1 (Research TU/e / Graduation TU/e), Applied Physics and Science Education]. Technische Universiteit Eindhoven.
<https://doi.org/10.6100/IR401068>

DOI:

[10.6100/IR401068](https://doi.org/10.6100/IR401068)

Document status and date:

Published: 01/01/1993

Document Version:

Publisher's PDF, also known as Version of Record (includes final page, issue and volume numbers)

Please check the document version of this publication:

- A submitted manuscript is the version of the article upon submission and before peer-review. There can be important differences between the submitted version and the official published version of record. People interested in the research are advised to contact the author for the final version of the publication, or visit the DOI to the publisher's website.
- The final author version and the galley proof are versions of the publication after peer review.
- The final published version features the final layout of the paper including the volume, issue and page numbers.

[Link to publication](#)

General rights

Copyright and moral rights for the publications made accessible in the public portal are retained by the authors and/or other copyright owners and it is a condition of accessing publications that users recognise and abide by the legal requirements associated with these rights.

- Users may download and print one copy of any publication from the public portal for the purpose of private study or research.
- You may not further distribute the material or use it for any profit-making activity or commercial gain
- You may freely distribute the URL identifying the publication in the public portal.

If the publication is distributed under the terms of Article 25fa of the Dutch Copyright Act, indicated by the "Taverne" license above, please follow below link for the End User Agreement:

www.tue.nl/taverne

Take down policy

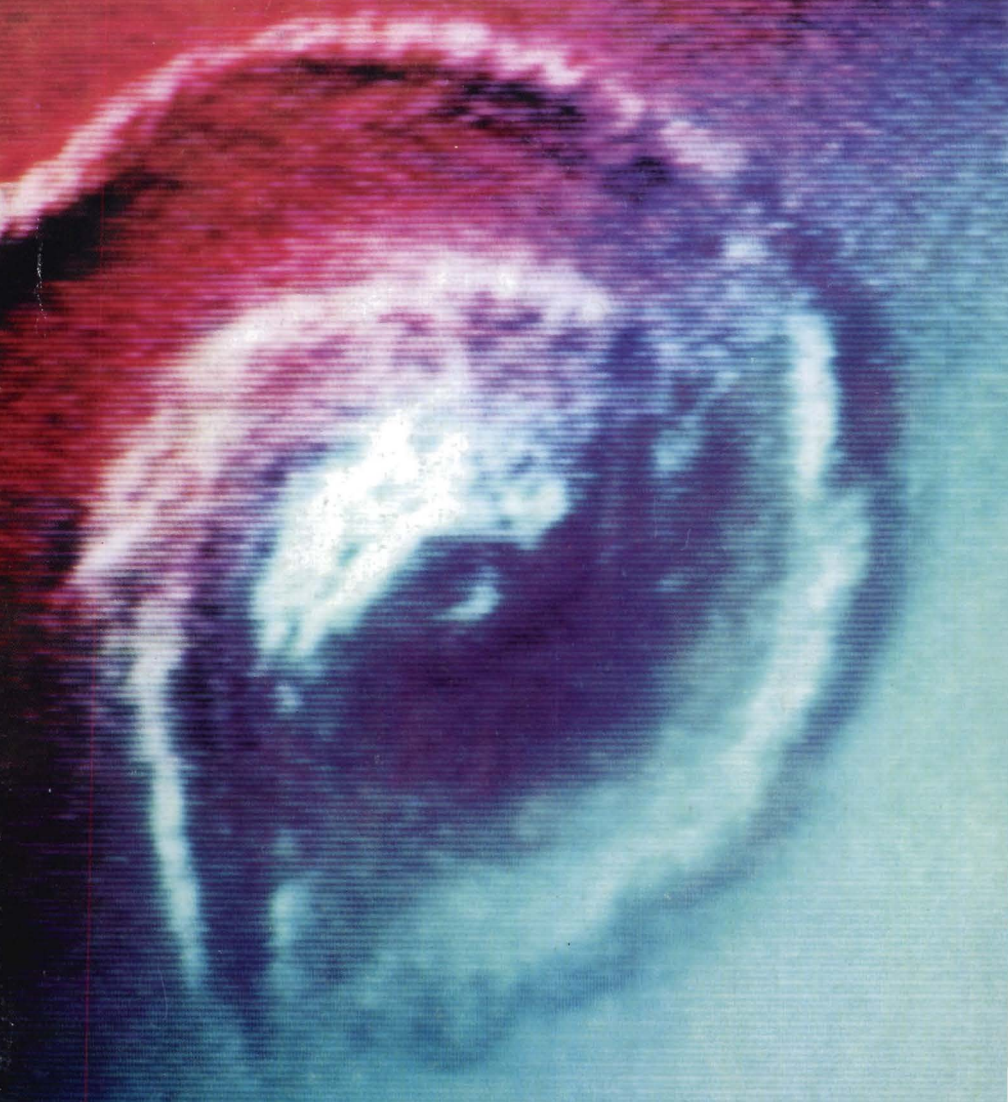
If you believe that this document breaches copyright please contact us at:

openaccess@tue.nl

providing details and we will investigate your claim.

AEROACOUSTIC SOURCES IN INTERNAL FLOWS

M.C.A.M. PETERS



AEROACOUSTIC SOURCES IN INTERNAL FLOWS

PROEFSCHRIFT

ter verkrijging van de graad van doctor aan de
Technische Universiteit Eindhoven, op gezag van
de Rector Magnificus, prof. dr. J.H. van Lint,
voor een commissie aangewezen door het College
van Dekanen in het openbaar te verdedigen op
vrijdag 3 september 1993 om 16.00 uur

door

MARINUS CAROLUS ADRIANUS MARIA PETERS
Geboren te Loon op Zand

Dit proefschrift is goedgekeurd door de promotoren:

prof. dr. ir. G. Vossers

en

prof. dr. ir. H.W.M. Hoeijmakers

en co-promotor

dr. ir. A. Hirschberg

This research project has been supported by Grant no. ETN 71.1403 of the Netherlands Foundation for Fundamental Research on Matter (FOM) and the Netherlands Foundation for Technical Sciences (STW) and by the N.V. Nederlandse Gasunie.

Vortices are the voice of the flow.

E.-A. MÜLLER & F. OBERMEIER
Fluid Dyn. Res. 3, (1988) 43 - 51.

aan Dorethé

CONTENTS

List of symbols	v
1 Introduction	1
1.1 Aeroacoustics	1
1.2 Problem definition	2
1.3 Vortex methods applied to aeroacoustic problems	5
1.4 Thesis overview	7
2 Theory	10
2.1 Aeroacoustics	10
2.1.1 Governing equations	10
2.1.2 Solution for high acoustic amplitudes	15
2.1.3 Application to internal flow	17
2.1.4 Conclusion	19
2.2 Vortex dynamics	19
2.2.1 Introduction	19
2.2.2 Methods for describing flows with distributed vorticity	22
2.2.3 Boundary conditions	30
2.2.4 Generation of vorticity	37
2.2.5 Simple vortex methods	44
2.2.6 Stability of vortex methods	48
2.2.7 The roll-up of the wake behind an elliptically loaded wing	53
2.3 Conclusions	56
3 Numerical simulation of starting flows	59
3.1 Introduction	59
3.2 Starting flow past a wedge	60
3.2.1 Infinite wedge of arbitrary included angle	60
3.2.2 90° Wedge	64
3.2.3 0° Wedge	74
3.3 Starting flow in a T-junction	78
3.3.1 Introduction	78
3.3.2 Similarity solution near the edge	80
3.3.3 Comparison of results of different flow methods	81
3.3.4 Experiment	89
3.4 Starting jet flow	91
3.4.1 Introduction	91
3.4.2 Sharp-edged nozzle	93
3.4.3 Square-edged nozzle	98
3.4.4 Experiment	102
3.5 Conclusions	109

4	Numerical simulation of periodic flows	111
4.1	Introduction	111
4.2	Sharp-edged nozzle	113
4.2.1	Introduction	113
4.2.2	Strouhal number of order unity	113
4.2.3	High Strouhal number	119
4.3	Periodic flow in a T-junction	122
4.3.1	Introduction	122
4.3.2	Flow visualization	124
4.3.3	Numerical simulation at high acoustic amplitudes	129
4.3.4	Moderate acoustic amplitude	137
4.4	Periodic flow in a cross-junction	140
4.4.1	Introduction	140
4.4.2	Flow visualization	142
4.4.3	Numerical simulation	144
4.5	Conclusions	149
5	The aeroacoustic behavior of an open pipe	152
5.1	Introduction	153
5.2	Setup and experimental procedure	156
5.2.1	Setup	156
5.2.2	Mean flow conditions	162
5.2.3	Determination of reflection coefficient and the damping	163
5.2.4	Influence of the acoustics of the room	165
5.3	Damping	167
5.3.1	Damping in absence of mean flow	167
5.3.2	Convective effects	168
5.3.3	Influence of turbulence	169
5.3.4	Experimental results	173
5.4	Open pipe end in a quiescent fluid	175
5.4.1	Influence of pipe end geometry	175
5.4.2	Nonlinear losses	178
5.5	Open pipe end with mean flow	182
5.5.1	Unflanged pipe termination	182
5.5.2	Thick-walled pipe end and horn	185
5.6	Conclusions	187
6	The aeroacoustic behavior of pipe systems with two closed side branches	191
6.1	Introduction	191
6.2	Determination of aero-acoustic source strength	195
6.2.1	Double T-junction geometry	195
6.2.2	Cross-junction geometry	200
6.3	Estimate of acoustic energy loss by friction and heat conduction	202
6.4	Nonlinear effects at high acoustic amplitude	203
6.5	Prediction of equilibrium amplitude	205

6.6	Experiments	206
6.6.1	Introduction	206
6.6.2	Influence of pipe geometry on pulsation amplitude	207
6.6.3	Influence of rounding the edges on pulsation amplitude	212
6.7	Conclusions	216
7	Summary and conclusions	218
7.1	Numerical simulation of unsteady internal flow	218
7.2	Interaction of a vorticity field with an acoustic field	219
7.3	Loss mechanisms of acoustic energy	220
7.4	Prediction of equilibrium amplitude of acoustic oscillation	221
	Appendix A: Governing equations for aero-acoustic sources.	223
	Appendix B: Single vortex model of the starting flow past a wedge.	228
	Samenvatting	233
	Nawoord	234
	Curriculum Vitae	236

LIST OF SYMBOLS

ROMAN SYMBOLS LOWERCASE

a	m	pipe radius
c_0	m s^{-1}	velocity of sound
c_p	$\text{J kg}^{-1} \text{K}^{-1}$	specific heat at constant pressure
c_v	$\text{J kg}^{-1} \text{K}^{-1}$	specific heat at constant volume
d	m	pipe wall thickness
\mathbf{e}_z		unity vector in direction normal to the 2D-plane
$e(\vec{x}, t)$	$\text{m}^2 \text{s}^{-2}$	specific internal energy
f	Hz	frequency
$f(\zeta)$		Schwarz-Christoffel transformation function
\bar{f}	N m^{-3}	external force
h	m	width of the main pipe
$h(\vec{x}, t)$	$\text{m}^2 \text{s}^{-2}$	specific enthalpy
i		$\sqrt{-1}$
k	m^{-1}	wave number
$k_n(s)$	m^{-1}	curvature of the vortex sheet
l_A	m	perimeter
n		parameter related to the interior angle of a wedge
\vec{n}		normal unit vector
p	Pa	pressure
q	$\text{kg m}^{-3} \text{s}^{-1}$	external mass source
$q(s)$	m s^{-1}	source strength distribution
q_h	$\text{J m}^{-2} \text{s}^{-1}$	heat flux
r	m	radius of curvature of the horn
s	m	arc length
t	s	time
u, v	m s^{-1}	velocity components in (x, y) direction
u_{Bern}	m s^{-1}	velocity obtained from Bernoulli's eqn.
v^*	m s^{-1}	friction velocity
\vec{v}	m s^{-1}	velocity vector
\vec{v}_{irr}	m s^{-1}	irrotational part of the velocity vector
\vec{v}_{sol}	m s^{-1}	solenoidal part of the velocity vector
x	m	real part of the complex variable z
y	m	imaginary part of the complex variable z
$z = x + iy$	m	complex coordinate in the physical plane

ROMAN SYMBOLS UPPERCASE

A	$m^2 s^{-1}$	coefficient of the attached flow rounding a wedge
A	m^2	cross-sectional area
B	$m^2 s^{-1}$	coefficient of the symmetric attached flow towards a sharp edge
C		boundary contour
D		proportionality constant of conformal mapping
D	m	dispersion
$E(\vec{x}, t)$	$m^2 s^{-2}$	specific total energy
\vec{F}	$N m^{-3}$	additional force in presence of a body
$G(\vec{x}, t \vec{y}, \tau)$		Green's function
$H(\vec{x}, t)$	$m^2 s^{-2}$	specific total enthalpy
H	m	width of the side branch
He		Helmholtz number
H_{ji}		transfer function
\vec{I}	$J m^2 s^{-1}$	intensity
J		scaled circulation in similarity solution
K_{ij}		influence coefficient
$K(z)$	m^{-1}	Biot-Savart kernel
$K_\delta(z)$	m^{-1}	desingularized Biot-Savart kernel
L	m	length of the side branch
\vec{L}	$m s^{-2}$	Lamb's vector
M		Mach number
NP		number of panels
NR		number of regions with uniform vorticity
NV		number of discrete vortices
P	$J s^{-1}$	acoustic power
Pr		Prandtl number
Q	$m^2 s^{-1}$	point source strength
Q	$kg m^{-3} s^{-1}$	additional mass source in presence of a body
R		pressure reflection coefficient
R_E		energy reflection coefficient
$R(s)$	m	distance between a point and a panel
$R_f(s)$	m	distance between a point and the tangential to a panel
Re		Reynolds number
S	$J kg^{-1} K^{-1}$	entropy
Sh		Shear number
Sr		Strouhal number
T	s	period of oscillation of the acoustic velocity field
T	K	absolute temperature
T_{ij}	$kg m^{-1} s^{-2}$	Lighthill's stress tensor
U_0	$m s^{-1}$	mean flow velocity
V	m^3	volume
Z		wall impedance

GREEK SYMBOLS

α_{\pm}	m^{-1}	damping coefficient in presence of a mean flow
α_0	m^{-1}	damping coefficient in absence of a mean flow
α		time power of attached potential flow rounding a wedge
β		time power of attached potential flow towards a sharp edge
β_i	rad	angle used in Schwarz-Cristoffel transformation
γ		Poisson's constant
$\gamma(s)$	$m s^{-1}$	vortex distribution
Γ	$m^2 s^{-1}$	circulation
$\Gamma(s)$	$m^2 s^{-1}$	dipole distribution
δ	m	desingularisation parameter
δ	m	end correction
δ_{ac}	m	acoustic boundary layer thickness ($= \sqrt{2\nu/\omega}$)
δ_i	m	viscous sublayer thickness ($\approx 10\nu/v^*$)
δ_{ij}		kroncker delta ($\delta_{ij} = 1$ if $i = j$, $\delta_{ij} = 0$ otherwise)
ζ		complex coordinate in the computational plane ($= \xi + i\eta$)
η		imaginary part of complex variable ζ
ϑ	m	momentum loss thickness
θ	rad	angle in the z -plane
κ	$J m^{-1} s^{-1} K^{-1}$	coefficient of thermal conductivity
λ	m	wave length
$\lambda(s)$		scaled arc length
Λ		constant
μ	$kg m^{-1} s^{-1}$	dynamic viscosity
ν	$m^2 s^{-1}$	kinematic viscosity
ξ		real part of complex variable ζ
ρ	$kg m^{-3}$	density
$\rho(\lambda)$		scaled radius in z -plane
τ	$kg m^{-1} s^{-2}$	wall shear stress
τ_{ij}	$kg m^{-1} s^{-2}$	viscous shear stress tensor
\vec{t}		tangential unit vector
φ	$m^2 s^{-1}$	scalar velocity potential
ϕ	rad	angle
Φ	$m^2 s^{-1}$	complex velocity potential ($= \varphi + i\psi$)
ψ	$m^2 s^{-1}$	stream function
ψ		turbulent friction factor
$\vec{\Psi}$	$m^2 s^{-1}$	vector stream function
ω	$rad s^{-1}$	radian frequency
$\bar{\omega}$	s^{-1}	vorticity
$\omega(\lambda)$		scaled coordinate in z -plane
$\chi(\lambda)$		scaled angle in z -plane

OTHER SYMBOLS

\mathcal{A}	amplification factor of reflection coefficient
\mathcal{D}	dissipation function
\mathcal{F}	fraction of displacement of panel in vortex-sheet method
\mathcal{H}	Hamiltonian
\mathcal{L}	wave operator
\mathcal{Q}	external energy source
\mathcal{R}	gas constant
\mathcal{S}	function describing a body surface

FUNCTIONS

$\Re(\dots)$	real part of ...
$\Im(\dots)$	imaginary part of ...
$\delta(z - z_j)$	Dirac delta function ($\delta \rightarrow \infty$ at $z = z_j$, $\delta = 0$ elsewhere)
$\mathcal{H}(C_j)$	Heaviside function ($\mathcal{H}=0$ interior the boundary contour C_j , 1 elsewhere)
$\text{sign}(\eta)$	sign of η ($\text{sign}(\eta) = 1$ for $\eta > 0$ and $\text{sign}(\eta) = -1$ for $\eta < 0$)

SUBSCRIPTS

+	upstream
-	downstream
o	refers to the attached flow
ac	refers to the acoustic flow
q	of the source distribution
γ	of the vortex distribution
Γ	of the discrete vortex
s	of the vortex sheet
v	of the discrete vortex
K	with application of the Kutta condition
NK	without application of the Kutta condition

SUPERSCRIPTS

+	value nondimensionalised with friction velocity and kinematic velocity
*	complex conjugate
*	dimensionless quantity
*	value at the expansion point (midpoint) of a panel
'	first derivative with respect to local variable (s)
"	second derivative with respect to local variable (s)
~	first estimate
^	amplitude

Chapter 1

Introduction

1.1 AEROACOUSTICS

The description by Lighthill (1952, 1954) of the phenomenon of sound production by a turbulent flow marked the beginning of aeroacoustics as a new field of research in fluid mechanics. Up to that period it was mainly assumed that sound was produced by wall vibrations like in loud speakers or in some music instruments. In Lighthill's now classical approach the sound is generated by: a fluctuating volume flux, which is a monopole-like sound source; a fluctuating force, which corresponds to a dipole-like sound source, corresponding to two monopole sound sources of opposite strength at a distance apart smaller than the wavelength of the generated sound; or higher-order in free space less efficient sound sources like quadrupoles, octopoles etc.

Lighthill (1952) derived his famous aeroacoustic analogy which, in absence of other sound sources, describes the quadrupole-like behavior of the sound produced by turbulent fluctuations of the velocity field. The success of Lighthill's theory is due to its ability to predict the noise generated by subsonic free jets, as well as providing a solution to the serious jet-noise problem.

It was shown later by Powell (1964) that for a low-Mach-number flow the strength of Lighthill's sound source could be rewritten explicitly in terms of the vorticity. This led for instance to the explanation of the sound generated by telephone wires, studied earlier by Strouhal, as being related to the periodic shedding of vortices by the wires, resulting in the von Kármán vortex street. The sound generated by vorticity is therefore called 'vortex sound'. Vortex sound is also responsible for flow-induced pulsations observed in internal flows. For example, in a whistling tea-kettle the sound is generated by the coupling of an acoustic resonance of a Helmholtz resonator with periodic vortex shedding at the two orifice plates at a certain value of the mean flow velocity. This configuration is also called Rayleigh's bird call configuration (Chanaud (1970)).

Similar flow-induced coupling occurs in internal flows in the presence of a large variety of resonators. The resonator accumulates the acoustic energy which under specific conditions can be extracted from the mean flow field by the vorticity field. The difference between aeroacoustical sound production in internal flows and sound generation in free space is that the amplitude of the periodic velocity fluctuations associated with the acoustic field can become of the same order of magnitude as the mean stationary flow. The high amplitude of the acoustic velocity field implies that there is a strong feedback from the acoustic perturbations to the vorticity generation, subsequently convection of vorticity along the shear layer and the formation of concentrated vortex structures in the shear layer. The flow depends on the acoustic field which it generates, an interaction which effect is usually

assumed negligible in free space. For specific flow conditions the feedback results in a control of the vortex shedding process by the acoustic velocity field and into self-sustained oscillations.

1.2 PROBLEM DEFINITION

Flow-induced oscillations in internal flow systems can cause severe noise and vibration problems in a number of engineering applications. For example in the pipe system of a compressor station used for the transport of gas by the N.V. Nederlandse Gasunie strong pulsations occurred (Bruggeman (1987a)). In a second example safety relief valves flow induced pulsations caused dangerous situations (Baldwin & Simmons (1986)). An extensive review of similar flow-induced vibrations and oscillations induced by impinging shear layers is given by Rockwell & Naudascher (1978, 1979) and Rockwell (1983).

In this thesis flow-induced pulsations are studied which occur at high Reynolds number and low Mach number in pipe systems with closed side branches. The intersection of a main pipe and a single side branch is further called a *T-junction*, while the intersection of a main pipe with a second pipe will be called a *cross-junction*. In the present study the flow in a tandem T-junction and a cross-junction geometry, as shown in figure 1.1, is studied, for pipes with a square and for pipes with a circular cross-section. The cause of the pulsations in the pipe system is an acoustic feedback loop in which flow separation at the sharp edges of the T-junction or cross-junction couples with the acoustic flow field, resulting in an unsteady vorticity field. The feedback loop develops as follows.

- Due to the flow separation at the sharp edges a free shear layer is formed which is unstable to disturbances.
- For small disturbances the instability occurs only for frequencies which correspond to hydrodynamic wavelengths which are large compared to the momentum thickness of the shear layer. If an acoustic field of such a frequency acts on the shear layer the disturbance grows exponentially until, due to nonlinearity, a region of concentrated vorticity is formed, i.e. a *vortex core*.
- These coherent vortical structures convect from the upstream to the downstream edge of the side branch, see figure 1.1.

If the time it takes a vortex to travel across the width of the side branch fits the oscillation period of an acoustic mode of the pipe system the vortex formation couples with the acoustic field and a resonance may occur. For a given source strength the amplitude of the pulsations is determined by the so-called quality factor of the resonator. The quality factor is determined by the losses in acoustic energy due to radiation, viscous and thermal effects occurring at the pipe walls and losses due to the interaction of the acoustic flow field with the turbulent mean flow.

Bruggeman (1987a) studied the self-sustained flow oscillations in a system with single and double closed side branches for low and moderate amplitudes of the acoustic field, for which $\hat{u}_{ac}/U_0 \ll 1$ and $\hat{u}_{ac}/U_0 = \mathcal{O}(M)$, respectively. Here \hat{u}_{ac} is a characteristic amplitude of the acoustic velocity field and U_0 is the main flow velocity. Ziada & Bühlmann

(1992) studied the flow-induced pulsations in a cross-junction configuration at moderate amplitudes of the acoustic field.

Bruggeman (1987a) argued that a single closed side branch is a perfect reflector for plane acoustic sound waves when the side branch length L is equal to an uneven multiple of $\lambda/4$, where λ is the wavelength of the sound wave. Two closed side branches an even multiple of $\lambda/2$ apart form therefore a resonator in which acoustic energy can accumulate.

From experimental data Bruggeman (1987a) determined the strength of the sound source up to moderate amplitudes of the acoustic field. It was found that the source strength is constant, so that the acoustic power generated varies linearly with the acoustic amplitude. In this case the total amount of vorticity contained in the shear layer is not strongly influenced by the acoustic field. The acoustic field only triggers the instability of the shear layer and the start of the formation of vortex structures. Assuming a weak interaction, and employing a simple model, in which the shear layer is represented by a single point vortex and using the vortex sound theory developed by Powell (1964) and Howe (1975), Bruggeman (1987a) predicted the order of magnitude of the source strength as found in the measurement. However, for high amplitudes of the acoustic field, $\hat{u}_{ac}/U_0 = \mathcal{O}(1)$, the assumption of a weak interaction between the shear layer and the acoustic velocity field is not valid anymore. Bruggeman (1987a) suggested that the highest attainable amplitude of the acoustic velocity field corresponds to a net source strength equal to zero.

The aim of the present study is to determine the strength of the source of aerodynamic sound at high amplitudes of the acoustic field, i.e. $\hat{u}_{ac}/U_0 = \mathcal{O}(1)$, for cases such as the flow in a pipe system with two closed side branches as shown in figure 1.1. The investigation has an experimental and a numerical component.

The investigation is limited to the case that the width H of the side branch is equal to the width h of the main pipe. The acoustic field with frequency f is resonating between the closed side branches. The walls of the pipe system are assumed to be rigid, so that radiation losses of acoustic energy through wall vibrations are negligible. Since for reso-

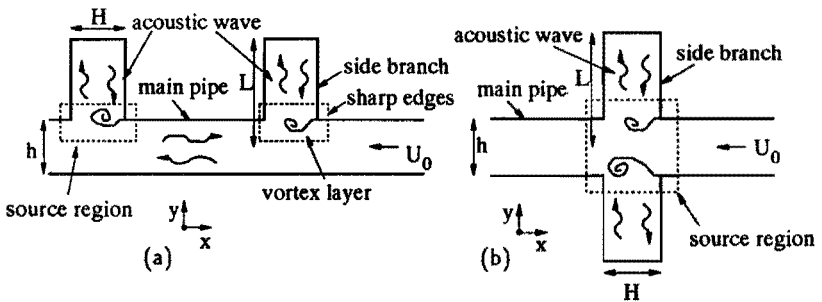


FIGURE 1.1: Double side branch geometries studied in this thesis. (a) tandem T-junction geometry (b) cross-junction geometry

nance frequencies of the pipe system shown in figure 1.1 radiation losses into the main pipe are negligible, the amplitude of the acoustic velocity field can become comparable to the amplitude of the mean flow.

In the present study only the flow of air is considered, which for the experimental conditions considered can be assumed an ideal gas. Within the flow itself it is assumed that the material properties of air such as density ρ_0 , kinematic viscosity ν , thermal diffusivity $\kappa/\rho_0 c_p$, where κ is the thermal conductivity and c_p is the specific heat at constant pressure, the gas constant R and Poisson's constant γ for the ratio of specific heats c_p/c_v and speed of sound c_0 are constant.

Where needed more accurate data have been used which take into account the dependency of the kinematic viscosity, density, thermal diffusivity and speed of sound on the ambient temperature, ambient pressure and on the humidity (see for example chapter 5 for details).

The following similarity parameters can be defined, all in absence of a mean flow:

$$\begin{aligned} \frac{H}{L} & : \text{ratio side branch width to length} \\ \frac{\mu c_p}{\kappa} & = Pr \quad : \text{Prandtl number} \\ \frac{\sqrt{\nu/2\pi f}}{H} & = Sh \quad : \text{Shear number} \\ \frac{fH}{\hat{u}_{ac}} & = Sr_{ac} \quad : \text{acoustic Strouhal number} \\ \frac{2\pi fH}{c_0} & = He \quad : \text{Helmholtz number} \end{aligned}$$

and in presence of a mean flow the additional similarity parameters

$$\begin{aligned} \frac{\hat{u}_{ac}}{U_0} & : \text{acoustic amplitude} \\ \frac{U_0}{c_0} & = M \quad : \text{Mach number} \\ \frac{U_0 H}{\nu} & = Re \quad : \text{Reynolds number} \\ \frac{fH}{U_0} & = Sr \quad : \text{mean flow Strouhal number} \end{aligned}$$

In the type of engineering applications considered the pulsations occur at high Reynolds numbers Re , typically $Re > 10^5$, but at a relatively low Mach number ($M \ll 1$) of the mean flow. The Shear number Sh is usually very small, so that viscous effects associated with oscillations of the acoustic velocity field are confined to thin boundary layers along the pipe wall.

In the present analysis, we will consider low frequencies of the acoustic field only, i.e. the Helmholtz number He is small $He \ll 1$. Under these conditions only plane acoustic waves

will propagate in the pipe system. At resonance conditions the mean flow Strouhal number St is usually of order one. In the present study we will focus on the case for which the ratio between the amplitude of the acoustic velocity field and the amplitude of the mean flow is of order one, i.e. $\hat{u}_{ac}/U_0 = \mathcal{O}(1)$, which corresponds to the high-amplitude case following the classification of Bruggeman (1987a). Since the side branch is long compared to its width, $H/L \ll 1$ and as a result for the first modes of resonance in the system $He \ll 1$ and the flow in the T- or cross-junction is compact. This implies that across the junction the phase shift of the acoustic waves due to the compressibility of air can be neglected.

An incompressible approximation of the unsteady flow in the junction can be coupled to the plane-wave approximation for the flow in the side branches. Formally the flow in a single side branch could be determined by application of the Method of Matched Asymptotic Expansions (see Bruggeman (1987a,b) and Lesser & Crighton (1976)).

In order to obtain the incompressible flow in the junction the periodic acoustic velocity field will be imposed as a boundary condition. At a given amplitude and frequency of the acoustic velocity field the interaction of the vorticity generated at the sharp edges with the acoustic field then determines the strength of the aero-acoustic source. From an acoustic energy balance for the complete resonator the amplitude of acoustic resonance can be obtained as the amplitude which is required to maintain the acoustic field at the a priori specified amplitude.

1.3 VORTEX METHODS APPLIED TO AEROACOUSTIC PROBLEMS

Following Powell's (1964) demonstration that Lighthill's aeroacoustic analogy can in a homentropic flow in free space be interpreted in terms of vorticity being the source of sound, vortex methods have been used to estimate the acoustic source strength. The sound generated by unsteady vorticity is commonly referred to as 'vortex sound' (e.g. Müller & Obermeier (1988)). Based on Powell's (1964) theory Stüber (1970) derived expressions for the sound produced by two spinning vortices, while Crighton (1972) found expressions for the sound generated by a point vortex convecting along a half plane. Cannel and Ffowcs-Williams (1973) discussed the sound produced by a point vortex pair convected through the exit of a two-dimensional channel. Howe (1975) extended the theory of Powell (1964) by including the sound produced by entropy inhomogeneities. Furthermore, Howe (1975) demonstrated that the vortex sound concept can be generalized to internal flows. Howe (1975) applied the theory to the sound production by a region of vorticity or an entropy spot convecting through a contraction into a hard-walled duct and along a rigid body. Möhring (1978) showed, by defining a vector Green's function that the sound produced by vorticity can be described in terms of the vorticity only.

An interesting application of resonances in an internal flow is the sound production in music instruments like a flue organ pipe, a recorder and a flute. In these instruments the sound is generated by the interaction of the resonating acoustic field with the vorticity generated at the nozzle of the flue channel and the vorticity generated at the sharp edge of the labium. Since the impingement of the starting vortex on the labium is of crucial importance for the first tones produced by the instrument the transient flow inside these instruments is of special interest. However, in the literature (e.g. Fletcher (1990)) this type

of flow is usually described by a quasi-steady model, in which a jet is already present during the transient period. Furthermore, it has been suggested by Fletcher (1979) that vortex shedding at the labium of the flute is a secondary effect. However, Howe (1975) showed, by using a single-point vortex method to describe the vortex formation in a flute, that vortex sound may play an important role in the transient behavior of a flute. Fabre (1992) found indeed that vortex shedding is crucial as a source of sound for higher harmonics of the fundamental oscillation mode of the flute but rather as a damping mechanism for the fundamental mode.

The vortex sound theory has been developed by Yates (1978) in order to study vortex noise and jet impingement noise. For the sound absorption by the vorticity field generated at an open pipe end Disselhorst (1978) and Disselhorst & van Wijngaarden (1980) used a multi-point-vortex method to describe the process of vorticity generation and convection. They computed the pressure difference due to the generation and convection of vortices with which the absorbed acoustic power could be determined. Later, Hirschberg *et al.* (1989) showed that Howe's (1975) vortex sound theory can be used to understand the sound production in a 'whistler nozzle' or in a pipe terminated by a horn.

Vortex sound in internal flows has also been studied extensively. Bruggeman *et al.* (1987a, 1991) employed a single-point vortex method to describe the vorticity generation and convection at the sharp edges of a T-junction. Welsh & Gibson (1979), Parker & Welsh (1983), Stokes & Welsh (1984, 1986) and Stoneman *et al.* (1988) investigated the interaction of sound waves with vortex shedding from bluff bodies situated within a duct. Welsh & Stokes (1984, 1986) used a multi-point vortex method to describe the flow and the interaction with the acoustic field and obtained the aeroacoustic power production by applying Howe's (1975) vortex sound theory. However, they ignored the problem brought to light by Brown and Michael (1954) that a point vortex with time-varying circulation cannot be considered as a free vortex convecting with the local flow velocity. This problem will be considered in detail in the present study.

Using the vortex-blob method Thompson *et al.* (1992) discussed the acoustic sources in a tripped flow past a resonator tube. Using the theory of vortex sound to describe the interaction between the acoustic field and the vorticity field critical Strouhal numbers at which resonances occur could be determined. However, a prediction of the amplitude of the periodic pulsations has not been given.

In this thesis the second-order vortex-sheet method developed at the National Aerospace Laboratory (NLR) in the Netherlands and described by Hoeijmakers & Vaatstra (1982), has been used as one of the methods to simulate the convection and roll-up of the vortex layer in an internal flow. In order to incorporate the generation of vorticity at sharp edges the possibility to impose the so-called Kutta condition at a sharp edge has been implemented in the original computational method. Furthermore, imposing the boundary condition of zero normal velocity at rigid boundaries is made easy by conformal mapping of physical flow domain into a computational plane, with the solid boundary along the plane of symmetry.

The results of this method have been compared with results of the vortex-blob method, developed at the University of Rome, *La Sapienza*, in cooperation with the Department of Aeronautics and Mechanics. Based on these methods simpler methods have been devel-

oped, which represent the complete vortex layer by a single point vortex. The generation of vorticity in these methods is improved by introducing a so called *edge vortex*. The strength of the aeroacoustic source can be determined from the results of each of these methods for the numerical simulation of the unsteady vortical flow by application of the vortex sound theory of Powell (1964) and Howe (1975).

1.4 THESIS OVERVIEW

The main text of this thesis comprises chapter 2 to 6. The basic equations describing the production of aeroacoustic sound are derived in the next chapter. Several approximations to the basic equations are presented leading to inhomogeneous convected wave equations. Also the different models found in the literature to describe the generation and convection of vorticity at high Reynolds numbers, some of which are also used in the present study, are described in some detail. Special attention will be given to the so-called Kutta condition, which in potential flow models accounts for the action of viscous forces at sharp edges.

In chapter 3 results of the various potential flow methods are compared for starting flows such as the starting flow past a wedge, out of a two-dimensional channel exit and in a T-junction. For a starting flow the moment of initial separation of the flow is exactly known, the flow is initially laminar and vorticity is only present in the shear layer generated at sharp edges. For the starting flow past a wedge a self-similar solution can be obtained. Therefore the starting flow about a wedge serves as a suitable generic flow problem which has been employed extensively to compare the results of the different numerical simulation methods.

Following a period of transient flow in aeroacoustic problems the flow becomes usually periodic. Chapter 4 is devoted to the periodic vortex formation process in several configurations. For the periodic flow problems it is assumed that the amplitude of the acoustic flow is fixed and not influenced by the interaction with the periodic mean flow field. The important parameters of the periodic flow problem appear to be the Strouhal number and the ratio of the amplitude of the acoustic field to the magnitude of the mean flow. Also in chapter 4 the periodic flow at moderate as well as at high amplitudes of the acoustic field is considered, both for a T-junction and a cross-junction. Without mean flow the vortex formation induced by a resonating acoustic field is a highly nonlinear process. Such a case is studied for the flow out of a sharp-edged two-dimensional nozzle. The conditions chosen correspond to two cases, the case of high acoustic Strouhal numbers Sr_{ac} , and the case of Sr_{ac} of order one.

Chapter 5 describes the results of an experimental investigation into the propagation and reflection of acoustic waves in a long open-ended pipe. Acoustic energy losses due to radiation at the open end, losses due to vortex formation at the sharp-edged nozzle and visco-thermal losses due to friction and heat conduction at the pipe walls are determined experimentally.

There is only scarce experimental data on the influence of a low Mach number (turbulent) mean flow on the reflection coefficient and damping coefficient. Damping coefficients obtained by Ronneberger (1975) are for high frequencies ($f \approx 1000$ Hz) and relatively high values of the Mach number ($M \approx 0.2$). The results of the effects of a mean flow component

on the reflection coefficient of an open pipe predicted by the theories of Munt (1977, 1990), Cargill (1982) and Rienstra (1981) cannot be validated with the experimental data found in literature. In the present study accurate experimental data has been obtained using a multi-microphone method.

As an application of the computational methods chapter 6 deals with flow-induced resonances in a system with two side branches, i.e. in a tandem T-junction and in a cross-junction. In this chapter experimental data on the influence on the aeroacoustic characteristics of the length of the side branch, the geometry of the edges of the junctions and the mean flow are presented. Employing the vortex methods the strength of the aeroacoustic source can be determined at a given value of both the Strouhal number and the acoustic amplitude. By estimating the energy losses due to friction and radiation in the resonator the equilibrium amplitude of the acoustic resonance can be predicted. Chapter 7 provides a summary, some final remarks and the main conclusions of the present investigation.

REFERENCES

- BALDWIN R.M. & SIMMONS H.R. (1986) Flow-induced vibration in safety relief valves. *J. Pressure Vessel Techn.* **108**, 267 - 272.
- BROWN C.E. & MICHAEL W.H. (1954) Effect of leading-edge separation on the lift of a delta wing. *J. Aero. Sci.* **21**, 690 - 694.
- BRUGGEMAN J.C. (1987a) Flow induced pulsations in pipe systems. PhD thesis Eindhoven University of Technology
- BRUGGEMAN J.C. (1987b) The propagation of low-frequency sound in a two-dimensional duct system with T-joints and right angles. *J. Acoust. Soc. Am.* **82** 3, 1045 - 1051.
- BRUGGEMAN J.C., HIRSCHBERG A., DONGEN M.E.H. VAN, WIJNANDS A.P.J. & GORTER J. (1991) Self-sustained aero-acoustic pulsations in gas transport systems: experimental study of the influence of closed side branches. *J. Sound & Vibr.* **150** 3, 371 - 393.
- CANNEL P. & FLOWERS WILLIAMS J.E. (1973) Radiation from line vortex filaments exhausting from a two-dimensional semi-infinite duct. *J. Fluid Mech.* **58** 1, 65 - 80.
- Cargill A.M. (1982) Low frequency acoustic radiation from a jet pipe - a second order theory. *J. Sound & Vibr.* **83** 3, 339 - 354.
- CHANAUD R.C. (1970) Aerodynamic Whistles. *Scientific American* **222**, 40 - 46.
- CRIGHTON D.G. (1972) Radiation from vortex filament motion near a half plane. *J. Fluid Mech.* **51** 2, 357 - 362.
- DISSELHORST J.H.M. (1978) Acoustic resonance in open tubes. PhD thesis Twente University of Technology
- DISSELHORST J.H.M & WIJNGAARDEN L. VAN (1980) Flow in the exit of open pipes during acoustic resonance. *J. Fluid Mech.* **99** 2, 293 - 319.
- FABRE B. (1992) La production du son dans les instruments de musique à embouchure de flûte. PhD thesis Université du Maine, Le Mans, France
- FLETCHER N.H. (1979) Air flow and sound generation in musical wind instruments. *Ann. Rev. Fluid Mech.* **11**, 123 - 146.
- FLETCHER N.H. (1990) Nonlinear theory of musical wind instruments. *Applied Acoustics* **30**, 85 - 115.

- HIRSCHBERG A., BRUGGEMAN J.C., WIJNANDS A.P.J. & SMITS N. (1989) The 'whistler nozzle' and horn as aeroacoustic sound sources in pipe systems. *Acustica* **68**, 157 - 160.
- HOWE M.S. (1975) Contributions to the theory of aerodynamic sound, with application to excess jet noise and the theory of the flute. *J. Fluid Mech.* **71** 4, 625 - 673.
- LESSER M.B. & CRIGHTON D.G. (1975) Physical acoustics and the Method of Matched Asymptotic Expansions. in *Physical acoustics* **11** Ed. by Mason, Academic Press.
- LIGHTHILL M.J. (1952) On sound generated aerodynamically I: General theory. *Proc. Roy. Soc. Lond. A* **211**, 564 - 587.
- LIGHTHILL M.J. (1954) On sound generated aerodynamically II: Turbulence as a source of sound. *Proc. Roy. Soc. Lond. A* **222**, 1 - 32.
- MÖHRING W. (1978) On vortex sound at low mach number. *J. Fluid Mech.* **85** 4, 685 - 691.
- MÜLLER E-A. & OBERMEIER F. (1988) Vortex Sound. *Fluid Dynamics Research* **3**, 43 - 51.
- MUNT R.M. (1977) The interaction of sound with a subsonic jet issuing from a semi-infinite cylindrical pipe. *J. Fluid Mech.* **83** 4, 609 - 640.
- MUNT R.M. (1990) Acoustic transmission properties of a jet pipe with subsonic jet flow: 1. The cold jet reflection coefficient. *J. Sound & Vibr.* **142** 3, 413 - 436.
- PARKER R. & WELSH M.C. (1983) Effects of sound on flow separation from blunt flat plates. *Int. J. Heat & Fluid flow.* **4** 2, 113 - 127.
- POWELL A. (1964) Theory of vortex sound. *J. Acoust. Soc. Am.* **36** 1, 177 - 195.
- RIENSTRA S.W. (1981) On the acoustical implications of vortex shedding from an exhaust pipe. *J. Eng. for Ind.* **103**, 378 - 384.
- ROCKWELL D. & NAUDASCHER E. (1978) Review - Self-sustained oscillations of flow past cavities. *J. Fluids Eng.* **100**, 152 - 165.
- ROCKWELL D. & NAUDASCHER E. (1979) Self-sustained oscillations of impinging free shear layers. *Ann. Rev. Fluid Mech.* **11**, 67 - 94.
- ROCKWELL D. (1983) Oscillations of impinging shear layers. *A.I.A.A. Journal* **21** 5, 645 - 664.
- RONNEBERGER D. (1975) Genaue Messung der Schalldämpfung und der phasengeschwindigkeit in durchstromten Rohren im Hinblick auf die Wechselwirkung zwischen Schall und Turbulenz. *Habilitationsschrift Math.-Naturw. Fak. Univ. Göttingen*
- STOKES A.N. & WELSH M.C. (1986) Flow-resonant sound interaction in a duct containing a plate II: square leading edge. *J. Sound & Vibr.* **104** 1, 55 - 73.
- STONEMAN S.A.T., HOURIGAN K., STOKES A.N. & WELSH M.C. (1988) Resonant sound caused by flow past two plates in tandem in a duct. *J. Fluid Mech.* **192**, 455 - 484.
- STÜBER B. (1970) Schallabstrahlung und korperschallanregung durch wirbel. *Acustica* **23**, 82 - 92.
- THOMPSON M.C., HOURIGAN K. & WELSH M.C. (1992) Acoustic sources in a tripped flow past a resonator tube. *A.I.A.A. Journal* **30** 6, 1484 - 1491.
- WELSH M.C. & GIBSON D.C. (1979) Interaction of induced sound with flow past a square-leading-edged plate in a duct. *J. Sound & Vibr.* **67** 4, 501 - 511.
- WELSH M.C. & STOKES A.N. (1984) Flow-resonant sound interaction in a duct containing a plate, part I: Semi-circular leading edge. *J. Sound & Vibr.* **95** 3, 305 - 323.
- YATES J.E. (1978) Application of the Bernoulli enthalpy concept to the study of vortex noise and jet impingement noise. *NASA contractor report* 2987
- ZIADA S. & BÜHLMANN E.T. (1992) Self-excited resonances of two side-branches in close proximity. *J. Fluids & Structures* **6**, 583 - 601.

Theory

Abstract

In this chapter the theory is developed which describes the sound generated by aerodynamic sources, in particular the theory underlying the vortex sound phenomenon. The source of vortex sound is unsteady vorticity, interacting with an acoustic field. For the description of the vorticity in an otherwise irrotational flow several vortex methods are discussed which can be used to estimate the intensity of the sources.

2.1 AEROACOUSTICS

2.1.1 Governing equations

At the end of the last century, following the time that Rayleigh published his '*Theory of Sound*' (1877), it was generally believed that the source of acoustic sound was primarily mechanical vibrations of structures. It was not until 1952 that, stimulated by the problem of predicting jet noise, Sir James Lighthill presented his famous articles '*On Sound Generated Aerodynamically*' (1952, 1954), which identified unmistakably unsteady flow as a so-called *aero-acoustic* source of sound. Lighthill (1952) considered a medium with speed of sound c_0 and density ρ_0 , quiescent everywhere except for a finite region with a fluctuating velocity field. Lighthill considered this region as the region with sources of sound. The derivation of Lighthill's equation starts from the general conservation laws for mass, momentum and energy, which in Einstein notation read

$$\frac{\partial \rho}{\partial t} + \frac{\partial}{\partial x_i}(\rho v_i) = q \quad (2.1)$$

$$\frac{\partial}{\partial t}(\rho v_i) + \frac{\partial}{\partial x_j}(\rho v_i v_j) = -\frac{\partial p}{\partial x_i} + \frac{\partial \tau_{ij}}{\partial x_j} + f_i \quad (2.2)$$

$$\frac{\partial}{\partial t}(\rho E) + \frac{\partial}{\partial x_i}(\rho E v_i) = \frac{\partial Q}{\partial t} - \frac{\partial q_h}{\partial x_i} - \frac{\partial}{\partial x_i}(\rho v_i) + \frac{\partial}{\partial x_i}(\tau_{ij} v_j) + f_i v_i \quad (2.3)$$

where $\vec{v} = (v_1, v_2, v_3)^T$ is the velocity, p denotes the static pressure, $E = e + \frac{1}{2}|\vec{v}|^2$ is the total energy per unit mass, with e the internal energy per unit mass. q_h is the heat flux which can be related to temperature T by Fourier's law for heat conduction $q_h = -\kappa \frac{\partial T}{\partial x_i}$ where κ the coefficient of thermal conductivity. Furthermore, q is a mass source, \vec{f} is a body force and Q is an energy source. For a Newtonian fluid in thermodynamic equilibrium

the viscous stress tensor τ_{ij} is given by

$$\tau_{ij} = \mu \left(\frac{\partial v_i}{\partial x_j} + \frac{\partial v_j}{\partial x_i} \right) - \frac{2}{3} \mu \left(\frac{\partial v_k}{\partial x_k} \right) \delta_{ij} \quad (2.4)$$

where Stokes' law has been employed to relate the second coefficient of viscosity to the dynamic viscosity μ of the fluid. Subtracting the divergence of the momentum equation from the time derivative of the mass conservation equation and subtracting $c_0^2 \nabla^2 (\rho - \rho_0)$ from both sides of the resulting equation, leads to

$$\left(\frac{\partial^2}{\partial t^2} - c_0^2 \frac{\partial^2}{\partial x_i^2} \right) \rho' = \frac{\partial q}{\partial t} - \frac{\partial f_i}{\partial x_i} + \frac{\partial^2 T_{ij}}{\partial x_i \partial x_j} \quad (2.5)$$

$$\text{with } T_{ij} = \rho v_i v_j + \tau_{ij} + (p - c_0^2 \rho') \delta_{ij} \quad (2.6)$$

where ρ_0 and c_0 are the time-independent density and speed of sound outside the source region, respectively. Furthermore, T_{ij} is Lighthill's Stress Tensor.

Equation (2.5) is an inhomogeneous wave equation for the density fluctuations $\rho' = \rho - \rho_0$ which, in absence of external mass sources and external forces, is Lighthill's wave equation. The formal solution of equation (2.5) in free space can be obtained from a convolution of the right-hand side of this equation with the appropriate Green's function. It appears (e.g. see Crighton (1975)) that a time-dependent mass source acts as an acoustic monopole, while a nonuniform body force acts as an acoustic dipole. The term with the second derivative of Lighthill's stress tensor represents an acoustic quadrupole. It contains contributions due to the fluctuating Reynolds stresses, viscous forces and entropy inhomogeneities in the source region. In fact, the contribution due to the viscous forces involves an additional space derivative, (see equation (2.4)) and therefore correspond to an octopole. However, entropy fluctuations can induce an acoustic monopole. In the present study it is assumed that external mass sources are absent and that the influence of external forces can be neglected. In that case the Lighthill stress tensor represents the only source of sound.

Outside the region of sound sources, the flow is described by the homogeneous wave equation for the density fluctuations ρ' . These disturbances propagate in the quiescent medium with the speed of sound c_0 of the ambient fluid.

In the presence of a body fluctuating forces on the body caused by the unsteady flow about the body, possibly in combination with the unsteady motion of the body, may act as sound sources which are actually more efficient than the sources of sound due to the unsteady flow itself.

If the surface of the body is given by $S(\vec{x}, t) = 0$ where $S(\vec{x}, t) > 0$ is defined as the region outside the body, it follows that

$$\frac{\partial S(\vec{x}, t)}{\partial t} + u_i \frac{\partial S(\vec{x}, t)}{\partial x_i} = 0 \quad (2.7)$$

where \vec{u} is the velocity of the point \vec{x} on the surface. Since the equations for the conservation of mass and momentum are valid outside the body only, the wave equation for the density fluctuations can be derived for the generalized function $\rho' \mathcal{H}(S)$, where $\mathcal{H}(S)$ is the Heaviside step function, which is equal to 1 outside the body and 0 inside the body. Multiplying the

equations of the conservation of mass and momentum (2.2), in absence of external mass sources and external forces, with $\mathcal{H}(\mathcal{S})$ and allowing a non-zero velocity \vec{v} at the surface $\mathcal{S}(\vec{x}, t)$, it is found (Crighton (1975)) that

$$\left(\frac{\partial^2}{\partial t^2} - c_0^2 \frac{\partial^2}{\partial x_i^2} \right) \rho' \mathcal{H}(\mathcal{S}) = \frac{\partial}{\partial t} (Q \delta(\mathcal{S})) - \frac{\partial}{\partial x_i} (F_i \delta(\mathcal{S})) + \frac{\partial^2}{\partial x_i \partial x_j} (T_{ij} \mathcal{H}(\mathcal{S})) \quad (2.8)$$

$$\text{with } Q = [\rho_0 v_i + \rho(u_i - v_i)] \frac{\partial \mathcal{S}}{\partial x_i}$$

$$F_i = [p \delta_{ij} + \rho u_i (u_j - v_j)] \frac{\partial \mathcal{S}}{\partial x_j}$$

where T_{ij} is given by equation (2.6) and $\delta(\mathcal{S})$ is the Dirac delta function, which is zero everywhere except at the boundary $\mathcal{S}(\vec{x}, t) = 0$ of the body. Outside the surface of the body Lighthill's equation (2.5), with $q = 0$ and $\vec{f} = 0$, is retained. However, due to the presence of the body, a monopole-like term arises from the rate of displacement of the fluid by the body and a dipole-like term due to the stresses exerted by the surface of the body on the fluid. Furthermore, when the body is permeable ($\vec{v} \neq \vec{u}$), additional monopole and dipole terms arise as given by the second parts of Q and \vec{F} , respectively.

Lighthill (1952) showed that the wave equation for the density fluctuations can be used to determine for example the sound production of free turbulent jets. This yields the famous M^8 law for the increase of acoustic power with the jet exhaust Mach number M . Lighthill's theory assumes that outside of the source region the medium is quiescent, so that the propagation of density fluctuations into the region exterior to the source region is described by the homogeneous wave equation given by the left-hand side of equation (2.5). This assumption is not valid for the case of the generation and propagation of sound in internal flows, where in absence of acoustic sources, the propagation of sound is described by a convected wave equation. A number of theories have been put forward to account for the effect of a non-zero mean flow on the propagation of sound. Phillips (1960) derived a convected wave equation for the acoustic variable $\Pi = \frac{1}{\gamma} \ln(p/p_0)$,

$$\left(\frac{D^2}{Dt^2} - \frac{\partial}{\partial x_i} \left(c^2 \frac{\partial}{\partial x_i} \right) \right) \Pi = \frac{\partial v_i}{\partial x_j} \frac{\partial v_j}{\partial x_i} + \frac{D}{Dt} \left(\frac{1}{c_p} \frac{DS}{Dt} \right) + \frac{\partial}{\partial x_i} \left(\frac{1}{\rho} \frac{\partial \pi_{ij}}{\partial x_j} \right) \quad (2.9)$$

where $\gamma = c_p/c_v$ denotes the ratio of the specific heat at constant pressure and the specific heat at constant volume, c is the local speed of sound and S the specific entropy. Furthermore, $\frac{D}{Dt} = \frac{\partial}{\partial t} + v_i \frac{\partial}{\partial x_i}$ is the substantial derivative. It has been proven by Lilley (1972) that the source terms of Phillips' equation still contain first-order terms in the perturbations and as a result the source terms do not vanish quadratically outside the source region. This implies that the homogeneous wave equation, given by the left-hand side of this equation does not accurately describe the propagation of perturbations outside the source region. Lilley (1972) presented an alternative third-order equation for Π which, together with Phillips' equation, is extensively discussed by Goldstein (1976). It appeared that both these wave equations are very well suited for many aero-acoustic problems involving supersonic jet flow. For subsonic isentropic flow however, results more useful than obtained when applying Lighthill's equation have not been obtained.

A more suitable generalization of Lighthill's wave equation allowing convection has been derived by Powell (1964) and Howe (1975).

In his 'Theory of vortex sound' Powell (1964) argued that for low Mach number, inviscid, isentropic flow the Lighthill tensor (2.6) can be approximated by

$$T_{ij} = \rho_0 v_i v_j + \mathcal{O}(M^2) \quad (2.10)$$

where \vec{v} is the velocity of the incompressible flow in the source region. The source term in Lighthill's wave equation then can be written as

$$\frac{\partial \rho_0 v_i v_j}{\partial x_i \partial x_j} = \rho_0 \nabla \cdot (\vec{\omega} \times \vec{v}) + \nabla^2 (\frac{1}{2} \rho_0 |\vec{v}|^2) \quad (2.11)$$

The first term on the right contains the vorticity $\vec{\omega} = \nabla \times \vec{v}$. It has been argued by Powell (1964), later confirmed by Crow (1970), that in an unbounded domain the second term on the right gives rise to a much less intense sound field than that associated with the first term. The first term has the appearance of a dipole-like term, however due to momentum conservation (in absence of a rigid body) the net vorticity must be zero, and as a result the first term represents a quadrupole source.

For an inviscid, ideal gas, which satisfies the relation $p = \rho RT$, with R the gas constant and T the absolute temperature, Howe (1975) showed that the propagation of irrotational acoustic perturbations in an irrotational isentropic mean flow is given by the homogeneous convected wave equation

$$\begin{aligned} \mathcal{L} H &= 0 \\ \text{with } \mathcal{L} &= \frac{D}{Dt} \left(\frac{1}{c^2} \frac{D}{Dt} \right) + \frac{1}{c^2} \frac{D\vec{v}}{Dt} \cdot \nabla - \nabla^2 \end{aligned} \quad (2.12)$$

where $H = h + \frac{1}{2} |\vec{v}|^2$, is the total enthalpy per unit mass with h the enthalpy per unit mass. For an irrotational flow, in absence of external forces, the total enthalpy can be related to the potential of the flow, obtained from $\vec{v} = \nabla \varphi$, by $H = -\frac{\partial \varphi}{\partial t}$.

\mathcal{L} is the appropriate wave operator for the propagation of acoustic disturbances into the region exterior to the source region. For an inviscid ideal gas, in presence of regions of vorticity, but neglecting heat conduction, Howe (1975) showed that the source terms for equation (2.12) are given by

$$\mathcal{L} H = \nabla \cdot \vec{L} - \frac{1}{c^2} \frac{D\vec{v}}{Dt} \cdot \vec{L} \quad (2.13)$$

where \vec{L} is the so-called 'Lamb vector', given by

$$\vec{L} = \vec{\omega} \times \vec{v} - T \nabla S \quad (2.14)$$

which yields a generalization of Powell's (1964) vortex sound theory. Since this convected wave equation has proven to be very useful in describing production and propagation of sound in internal ducts, it is the basic equation which will be used furtheron in this thesis. A detailed derivation of the equation is given in Appendix A.

For many low speed aero-acoustic problems, it is much more convenient to solve the wave equation derived by Howe (1975), i.e. equation (2.13), than Lighthill's wave equation, i.e. equation (2.5). The reason is that in an incompressible high-Reynolds-number flow the vorticity is often confined to thin vortex layers and slender elongated vortex cores, i.e. vortex sheets and vortex filaments, respectively. These delta-function type of vorticity distributions simplify the solution of the equations. Furthermore, by taking the rotation of the Euler equations for an incompressible, homentropic flow a purely kinematic equation in terms of \vec{v} and $\vec{\omega}$ is obtained. In an inviscid flow the pressure can be obtained after the velocity has been determined from the Bernoulli equation. For a low-Mach-number, high-Reynolds-number, isentropic internal flow a first-order approximation of Howe's equation (2.13) has been derived by Bruggeman (1987) for two ranges of values of the amplitude of the acoustic field. The first case is the case assuming moderate values of the amplitude of the acoustic velocity field \hat{u}_{ac} , i.e. $\hat{u}_{ac}/U_0 = \mathcal{O}(M)$. The second case corresponds to the case of high values of the acoustic amplitude, i.e. $\hat{u}_{ac}/U_0 = \mathcal{O}(1)$. Because acoustic resonances in pipe systems typically occur for a Strouhal number $\omega H/U_0 = \mathcal{O}(1)$, based on the side branch width H and the frequency ω of the acoustic field, Bruggeman (1987) considered this Strouhal number only.

For the moderate-amplitude case and for a Strouhal number of order unity, the amplitudes of the fluctuating parts of the velocity u_{ac} , pressure p' and specific enthalpy H' are of the order $\mathcal{O}(MU_0)$, $\mathcal{O}(\rho_0 U_0^2)$ and $\mathcal{O}(U_0^2)$, respectively.

The first-order approximation of equation (2.13) is then given by

$$\left(\frac{1}{c_0^2} \frac{D^2}{Dt^2} - \nabla^2 \right) H'(\vec{x}, t) = \nabla \cdot (\vec{\omega} \times \vec{v}) \quad (2.15)$$

which is a modification of Powell's (1964) wave equation for the case without a mean velocity field into a convected wave equation for the case with a mean velocity field.

For high values of the acoustic amplitude, and Strouhal numbers of order unity, the fluctuating parts of the velocity, pressure and specific enthalpy are $\mathcal{O}(U_0)$, $\mathcal{O}(\rho_0 c_0 U_0)$ and $\mathcal{O}(c_0 U_0)$, respectively. The first-order approximation of equation (2.13) is then given by a wave equation for the pressure

$$\left(\frac{1}{c_0^2} \frac{\partial^2}{\partial t^2} - \nabla^2 \right) p'(\vec{x}, t) = \rho_0 \nabla \cdot (\vec{\omega} \times \vec{v}) \quad (2.16)$$

in which nonlinear effects and convective effects in the wave propagation have been neglected. The case of moderate amplitudes has been studied in detail by Bruggeman *et al.* (1987, 1991) for a pipe system consisting of a main pipe with a single closed side branch. In the present study the case of high amplitude is considered for a pipe system with two closed side branches. The side branches can be placed behind each other (tandem T-junction configuration), or opposite to each other (cross-junction configuration), e.g. see figure 1.1. In both cases a closed acoustic resonator is obtained with a high quality factor due to low radiation losses. Powell's theory will be used to estimate the aeroacoustic source strength for this high-amplitude case.

More extensive reviews of aerodynamically generated sound, i.e. aeroacoustics, can be found in Ffowcs-Williams (1972, 1977, 1982), Doak (1973), Crighton (1975, 1981) and Powell (1990).

2.1.2 Solution for high acoustic amplitudes

A formal solution of the wave equation (2.16), can be obtained in integral form by using Green's theorem. The Green's function associated with the linear wave operator can be derived by solving for the pulse response

$$\left(\frac{1}{c_0^2} \frac{\partial^2}{\partial t^2} - \nabla^2\right) G(\vec{x}, t|\vec{y}, \tau) = \delta(\vec{x} - \vec{y})\delta(t - \tau) \quad (2.17)$$

where the pulse is released at point \vec{y} at time τ and the Green's function determines the pulse response at position \vec{x} at time t . The causality condition for the Green's function requires that the pulse response at time t originates from the pulse at time τ and therefore $G(\vec{x}, t|\vec{y}, \tau) = 0$ and $\frac{\partial}{\partial t}G(\vec{x}, t|\vec{y}, \tau) = 0$ for $t \leq \tau$. By multiplying equation (2.16) with $G(\vec{x}, t|\vec{y}, \tau)$ and subtracting equation (2.17) multiplied with $p'(\vec{y}, \tau)$ and subsequently performing an integration in time and space we find (Goldstein (1976))

$$\begin{aligned} p'(\vec{x}, t) &= \int_{-\infty}^t \iiint_V G(\vec{x}, t|\vec{y}, \tau) \rho_0 \nabla_y \cdot (\vec{\omega} \times \vec{v}) dV(\vec{y}) d\tau \\ &+ \frac{1}{c_0^2} \int_{-\infty}^t \iiint_V \left(p(\vec{y}, \tau) \frac{\partial^2 G(\vec{x}, t|\vec{y}, \tau)}{\partial \tau^2} - G(\vec{x}, t|\vec{y}, \tau) \frac{\partial^2 p(\vec{y}, \tau)}{\partial \tau^2} \right) dV(\vec{y}) d\tau \\ &- \int_{-\infty}^t \iiint_V \left(p(\vec{y}, \tau) \nabla_y^2 G(\vec{x}, t|\vec{y}, \tau) - G(\vec{x}, t|\vec{y}, \tau) \nabla_y^2 p(\vec{y}, \tau) \right) dV(\vec{y}) d\tau \end{aligned} \quad (2.18)$$

where ∇_y denotes the gradient with respect to \vec{y} . By performing an integration by parts of the last two terms on the right, and using boundary conditions, we find

$$\begin{aligned} p'(\vec{x}, t) &= \int_{-\infty}^t \iiint_V G(\vec{x}, t|\vec{y}, \tau) \rho_0 \nabla_y \cdot (\vec{\omega} \times \vec{v}) dV(\vec{y}) d\tau \\ &+ \int_{-\infty}^t \iint_S \left(G(\vec{x}, t|\vec{y}, \tau) \frac{\partial p(\vec{y}, \tau)}{\partial n} - p(\vec{y}, \tau) \frac{\partial G(\vec{x}, t|\vec{y}, \tau)}{\partial n} \right) dS(\vec{y}) d\tau \\ &- \frac{1}{c_0^2} \left[\iiint_V \left(G(\vec{x}, t|\vec{y}, \tau) \frac{\partial p(\vec{y}, \tau)}{\partial \tau} - p(\vec{y}, \tau) \frac{\partial G(\vec{x}, t|\vec{y}, \tau)}{\partial \tau} \right) dV(\vec{y}) \right]_{-\infty}^t \end{aligned} \quad (2.19)$$

where $\frac{\partial}{\partial n} = \vec{n} \cdot \nabla_y$ denotes the derivative in the direction normal to the surface. The last term on the right vanishes at the upper limit due to the causality condition. The lower limit represents the initial condition. If we assume that the flow starts from rest or that the influence of the initial conditions on the solution at time t is negligible, for example such as for a stationary sound field, this term vanishes also.

The boundary conditions for the pressure $p'(\vec{x}, t)$ can be related to kinematic boundary conditions by using the momentum equation for an isentropic and inviscid flow, i.e.

$$\nabla p'(\vec{x}, t) = -\rho_0 \frac{\partial \vec{v}}{\partial t} - \rho_0 (\vec{\omega} \times \vec{v}) - \nabla \frac{1}{2} \rho_0 |\vec{v}|^2 \quad (2.20)$$

If the boundary S is chosen outside the source region then $\vec{\omega} = 0$ and because convective effects are neglected, we obtain $\vec{n} \cdot \nabla p(\vec{x}, t) = -\rho_0 \frac{\partial \bar{p}}{\partial t} \cdot \vec{n}$. At solid, non-moving boundaries the normal velocity vanishes and we find $\vec{n} \cdot \nabla p(\vec{x}, t) = 0$. At an ideal open end, the acoustic pressure $p'(\vec{x}, t) = 0$.

Now if for the Green's function we require that $\vec{n} \cdot \nabla G(\vec{x}, t|\vec{y}, \tau) = 0$ at rigid walls and $G(\vec{x}, t|\vec{y}, \tau) = 0$ at open ends, i.e. similar boundary conditions hold as for $p(\vec{x}, t)$, the fundamental solution is called a 'tailored' Green's function, and the solution is given by

$$p'(\vec{x}, t) = \int_{-\infty}^t \iiint_V G(\vec{x}, t|\vec{y}, \tau) \rho_0 \nabla_{\vec{y}} \cdot (\vec{\omega} \times \vec{v}) dV(\vec{y}) d\tau \quad (2.21)$$

By integrating equation (2.21) by parts we find

$$p'(\vec{x}, t) = \int_{-\infty}^t \iiint_V \rho_0 (\vec{\omega} \times \vec{v}) \nabla_{\vec{y}} \cdot G(\vec{x}, t|\vec{y}, \tau) dV(\vec{y}) d\tau \quad (2.22)$$

where the surface integral vanishes since $\vec{\omega} = 0$ ¹. In a real flow however, viscous effects and thermal conduction causes the vorticity to be non-zero at the rigid walls, while the pressure is not exactly zero at the open ends. This can be incorporated into the theory by considering a boundary just outside the boundary layer near the rigid walls, so that $\vec{\omega} = 0$. Due to viscothermal effects, the normal velocity is not zero at this boundary. If the Green's function is derived for ideal boundaries, with boundary conditions given above, we obtain

$$\begin{aligned} p(\vec{x}, t) &= \int_{-\infty}^t \iiint_V \rho_0 (\vec{\omega} \times \vec{v}) \nabla_{\vec{y}} \cdot G(\vec{x}, t|\vec{y}, \tau) dV(\vec{y}) d\tau \\ &+ \int_{-\infty}^t \iint_{S_{\text{rigid}}} G(\vec{x}, t|\vec{y}, \tau) \frac{\partial p(\vec{y}, \tau)}{\partial n} dS(\vec{y}) d\tau \\ &- \int_{-\infty}^t \iint_{S_{\text{open}}} p(\vec{y}, \tau) \frac{\partial G(\vec{x}, t|\vec{y}, \tau)}{\partial n} dS(\vec{y}) d\tau \end{aligned} \quad (2.23)$$

where the first term on the right-hand side describes the effect of the aeroacoustic source, the second term describes the viscothermal losses at the rigid boundaries and the third term describes radiation at open boundaries. For a periodic flow with stationary amplitude, the time average $\langle p'(\vec{x}, t) \rangle$ of the left-hand side of equation (2.23) is zero, and we obtain an energy balance between the production of acoustic energy by unsteady vorticity and dissipation by viscothermal effects and radiation of acoustic energy out of the region considered by averaging equation (2.23) over an oscillation period.

A generalization of this solution for the convected wave equation, equation (2.15), obtained for low acoustic amplitudes, can be found in Goldstein (1976).

¹Here it is assumed that the contribution of the separation point of the boundary where obviously $\omega \neq 0$ does not result into a significant value of the boundary integral.

2.1.3 Application to internal flow

In this section the formal solution of the wave equation for isentropic, inviscid flow will be applied to an internal flow with a region of non-zero, unsteady vorticity. The solution could be obtained in the *time domain* by searching for a periodic solution. In this case the frequency as well as the amplitude of the acoustic field could be determined. This procedure was used by Hardin & Pope (1992) to determine the sound generation by a stenosis in a pipe. Two different grids have been used, a fine grid to calculate the flow in the pipe and a course grid to obtain the generated sound field. This procedure of splitting the determination of the sound generation from the flow field is only possible at low amplitudes of the acoustic field, i.e. when the flow field is not strongly influenced by the acoustic velocity field. For high amplitudes of the acoustic field, the splitting of flow field and acoustic field is not valid anymore, since the flow field is strongly influenced by the acoustic velocity field.

In the present study acoustic resonances are studied for which the frequency is usually imposed by the acoustical resonator. In that case the amplitude of the acoustic pulsations can be obtained for a specific *frequency* by assuming an harmonic approximation of the solution. Balancing the energy of the acoustic sources with the losses by radiation and visco-thermal damping at the walls yields the amplitude of the acoustic field at the given frequency.

In absence of a mean flow the acoustic energy balance can be obtained from the energy equation (2.3), omitting external energy sources, friction and heat conduction, as

$$\rho_0 \frac{D}{Dt} (e + \frac{1}{2} |\vec{v}|^2) = -\nabla \cdot (p\vec{v}) + \vec{f} \cdot \vec{v} \quad (2.24)$$

By expanding the internal energy e around an equilibrium state e_0 , the acoustic energy balance can be written as (Pierce (1989), Hirschberg & Rienstra (1992))

$$\begin{aligned} \frac{\partial E_{ac}}{\partial t} + \nabla \cdot \vec{I}_{ac} &= -\mathcal{D} \\ \text{with } E_{ac} &= \frac{p'^2}{2\rho_0 c_0} + \frac{1}{2} \rho_0 |\vec{v}'|^2 \\ \vec{I}_{ac} &= p' \vec{v}' \\ \mathcal{D} &= -\vec{v}' \cdot \vec{f} \end{aligned} \quad (2.25)$$

where $p'(\vec{x}, t) = p(\vec{x}, t) - p_0(\vec{x})$ is the acoustic pressure, $\vec{v}'(\vec{x}, t) = \vec{v}(\vec{x}, t)$ is the acoustic velocity. Furthermore, E_{ac} is the acoustic energy, \vec{I}_{ac} is the acoustic intensity vector and \mathcal{D} is the dissipation function. If the acoustic field is periodic, the acoustic energy E_{ac} averaged over a period is constant. As a result, upon integrating the energy equation (2.25) over a fixed closed volume V and averaging over a period, one obtains

$$\iint_S \langle \vec{I}_{ac} \cdot \vec{n} \rangle dS = - \iiint_V \langle \mathcal{D} \rangle dV \quad (2.26)$$

where $\langle \rangle$ denotes the average over a period of the acoustic field. The term on the left is the acoustic power flux across the surface S of volume V , i.e. the net acoustic energy

production during one period of the acoustic field. If the source region contains an unsteady vorticity distribution, acting as a sound source, the effective time-dependent source strength (acoustic power output) can be determined as follows. The total velocity can be decomposed by the Helmholtz decomposition into an irrotational and a solenoidal part, i.e.

$$\vec{v} = \vec{v}_{irr} + \vec{v}_{sol} = \nabla\phi + \nabla \times \vec{\Psi} \quad (2.27)$$

Since $\nabla \cdot \vec{v} = \nabla \cdot \vec{v}_{irr}$, the compressible part of the flow is described by \vec{v}_{irr} , while the vorticity $\vec{\omega} = \nabla \times \vec{v} = \nabla \times \vec{v}_{sol}$ depends only on \vec{v}_{sol} . Therefore \vec{v}_{sol} describes the velocity induced by the vorticity, while the time-dependent part of \vec{v}_{irr} is identified as the acoustic field.

The Coriolis force acting on the vorticity embedded in the local velocity field is given by $\rho_0(\vec{\omega} \times \vec{v})$. The Coriolis force is acting as an external force on the acoustic irrotational flow field \vec{u}_{ac} . The rate of production of acoustic energy is then given by

$$P(t) = - \iiint_V \mathcal{D} dV = \iiint_V \rho_0(\vec{\omega} \times \vec{v}) \cdot \vec{u}_{ac} dV \quad (2.28)$$

where \vec{u}_{ac} is the time dependent part of the potential velocity \vec{v}_{irr} . This equation for the acoustic power produced by unsteady vorticity was first derived by Howe (1975). If it is assumed that the resonating acoustic field \vec{u}_{ac} and the Green's function in equation (2.23) have the same spatial distribution it is observed that the time average of equation (2.23) is equivalent with equation (2.28). This approximation is obvious if the acoustic pressure and Green's function are expanded in modes of the resonator and only a limited number of modes are retained.

In the presence of a mean flow \vec{v}_0 the energy conservation law is still given by equation (2.3). An acoustic energy balance in the presence of a mean flow in the form of equation (2.25) can be obtained in several ways. For low acoustic amplitudes $\hat{u}_{ac}/U_0 \ll 1$ Myers (1986) derived an acoustic energy balance from a Taylor series expansion of the energy equation, which agrees with the expression given by Goldstein (1976). However this expression is not valid for the high-amplitude case which is studied here. Using Howe's (1975) definition of the acoustic velocity, namely the time-dependent irrotational part of the total velocity, in combination with the solution for the convected wave equation given by Goldstein (1976) it can be shown that in presence of a mean flow the acoustic source strength is given by

$$P(t) = \iiint_V \rho_0(\vec{\omega} \times \vec{v}) \cdot \left(\vec{u}_{ac} + \frac{\rho'}{\rho_0} \vec{v}_0 \right) dV \quad (2.29)$$

This equation is one of the approximations derived by Jenvey (1989) and is an extension of the relation derived by Howe (1975) and given in equation (2.28). The correction factor due to the presence of a mean flow is of $\mathcal{O}(M^2)$ for low acoustic amplitudes, and of $\mathcal{O}(M)$ for high acoustic amplitudes. Since for the cases considered in the present study the acoustic source is performing work in a density node of the acoustic field, the density fluctuations are determined by hydrodynamic fluctuations which are of $\mathcal{O}(M^2)$ and negligible for a low Mach number flow.

2.1.4 Conclusion

In internal flows self-sustained pulsations are caused by the coupling between vortex shedding and a resonating acoustic field. This phenomenon can be described by the vortex sound theory by Powell (1964) and Howe (1975). For high values of the amplitude of the acoustic field, when acoustic pressure fluctuations are of the order $\mathcal{O}(\rho_0 c_0 U_0)$, the propagation of acoustic pressure fluctuations is described to first order by the non-convected wave equation (2.16). The aero-acoustic source of the acoustic pressure waves can be obtained from the theory of Powell (1964), which implies that the source can only be non-zero in a region where vorticity is present. For a periodic acoustic field the acoustic energy generated by the aeroacoustic source is dissipated by visco-thermal action or radiated energy from the region of interest. When the source region is small compared to the acoustic wave length the strength of the aeroacoustic source can be determined from an incompressible flow model describing the generation and convection of vorticity in the compact source region. In the next section different methods describing flows with vorticity will be presented.

2.2 VORTEX DYNAMICS

2.2.1 Introduction

For a low-Mach-number, isentropic flow we found from equation (2.13) that in absence of moving boundaries, non-uniformly distributed unsteady vorticity is the most important source of sound. For this reason the sound generated by a region of non-zero vorticity is usually called '*vortex sound*'. In order to quantify the source term in the wave equation, the flow field in the source region has to be determined in detail.

In this section different methods will be presented which describe the generation and convection of vorticity as well as the formation of vortex cores with concentrated vorticity. At high Reynolds numbers vorticity is concentrated in thin regions at solid boundaries, i.e. boundary layers. However, if separation of the flow occurs at a sharp edge or on a smooth part of the surface in a region with a strong adverse pressure gradient, vorticity is convected away from the solid surface and can reach a region far removed from the boundaries, i.e. shear layers. Since the Reynolds number in our experiments is usually larger than 10^5 , the boundary layers are thin compared to the characteristic dimension of the geometry. This implies that the vorticity is initially confined to thin free shear layers. In the limit of infinite Reynolds number, which we will consider in the mathematical modeling of the flow, vorticity is confined to an infinitesimally thin vortex sheet. The flow is irrotational everywhere except at the vortex sheet itself and can therefore be described by a velocity potential. The stability of vortex sheets and of finite-thickness vortex layers is discussed at the end of this section.

In real flows, due to the influence of molecular diffusion or turbulence, vorticity is diffused in space and annihilates when it merges with vorticity of opposite sign. In the mathematical model of inviscid flow used here, vorticity is not diffused while the annihilation of vorticity has to be included artificially in the model for cases where long-time behavior is to be investigated. The problem of annihilation of vorticity in the numerical model is avoided here. In all numerical simulations the onset of an oscillatory flow is considered

during four periods of oscillation at most, and annihilation of vorticity is not considered.

For the geometries considered the region where the vorticity is an aerodynamic source of sound is small compared to the acoustic wavelength. As a result, to first-order approximation, the source region can be considered as locally incompressible with

$$\nabla \cdot \vec{v} = 0 \quad (2.30)$$

describing conservation of mass in the source region. Using this relation a stream function $\vec{\Psi}$ can be defined as $\vec{v} = \nabla \times \vec{\Psi}$. The conservation of momentum can then be written, in absence of external forces, as

$$\frac{D\vec{v}}{Dt} = -\frac{1}{\rho}\nabla p + \nu\nabla^2\vec{v} \quad (2.31)$$

The static pressure p can be eliminated by taking the curl of the equation, resulting in the vorticity transport equation

$$\frac{D\vec{\omega}}{Dt} = (\vec{\omega} \cdot \nabla)\vec{v} + \nu\nabla^2\vec{\omega} \quad (2.32)$$

where $\vec{\omega} = \nabla \times \vec{v}$ is the vorticity vector.

Vorticity is a material property, attached to the fluid particles, and convects with the local fluid velocity. Taking the surface integral of equation (2.32) shows that the circulation of a closed contour, enclosing a region of non-zero vorticity, traveling with the flow can only change by diffusion of vorticity through the contour, so that for negligible viscosity the circulation is conserved.

This was first derived by Kelvin, and is therefore called Kelvin's theorem.

$$\frac{\partial\Gamma}{\partial t} = -\nu \oint_C (\nabla \times \vec{\omega}) \cdot d\vec{l} \quad (2.33)$$

where $\Gamma = \iint_A \vec{\omega} \cdot \vec{n} dS = \oint_C \vec{v} \cdot d\vec{l}$ is the circulation. In the derivation of equation (2.33) we have used Stokes' theorem and that for an incompressible flow $\nabla^2\vec{\omega} = -\nabla \times \nabla \times \vec{\omega}$. In general, the velocity vector \vec{v} can be written as the sum of an irrotational part \vec{v}_{irr} and a solenoidal part \vec{v}_{sol} according to equation (2.27) which can be described by a scalar velocity potential ϕ and a vector stream function $\vec{\Psi}$, respectively. Substitution of this decomposition of the velocity into the conservation of mass, given by equation (2.30), yields the Laplace equation for the scalar velocity potential. The vorticity depends only on the vector velocity potential, which follows from taking the curl of equation (2.27).

$$\nabla^2\phi = 0 \quad \vec{\omega} = \nabla \times \nabla \times \vec{\Psi} \quad (2.34)$$

In this way the irrotational flow, consisting of a mean flow component and a superimposed acoustic field and the flow field induced by the vorticity field can be considered as separate contributions in the total velocity. The solenoidal velocity \vec{v}_{sol} induced by the distributed vorticity can be obtained from the linear Poisson equation

$$\nabla^2\vec{v}_{sol} = -\nabla \times \vec{\omega} \quad (2.35)$$

The acoustic flow field is defined by the time-dependent part $\phi_{ac}(\vec{x}, t)$ of the scalar velocity potential, while the mean flow is described by the time-independent part $\phi_0(\vec{x})$ so that $\phi(\vec{x}, t) = \phi_0(\vec{x}, t) + \phi_{ac}(\vec{x}, t)$. The contribution due to the vorticity is described by the vector stream function $\vec{\Psi}$.

Since the present study is limited to two-dimensional flows, from now on we will describe the two-dimensional situation. For this case a notation in complex variables is very convenient and will be used throughout. In a two-dimensional flow, the term $(\vec{\omega} \cdot \nabla)\vec{v}$, which describes the rate of deformation of vortex lines, also called vortex stretching, vanishes and the vorticity has only one component ω , which is in the direction normal to the two-dimensional plane. Also the vector stream function has only one component ψ , also in the direction normal to the flow.

For two-dimensional flow the vorticity transport equation, neglecting viscosity, becomes

$$\frac{D\omega}{Dt} = 0 \quad (2.36)$$

and the vorticity, which is now a scalar quantity is related to the stream function by

$$\nabla^2\psi = -\omega \quad (2.37)$$

The solenoidal part of the velocity, due to the distributed vorticity, can be obtained from

$$v_{sol}^*(z_0) = \frac{1}{2\pi i} \iint_A \frac{\omega(z)}{z_0 - z} dz \quad (2.38)$$

where $z = x + iy$ is the complex coordinate with $i = \sqrt{-1}$, $v(z) = v_x + iv_y$ is the complex-valued velocity in a point z , with an asterisk denoting the complex conjugate. The integration is over the region of non-zero vorticity.

A further simplification is obtained if the vorticity is confined to a number of regions A_j , $j = 1..NR$ each of uniform vorticity ω_j , i.e. vorticity distribution $\omega(z) = \sum_{j=1}^{NR} \omega_j \mathcal{H}(A_j)$ with $\mathcal{H}()$ the Heaviside function which is one inside the region A_j and zero outside. Equation (2.38) then becomes

$$v_{sol}^*(z_0) = \sum_{j=1}^{NR} \frac{\omega_j}{2\pi i} \oint_{\partial A_j} \ln(z_0 - z) dz \quad (2.39)$$

where the integration is along the boundary ∂A_j of each region A_j . The method of determining the velocity field due to patches of piecewise uniform vorticity is called the 'contour dynamics' method and is described in more detail by Zabusky *et al.* (1979).

The vorticity can be confined to a number of curves C_j , $j = 1..NL$, given by $z = z_j(s)$, with s the arc length along the curve C_j , and vorticity distribution $\omega(z) = \sum_{j=1}^{NL} \gamma_j(s) \delta(z - z_j(s))$, with $\delta()$ the Dirac delta function and $\gamma_j(s)$ is the vortex distribution on curve C_j . The velocity, induced by these vortex sheets follows from equation (2.38)

$$v_{sol}^*(z_0) = \sum_{j=1}^{NL} \frac{1}{2\pi i} \int_{C_j} \frac{\gamma_j(s)}{z_0 - z_j(s)} ds \quad (2.40)$$

where the integration is along the curves C_j , and we have used that $\left| \frac{dz}{ds} \right| = 1$. Methods based on this kind of vorticity distributions are called 'vortex sheet' methods and will be described in the next section.

Finally the vorticity can be confined to a number of discrete points $X_j, j = 1..NV$, so that the vorticity distribution is given by $\omega(z) = \sum_{j=1}^{NV} \Gamma_j \delta(z - z_j)$, where Γ_j is the circulation of the point vortex at position z_j . The velocity induced by this vorticity distribution can be obtained from equation (2.38) by performing the integration over the region of non-zero vorticity, leading to

$$v_{sol}^*(z_0) = \sum_{j=1}^{NV} \frac{1}{2\pi i} \frac{\Gamma_j}{z_0 - z_j} \quad (2.41)$$

where the summation is taken over all vortices. Methods based on this kind of vorticity distributions are called 'discrete-vortex' methods and will also be described in the next section.

The different ways of representing regions with distributed vorticity are illustrated in figure 2.1a-c and can be combined to a more complex description of the flow, as for example shown in figure 2.1d. The velocity at a point in the flow field is a summation of the local potential flow due to the irrotational mean flow and the acoustic flow and finally the solenoidal part of the velocity induced by the vorticity distribution.

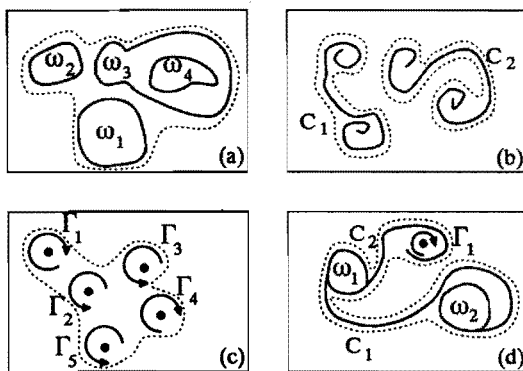


FIGURE 2.1: Different ways to describe a region with distributed vorticity (given by $- - -$). (a) patches of constant vorticity (b) vortex sheets (c) discrete vortices (d) combination of vortex sheets, point vortices and vortex patches.

2.2.2 Methods for describing flows with distributed vorticity

Methods for the description of the motion of thin vortex layers have been developed since the thirties. At that time calculations were performed by hand, which restricted the

applications of discrete-vortex methods to only a few vortices and a limited number of time steps. Since then, computer facilities have offered the possibility to use more vortices to describe the vortex layer and to extend the computation to longer times. Also vortex-sheet methods and vortex-patch methods (i.e. contour dynamics) have become feasible. Many reviews of vortex methods for two-dimensional flows have been made by among others Clements & Maull (1975), Saffman & Baker (1979), Leonard (1980), Aref (1983), Hoeijmakers (1983) and Sarpkaya (1989). For vortex methods for three-dimensional flow we refer to Hoeijmakers (1983, 1990) and Leonard (1985).

In this section, we will briefly review vortex methods, which are used to describe the motion of vortex sheets in a two-dimensional potential flow. Discussed will be the implementation of the boundary conditions and the Kutta condition for the generation of vorticity, as well as the stability of the various discrete representations of the vortex sheet.

Discrete-vortex methods

An early attempt to compute the motion of vortex sheets was published by Rosenhead (1931). Rosenhead (1931) introduced the so-called point vortex method to describe the Kelvin-Helmholtz instability of a two-dimensional shear layer. Westwater (1935) used a point-vortex method involving 20 vortices to calculate the roll-up of a vortex sheet behind an elliptically loaded wing. Using early main-frame computers, Hama & Burke (1960) showed that the point-vortex method is unstable in the limit that the number of vortices $NV \rightarrow \infty$ and the time step $\Delta t \rightarrow 0$. This is due to the singular behavior of the velocity induced by a point vortex near its own location, the velocity induced by the vortices on themselves increases like $(1/d)$ when the distance d between the point vortices decreases. It was shown later by Aref (1983), that point vortices in a two-dimensional free space moving under influence of the velocity induced by each other show chaotic behavior if the number of vortices is equal to or larger than four.

Several methods have been proposed to reduce the instability of the point-vortex method. A first approach, used by Clements & Maull (1975) in describing vortex formation in the wake behind a square-based body, is amalgamation of two point vortices when they have approached each other too closely or when due to stretching of the sheet the discrete vortices have to describe a too large part of the rolled-up sheet. In the latter case the two vortices are lumped into a vortex core. This technique was also used by Moore (1974) to describe the roll-up of a vortex sheet with an initially elliptic distribution of the circulation. In the method of redistribution, called the sub-vortex technique, which has been proposed by Maskew (1977) a vortex is distributed into sub-vortices, when the portion of the vortex sheet it represents is approached too closely. Finally a discrete-vortex vortex sheet discretisation scheme is proposed by Fink & Soh (1978). The latter technique prevents vortices to approach each other too closely. Although by using the redistribution technique, Fink & Soh (1978) were able to obtain a stable solution for long times, Baker (1980) showed that this method eventually ends into chaos as well. Moore (1981) showed that the chaotic behavior is due to the representation of the vortex sheet by point vortices, which causes a discrete form of the inherent Kelvin-Helmholtz instability which we will further discuss in the last part of this section.

A successful attempt to reduce the instability of the point vortex method has been proposed by Chorin & Bernard (1973), the so-called vortex-blob method. The vortex-blob method reduces the singular behavior of the velocity field induced by the point vortex, by smoothing out the vorticity in a region around the center of the discrete vortex.

Consider the velocity induced by a set of discrete vortices ($j = 1..NV$) with the vortex center at position z_j and with circulation equal to Γ_j , which can be written in complex notation as

$$v^*(z) = \sum_{j=1}^{NV} K(z - z_j) \Gamma_j \quad (2.42)$$

where $K(z)$ is the Biot-Savart kernel, which for a point vortex is equal to

$$K(z) = \frac{-i}{2\pi z} \quad (2.43)$$

The velocity field induced by a set of vortex blobs is given by

$$v^*(z) = \sum_{j=1}^{NV} K_\delta(z - z_j) \Gamma_j \quad (2.44)$$

where $K_\delta(z)$ is a desingularised kernel which removes the singular behavior of the velocity for $z \rightarrow z_j$. Several methods for the desingularisation of the kernel have been proposed. For example Chorin & Bernard (1973) proposed

$$K_\delta(z) = \begin{cases} K(z) & \text{for } |z| > \delta \\ K(z) |z|/\delta & \text{for } |z| \leq \delta \end{cases} \quad (2.45)$$

where δ is a small cut-off distance, which represents an artificial viscosity which allowing the vorticity to have a finite value and to occupy a small but finite region unlike the case of point vortices for which the vorticity is zero everywhere except at $z = z_j$ where it is infinite. The 'diffusion' is artificial, because δ is a parameter of the computational method and is time-independent, so that its effect is not cumulative in time. Also the local deformation of the fluid by stretching is not taken into account in this method.

Using the desingularised kernel the circumferential velocity is equal to the induced velocity by a point vortex for the region $|z| > \delta$, and is constant for the region $|z| \leq \delta$. The vorticity is zero for $|z| > \delta$ while for $|z| \leq \delta$, $\omega_j = \Gamma_j/2\pi\delta|z - z_j|$, i.e. algebraically singular at the center. The circulation is equal to Γ_j for $|z| > \delta$.

Chorin & Bernard (1973) found that using the vortex-blob method, instabilities were damped, and a regular roll-up process could be obtained. The results were shown to be insensitive to the value of δ within a wide range of δ . Other desingularised kernels have been proposed by Beale & Majda (1985) and Krasny (1987). Krasny (1987) proposed the desingularised kernel

$$K_\delta(z) = K(z) \frac{|z|^2}{\delta^2 + |z|^2} \quad (2.46)$$

for all z , where δ is the desingularisation parameter. The vorticity associated with this kernel is regular for $\delta \neq 0$, and is given by

$$\omega_j(z) = \frac{\Gamma_j}{2\pi} \frac{2\delta^2}{(|z - z_j|^2 + \delta^2)^2} \quad (2.47)$$

Beale & Majda (1985) proposed the alternative kernel

$$K_\delta(z) = K(z) \left(1 - \sum_{k=1}^{k_{max}} a_k e^{-b_k \frac{|z|^2}{\delta^2}} \right) \quad (2.48)$$

which they call a regularised kernel. Depending on the number of terms k_{max} , the constants a_k, b_k have different values, which are summarized by Riccardi & Piva (1992). The vorticity distribution of the various vortex-blob methods is shown in figure 2.2. For all vortex-blob

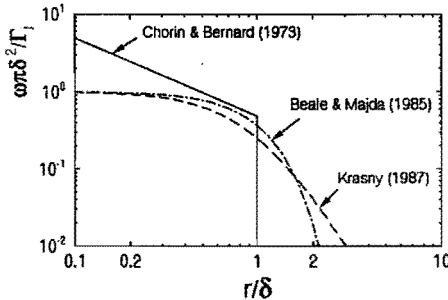


FIGURE 2.2: Vorticity distribution for different vortex blob methods. (—) Chorin & Bernard (1973) (---) Krasny (1987) (- · - · -) Beale & Majda (1985) for $k_{max} = 1$, $a_1 = 1$, $b_1 = 1/2$

methods, the vorticity distribution approximates a delta function behavior in the limit $\delta \rightarrow 0$.

The vortex-blob method has a number of advantages compared to the point-vortex method. The method is stable in the limit $NV \rightarrow \infty$ and $\Delta t \rightarrow 0$, for $\delta \neq 0$. The vortex blobs concentrate in regions of steep gradients, i.e. vortex cores and appears to be able to describe the physical Kelvin-Helmholtz instability of shear layers. By choosing a finite value for the desingularisation parameter δ a shear layer of finite thickness can be simulated, although it is assumed in the method that each vortex blob convects as a rigid body and during convection does not deform nor change its vorticity distribution. Beale & Majda (1985) showed that the advantage of the kernel defined by equation (2.48) is that, by taking more terms into account, the error induced by the approximation can be reduced.

Chorin & Bernard (1973) and Krasny (1987) found, that the main features of the vortex sheet roll-up are not influenced by the value of δ , or the kind of desingularised kernel used. However the number of turns describing a rolled-up part of the vortex sheet, representing a vortex core, is determined by the value of δ . Alternative vortex-blob methods which in some approximate form incorporate viscous diffusion are described by Sarpkaya (1989).

An alternative method to reduce the singular behavior of the point vortices is developed by Christiansen (1973) and is called the Cloud in Cell (C.I.C.) technique. It is a method which is combination of an Eulerian method in which the space is divided into a grid, on

which the equations are solved at each time step and a Lagrangian point-vortex approach where the vorticity is convected with the local velocity. The C.I.C. method solves the Poisson equation for the scalar stream function ψ , given by equation (2.37). This equation is solved on a uniform rectangular grid, where the vorticity $\omega_{i,j}$ at grid point i, j is an area-weighted value of the circulation of the point vortex Γ_0 within the cell, see figure 2.3. The

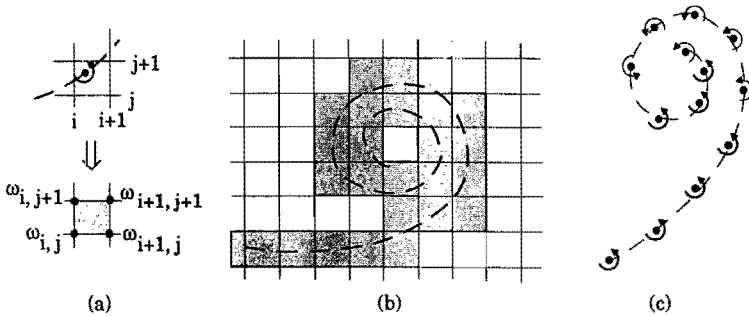


FIGURE 2.3: The cloud-in-cell method (C.I.C.) as proposed by Christiansen (1973). (a) area-weighted vorticity distribution $\omega_{i,j} = A_{i,j}\Gamma/\Delta x_i\Delta y_j$, (b) Vortex roll-up described by C.I.C. method (c) Vortex sheet roll-up described by the discrete vortex method

velocities at the grid points are obtained from the differential form of the definition of the stream function $u_x = \partial\psi/\partial y$, $u_y = -\partial\psi/\partial x$, and finally the velocity at the point vortex is obtained by an area-weighted interpolation. Baker (1979) applied the C.I.C. method to vortex sheet roll-up and found the development of the Kelvin-Helmholtz instability, but only for small values of the grid spacing. The large scale vortical flow structure agreed with the results obtained by other discrete-vortex methods. An advantage of the C.I.C. method compared to the other discrete-vortex methods is that the computation time increases like $M \log M$, where M is the number of grid points, which is usually much larger than the number of vortices NV . This may be smaller than the computation time of a discrete-vortex method, which increases with $(NV)^2$, where NV is the number of discrete vortices used for the discretisation of the vortex sheet. However, since a first order explicit Euler integration method is used for the convection of the vortices, more time steps are required to obtain the same accuracy compared to the vortex-blob method. In practice, the computation time used for C.I.C. method and vortex-blob method are comparable.

Vortex-sheet methods

A more accurate description of a thin shear layer is provided by a continuous vortex-sheet. In the vortex-sheet method the sheet is divided into a number of continuous segments (panels), and the velocity field induced by the vortex sheet is evaluated as the sum over the contribution of each panel. The contribution of each panel is computed to some consistent order of approximation. If the coordinates of the points on the vortex sheet are given by

$z(s) = x(s) + iy(s)$, where s is the arc length parameter along the vortex sheet and the vortex distribution on the vortex sheet is given by $\gamma(s)$, then $z(s)$ and $\gamma(s)$ are described by piecewise polynomial representations, where the degree of the polynomial determines the accuracy of the method. Mokry & Rainbird (1975) have used a first-order panel method, in which the panels are straight segments, with a panel-wise constant vortex distribution. Hocijmakers & Vaatstra (1983) used a second-order panel method, with curved segments and a linearly varying surface vortex distribution on each panel. In complex notation, the velocity induced by a vortex sheet is given by

$$v^*(z_0) = \frac{1}{2\pi i} \int_{s_0}^{s_\infty} \frac{1}{z_0 - z(s)} d\Gamma(s) \quad (2.49)$$

where $\Gamma(s)$ is the dipole strength of the vortex sheet which is related to the vortex distribution by $\frac{d\Gamma}{ds} = \gamma(s)$ and s_0 and s_∞ are the first and last point of the sheet, respectively. For a point close to the sheet, the velocity is given by

$$v^*(z(s_0)^\pm) = \mp \frac{1}{2} \gamma(s_0) \frac{dz^*}{ds}(s_0) + \frac{1}{2\pi i} \int_{s_0}^{s_\infty} \frac{1}{z(s_0) - z(s)} d\Gamma(s) \quad (2.50)$$

where the integral \int denotes the Cauchy principle value of the integral, which is equal to the self-induced velocity of the vortex sheet. The vortex distribution on the sheet $\gamma(s)$ is given by the jump of tangential velocity across the sheet

$$\gamma(s_0) \frac{dz}{ds} = v(z(s_0)^-) - v(z(s_0)^+) \quad (2.51)$$

where \pm denotes the left- and right-hand side when moving along the curve in the direction of increasing arc length of the sheet, respectively and $\partial z(s)/\partial s$ is the unit tangential vector along the sheet. On each panel, we write for the second-order method

$$\Gamma(s) = \Gamma(s_j^*) + (s - s_j^*) \frac{d\Gamma}{ds}(s_j^*) + \frac{1}{2} (s - s_j^*)^2 \frac{d^2\Gamma}{ds^2}(s_j^*) + \mathcal{O}(\Delta s_j^3) \quad (2.52)$$

$$z(s) = z(s_j^*) + (s - s_j^*) \frac{dz}{ds}(s_j^*) + \frac{1}{2} (s - s_j^*)^2 \frac{d^2z}{ds^2}(s_j^*) + \mathcal{O}(\Delta s_j^3) \quad (2.53)$$

where s_j^* is the expansion point, usually the midpoint of the panel and $\Delta s_j = s_{j+1} - s_j$ is the panel size in terms of for instance the arc length. For the first-order panel method, only the first two terms in equation (2.52) and (2.53) are used. The velocity can be calculated everywhere in the flow field, including at points situated on the vortex sheet. However, for the latter case care must be taken to properly handling the singular character of the integrand in equation (2.49). Therefore a small curvature expansion is proposed by Hocijmakers & Vaatstra (1983), in which $R(s) = z_0 - z(s)$ is approximated by the distance to the tangent of the panel at the expansion point plus a second order term, see figure 2.4.

$$R(s) = R_f(s) - \frac{1}{2} (s - s_j^*)^2 \frac{d^2z}{ds^2}(s_j^*) + \mathcal{O}(\Delta s_j^3) \quad (2.54)$$

$$\text{with } R_f(s) = z_0 - z(s_j^*) - (s - s_j^*) \frac{dz}{ds}(s_j^*)$$

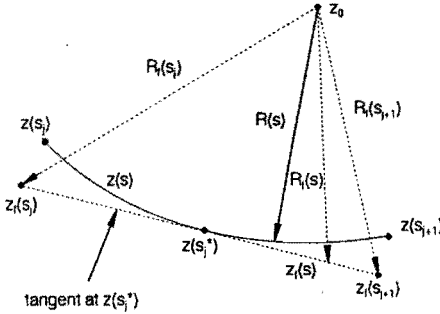


FIGURE 2.4: The small curvature expansion used in the second-order panel method by Hooijmakers & Vaatstra (1983).

Substitution of this approximation into equation (2.49) gives the induced velocity, in second-order accurate approximation

$$v^*(z_0) = \sum_{j=1}^{NP} \left[\frac{d\Gamma}{ds}(s_j^*) \left(E_0 + \frac{d^2z}{ds^2}(s_j^*) E_1 \right) + \frac{d^2\Gamma}{ds^2}(s_j^*) E_2 \right] + \mathcal{O}(\delta_0^2) \quad (2.55)$$

where δ_0 is the average panel size and the sum is taken over all panels NP . The second derivative of the coordinate $z(s)$ is related to the curvature $k_n(s)$ of the sheet according to $\frac{d^2z(s)}{ds^2} = ik_n(s) \frac{dz(s)}{ds}$, since the curvature is defined as $k_n(s) = \Im \left[\frac{dz^*(s)}{ds} \frac{d^2z(s)}{ds^2} \right]$. Furthermore E_0 , E_1 and E_2 are given by

$$E_0 = \frac{1}{2\pi i} \int_{s_j}^{s_{j+1}} \frac{1}{R_f(s)} ds \quad (2.56)$$

$$E_1 = \frac{1}{2\pi i} \int_{s_j}^{s_{j+1}} \frac{\frac{1}{2}(s - s_j^*)^2}{R_f(s)^2} ds \quad (2.57)$$

$$E_2 = \frac{1}{2\pi i} \int_{s_j}^{s_{j+1}} \frac{(s - s_j^*)}{R_f(s)} ds \quad (2.58)$$

Equations (2.56), (2.57) and (2.58) can be expressed in closed form in a similar fashion as given by Hooijmakers (1989), i.e.

$$E_0 = \frac{-1}{2\pi i \frac{dz}{ds}(s_j^*)} \ln \left(\frac{R_f(s_{j+1})}{R_f(s_j)} \right) \quad (2.59)$$

$$E_1 = \frac{1}{4\pi i \frac{dz}{ds}(s_j^*)} \left[\Delta s_j + \frac{2(z_0 - z(s_j^*))}{\frac{dz}{ds}(s_j^*)} \ln \left(\frac{R_f(s_{j+1})}{R_f(s_j)} \right) \right]$$

$$E_2 = \frac{(z_0 - z(s_j^*))^2}{2\pi i \frac{dz}{ds}(s_j^*)} \left[\frac{1}{R_f(s_{j+1})} - \frac{1}{R_f(s_j)} \right] - \frac{1}{2\pi i \frac{dz}{ds}(s_j^*)} \left[\Delta s_j + \frac{z_0 - z(s_j^*)}{\frac{dz}{ds}(s_j^*)} \ln \left(\frac{R_f(s_{j+1})}{R_f(s_j)} \right) \right]$$

with $R_f(s_{j+1}) = z_0 - z(s_j^*) - \frac{1}{2}\Delta s_j \frac{dz}{ds}(s_j^*)$ and $R_f(s_j) = z_0 - z(s_j^*) + \frac{1}{2}\Delta s_j \frac{dz}{ds}(s_j^*)$.

In the first-order panel method, the approximation for the induced velocity is given by

$$v^*(z_0) = \sum_{j=1}^{NP} \frac{d\Gamma}{ds}(s_j^*) E_0 + \mathcal{O}(\delta_0) \quad (2.60)$$

where E_0 is given by equation (2.59). For points z_0 in the far field of a panel j , the expression for the induced velocity can be simplified to consistent order of approximation by taking for the contribution of panel j in the summation of equation (2.55)

$$v_j^*(z_0) = \frac{1}{2\pi i} \frac{\Delta s_j}{z_0 - z(s_j^*)} \left(\frac{d\Gamma}{ds}(s_j^*) \right) + \mathcal{O}(\delta_0^2) \quad (2.61)$$

The velocity induced at a point on the vortex sheet is mainly due to the velocity induced by the panel on which the point is situated. The velocity induced at the panel midpoint can be derived from equation (2.50) as

$$v^*(z(s_j^*)) = \left[-\frac{1}{2} \frac{d\Gamma}{ds}(s_j^*) \text{sign}(\zeta) + \frac{1}{4\pi} \Delta s_j \frac{d\Gamma}{ds}(s_j^*) k_n(s_j^*) - \frac{\Delta s_j}{2\pi i} \frac{d^2\Gamma}{ds^2}(s_j^*) \right] \frac{dz^*}{ds}(s_j^*) \quad (2.62)$$

where $\text{sign}(\zeta) = \pm 1$ on the left- and right-hand side of the sheet when progressing along the sheet in positive s -direction, respectively. The tangential component of the velocity induced by the panel at its own midpoint experiences a jump across the panel of magnitude $\gamma(s_j^*)$ while the mean tangential velocity is non-zero if the panel has non-zero curvature. If the vortex distribution $\gamma(s)$ along the panel varies, also a mean normal velocity is induced at the panel midpoint. For a first-order panel method the last two terms vanish, since the panel curvature is not accounted for (*i.e.* $k_n(s_j^*) = 0$) and the vortex distribution is constant (*i.e.* $\frac{d^2\Gamma}{ds^2}(s_j^*) = 0$).

In regions of high curvature or high curvature gradients, the accuracy of the approximation decreases, unless locally the panel size is decreased in some proportion to these quantities. Therefore, regions where the vortex sheet has rolled-up tightly would require a large number of panels to represent and are usually described by a vortex patch ('finite core method') or by a point vortex, connected to the end of the vortex sheet by a so-called 'feeding sheet' as shown in figure 2.5 for the case of a single-branched vortex. If at other parts of the sheet the curvature increases above a critical value, indicative for the formation of a double-branched vortex, a point vortex is introduced which replaces the highly rolled-up part of the vortex sheet. The point vortex is placed at the center of vorticity of the cut-off portion of the vortex sheet, and the circulation of the point vortex is equal to the circulation of the cut-off part of the sheet. In both single- and double-branched vortices the number of turns around the point vortex can be restricted to a user-specified angular

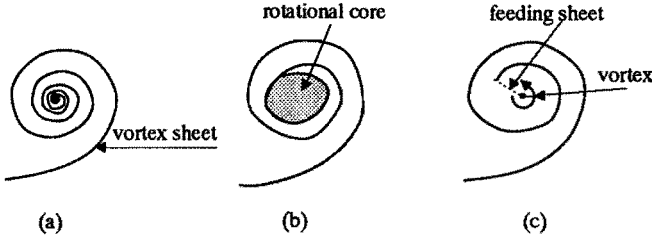


FIGURE 2.5: Different core representations used to describe a strongly rolled-up vortex sheet. (a) rolled-up vortex sheet for $Re \rightarrow \infty$ (b) finite core method (c) point vortex/feeding sheet method

extent while the rest of the sheet is amalgamated with the point vortex. The contribution of the point vortices to the flow field is given by equation (2.41) with $NV = 1$.

During the vortex sheet roll-up, parts of the vortex sheet are stretched, while other parts can be compressed. As a result, the accuracy of the calculated induced velocity becomes non-uniform along the vortex sheet. In a similar way as has been proposed by Fink & Soh (1978) for the redistribution of the point vortices in the discrete vortex approach, Hoeijmakers & Vaatstra (1983) propose a curvature-dependent discretisation scheme, which is governed by two parameters, namely a maximum permissible panel size Δs_{max} and a maximum permissible angular extent θ_{max}/\tilde{k}_n , where \tilde{k}_n is the average curvature of the panel. The parameter θ_{max} ensures that on a highly curved part of the sheet, the second-order accuracy of the induced velocity is maintained by reducing the panel size Δs_j .

2.2.3 Boundary conditions

If fixed, non-porous boundaries are present in the flow problem, two boundary conditions should be satisfied on the solid surface. The normal velocity should vanish at the wall ($\vec{v} \cdot \vec{n} = 0$) while due to viscous action there should be no slip velocity at the wall ($\vec{v} \cdot \vec{\tau} = 0$). However, in a potential-flow model, viscosity is neglected, and the no-slip condition has to be relaxed. We will now discuss two methods to satisfy the condition of zero normal velocity at the solid wall, namely the conformal mapping technique and the boundary element method.

Schwarz-Christoffel transformation

The condition of zero normal velocity at a boundary can be satisfied exactly by mirroring the sources and vortices in the wall. Directly, this is only possible for simple geometries like an infinite wall or a circle. For more complex geometries it is sometimes possible to map the geometry in the physical domain into a simpler geometry in a compu-

tational domain by a conformal transformation. In the computational domain the method of images can then be applied, again to exactly satisfy the normal-velocity boundary condition. For a polygon the transformation is given by the Schwarz-Christoffel transformation, see figure 2.6. The transformation from the physical plane $z = x + iy$ to the computational

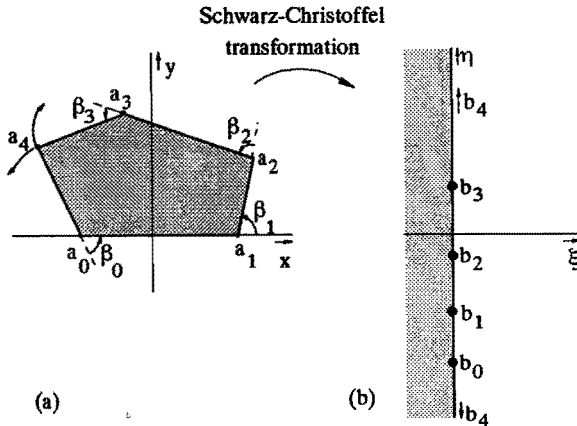


FIGURE 2.6: Schwarz-Christoffel transformation of the inside of a polygon onto a semi-plane. (a) physical plane $z = x + iy$ (b) computational plane $\zeta = \xi + i\eta$

plane $\zeta = \xi + i\eta$ is given by $z = f(\zeta)$, where

$$f'(\zeta) = K \prod_{i=1}^N (\zeta - \zeta_i)^{\beta_i/\pi} \quad (2.63)$$

where the prime denotes the derivative with respect to ζ and the angle β_i is denoted in figure 2.6. The parameter K is a complex-valued constant and the product is taken over all edge points of the polygon. While the derivative of the transformation function $f(\zeta)$ can be found for any polygon, the function $f(\zeta)$ itself and the inverse transformation usually cannot be obtained in algebraic form.

Since the transformation is conformal, the complex potential in the computational plane is equal to its value at a corresponding position in the physical plane and if the normal velocity boundary condition is satisfied in the computational plane, it is also satisfied in the physical plane. The complex potential is defined as $\Phi = \phi + i\psi$, where ϕ and ψ are the scalar potential and scalar stream function, respectively. The velocity $v^*(z) = \frac{d\Phi}{dz}(z)$ in the physical plane, at a point where the velocity is not singular, can be obtained from the complex velocity potential Φ in the computational plane from

$$\frac{d\Phi}{dz}(z) = \frac{d\Phi}{d\zeta}(\zeta) \frac{dz}{d\zeta}(\zeta) \quad (2.64)$$

However, at points where the complex potential is singular, like at point vortex positions, an additional term arises due to the transformation which is known as Routh's correction (e.g. Clements (1973)) must be included, e.g. the velocity at a point $z = z_v$ where a point vortex of circulation Γ_v is located, is

$$\frac{d\Phi}{dz}(z_v) = \lim_{\zeta \rightarrow \zeta_v} \left\{ \left(\frac{d\Phi}{d\zeta}(\zeta) + \frac{i\Gamma_v}{2\pi} \frac{1}{\zeta - \zeta_v} \right) / \frac{dz}{d\zeta} + \underbrace{\frac{i\Gamma_v}{4\pi} \frac{d^2z}{d\zeta^2} / \left(\frac{dz}{d\zeta} \right)^2}_{\text{Routh's correction}} \right\} \quad (2.65)$$

When analytical solutions of the transformation function are not available, numerical procedures to find the Schwarz-Christoffel transformation function have been developed by Trefethen (1980). When such a transformation cannot be used, the boundary-element method is an alternative method to satisfy the boundary condition of zero normal velocity at a number of discrete points, i.e. not exactly but approximately.

Boundary-element method

In the boundary element method, the boundary of the geometry is divided into elements (panels), either straight or curved, depending on the order of accuracy of the method, carrying a source and/or vortex distribution, represented by element-wise polynomials. On a panel with a source distribution $q(s)$ and vortex distribution $\gamma(s)$, the normal and tangential velocities jump by an amount of $q(s)$ and $\gamma(s)$, respectively. The velocity at an arbitrary point z_0 in the computational domain can be obtained from the contribution of the vortex and source distribution on the boundary and the contributions of the singularities inside the flow field. If the boundary is described by $z(s)$ and the vortex sheet is described by discrete vortices, the velocity is given by

$$v^*(z_0) = \oint \frac{q(s) - i\gamma(s)}{2\pi} \frac{1}{z_0 - z(s)} ds + \sum_{j=1}^{NV} K(z_0 - z_j) \Gamma_j \quad (2.66)$$

where s is the arc length along the boundary and $K(z)$ is the Biot Savart kernel for point vortices given by equation (2.43) or K_δ given by equation (2.46) in case of vortex blobs according to Krasny (1987). For the velocity at singular points, such as the discrete vortices, the infinite or regularised self-induced velocity $\lim_{z \rightarrow z_j} K(z - z_j) \Gamma_j$ is omitted. In order to obtain the velocity in the midpoint of a panel $z(s_j^*)$ of the contour, the principle value of the integral has to be taken, according to

$$v^*(z(s_j^*)) = \mp \frac{1}{2} (\gamma(s_j^*) - iq(s_j^*)) + \oint \frac{q(s) - i\gamma(s)}{2\pi} \frac{1}{z_0 - z(s)} ds + \sum_{j=1}^{NV} K(z_0 - z_j) \Gamma_j \quad (2.67)$$

where \oint denotes the principle value of the integral. On the boundary either the Neumann condition ($d\phi/dn = \text{specified}$) or the Dirichlet condition ($\phi = \text{specified}$) is used. For an internal flow problem, we require that the velocities on the outside contour are zero. This requires for a rigid impermeable boundary a zero source strength, while at parts of the boundary where there is in- or outflow the source strength is specified, i.e. determined by the inflow velocity.

As a result, only the vortex distribution is unknown which is obtained by imposing the integral equation at a number of collocation points. For the present first order scheme, with panel-wise constant vortex and source distribution γ_j and q_j , respectively the collocation points are chosen as the midpoints of the straight-line panels. The Dirichlet condition is implemented by imposing a zero tangential velocity on the outside of each panel $j = 1..NP$, where NP is the total number of panels. It results in the following form of the discretized integral equation

$$\frac{1}{2}\gamma_j + \sum_{k=1, k \neq j}^{NP} \gamma_k K_\gamma(j, k) + \sum_{k=1}^{NP} q_k K_q(j, k) + \sum_{k=1}^{NV} \Gamma_k K_\Gamma(j, k) = 0 \text{ for } j=1..NP \quad (2.68)$$

where the third term is the velocity due to discrete vortices inside the computational region. $K(j, k)$ is the aerodynamic influence coefficient (a.i.c.) which determines the influence of the vortex distribution on panel k exercised at the midpoint of panel j . The a.i.c. K_q and K_γ only depends on the geometry and are for panels on a solid boundary time-independent. The a.i.c. K_Γ determines the induced velocity by a discrete vortex of unit circulation at position $z = z_k$ at the midpoint of panel j . Since the discrete vortices convect with the flow, the a.i.c. K_Γ is time-dependent and has to be calculated each time step. In general the a.i.c.'s can be written as

$$\begin{aligned} K_\gamma(j, k) &= \Re \left[\frac{1}{2\pi i} \left(\frac{dz}{ds} \right) (s_j^*) \int_{s_k}^{s_{k+1}} \frac{1}{z(s_j^*) - z(s)} ds \right] \\ K_q(j, k) &= \Re \left[\frac{1}{2\pi} \left(\frac{dz}{ds} \right) (s_j^*) \int_{s_k}^{s_{k+1}} \frac{1}{z(s_j^*) - z(s)} ds \right] \\ K_\Gamma(j, k) &= \Re \left[\frac{1}{2\pi i} \left(\frac{dz}{ds} \right) (s_j^*) \frac{1}{z(s_j^*) - z_k} \right] \end{aligned} \quad (2.69)$$

In matrix form, equation (2.68) can be written as

$$\begin{aligned} [K_\gamma] \{\gamma\} &= \{b\} \\ \text{with } \{b\} &= -[K_q] \{q\} - [K_\Gamma] \{\Gamma\} \end{aligned} \quad (2.70)$$

where the right-hand side $\{b\}$ is known, but can be time dependent. This is the case for a starting flow or for a periodic acoustic inflow.

In a zeroth-order approximation, the vortex distribution on a panel is concentrated in a single point vortex with circulation $\Gamma_j = \gamma_j \Delta s_j$, usually positioned in the midpoint of the panel. In that case, the a.i.c. K_γ is equal to the a.i.c. of the point vortices inside the flow field K_Γ . In a first-order approximation, the panels are straight line segments, with constant source and vortex distribution and the a.i.c. simplifies to $K_\gamma = \Re[E_0 \frac{dz}{ds}(s_j^*)]$, where E_0 is given by equation (2.56), and further $K_q = i K_\gamma$. The vortex distribution is obtained by solving the set of NP linear equations for $\gamma_j, j = 1..NP$.

This first-order approximation for the panel shape and vortex distribution is used for the application of the boundary-element method as described in the following chapters. It should be remarked, that in contrast to the conformal mapping method described in the previous section in the boundary element method the normal velocity boundary condition is not exactly satisfied, but to some order of approximation.

Boundary conditions on the vortex sheet

The boundary conditions on a vortex sheet are that the vortex sheet is a stream surface, i.e. $\Im(v(z)\frac{dz^*}{ds}) = 0$ and that the vortex sheet cannot sustain any forces, so that the pressure difference across the sheet is zero, i.e. $\rho\frac{\partial\varphi}{\partial t} + \frac{1}{2}\rho|\nabla\varphi|^2$ is identical on both sides of the sheet. Combining the two conditions yields that the vorticity once generated at a sharp edge is convected with the local flow velocity

$$\frac{dz_0^*}{dt} = \frac{d\Phi}{dz}(z_0) \quad (2.71)$$

where the local flow velocity can be obtained from equation (2.64), (2.65) or (2.66). This convection velocity is called the free vortex velocity and is used in the numerical scheme for the convection of a discrete vortex of constant strength and for the convection of the panel midpoints in the vortex-sheet method.

In the numerical model for the discrete vortex nascent at a sharp edge the circulation increases in time from zero to the value reached at the time the next vortex is formed. As a result the nascent point vortex has to be connected to the edge by a so-called feeding sheet. For the point-vortex with feeding sheet combination, Brown & Michael (1954) argued, that the point vortex/feeding sheet system is not force-free if the vortex is assumed to convect with the local flow velocity. This is due to the increasing circulation of the point vortex and can be understood as follows. The static pressure is continuous across the vortex sheet, so that the application of the unsteady Bernoulli equation at points a and b , see figure 2.7, yields, with $\Gamma(s)$ the circulation along the contour shown

$$\begin{aligned} \frac{1}{2}\rho(|v_a|^2 - |v_b|^2) &= \rho\frac{d}{dt}(\varphi_a - \varphi_b) \\ \text{or } \rho\gamma(s)v_{sheet}(s) &= \rho\frac{d\Gamma}{dt} \end{aligned} \quad (2.72)$$

where $\frac{1}{2}(|v_a| + |v_b|) = v_{sheet}$ and $\gamma(s) = \frac{d\Gamma}{ds} = |v_a| - |v_b|$. The normal velocity is continuous across the sheet, while the tangential velocity is discontinuous. For a nascent point vortex, application of the Bernoulli equation gives a uniform time-dependent pressure difference across the feeding sheet since the velocity is continuous across the feeding sheet ($|v_a| = |v_b|$), but the velocity potential is discontinuous, i.e.

$$\Delta p_{ab} = \rho\frac{d\Gamma_v}{dt} \quad (2.73)$$

As a result a pressure force

$$F_p = i\rho\frac{d\Gamma_v}{dt}(z_v - z_{edge}) \quad (2.74)$$

is acting on the feeding sheet. Brown & Michael (1954) argued that this force is to be balanced by a Magnus force acting on the point vortex. This implies that at the nascent vortex the velocity is not equal to the local velocity, as would have been the case when the vortex convects with the local flow, but due to the imposed Magnus force there is a non-zero slip velocity.

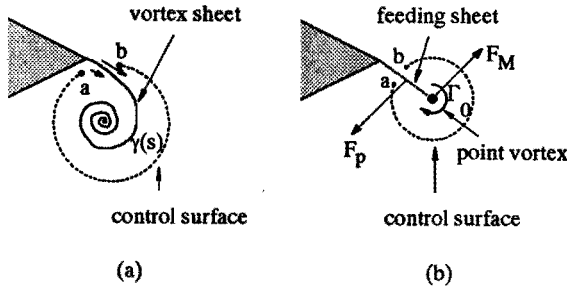


FIGURE 2.7: Derivation of zero-force condition for discrete-vortex/feeding sheet system. (a) continuous vortex sheet (b) discrete-vortex/feeding sheet combination

$$F_M = -i\rho\Gamma_v \left(\frac{dz_v}{dt} - \left(\frac{d\Phi}{dz}(z_v) \right)^* \right) \quad (2.75)$$

Balancing the pressure and Magnus force yields the velocity of the vortex

$$\frac{dz_v^*}{dt} = \frac{d\Phi}{dz}(z_v) - \frac{z_v^* - z_{edge}^*}{\Gamma_v} \frac{d\Gamma_v}{dt} \quad (2.76)$$

The correction on the velocity is directed along the feeding sheet which can be different from the direction of the local velocity vector at the vortex position. For a point vortex of constant strength Γ_v , this relation results in equation (2.71), i.e. the vortex convects again with the local velocity just like any other free vortex. However, if the vortex strength increases, the vortex is necessarily connected to the edge by a feeding sheet, while the vortex convects with a velocity which differs from the local flow velocity.

The 'force free' Brown & Michael concept has been used in the literature in point-vortex methods for predicting the lift and drag coefficient due to the unsteady vortex shedding process occurring for instance behind wings or bluff bodies. Using the force-free method the spurious forces introduced during the vortex generation process are prevented. However, if one is interested in acoustic power absorption by vortices the prime requirement for any vortex method must be that no spurious acoustic sources are introduced. Because the Magnus force acts on the vortex, while the pressure force is distributed uniformly on the feeding sheet, the aeroacoustic source strength related to these forces can differ significantly.

Howe (1975) has shown that the acoustic power absorbed by a vorticity field can be obtained from equation (2.28). In complex notation the local flow velocity at the vortex position can be obtained from $(d\Phi/dz)^*$ and the acoustic velocity is $u_{ac}(z) = (d\Phi_{ac}/dz)^*$. For a free point vortex, the instantaneous acoustic power production can be written in complex notation as

$$P(t) = \Re \left[i\rho_0\Gamma_v u_{ac}^*(z_v) \frac{dz_v}{dt} \right] \quad (2.77)$$

However, as remarked by Peters & Hirschberg (1993) for a point vortex/feeding sheet combination, with external pressure force F_p and Magnus force F_{Magnus} , two additional acoustic power sources are present, with acoustic power production

$$\begin{aligned} P_{Magnus} &= \Re \left(i\rho_0 \Gamma_v u_{ac}^*(z_v) \left[\frac{dz_v}{dt} - \left(\frac{d\Phi}{dz}(z_v) \right)^* \right] \right) \\ &= \Re \left(i\rho_0 \Gamma_v \frac{d\Phi_{ac}}{d\zeta}(\zeta_v) \left[\frac{d\zeta_v}{dt} - \frac{d\zeta}{dz} \left(\frac{d\Phi}{dz}(z_v) \right)^* \right] \right) \end{aligned} \quad (2.78)$$

$$\begin{aligned} P_{pressure} &= \Re \left(\int_{z_v}^{z_{edge}} i\rho_0 \frac{d\Gamma_v}{dt} \left(\frac{d\Phi_{ac}}{dz}(z_v) \right) dz \right) \\ &= \Re \left(i\rho_0 \frac{d\Gamma_v}{dt} \left(\frac{d\Phi_{ac}}{d\zeta}(\zeta_v) \right) (\zeta_v - \zeta_{edge}) \right) \end{aligned} \quad (2.79)$$

for an acoustic velocity field around the edge. These spurious acoustic sources cancel if

$$\frac{dz_v}{dt} = \left(\frac{d\Phi}{dz}(z_v) \right)^* - \frac{\zeta_v - \zeta_{edge}}{\Gamma_v} \left(\frac{dz}{d\zeta} \right) \frac{d\Gamma_v}{dt} \quad (2.80)$$

$$(2.81)$$

which again agrees with equation (2.71) for the 'free' vortex if the strength of the vortex is constant, but differs from the result obtained for the force-free approximation given by equation (2.76) and is therefore called the source-free approach.

The convection velocity of the vortex sheet in the computational plane is given by

$$\frac{d\zeta}{dt} = \frac{dz}{dt} \frac{1}{f'(\zeta)} \quad (2.82)$$

$$= \left(\frac{d\Phi}{d\zeta}(\zeta) \right)^* \left| \frac{1}{f'(\zeta)} \right|^2 \quad (2.83)$$

where the first derivative of the velocity potential Φ can be obtained from equation (2.64), (2.65) and (2.63). For a point vortex this results into

$$\frac{d\zeta_v}{dt} = \lim_{\zeta \rightarrow \zeta_v} \left(\frac{d\Phi}{d\zeta} + \frac{i\Gamma_v}{2\pi} \frac{1}{\zeta - \zeta_v} + \frac{i\Gamma_v}{4\pi} \frac{f''(\zeta)}{f'(\zeta)} \right)^* \left| \frac{1}{f'(\zeta_v)} \right|^2 \quad (2.84)$$

As a result, the first and second derivative of the transformation function $f(\zeta)$, not the function itself, are required to calculate the convection of the vortex system in the computational plane. The convection of the vortex sheet is performed by an integration in time of the convection velocity of the vortex panels and point vortices. In the vortex-sheet method the integration in time is performed by a first-order explicit Euler scheme, with an error of Δt^2 . The time step Δt can be restricted by allowing a maximum displacement of each panel as a fraction of its panel size only. In the discrete vortex methods, a multi-step Runge-Kutta scheme of second or fourth order is used to convect the vortices. The time step is then chosen to be fixed.

2.2.4 Generation of vorticity

In actual flows, due to the action of viscous forces, vorticity is generated at solid boundaries. In a high-Reynolds-number flow, the region with rotational flow is in general limited to a thin boundary layer near the wall. However, at sharp corners or on a strongly curved part of the wall, the boundary layer containing vorticity can separate from the wall. A free shear layer is then formed. In any inviscid model of the flow separation and the associated generation of vorticity is not included explicitly. The separation of the flow must be imposed through a Kutta condition². The Kutta condition requires the velocity to remain finite at sharp edges. This usually implies that the flow must separate tangentially thus anticipating the effects due to the action of viscosity.

At sharp edges, in an unsteady potential flow, this Kutta condition is not fulfilled without introducing vorticity in the flow. The velocity induced by the vorticity removes the singular behavior of the potential flow around the edge, and a finite velocity at the edge remains. Different methods to impose the Kutta condition have been proposed. Related to the way in which the boundary conditions are satisfied, either by using a conformal mapping or by using a boundary element method, the implementation takes a different form. Both methods will be described in detail.

Using a similarity solution as a procedure for the generation of vorticity

If the boundary condition of zero normal velocity is satisfied by using a conformal mapping of the flow region onto a semi-plane, in combination with image singularities, the Kutta condition can best be applied in the computational plane. To determine the initial position and the circulation of the generated vorticity, a local approximation of the flow near the edge can be used. Locally, near the edge, the flow can be considered as the flow around a semi-infinite wedge, as shown in figure 2.8. The transformation function $z = f(\zeta)$ can then be expressed as

$$f(\zeta) = \left(\frac{\zeta}{D}\right)^{1/n} \quad (2.85)$$

where D is a complex-valued proportionality constant which depends on the complete geometry and $n = \pi/(2\pi - \theta)$ varies between 0.5 and 1 and depends on the interior angle θ of the wedge. The origin of both the physical plane and the computational plane are taken at the edge point. Near the edge, the attached (irrotational) main flow can be split into a component rounding the edge and a component flowing symmetrically towards the edge. The first terms in the local expansion of the complex velocity potential in the computational plane are then given by

$$\Phi_0(\zeta) = -iA\zeta + B\zeta^2 + \dots \quad (2.86)$$

where $A = at^\alpha$ and $B = bt^\beta$ with a and b real constants and t is the time since the start of the flow. Although the theory is not restricted to this case, α and β are usually taken to be positive. The second term describes the symmetric flow towards the edge. In a

²Sometimes referred to as the Kutta-Joukowski condition.

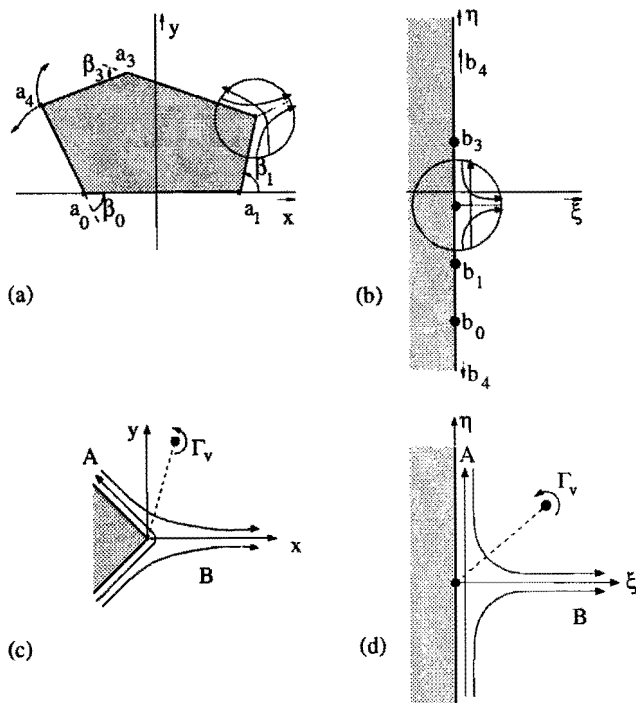


FIGURE 2.8: Local approximation of the Schwarz-Christoffel transformation of a polygon near an edge. (a) physical plane $z = x + iy$ (b) computational plane $\zeta = \xi + i\eta$ (c) local approximation in physical plane (d) local approximation in the computational plane.

single-point-vortex method the vorticity generated at the edge is concentrated in a point vortex. The velocity potential at a point ζ in the computational plane due to the point vortex at position ζ_v and the mirror imaged vortex at $\zeta = -\zeta_v^*$ is given by

$$\Phi_v(\zeta) = \frac{\Gamma_v}{2\pi i} \ln \left(\frac{\zeta - \zeta_v}{\zeta + \zeta_v^*} \right) \quad (2.87)$$

where Γ_v is the circulation of the point vortex. The complex velocity potential is the sum of the velocity potential due to the attached mean flow (equation (2.86)) and that due to the point vortex (equation (2.87)).

$$\Phi(\zeta) = \Phi_0(\zeta) + \Phi_v(\zeta) \quad (2.88)$$

The complex conjugate velocity at a point z_i in the physical plane is given by

$$\left(\frac{d\Phi}{dz}(z_i)\right) = \left(\frac{d\Phi}{d\zeta}(\zeta_i)\right) \frac{1}{f'(\zeta_i)} \quad (2.89)$$

The velocity at the vortex position is given by equation (2.65) with the transformation function (2.85) and the velocity potential (2.88). The Kutta condition requires the velocity to be finite at the edge. Since $f'(\zeta)$ becomes unbounded for $\zeta \rightarrow 0$, it follows from equation (2.89) that this condition requires

$$\frac{d\Phi}{d\zeta}(0) = 0 \quad (2.90)$$

From the velocity potential, given by equation (2.88), we then find

$$\Gamma_v = 2\pi A \frac{|\zeta_v|^2}{\zeta_v^* + \zeta_v} \quad (2.91)$$

In a free-vortex method, the vortex convects with the local flow velocity, expressed in the computational plane by equation (2.84). The nonlinear equations for the vortex position and circulation, i.e. equation (2.91) and (2.84) can be solved analytically for the case that $0 < |a| \ll |b|$ as well as for the case that $|b| \ll |a|$, see appendix B. For the case $|b| \ll |a|$ we obtain with $z_v = r_v e^{i\phi_v}$

$$\begin{aligned} r_v &= (|A|DK_1 t)^{\frac{1}{2-n}} \\ \phi_v &= \frac{1}{n} \arccos \frac{1}{2\sqrt{n}} \\ \Gamma_v &= 2\pi\sqrt{n}ADr_v^n \\ \text{where } K_1 &= \frac{n(1-n)(2-n)(1-\frac{1}{4n})^{\frac{1}{2}}}{1+\alpha} \end{aligned} \quad (2.92)$$

For $0 < |a| \ll |b|$ we find

$$\begin{aligned} r_v &= (|B|D^2K_2 t)^{\frac{1}{2-n}} \\ \phi_v &= 0 \\ \Gamma_v &= \pi ADr_v^n \\ \text{where } K_2 &= \frac{4n(1-n)}{1+\beta} \end{aligned} \quad (2.93)$$

For the latter case the vortex convects along the center line of the wedge, see figure 2.9. If $a = 0$ while $b \neq 0$, no vorticity is generated since the edge of the wedge is a stagnation point of the flow.

If the vortex is convected with the local velocity, given by equation (2.84), the point vortex/feeding sheet combination is not force-free. For the case the vortex system is represented by a point vortex/feeding sheet combination according to Brown & Michael (1954) again an analytical solution can be obtained. This solution is identical to the solution given

in equations (2.92) and (2.93) but with different constants K_1 and K_2 . For the force-free feeding sheet/vortex combination with the vortex velocity given by equation (2.76) we find

$$K_1 = \frac{n(1-n)(2-n)(1-\frac{1}{4n})^{\frac{1}{2}}}{3\alpha+n+1} \quad (2.94)$$

$$K_2 = \frac{4n(1-n)}{(1+\beta)(n+1)+2\alpha(1-n)}$$

while for the acoustic source-free feeding sheet/vortex combination with the vortex velocity expressed in equation (2.80) we obtain

$$K_1 = \frac{n^2(1-n)(2-n)(1-\frac{1}{4n})^{\frac{1}{2}}}{2\alpha+\alpha n+2n} \quad (2.95)$$

$$K_2 = \frac{4n^2(1-n)}{2n(1+\beta)+2\alpha(1-n)}$$

Assuming a starting flow, at each time step the similarity solution near the edge determines the initial position and strength of the newly formed point vortex.

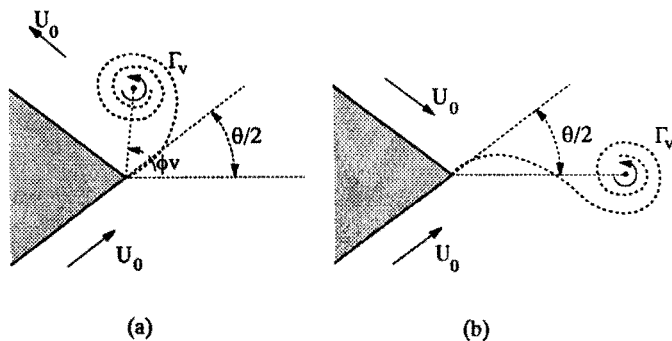


FIGURE 2.9: Similarity solutions for the flow around a semi-infinite wedge. (a) for $|b| \ll |a|$ (b) for $0 < |a| \ll |b|$

Vorticity generation in a similarity solution; vortex-segment method

The process of vorticity generation by the calculation of a similarity solution near the sharp edge where vorticity is generated cannot be used in the vortex-sheet method, since the vortex sheet is connected to the edge and does not allow a local approximation of the flow near the edge according to equation (2.86). If, in a numerical scheme, the panels describing the vortex sheet are convected, also the vorticity contained in the panel connected to the sharp edge is convected, with a finite velocity, away from the edge. After convection, the

vortex sheet does not satisfy the Kutta condition, i.e. equation (2.90) at the sharp edge since a non-zero velocity remains at the edge point in the computational plane.

Introducing a point vortex in order to remove the singularity in the velocity at the edge implies that the edge point is a stagnation point of the flow. This is not an accurate description of the local behavior of the flow near the edge, since the vortex sheet leaves the edge either tangentially to the lower surface or tangentially to the upper surface of the wedge, and the edge point is then a stagnation point for the flow on the upper or lower surface, respectively. The velocity is discontinuous across the vortex sheet which emanates from the edge.

A more accurate description of the flow near the edge would be to add a vortex segment. In first-order approximation this vortex segment of length S_z can be assumed to be straight with constant vortex distribution γ_z . In the computational plane, the vortex distribution is therefore given by $\gamma_\zeta = \gamma_z \left| \frac{dz}{d\zeta} \right|$. The vortex sheet, and therefore also the present vortex segment, is assumed to leave the edge tangentially along the upper surface or lower surface. The coordinate of the vortex segment in the computational plane is given by $\zeta(s) = se^{i\theta_\zeta}$ for $0 < s < S_\zeta$ with $\theta_\zeta = \pi n - \frac{1}{2}\pi$. The length of the vortex segment in the computational plane is equal to $S_\zeta = DS_z^n$. The velocity induced at the origin of the computational plane by the single vortex segment and the mirror-imaged segment is given by

$$\frac{d\Phi}{d\zeta}(0) = \frac{\gamma_z}{2\pi i n} \left(\frac{1}{D} \right)^{1/n} \left(e^{i\theta_\zeta} + e^{-i\theta_\zeta} \right) \int_{s=0}^{S_\zeta} s^{\frac{1}{n}-2} ds \quad (2.96)$$

In order to satisfy the Kutta condition at the edge given by equation (2.90), we require that in the origin of the computational plane the velocity induced by the vortex segment and the mirror-imaged segment balances the attached flow, which yields

$$A = \frac{\sin(\pi n)}{D\pi(1-n)} \gamma_z S_z^{1-n} \quad (2.97)$$

If the internal angle of the wedge $\theta > 0^\circ$ the length S_z the vortex segment has obtained in the time period $t - t_0$ since the formation of the segment started can be related to the vortex distribution by $S_z = \frac{1}{2}\gamma_z(t - t_0)$. Since the circulation contained in the vortex segment is given by $\Gamma_z = S_z\gamma_z$, we find $S_z = \sqrt{\frac{1}{2}\Gamma_z\Delta t}$, where $\Delta t = t - t_0$. The vortex distribution and center of the vortex segment are given by

$$\begin{aligned} \gamma_z &= \frac{2}{\Delta t} \left[\frac{\pi(1-n)}{2\sin(n\pi)} D|A|\Delta t \right]^{\frac{1}{2-n}} \\ z &= \frac{1}{2} S_z e^{i\theta/2} \end{aligned} \quad (2.98)$$

The vorticity generated in the time interval $[t_0, t]$ is given by $\Gamma_z = S_z\gamma_z$,

$$\Gamma_z = \frac{2}{\Delta t} \left[\frac{\pi(1-n)}{2\sin(n\pi)} D|A|\Delta t \right]^{\frac{2}{2-n}} \quad (2.99)$$

The dependence of the circulation on A , D and $\Delta t = t - t_0$ is similar to what has been obtained for the single-vortex approximation in case of a dominating flow rounding the wedge, equation (2.92), with a different value for the constant K_1 , namely

$$K_1 = \left(\frac{\pi(1-n)}{2^{n/2} \sin(n\pi)} \right)^{2/n} \quad (2.100)$$

With the vortex segment attached to the edge, at the edge the velocity is zero on the upper side of the wedge, while it is γ_z on the lower side. If a point vortex with circulation equal to Γ_z is used to replace the panel, it satisfies the Kutta condition if it is placed at $z = \frac{1}{2}(1-n)^{\frac{1}{2}} S_z e^{i\theta/2}$, which is closer to the edge than the midpoint of the original vortex segment. If $\theta = 0^\circ$ ($n = 1/2$), which is the case for a flat plate, the velocity is non-zero on both sides of the plate, and the position and circulation of the vortex segment cannot be obtained from equations (2.98) and (2.99). In that case, the length of the segment is given by $S_z = \frac{1}{2}(v^- + v^+) \Delta t$, while the vorticity distribution is given by $\gamma_z = v^- - v^+$, with v^\pm the velocity on the upper and lower side, respectively. Application of the Kutta condition, see equation (2.97) for $n = 0.5$, requires that

$$\Gamma_z = \frac{\pi}{2} AD \sqrt{S_z} \quad (2.101)$$

and with $\gamma_z = \Gamma_z / S_z$

$$\gamma_z = \frac{\pi AD}{2\sqrt{S_z}} \quad (2.102)$$

From application of l'Hopitals rule we find for $u^\pm = \lim_{\zeta \rightarrow 10} \left(\frac{\partial \Phi}{\partial \zeta} \right) / \left(\frac{\partial z}{\partial \zeta} \right)$

$$U^\pm = \frac{1}{2} D^2 B \pm \frac{1}{2} \gamma_z \quad (2.103)$$

as a result

$$S_z = \frac{1}{2} D^2 B \Delta t \quad (2.104)$$

Vorticity generation in the vortex-sheet method

The second-order panel method, used in the present vortex-sheet method, takes into account the curvature and a linear vortex distribution on the vortex segment connected to the sharp edge. The computational procedure in the vortex-sheet method implemented in the computational (ζ -) plane, in which the Kutta condition is imposed consists of six subsequent sub-steps.

1. Given the position $\zeta(s, t)$ and dipole strength $\Gamma(s, t)$ as a function of the arc length s along the vortex sheet at time t cubic spline interpolations are computed based on discrete values at s_j for $j \in [1, \dots, NP + 1]$.
2. A new panel distribution \hat{s}_j for $j \in [1, \dots, NP + 1]$ is determined by an adaptive curvature-dependent scheme, which preserves the second-order accuracy in space. Also, if a too strong variation of the transformation function $z = f(\zeta)$ occurs on a

panel, the panel width is reduced, which restricts the panel width in regions strongly deformed by the Schwarz-Christoffel transformation. In the adaptive scheme the panel size is further restricted to a maximum value $\Delta s = \min(\Delta s_{max}, \Delta \theta_{max}/\bar{k}_n)$, where \bar{k}_n is the average curvature of the panel. The maximum panel size Δs_{max} is also checked in the physical plane. The angular extent θ_v of the vortex sheet around the point vortex representing the vortex core can also be restricted. The part of the vortex sheet that exceeds the specified angular extent θ_v is amalgamated with the core vortex. In this amalgamation process, carried out in the physical plane, the center of vorticity of the core vortex before amalgamation and the part of the vortex sheet that has been cut off is conserved.

The result at this sub-step: the position $\zeta(\hat{s}_j, t)$ and dipole strength $\Gamma(\hat{s}_j, t)$ for $j \in [1, \dots, NP + 1]$ at the edge points of the individual panels.

3. The velocity at the panel midpoints, i.e. $\zeta(\tilde{s}_j, t)$ for $j \in [1, \dots, NP + 1]$, are computed using the second order panel method operating on the vortex sheet in the computational plane. This velocity, computed from equation (2.55) with z replaced by ζ consists of the free stream velocity, the velocity induced by the vortex panels and the velocity induced by the core vortices. Using this velocity in the right-hand side of equation (2.83), the velocity used to advance the position of the vortex sheet in time is obtained. Similarly, the velocity at the core vortex is used to compute the right-hand side of equation (2.84), which includes Routh's correction.

The displacement at the begin and end points of the vortex sheet are derived from an quadratic extrapolation of the velocity at the first and last three mid points on the vortex sheet, respectively. However, if the edge point is connected to the sharp edge where, vorticity is generated, the extrapolation of the almost entirely tangential velocity is performed in the physical plane, rather than in the computational plane. The reason is the following. Although the Kutta condition, given by equation (2.90), requires the derivative of the complex velocity potential in the ζ -plane to be zero, it tends to zero in a non-polynomial fashion, i.e. with a second order derivative becoming infinite at the edge. However, the velocity on the vortex sheet in the physical (z -) plane is finite at the edge, i.e. vorticity convects away from the edge with a finite velocity, also enabling a more accurate extrapolation.

4. The new position of the midpoints of the panels, that of the first and last edge point of the vortex sheet and that of the core vortices is found by application of a first-order Euler scheme, e.g.

$$\zeta(\tilde{s}_j, t + \Delta t) = \zeta(\tilde{s}_j, t) + \frac{d\zeta}{dt}(\tilde{s}_j, t)\Delta t \quad j = 0 \dots NP \quad (2.105)$$

The time step in the Euler scheme used for the convection of the panel midpoints, vortex sheet begin and end points and the core vortices is adaptive, in that the time step Δt is limited such that it does not exceed Δt_{max} and simultaneously such that none of the midpoints $\zeta(\tilde{s}_j, t)$ is displaced more than a specified fraction \mathcal{F} of its own width in terms of the arc length or more than a certain maximum displacement

Δx_{max} , Δx_{max} , Δt_{max} and \mathcal{F} are to be chosen such that the accuracy of the time integration is preserved in time and also such that it is in balance with the spatial accuracy.

5. A new panel is inserted reconnecting the edge and the convected first edge point of the vortex sheet. The 'bridging' panel is not necessarily directed tangentially to either side of the sharp edge. The dipole strength $\Gamma(0, t + \Delta t)$ at the edge is determined from the application of the Kutta condition that the velocity induced in the computational plane by the sheet in its new position vanishes at the edge.
6. The new location $\zeta(\hat{s}_j, t + \Delta t)$ of the panel edge points at time $t + \Delta t$ is calculated by a second-order spline, fitted through the new location of the panel mid points. The new value of the dipole strength $\Gamma(\hat{s}_j, t + \Delta t)$ at the edge points equals the value at time t , i.e. the dipole strength is convected with the sheet.

Vorticity generation in the boundary-element/vortex-blob method

If the local expansion of the complex velocity potential in the physical plane given by equation (2.85) and (2.86), near the edge where the flow separates is unknown, the procedure described above cannot be used. The vorticity generation process in the boundary element method is accomplished by the introduction of a new vortex at a point which is equal to or close to the edge. The initial position of the nascent vortex is either chosen to be fixed or determined by the local flow. In the boundary-element method used in the present study the position and circulation of the vortex is determined by the local flow field near the edge. The local velocity is obtained as the average velocity at the midpoints of the two panels adjacent to the edge. The circulation is obtained from the vortex distribution on these panels. The vortex distribution on these panels is assumed to convect onto the vortex sheet. The vortex distribution in the panels can be obtained from the tangential velocity at the panels.

$$\begin{aligned}\vec{x}_v &= \vec{v}_{edge}\Delta t \\ \vec{v}_{edge} &= \frac{1}{2}(\vec{v}^- + \vec{v}^+) \\ \Gamma_v &= (\vec{v}^- \cdot \vec{\tau}^- + \vec{v}^+ \cdot \vec{\tau}^+)|\vec{v}_{edge}|\Delta t\end{aligned}\tag{2.106}$$

The method of generation of vorticity by introducing a nascent vortex with its position determined by the local flow is also used by Sarpkaya (1975). An alternative vorticity generation method, in which the position of the nascent discrete vortex is fixed to $z_v = z_{edge} + \epsilon$, where ϵ is small, while the circulation of the point vortex is obtained from $\Gamma_v = \frac{1}{2}U_{edge}^2\Delta t$, where U_{edge} is the velocity at the point z_v is used by Clements (1973), Clements & Maull (1975) and Kiya & Arie (1977). This latter method will be less accurate than the first method, since the position of the nascent vortex can be chosen arbitrary.

2.2.5 Simple vortex methods

Practical useful methods to represent a vortex sheet embedded in a potential flow can be obtained by limiting the number of discrete vortices used to describe the sheet, i.e. use an

amalgamation procedure to combine vortices which have convected a certain distance away from the edge. Three methods will be described, two employ the most simple from of the discrete-vortex approach (*single-vortex* and *two-vortex method*) and one utilizes the most simple form of the vortex-sheet method (*single-panel method*). First the amalgamation procedure will be described.

Amalgamation

If two vortices are combined into a single vortex, the position and circulation of the newly formed vortex have to be determined. For the convection of a system of point vortices in free space, several invariants have been derived by Lamb (1932):

$$\sum_{j=1}^{NV} \Gamma_j = \Gamma_{tot} \quad : \text{total circulation} \quad (2.107)$$

$$\sum_{j=1}^{NV} \Gamma_j z_j / \Gamma_{tot} = z_{cov} \quad : \text{center of vorticity} \quad (2.108)$$

$$\sum_{j=1}^{NV} \Gamma_j z_j^2 / \Gamma_{tot} = D^2 \quad : \text{dispersion} \quad (2.109)$$

$$\frac{-1}{2\pi} \sum_{j=1}^{NV} \sum_{k=j}^{NV} \Gamma_j \Gamma_k \log(|z_j - z_k|) = H \quad : \text{Hamiltonian} \quad (2.110)$$

all independent of time t . In a discrete vortex approximation, in which the vorticity is distributed in a region around the center of each vortex blob, the invariants are slightly changed. For example the Hamiltonian of a system of vortex blobs with velocity kernel given by equation (2.46) is according to Krasny (1987) given by

$$\frac{-1}{4\pi} \sum_{j=1}^{NV} \sum_{k=j}^{NV} \Gamma_j \Gamma_k \log(|z_j - z_k|^2 + \delta^2) = H \quad (2.111)$$

Since only three unknowns are involved in the amalgamation process (Γ_{new}, z_{new}), not all invariants can be conserved during amalgamation. Usually the circulation is conserved (Kelvin's theorem) and the position of the center of vorticity. However, in the presence of a body, the velocity induced by the combined vortex can differ considerably from the velocity induced by the original separate vortices, specifically if (one of) the vortices are close to the body.

Furthermore, Disselhorst (1978) argued that in the presence of a sharp-edged body, the amalgamation procedure can strongly influence the calculated sound absorption by the vortices. Disselhorst (1978) proposed an amalgamation procedure in which the amount of absorbed acoustic energy is not influenced. In that amalgamation procedure the velocity potential at points far from the vortex system induced by the vorticity is not influenced by the amalgamation. For a vortex pair close to a wedge this amalgamation procedure results into

$$\Gamma_{new} = \Gamma_1 + \Gamma_2 \quad (2.112)$$

$$\zeta_{\text{new}} = \frac{\zeta_1 \Gamma_1 + \zeta_2 \Gamma_2}{\Gamma_1 + \Gamma_2}$$

which is the requirement that the circulation is conserved and the location of the center of vorticity in the computational plane are the invariants of the amalgamation procedure.

For more complex geometries, the amalgamation procedure in which the velocity potential at a point far away from the vortices is not influenced is more complex. In general, such amalgamation procedures allow to choose two points in the far field where the velocity potential is not changed by the amalgamation procedure. An example can be found in Disselhorst (1978) and Disselhorst & van Wijngaarden (1980) for the problem of the flow out of an open pipe, where the velocity potential is not affected at a point far inside the pipe and at a point in the far field outside the pipe.

Single-vortex method

In a single-vortex method, the whole vortex sheet generated at the sharp edge is represented by a single point vortex. The circulation of this vortex is determined by the Kutta condition, given by equation (2.91), where the value A describing the local flow near the edge is determined from the velocity potential of the attached-flow component of the flow around the edge (equation (2.86)). Since the vortex convects with the flow the circulation changes in time. As a result, the single vortex is connected to the sharp edge by a so-called feeding-sheet. Depending on the conditions required for the point vortex/feeding sheet combination, the velocity at which the point vortex convects is different. For the free vortex, the force-free vortex and the source-free vortex methods, the convection velocity of the point vortex is given by equation (2.71), (2.76) and (2.80), respectively.

Two-vortex method

A method ranking between the single-vortex method and the discrete-vortex method is the two-vortex method. The whole vortex sheet is described by a main point vortex representing the center of vorticity of the vortex sheet away from the edge, while a second point vortex, the so-called *edge vortex*, represents the vorticity close to the sharp edge.

The single-vortex similarity solution for a single point vortex determines the initial position z_v and strength Γ_v of the main vortex at $t = t_1$. To obtain this similarity solution, the attached main flow Φ_0 near the edge is approximated by

$$\Phi_0(\zeta) = -iA_0\zeta + B_0\zeta^2 + \dots \quad (2.113)$$

Now each time step the main vortex is convected with the local velocity given by equation (2.71). This results in an estimate of the new vortex position

$$\tilde{z}_v(t + \Delta t) = z_v(t) + \left(\frac{d\Phi}{dz}(z_v) \right)^* \Delta t \quad (2.114)$$

where $\tilde{}$ denotes an estimate value. The complex velocity potential is then given by

$$\Phi(\zeta) = \Phi_0(\zeta) - \frac{i\Gamma_v}{2\pi} \ln \left(\frac{\zeta - \tilde{z}_v}{\zeta + \tilde{z}_v^*} \right) \quad (2.115)$$

which near the edge can be expanded as

$$\Phi(\zeta) = -iA\zeta + B\zeta^2 + \dots \text{ for } \zeta \ll \zeta_v \quad (2.116)$$

with A and B real constants

$$A = A_0 - \frac{\Gamma_v \tilde{\zeta}_v + \tilde{\zeta}_v^*}{2\pi |\tilde{\zeta}_v|^2} \quad (2.117)$$

$$B = B_0 - \frac{i\Gamma_v \tilde{\zeta}_v^2 - \tilde{\zeta}_v^{*2}}{4\pi |\tilde{\zeta}_v|^4} \quad (2.118)$$

Here, the value of A is zero for $t = t_1$, because the Kutta condition is satisfied by the similarity solution. However, also for $t > t_1$ the assumption is valid that $|A| \ll |B|$, as remarked by Graham (1983).

The position and strength of the new edge vortex are determined as follows. Assume that the vorticity generation process at the edge can be considered as an impulsively started flow problem as discussed in section (2.2.4) with A and B given by (2.117) and (2.118). The position z_1 and circulation Γ_1 of the edge vortex can be determined from the similarity solution given by equation (2.93) with $t = \Delta t$. Following the generation, the edge vortex is combined with the main vortex by an amalgamation procedure. Since the circulation of the system must remain constant the circulation of the new main vortex is the sum of the strengths of the two vortices. To obtain the position of the new main vortex three different amalgamation processes can be defined which correspond to the definition of the three different single-vortex methods discussed in the previous section.

For the free two-vortex method the position of the new main vortex is equal to that of the old main vortex, i.e.

$$z_v(t + \Delta t) = \tilde{z}_v(t + \Delta t) \quad (2.119)$$

For the force-free two-vortex method the position of the new main vortex is equal to the center of vorticity of the vortex pair, so that the amalgamation process (in the physical plane) is force free, i.e.

$$z_v(t + \Delta t) = \frac{\tilde{z}_v \Gamma_v + z_1 \Gamma_1}{\Gamma_v + \Gamma_1} \quad (2.120)$$

Using equation (2.114) the vortex position of the new main vortex can now be written as

$$z_v(t + \Delta t) = z_v(t) + \left[\left(\frac{d\Phi}{dz}(z_v) \right)^* - \left(\frac{\tilde{z}_v - z_1}{\Gamma_v + \Gamma_1} \right) \frac{\Gamma_1}{\Delta t} \right] \Delta t \quad (2.121)$$

where $\left(\frac{d\Phi}{dz}(z_v) \right)$ is given by equation (2.65) and the term inside the brackets corresponds to the discretized form of the zero-force condition, i.e. equation (2.76).

Finally an amalgamation process is defined in which the velocity potential induced at two points at infinity in the physical plane is conserved. For the simple case of the flow past a wedge this appears to result in a new position of the vortex at the center of vorticity in the computational plane, i.e.

$$\zeta_v(t + \Delta t) = \frac{\tilde{\zeta}_v \Gamma_v + \zeta_1 \Gamma_1}{\Gamma_v + \Gamma_1} \quad (2.122)$$

after which the new position of the main vortex in the physical plane is obtained from the transformation $z_v = f(\zeta_v)$. For more complex geometries this amalgamation procedure is more complicated as we will show later for the flow in a T-junction. It can be shown that this amalgamation procedure is the discretized form of the no-acoustic-source condition, i.e. equation (2.80) and therefore this method is called the source-free two-vortex method.

Single-panel method

The single panel method is the most simple form of the first-order vortex-sheet method. The vortex sheet away from the edge is represented by a point vortex while the portion of the vortex sheet attached to the edge is represented by a straight vortex segment with a constant vortex distribution. The main point vortex describes the center of vorticity of the vortex sheet. The initial position of the main vortex at $t = t_1$ is again determined by the single-vortex similarity solution of the local flow near the edge. Similar to the two-vortex method the main vortex is convected by the local velocity while simultaneously a vortex segment is generated at the edge.

The vortex distribution γ_z and midpoint z of the vortex segment is determined from the local velocity at the edge, given by equation (2.98). Following the generation of the vortex segment, the vortex segment and the main vortex are combined into a new main vortex during an amalgamation process, which is equivalent to that described for the two-vortex method.

It should be remarked here that both the two-vortex method and the single-panel method are essentially single-vortex methods with an improved procedure for generating vorticity at the edge, i.e. satisfying the Kutta condition. Furthermore the simplified methods have only limited applicability because they only converge to a solution different from the single-vortex solution, if the circulation of the edge vortex or edge segment increases linearly with time. For the two-vortex method this appears to be valid for a 90° -wedge, while the single-panel method converges for a 0° -wedge.

2.2.6 Stability of vortex methods

The way the stability of vortex layers is handled by vortex methods computing the evolution of vortex sheets is studied for the problem of a vortex layer between two equal, but opposite parallel flows. If the two flows are uniform potential flows the vortex layer is infinitesimally thin and is a vortex sheet of uniform vortex strength. It is well known that such a vortex sheet is susceptible to the Kelvin-Helmholtz instability. Infinitesimally small disturbances of the vortex sheet tend to be amplified, which in the subsequent non-linear finite-amplitude phase results into a vortex street with highly rolled-up regions in which the vorticity concentrates, see figure 2.10. If the undisturbed twodimensional flow $\vec{u} = u(y)\vec{e}_x$ is disturbed by $u' \ll u$ and $v' \ll u$ a perturbation stream function can be defined by $u' = \nabla \times \psi'$. For a sinusoidal disturbance the stream function can be written as

$$\psi'(x, y, t) = \Re \left(\hat{\psi}(y) e^{i(kx - \omega t)} \right) \quad (2.123)$$

where $\hat{\psi}(y)$ is the amplitude and $k = k_r + ik_i$ is the complex wave number, while $\omega = \omega_r + i\omega_i$ is the complex frequency. For a spatial instability ω_i is set to zero and the disturbance is

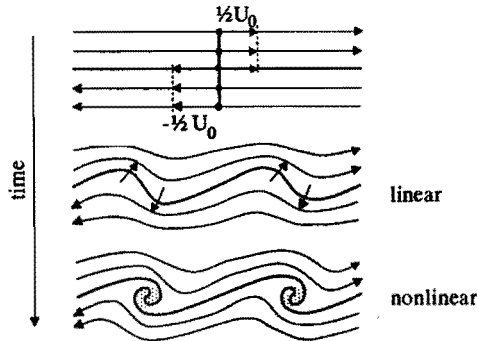


FIGURE 2.10: The formation of a highly rolled-up region resulting from the Kelvin-Helmholtz instability for an initially straight vortex sheet of constant strength $\gamma = U_0$.

spatially amplified if $k_i < 0$. For a temporal instability k_i is set to zero, and the disturbance is amplified in time if $\omega_i < 0$. In the present paragraph only a temporal instability is considered and the amplification factor of the disturbances is denoted as $\alpha = -\omega_i$.

For a vortex sheet linear stability analysis shows that an initially infinitesimally small spatially uniform disturbance amplifies exponentially in time with an amplification factor α , obtained from the dispersion relation

$$\left(\frac{\alpha}{U_0}\right)^2 = \frac{1}{4}k^2 \quad (2.124)$$

where k is the real-valued wavenumber of the disturbance and $U_0 = \gamma$ is the strength of the sheet, which is equal to the discontinuity in the tangential velocity across the sheet. Due to nonlinear effects the initially high rate of growth is reduced and rolled-up vortex cores are formed within the vortex sheet (figure 2.10).

For a vortex sheet the highest amplification factor is found to be for the disturbance with the highest wavenumber, i.e. the shortest wavelengths. In real fluids the shear layer has a finite thickness, i.e. the action of viscosity spreads the vorticity in a layer of finite thickness. Assuming a linear variation of the velocity between the two uniform flows, i.e.

$$\frac{u(y)}{U_0} = \begin{cases} \frac{1}{2}y/|y| & \text{for } |y| > L \\ \frac{1}{2}y/L & \text{for } |y| < L \end{cases} \quad (2.125)$$

the momentum thickness of this vortex layer is

$$\frac{\theta}{L} = \int_{-\infty}^{+\infty} \frac{u(y)}{U_0} \left(1 - \frac{u(y)}{U_0}\right) d\left(\frac{y}{L}\right) = \frac{1}{2} \quad (2.126)$$

Drazin & Howard (1966) derived the dispersion relation for small disturbances of this velocity profile, which leads to

$$\left(\frac{\alpha L}{U_0}\right)^2 = \frac{e^{-4kL} - (1 - 2kL)^2}{(2kL)^2} \quad (2.127)$$

which shows that the layer is unstable ($\alpha > 0$) for $kL < 0.64$. The amplification factor α is shown in figure 2.11. A maximum amplification is observed for $kL = 2k\theta \approx 0.4$, where the amplification rate is $\alpha L/U_0 \approx 0.1$.

Michalke (1964) studied the temporal instability of a shear layer with a more realistic velocity profile, i.e. the hyperbolic tangent profile

$$\frac{u(y)}{U_0} = \frac{1}{2} \tanh(y/L) \quad (2.128)$$

The momentum thickness as defined in equation (2.126) is again equal to $\theta = \frac{1}{2}L$. For this problem an analytical solution is not available for the dispersion relation. Michalke (1964) derived the temporal growth rate for initial disturbances numerically. The result is included in figure 2.11. From this figure we observe a maximum amplification rate for $2k\theta \approx 0.44$ of $\alpha L/U_0 \approx 0.095$. Apparently the maximum amplification and the wavenumber at which the maximum amplification occurs is not very sensitive for the details of the mean velocity profile. Furthermore for low wave numbers the solution corresponds with the instability mode of an infinitesimally thin vortex sheet, $\alpha/U_0 = k/2$.

Michalke (1965) also studied the spatial instability of a hyperbolic tangent velocity profile. It could be shown, that the amplification of disturbances as a function of the wave number for the spatial instability differs only slightly from the amplification rate for the temporal instability.

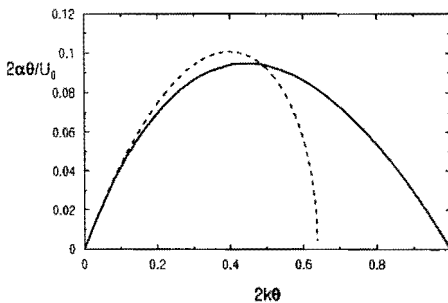


FIGURE 2.11: Temporal growth rates of initial disturbances for a vortex layer of uniform strength, (---) obtained by Drazin & Howard (1966) and for a undisturbed flow with a hyperbolic tangent velocity profile (—) by Michalke (1964).

The stability of an infinite vortex sheet of constant strength simulated by a discrete vortex method has been addressed by Krasny (1986a). For the evolution of a number

of point vortices positioned on a straight line segment with periodic boundary conditions Krasny (1986a) showed, using linear stability analysis, that the following discrete dispersion relation is valid

$$\left(\frac{\alpha}{U_0}\right)^2 = \frac{1}{4}k^2(1 - k/NV)^2 \text{ for } k < NV/2 \quad (2.129)$$

where NV is the number of point vortices. This shows that in the limit $NV \rightarrow \infty$ the dispersion relation for the continuous infinitesimally thin vortex sheet is recovered.

Using the vortex-blob method, with desingularised kernel given by equation (2.46), Krasny (1986b) found that in the limit of the number of vortex blobs $NV \rightarrow \infty$ the dispersion relation is given by

$$\left(\frac{\alpha}{U_0}\right)^2 = \frac{k(1 - e^{-k\cosh^{-1}(1+\delta^2)})e^{-k\cosh^{-1}(1+\delta^2)}}{4\delta\sqrt{2 + \delta^2}} \quad (2.130)$$

which for $\delta \rightarrow 0$ again tends to the dispersion relation for the continuous infinitesimally thin vortex sheet, i.e. equation (2.124). Figure 2.12 presents the amplification factor α for $\delta \rightarrow 0$, equation (2.129) for different values of NV is presented, as well as α for $NV \rightarrow \infty$, equation (2.130) for different values of δ , all as a function of the wave number k .

For a finite value of the desingularisation parameter δ , a maximum amplification is obtained

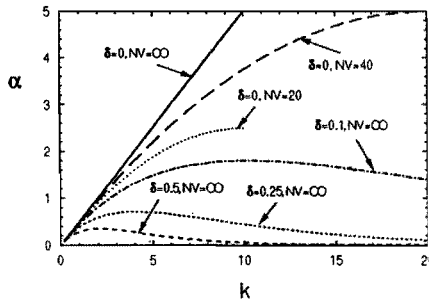


FIGURE 2.12: Temporal growth rates for initial disturbances for a discrete vortex method with point vortices, for different number of vortices NV , and with desingularised kernel according to Krasny (1986b), for different values of the desingularisation parameter δ .

at $k\delta \approx 1$ where $\alpha\delta/U_0 = 0.2$.

Comparing this with the values ($2k\theta \approx 0.4$, $2\alpha\theta/U_0 \approx 0.1$) obtained for a linear or a hyperbolic-tangent profile of the velocity across the vortex layer we conclude that the vortex-blob method results in a similar behavior in the limit $NV \rightarrow \infty$, if the desingularisation parameter is chosen as $\delta \approx 4\theta$.

The stability of a vortex sheet between two uniform flows of opposite sign has been studied by Hoeijmakers (1989) applying the vortex-sheet method. The amplification rate for small disturbances according to the linear stability analysis, given by equation (2.124)

could be realized for the case that of the order of 40 panels per wave length were used to discretise the vortex sheet. For the case for which less than 10 panels are distributed on a single wave length, the wave is not amplified.

In the computations with the vortex-blob method described in the next chapters the vortex sheet is not straight, does not have a constant vortex distribution and has a finite extent. As a result a relation between the value of δ used in the computational scheme and the thickness of the shear layer θ to be simulated by the method is not necessarily given by $\delta \approx 4\theta$. Furthermore, the value of δ is taken to remain constant during the calculation,

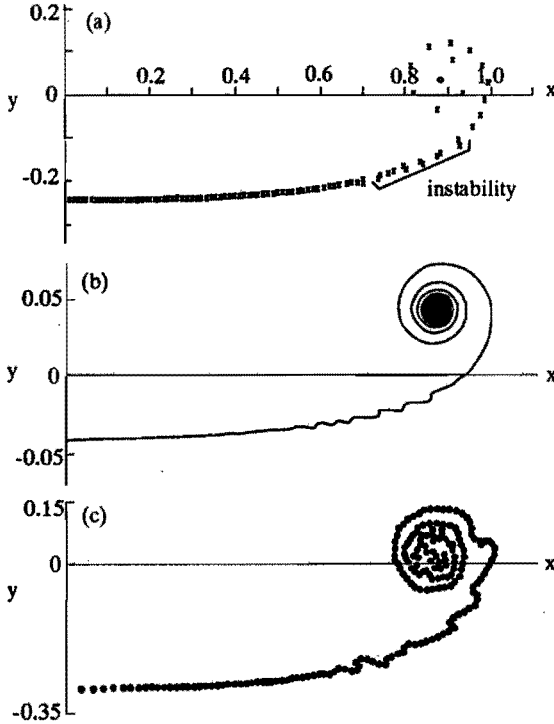


FIGURE 2.13: Onset of instability in the solution of vortex methods used to simulate the evolution of the wake behind an elliptically loaded wing. (a) Point-vortex method by Moore (1974), $tU/a = 0.5$, $NV = 98$. (b) Vortex-blob method by Krasny (1987), $tU/a = 0.1$, $NV = 2000$, $\delta = 0.003$, $\Delta t = 0.0005$. (c) Cloud-in-Cell method by Baker (1979), $tU/a = 0.6$, $NV = 2000$, $M = 129$

while of course the value of the momentum thickness θ usually varies during the evolution of a real shear layer. Therefore the value δ is taken as $\delta = 4\bar{\theta}$, where $\bar{\theta}$ is an estimated average value of the momentum thickness of the shear layer during the time of calculation.

A posteriori the effect of the choice of δ on the solution is assessed by varying δ by a factor two up and down.

2.2.7 The roll-up of the wake behind an elliptically loaded wing

Many of the vortex methods described in this chapter have been used to simulate the roll-up of the wake behind an elliptically loaded wing. This basically stationary three-dimensional problem can be transformed into an initial-value problem in the two-dimensional Trefftz plane (see Batchelor (1967)). The initial vortex sheet strength is

$$\gamma(s) = U \frac{s}{\sqrt{a^2 - s^2}} \quad (2.131)$$

where the initial position of the sheet is $z = s$, with $-a < s < a$. The initial downward velocity of the vortex sheet is equal to $v = -\frac{1}{2}U$ uniform along the vortex sheet. However, the self-induced (upward) velocity at the tip of the sheet ($s = \pm a$) is infinite and as a result, the two ends of the vortex sheet roll up into two counter-rotating spirals. Using a discrete-vortex method Westwater (1935) found that the solution became unstable near the highly rolled-up regions of the vortex sheet. Using a discrete-vortex method Moore (1974) obtained a smooth solution by introducing an explicit tip vortex to represent the tightly rolled-up part of the sheet and an amalgamation procedure to feed the tip vortex. However, when increasing the number of point vortices an instability sets in between the rolled-up part and the yet straight part of the sheet, see figure 2.13a.

Using a vortex-blob method Chorin & Bernard (1973) showed that removing the singular character of the velocity field of the discrete vortices can lead to a stable solution near the edges of the sheet. However, Krasny (1987) found instabilities of the vortex sheet if the calculation is performed with single-precision accuracy (7-digit arithmetic). The instabilities occur in the same part of the vortex sheet as found by Moore (1974) (see figure 2.13b). If the calculations is performed employing double precision accuracy (14-digit arithmetic) the instabilities did appear at a later moment in time.

Application of the Cloud-in-Cell method by Baker (1979) to this problem showed an instability similar to the one in the results obtained by the discrete-vortex methods.

Using a second-order panel method Hoeijmakers & Vaatstra (1983) obtained a stable solution of the vortex sheet roll-up. In their solution procedure with a curvature dependent adaptive repaneling the maximum panel size was increased during the calculation from $\Delta s_{max} = 0.01$ for small times to 0.1 for longer times. However, our present application of the method in which the maximum panel size is kept fixed at $\Delta s_{max} = 0.01$ showed that at $tU/a = 0.25$ an instability sets in for a part of the vortex sheet where the vortex strength attains a maximum. The geometry of the vortex sheet at $tU/a = 0.30, 0.40$ and 0.48 is shown in figure 2.14, together with the vortex distribution and the curvature along the sheet. In the unstable part of the vortex sheet the vorticity concentrates into regions where the curvature shows a maximum variation.

The calculation has been repeated with double-precision arithmetic, see figure 2.15. It is observed that the instability sets in at a later moment in time at $tU/a = 0.5$. At $tU/a = 1.62$ new, highly curved, rolled-up regions have formed within the unstable region of the

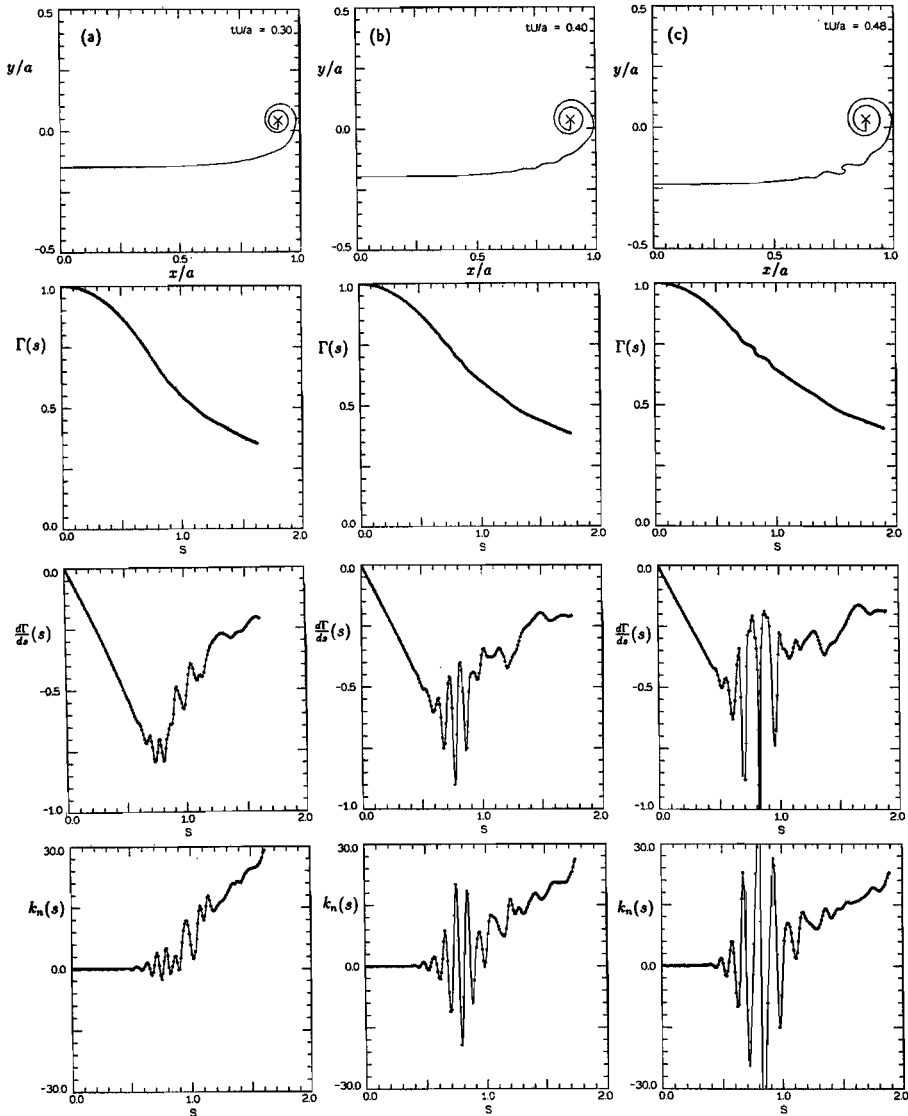


FIGURE 2.14: Onset of instability in the vortex sheet computed by the second-order vortex-sheet method (Hoeijmakers & Vaatstra (1983)) for the evolution of the wake behind an elliptically loaded wing. Solution at different moments in time, with maximum panel size $\Delta s_{max} = 0.01$ number of panels $NP \approx 140$; calculation single precision arithmetic.
 (a) $tU/a = 0.30$, (b) $tU/a = 0.40$, (c) $tU/a = 0.48$

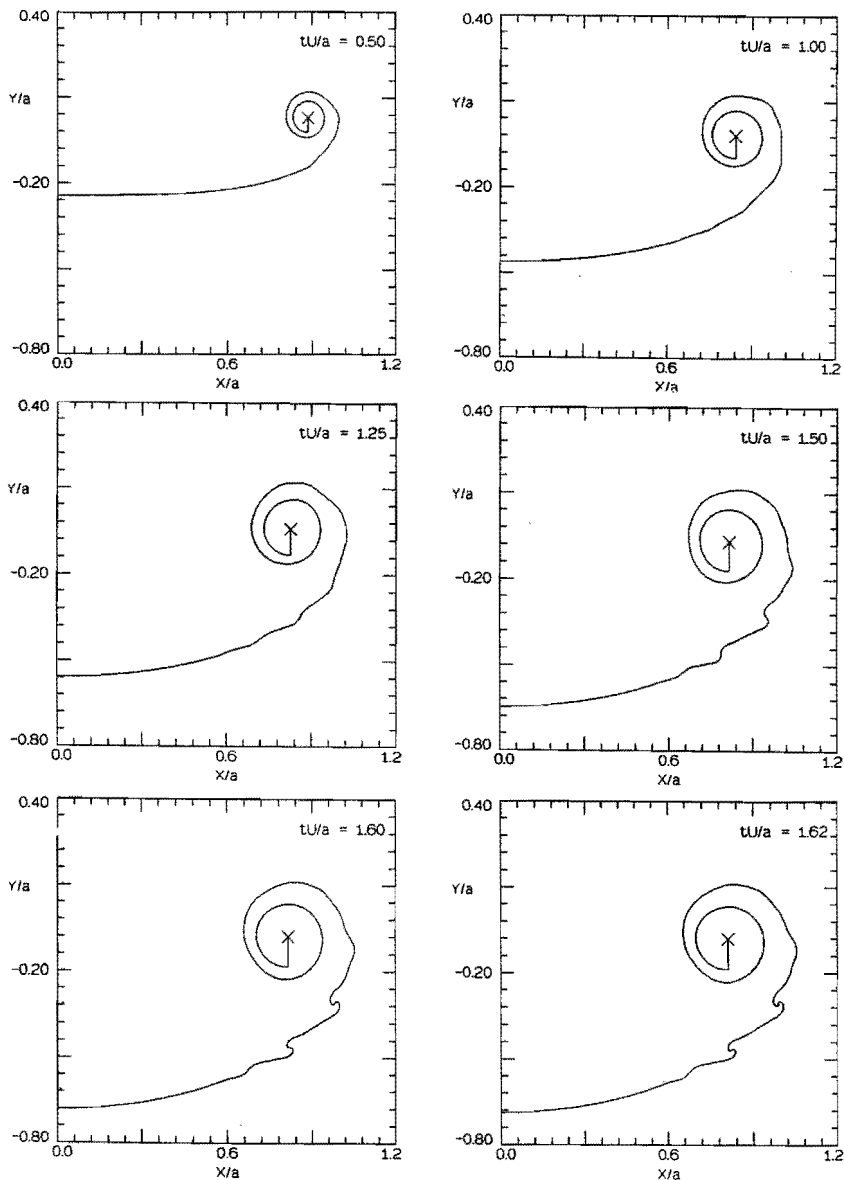


FIGURE 2.15: Onset of instability in the vortex sheet computed by the second-order vortex-sheet method (Hoeijmakers & Vaatstra (1983)) for the evolution of the wake behind an elliptically loaded wing. Solution at different moments in time, with maximum panel size $\Delta s_{max} = 0.01$ number of panels $NP \approx 200$; calculation double precision arithmetic.

vortex sheet. This suggests that the infinitesimally thin vortex sheet with initial elliptical vortex distribution is unstable for infinitesimally small disturbances at the position of the vortex sheet where it has still relatively small curvature and $\frac{d\Gamma^2}{ds^2} = 0$, with $\frac{d\Gamma}{ds}$ at a maximum.

2.3 CONCLUSIONS

For incompressible flows at high Reynolds number the vorticity generation at sharp edges and the convection of the generated vorticity can be described by a potential flow model, in which the spatial vorticity is condensed into vortex sheets. The generation of vorticity is in the potential flow model described by the Kutta condition. The normal-velocity boundary condition on rigid walls can either be satisfied by a conformal mapping of the physical flow domain onto a half-plane and introducing mirror-imaged vorticity, or by a boundary element method with a surface vortex and source distribution.

The vortex sheets can be discretized by discrete vortices (*discrete-vortex and vortex blob method*) or vortex segments (*vortex-sheet method*). A further simplification can be obtained if the complete vortex sheet is described by a single point vortex. In that case a more accurate description of the vorticity generation can be obtained by introducing a so-called edge vortex. Application of the various vortex methods for the roll-up of the wake behind an elliptically loaded wing shows that both the discrete-vortex and the vortex-sheet method are able to describe the inherent Kelvin-Helmholtz instability of a vortex sheet.

Results of the various methods described in this chapter are compared with each other and with measured data in the next chapter when applied to starting flows and in chapter 4 when applied to periodic flows.

REFERENCES

- AREF H. (1983) Integrable, chaotic, and turbulent vortex motion in two-dimensional flows. *Ann. Rev. Fluid Mech.* **15**, 345 - 389.
- BAKER G.R. (1979) The 'cloud in cell' technique applied to the roll up of vortex sheets. *J. Comp. Phys.* **31**, 76 - 95.
- BAKER G.R. (1980) A test of the method of Fink and Soh for following vortex-sheet motion. *J. Fluid Mech.* **100** 1, 209 - 220.
- BEALE J.T. & MAJDA A. (1985) High order accuracy vortex methods with explicit velocity kernels. *J. Comp. Phys.* **58**, 188 - 208.
- BROWN C.E. & MICHAEL W.H. (1954) Effect of leading-edge separation on the lift of a delta wing. *J. Aero. Sci.* **21**, 690 - 694.
- BRUGGEMAN J.C. (1987) Flow induced pulsations in pipe systems. PhD thesis Eindhoven University of Technology
- BRUGGEMAN J.C., HIRSCHBERG A., DONGEN M.E.H. VAN, WIJNANDS A.P.J. & GORTER J. (1991) Self-sustained aero-acoustic pulsations in gas transport systems: experimental study of the influence of closed side branches. *J. Sound & Vibr.* **150** 3, 371 - 393.
- CHORIN A.J. & BERNARD P.S. (1973) Discretisation of a vortex sheet, with an example of roll-up. *J. Comp. Phys.* **13**, 423 - 429.
- CHRISTIANSEN J.P. (1973) Numerical simulation of hydrodynamics by the method of point vortices, *J. Comp. Phys.* **13**, 363 - 393

- CLEMENTS R.R. (1973) An inviscid model of two-dimensional vortex shedding. *J. Fluid Mech.* **57** 2, 321 - 336.
- CLEMENTS R.R. & MAULL D.J. (1975) The representation of sheets of vorticity by discrete vortices. *Prog. Aeron. Sci.* **16** 2, 129 - 146.
- CRIGHTON D.G. (1975) Basic principles of aerodynamic noise generation. *Prog. Aerosp. Sci.* **16** 1, 31 - 96.
- CRIGHTON D.G. (1981) Acoustics as a branch of fluid mechanics. *J. Fluid Mech.* **106**, 261 - 298.
- CROW S.C. (1970) Aerodynamic sound emission as a singular perturbation problem. *Stud. in Appl. Math.* **49**, 21 - 44.
- DISSELHORST J.H.M. (1978) Acoustic resonance in open tubes. PhD thesis Twente University of Technology
- DISSELHORST J.H.M. & WIJNGAARDEN L. VAN (1980) Flow in the exit of open pipes during acoustic resonance. *J. Fluid Mech.* **99** 2, 293 - 319.
- DOAK P.E. (1973) Fundamentals of aerodynamic sound theory and flow duct acoustics. *J. Sound & Vibr.* **28** 3, 527 - 561.
- DRAZIN P.G. & HOWARD L.N. (1966) Hydrodynamic stability of parallel flow of inviscid fluid. *Adv. Appl. Mech.* **9**, 1 - 89.
- FFOWCS WILLIAMS J.E. (1972) Hydrodynamic noise. *Ann. Rev. Fluid Mech.* **1**, 197 - 222.
- FFOWCS WILLIAMS J.E. (1977) Aeroacoustics. *Ann. Rev. Fluid Mech.* **9**, 447 - 468.
- FFOWCS WILLIAMS J.E. (1982) Sound sources in aerodynamics - Fact and fiction. *A.I.A.A. Journal* **20** 3, 307 - 315.
- FINK P.T. & SOH W.K. (1978) A new approach to roll-up calculations of vortex sheets. *Proc. Roy. Soc. Lond. A* **362**, 195 - 209.
- GOLDSTEIN M.E. (1976) Aeroacoustics, McGraw-Hill Book Company
- GRAHAM J.M.R. (1983) The lift on an aerofoil in starting flow. *J. Fluid Mech.* **133**, 413 - 425.
- HAMA F.R. & BURKE E.R. (1960) On the rolling up of a vortex sheet. University of Maryland, technical note B.N. 220
- HARDIN J.C. & POPE D.S. (1992) Sound generation by a stenosis in a pipe. *A.I.A.A. Journal* **30** 2, 312 - 317.
- HIRSCHBERG A. & RIENSTRA S.W. (1992) Aero-akoestiek, Lecture notes Eindhoven University of Technology, IWDE Report 92-06
- HOEIJMAKERS H.W.M. & VAATSTRA W. (1983) A higher order panel method applied to vortex sheet roll-up. *A.I.A.A. Journal* **21** 4, 516 - 523.
- HOEIJMAKERS H.W.M. (1983) Computational vortex flow aerodynamics. *AGARD CP* **342** 18, 1 - 35.
- HOEIJMAKERS H.W.M. (1989) Computational Aerodynamics of ordered vortex flows. PhD thesis Delft University of Technology, also NLR Report TR 88088 U.
- HOEIJMAKERS H.W.M. (1990) Modeling and numerical simulation of vortex flow in aerodynamics. *AGARD CP* **494** 1, 1 - 46.
- HOWE M.S. (1975) Contributions to the theory of aerodynamic sound, with application to excess jet noise and the theory of the flute. *J. Fluid Mech.* **71** 4, 625 - 673.
- JENVEY P.L. (1989) The sound power from turbulence: A theory of the exchange of energy between the acoustic and non-acoustic field. *J. Sound & Vibr.* **131** 1, 37 - 66.
- KIYA M. & ARIE M. (1977) A contribution to an inviscid vortex-shedding model for an inclined flat plate in uniform flow. *J. Fluid Mech.* **82** 2, 223 - 240.
- KRASNY R. (1986a) A study of singularity formation in a vortex sheet by the point vortex method. *J. Fluid Mech.* **167**, 65 - 93.
- KRASNY R. (1986b) Desingularisation of periodic vortex sheet roll-up. *J. Comp. Phys.* **65**, 292 - 313.

- KRASNY R. (1987) Computation of vortex sheet roll-up in the Trefftz plane. *J. Fluid Mech.* **184**, 123 - 155.
- LAMB H. (1932) Hydrodynamics, Dover Publishers 6th Ed.
- LEONARD A. (1980) Vortex methods for flow simulation. *J. Comp. Phys.* **37**, 289 - 335.
- LEONARD A. (1985) Computing three-dimensional incompressible flows with vortex elements. *Ann. Rev. Fluid Mech.* **17**, 523 - 559.
- LIGHTHILL M.J. (1952) On sound generated aerodynamically I: General theory. *Proc. Roy. Soc. Lond. A* **211**, 564 - 587.
- LIGHTHILL M.J. (1954) On sound generated aerodynamically II: Turbulence as a source of sound. *Proc. Roy. Soc. Lond. A* **222**, 1 - 32.
- LILLEY (1972) Generation of sound in a mixing region. *Lockheed Aircraft Company Progress report on contract F-33615-71-C-1663*.
- MASKEW B. (1977) Subvortex technique for the close approach to a discretized vortex sheet. *J. Aircraft* **14** 2, 188 - 193.
- MICHALKE A. (1964) On the inviscid instability of the hyperbolic-tangent velocity profile. *J. Fluid Mech.* **19** 4, 543 - 556.
- MICHALKE A. (1965) On spacially growing disturbances in an inviscid shear layer. *J. Fluid Mech.* **23** 3, 521 - 544.
- MOKRY M. & RAINBIRD W.J. (1975) Calculation of vortex sheet roll-up in a rectangular wind tunnel. *J. Aircraft* **12** 9, 750 - 752.
- MOORE D.W. (1974) A numerical study of the roll-up of a finite vortex sheet. *J. Fluid Mech.* **63** 2, 225 - 235.
- MOORE D.W. (1981) On the point vortex method. *SIAM J. Sci. Stat. Comput.* **2** 1, 65 - 84.
- MYERS M.K. (1986) An exact energy corollary for homentropic flow. *J. Sound & Vibr.* **109** 2, 277 - 284.
- PETERS M.C.A.M. & HIRSCHBERG A. (1993) Acoustically induced periodic vortex shedding at sharp-edged open channel ends: Simple vortex models. *J. Sound & Vibr.* **161** 2, 281 - 299.
- PHILLIPS O.M. (1960) On the generation of sound by supersonic turbulent shear layers. *J. Fluid Mech.* **9**, 1 - 28.
- PIERCE A.D. (1989) Acoustics, an introduction to its physical principles and applications. McGraw-Hill Book Company.
- POWELL A. (1964) Theory of vortex sound. *J. Acoust. Soc. Am.* **36** 1, 177 - 195.
- POWELL A. (1990) Some aspects of aeroacoustics: From Rayleigh until today. *J. Vibr. & Acoustics* **112**, 145 - 159.
- RAYLEIGH LORD (1896) The theory of sound. Vol II, 2nd ed., The Macmillian Company
- RICCARDI G. & PIVA R. (1992) Models for inviscid vortex dynamics. *Conference proceedings*, private communication, 1-10.
- ROSENHEAD L. (1931) The formation of vortices from a surface of discontinuity. *Proc. Roy. Soc. Lond. A* **134**, 170.
- SAFFMAN P.G. & BAKER G.R. (1979) Vortex interactions. *Ann. Rev. Fluid Mech.* **11**, 95 - 122.
- SARPKAYA T. (1975) An inviscid model of two-dimensional vortex shedding for transient and asymptotically steady separated flow over an inclined plate. *J. Fluid Mech.* **68** 1, 109 - 128.
- SARPKAYA T. (1989) Computational methods with vortices - The 1988 Freeman scholar lecture. *J. Fluids Eng.* **111**, 5 - 52.
- TREFETHEN L.N. (1980) Numerical computation of the schwarz-christoffel transformation. *SIAM J. Sci. Stat. Comput.* **1** 1, 82 - 102.
- WESTWATER F.L. (1935) Rolling-up of the surface of discontinuity behind an aerofoil of finite span. *Aero. Res. Council. R & M*, 1692.
- ZABUSKY N.J., HUGHES M.H. & ROBERTS K.V. (1979) Contour dynamics for the Euler equations in two dimensions. *J. Comp. Phys.* **30**, 96 - 106.

Numerical simulation of starting flows

Abstract

The two-dimensional potential flow models of the generation and convection of vorticity developed in chapter 2 are used to describe the impulsively started flows in a T-junction and out of a nozzle. Before these applications are considered the generic problem of the starting flow about a wedge is used to compare the results of simplified methods with those of more elaborate methods.

The virtue of simple methods depends on the type of geometry studied. A single vortex method usually fails. However, if the vorticity generation near the edge is described locally by introducing a second vortex, such as in a so-called two-vortex method the generation and convection of the center of vorticity is described satisfactory during the initial phase.

3.1 INTRODUCTION

In this section results of various methods used to describe two-dimensional vortex formation at sharp edges will be compared mutually and with results of flow visualization experiments. The inviscid, incompressible, starting flow is studied for a number geometries. The primary present interest is in the periodic vortex formation at sharp edges in pipe systems, for example at T-junctions. However, the starting flow in a T-junction with sharp edges is a more suitable test for the numerical methods because in a starting flow the initial conditions are well-defined and in contrast to the periodic flow a model for the decay of vortex strength by annihilation does not have to be developed. Furthermore the moment of the start of the generation of a vortex structure is clearly defined as $t = 0$.

The second geometry studied is the flow out of a two-dimensional sharp-edged or square-edged nozzle. The starting flow is simulated numerically and compared with experimental results by Blondeaux & Bernardinis (1983) and Auerbach (1987). The vortex formation in this geometry differs from that in the T-junction geometry by the fact that the vortex structure does not impinge on a downstream edge at a distance comparable to the channel width but forms a free jet with streamwise dimensions much larger than the channel width.

Before investigating these geometrically and fluid mechanically more complex cases a more generic type of flow problem is considered first: the starting flow past an infinite wedge of different wedge angles. This flow has been studied theoretically by Rott (1956), Blenderman (1969), Graham (1977) and Pullin (1978). In an inviscid flow, if the velocity increases as a power of the time ($U_0 = at^\alpha$) the problem admits a self-similar solution, this since no characteristic length or time scale are involved in this problem. Experiments

on the starting flow past a wedge have been performed by Rott (1956), Pierce (1961) and Pullin & Perry (1980).

Using the single-vortex method proposed by Brown & Michael (1954), Rott (1956), Howe (1975) and Graham (1983), the complete vortex layer is modeled by a single point vortex positioned at the center of vorticity of the vortex sheet. Using this single-vortex method an analytical solution can be obtained.

For the impulsively started flow ($\alpha = 0$), the results of the single-vortex method will be compared with the results of the more accurate second-order vortex-sheet method, developed in the present study and based on the vortex-sheet method proposed by Hoesjmakers & Vaatstra (1983) for the evolution of rolling-up vortex wakes behind wings. In this method in contrast to Pullin's (1978) approach similarity of the solution is not assumed. As a result the method can also be used for non-similar problems. Also results of a vortex-blob method and of a two-vortex method will be discussed. As far as the level of complexity and physical relevance is concerned the two-vortex method can be considered to be at an intermediate level between that of the single-vortex method and that of the more complex vortex-sheet and vortex-blob methods. In the single-vortex method, the two-vortex method and the vortex-sheet method all or some of the vorticity is combined by an amalgamation process into the main vortex representing the highly rolled-up vortex core of the vortex sheet. It will be demonstrated that the vorticity amalgamation process must be handled with care and the influence of different amalgamation procedures on the solution will be discussed.

3.2 STARTING FLOW PAST A WEDGE

3.2.1 *Infinite wedge of arbitrary included angle*

As a generic model of the type of flows to be investigated the starting flow around an infinite wedge is considered. Due to the action of viscous forces the flow separates at the sharp edge of the wedge and vorticity is generated. The vorticity generated at the edge convects with the local flow velocity away from the edge into the flow field. The continuously distributed vorticity is concentrated in the free shear layer emanating from the edge.

For a high-Reynolds-number flow the vorticity in the shear layer near the edge will be distributed along a thin vortex layer, across which a rapid variation in tangential velocity takes place. Further away from the edge the vortex layer starts to spiral and rolls up into a vortical core. Within the core the vorticity is spatially distributed in a smooth fashion with a maximum at the center of the vortex core. In the core, the individual turns of the spiraling free shear layer cannot be identified anymore. In a potential-flow model of the flow the vortex layer is assumed to be infinitesimally thin with all the vorticity contained in this vortex sheet. In the potential-flow model the vortex core should ideally be represented by a tightly wound spiral of infinite length. In practice the vorticity in the inner spirals is concentrated into a single point vortex. The effect of viscosity is accounted for by the Kutta condition, which requires the velocity to be finite at the sharp edge, accomplished by the introduction of the vortex sheet.

Complex function theory is used to find a solution satisfying the normal-velocity boundary condition. By conformal transformation the flow domain in the physical plane $z = x + iy$ is mapped onto a half-plane $\xi > 0$ in the computational plane $\zeta = \xi + i\eta$, see figure 3.1. The mapping is given by $z = f(\zeta)$ with

$$z = \left(\frac{\zeta}{D} \right)^{1/n} \quad (3.1)$$

with $n = \pi/(2\pi - \theta)$

D is a complex constant while the value of n is determined by the included angle θ of the wedge and varies between $n = 0.5$ for included angle $\theta = 0$ and $n = 1$ for $\theta = \pi$. The attached flow around the edge is described by a complex velocity potential which, in

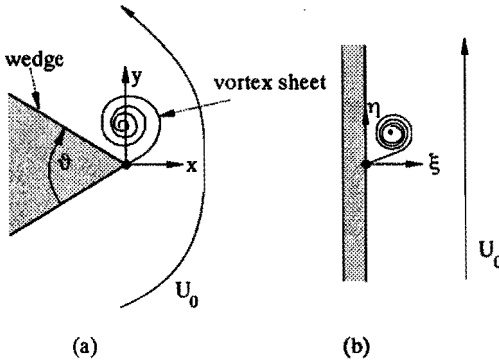


FIGURE 3.1: Schwarz Christoffel transformation of a wedge.
 (a) physical plane $z = x + iy$ (b) computational plane $\zeta = \xi + i\eta$

the computational plane, is given by

$$\Phi_0(\zeta) = -iat^\alpha \zeta \quad (3.2)$$

where a is a real constant and t denotes the time.

In case the flow separates at the edge the velocity potential at a point ζ in the computational plane is a superposition of the onset flow $\Phi_0(\zeta)$ given by equation (3.2) and the flow induced by the vortex sheet $\Phi_s(\zeta)$, i.e.

$$\Phi_s(\zeta) = \frac{1}{2\pi i} \int_0^{s_{tot}} \gamma(s) \ln \left(\frac{\zeta - \zeta_s(s)}{\zeta + \zeta_s^*(s)} \right) ds \quad (3.3)$$

where $\gamma(s)$ is the vortex distribution and the integration is along the vortex sheet, which position is described by $\zeta = \zeta_s(s)$. Note that the boundary condition on the rigid wall

in the computational plane ($\xi = 0$) is satisfied by mirror-imaging the vortex sheet in the positive half-plane into the vertical plane. The circulation along the sheet is defined as the jump in the value of the velocity potential across the sheet. At a point s of the sheet it can be determined from

$$\Gamma(s) = \int_s^{s_{tot}} \gamma(s^*) ds^* \quad (3.4)$$

where the integral is taken from the point s on the sheet to the endpoint of the rolled-up vortex sheet. The circulation $\Gamma(0)$ contained within the vortex sheet corresponds to the value of the dipole strength at $s = 0$, where the sheet is connected to the edge of the wedge.

The velocity at a point z in the physical plane is given by equation (2.64) applied to the total velocity potential $\Phi(\zeta) = \Phi_0(\zeta) + \Phi_s(\zeta)$. By using equation (3.1), (3.2) and (3.3) we obtain

$$\left(\frac{d\Phi}{dz}\right)(z) = \left[-iat^\alpha + \frac{1}{2\pi i} \int_0^{s_{tot}} \gamma(s) \left(\frac{1}{\zeta - \zeta_s(s)} - \frac{1}{\zeta + \zeta_s^*(s)}\right) ds\right] nD^{\frac{1}{n}} \zeta^{1-\frac{1}{n}} \quad (3.5)$$

where the integral is taken over the whole vortex sheet and the value of n depends on the interior angle of the wedge θ according to equation (3.1). To obtain the velocity at a point $\zeta = \zeta_*$ on the vortex sheet, the Cauchy principle value of the integral in equation (3.5) should be taken.

The Kutta condition requires that the singular behavior of the velocity field due to $\Phi_0(\zeta)$ at the edge $\zeta = 0$ is compensated by the velocity induced by the vortex sheet, see equation (2.90). Using equation (3.5) one finds

$$at^\alpha = \frac{1}{2\pi} \int_0^{s_{tot}} \gamma(s) \left(\frac{1}{\zeta_s(s)} - \frac{1}{\zeta_s^*(s)}\right) ds \quad (3.6)$$

Because of the absence of a length scale the problem can be brought in a self-similar form in terms of time-scaled variables, both for the coordinates as well as the circulation of the vortex sheet (see Pullin (1978)) by

$$\begin{aligned} z &= (Cat^{\alpha+1}D)^{\frac{1}{2-n}} \omega(\lambda) \\ \Gamma(0) &= (Ct)^{\frac{n}{2-n}} (at^\alpha D)^{\frac{2}{2-n}} J \\ \text{with } C &= \frac{(2-n)(1-n)}{1+\alpha} \end{aligned} \quad (3.7)$$

where $\omega(\lambda) = \rho(\lambda) e^{i\chi(\lambda)}$ and J are the scaled coordinates and the scaled circulation, respectively. The parameter λ is one minus the scaled circulation along the vortex sheet and is zero at the edge and one at the end of the vortex sheet. If $\Gamma(s)$ is a monotonic function of the arc length s along the vortex sheet, λ can be used as an independent variable along the vortex sheet.

$$\lambda(s) = 1 - \frac{\Gamma(s)}{\Gamma(0)} \quad (3.8)$$

The vortex sheet is convected with the local flow velocity according to equation (2.71). Equations (3.5), (3.6) and (2.71) form a nonlinear system of equations, which has to be solved numerically.

Pullin (1978) solved the problem of the starting flow around a wedge formulated in the similarity variables numerically employing a Newton-Raphson scheme. He discretised the portion of the vortex sheet attached to the edge by a number (75) of segments. The rolled-up part of the vortex sheet is represented by a point vortex. The single-vortex solution from Rott (1956) for the flow with separation about a semi-infinite flat plate ($n = 1/2$) with a streakline of the flow emanating from the edge has been used as an initial guess for the position of the vortex sheet and iteratively improved. Subsequently the solution for the flat plate was then used as an initial guess for the solution for the flow around a wedge ($n > 1/2$). For the wedge with interior angle of 90° Pullin (1978) obtained for the scaled circulation $J = 2.53$ and for the scaled position of the core vortex $\omega_v = \rho_v e^{i\chi_v}$, $\rho_v = 0.54$ and $\chi_v = 98^\circ$ (see table 3.1). The scaled circulation of the point vortex representing the vortex core was $J_v = 1.09$.

Single-vortex methods

If it is assumed that the vortex layer generated at the sharp edge can be modeled by a concentrated single point vortex connected to the edge by a cut, the so called *feeding sheet*, the vortex position and its circulation can be determined analytically from the Kutta condition applied to the edge and the conditions imposed on the point vortex/feeding sheet combination. The form the solution takes depends strongly on these conditions. For the conditions corresponding to the free vortex, the force-free vortex and the source-free vortex methods, the convection velocity of the point vortex is given by equation (2.71), (2.76) and (2.80), respectively. The position of the point vortex in terms of scaled coordinates $\omega_v = \rho_v e^{i\chi_v}$ and circulation J , defined by equation (3.7), can be obtained from the solution given by equation (2.92), (2.94) and (2.95), respectively. The result is

$$\begin{aligned}
 \text{FREE VORTEX : } \rho_v &= \left[n \sqrt{1 - \frac{1}{4n}} \right]^{\frac{1}{2-n}} \\
 \text{FORCE-FREE VORTEX : } \rho_v &= \left[n \sqrt{1 - \frac{1}{4n} \left(\frac{1+\alpha}{3\alpha+n+1} \right)} \right]^{\frac{1}{2-n}} \\
 \text{SOURCE-FREE VORTEX : } \rho_v &= \left[n \sqrt{1 - \frac{1}{4n} \left(\frac{1+\alpha}{2\alpha/n+\alpha+2} \right)} \right]^{\frac{1}{2-n}} \\
 \text{AND FOR EACH OF THE METHODS : } &\begin{cases} \chi_v = \frac{1}{n} \arccos \left(\frac{1}{2\sqrt{n}} \right) \\ J = 2\pi \sqrt{n} \rho_v^n \end{cases}
 \end{aligned} \tag{3.9}$$

In figure 3.2 the similarity solutions obtained with the different single vortex methods are compared with the position of the core vortex of the vortex-sheet solution obtained by Pullin (1978).

From figure 3.2 it is clear, that the free-vortex method strongly overestimates the distance of the point vortex to the edge and the circulation, i.e. the total vorticity generated, while the results of both the force-free and the source-free single-vortex method are much closer to the results of Pullin's (1978) first-order vortex-sheet method.

It should be noted that Pullin's comparison of the position of the vortex of a single-vortex

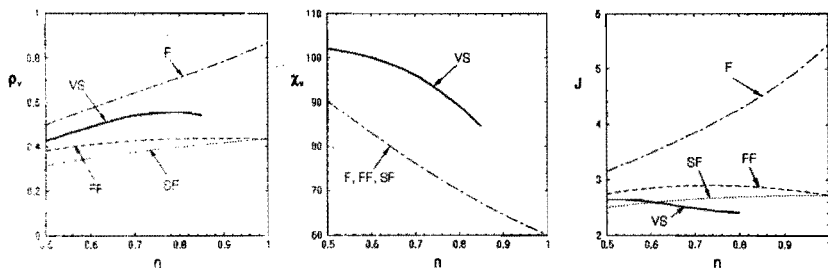


FIGURE 3.2: Influence of wedge angle parameter $n = \pi/(2\pi - \theta)$ on the position of the point vortex $\omega_v = \rho_v e^{i\chi_v}$ and its circulation J for an impulsively started flow $\alpha = 0$ past a wedge. Results of the single-vortex method are compared with results of a first-order vortex-sheet method VS obtained by Pullin (1978). F: free vortex method; FF: force-free vortex method; SF: source-free vortex method.

method with the position of the point vortex of his vortex-sheet method is not so relevant, since the point vortex of the single-vortex method represents the center of vorticity of the whole vortex system, rather than that of the rolled-up core of the vortex sheet. However, since data on the center of vorticity have not been reported by Pullin (1978), a more detailed comparison cannot be made.

In the following we will only consider the cases the interior angle of the wedge θ equals 90° and 0° , corresponding with a value of $n = 2/3$ and $n = 1/2$, respectively. These two angles correspond with the edges occurring in the specific pipe system geometries studied later on.

3.2.2 90° Wedge

Single-vortex method

For the comparison of the results of the different vortex methods discussed in chapter 2, we consider the impulsively started flow around a wedge with an interior angle of 90° . The single-vortex solution for this problem is given by equation (3.9), with $n = 2/3$, i.e.

$$\begin{aligned}
 \rho_v &= \left(\frac{\sqrt{10}}{4} \Lambda \right)^{3/4} \\
 \chi_v &= \frac{3}{2} \arccos \left(\frac{\sqrt{6}}{4} \right) \\
 J &= 2\sqrt[4]{10} \pi \sqrt{\frac{\Lambda}{6}}
 \end{aligned} \tag{3.10}$$

where $\Lambda = 2/3$, $2/5$ and $1/3$ for the free, force-free and source-free vortex method, respectively. The data are collected in table 3.1. Since only a single vortex is present in these methods the position of the center of vorticity $\omega_{c.o.v.}$ is equal to that of the point vortex center ω_v , and the circulation J of the vortex system is equal to the point vortex strength J_v .

METHOD		$\rho_{c.o.v.}$	$\chi_{c.o.v.}$	J	ρ_v	χ_v	J_v
SINGLE VORTEX	<i>free</i> ($\Lambda = 2/3$)	0.62	78.4°	3.72	see		
	<i>force-free</i> ($\Lambda = 2/5$)	0.42	78.4°	2.89	c.o.v.		
	<i>source-free</i> ($\Lambda = 1/3$)	0.37	78.4°	2.63			
TWO VORTEX	<i>amalg. vorticity only</i>	0.66	88.8°	3.24	see		
	<i>amalg. z-plane</i>	0.45	88.8°	2.53	c.o.v.		
	<i>amalg. ζ-plane</i>	0.40	88.8°	2.33			
VORTEX BLOB	$\lambda_{NP} = 1.00$	0.48	93.4°	2.51	-	-	-
VORTEX SHEET	$\lambda_{NP} = 0.57, \theta_v = 1620^\circ$	0.49	94.0°	2.58	0.52	96.6°	1.12
PULLIN (1978)	$\lambda_{NP} = 0.57, \theta_v = 1620^\circ$	-	-	2.53	0.54	98.0°	1.09

TABLE 3.1: Position of center of vorticity $\omega_{c.o.v.} = \rho_{c.o.v.} e^{i\chi_{c.o.v.}}$, circulation J and point vortex position $\omega_v = \rho_v e^{i\chi_v}$ and its circulation J_v obtained with different vortex methods. Impulsively started flow ($\alpha = 0$) past a wedge with $\theta = 90^\circ$ ($n = 2/3$).

Vortex-sheet method

In the vortex-sheet method parts of the vortex sheet is modeled by continuous vortex sheets, while the highly rolled-up parts of the vortex sheet, representing the vortex cores, are modeled by discrete vortices. The latter are connected to the vortex sheet by cuts, so called *feeding sheets*, across which the potential experiences a jump. The angular extent of the vortex sheet around the vortex core θ_v is a parameter of the vortex-sheet method. In general the value of θ_v is chosen to be fixed during the computation.

The complex velocity potential is given by

$$\Phi(\zeta) = \Phi_0(\zeta) + \Phi_s(\zeta) + \Phi_v(\zeta) \quad (3.11)$$

where $\Phi_0(\zeta)$ is the attached flow component, given by equation (3.2), $\Phi_s(\zeta)$ is the potential due to the continuous parts of the vortex sheet, equation (3.3), and $\Phi_v(\zeta)$ the potential due to the point vortices, equation (2.87).

The circulation of the vortex sheet plus vortex core is equal to the dipole strength $\Gamma(0)$ at the edge, which can be compared with the circulation of the vortex in the single-vortex methods. The center of vorticity of the vortex sheet plus core can be compared with the vortex position of the single-vortex methods.

The initial position of the vortex core is obtained from the force-free point vortex similarity solution for the impulsively started, separated flow, discussed in the previous

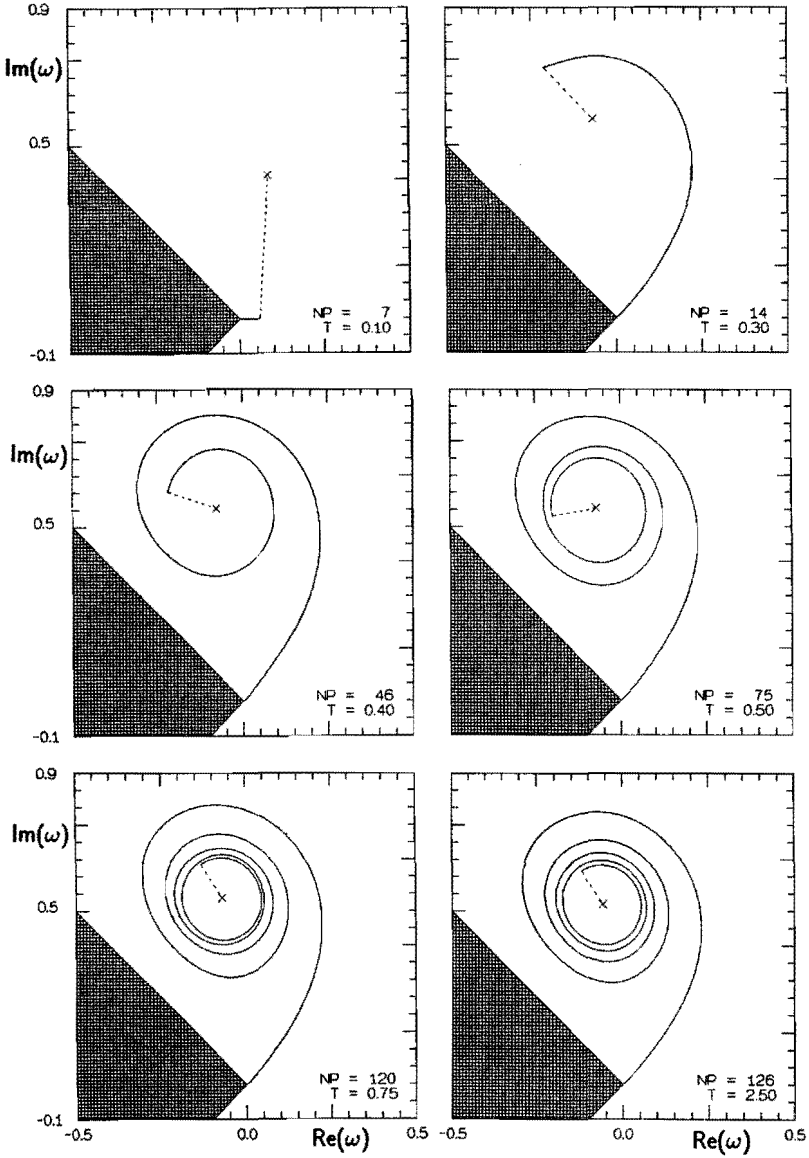


FIGURE 3.3: Development of the vortex sheet computed with the vortex-sheet method. The vortex sheet geometry is given in similarity coordinates $\omega(\lambda)$. The steady state similarity solution is obtained at $t = 2.5$.

section. The initial solution for $t \leq t_1$ constitutes the point vortex at the location given by equation (3.10) with $\Lambda = 2/5$ and a flat vortex sheet segment of constant dipole strength $\Gamma(s_i) = J$ along the extension of the bisector of the wedge, discretised into five panels. The vortex sheet starts to convect with the flow and to gain in circulation through the new vorticity introduced by the application of the Kutta condition at the edge.

The results for this similarity problem are presented in the similarity variables $\omega(\lambda)$ and J for the position of the vortex system and its circulation, respectively. The parameter λ along the vortex sheet can be written as, see equation (3.8)

$$\lambda_i = 1 - \frac{\Gamma(s_i)}{\Gamma(0)} \text{ for } i = 1 \dots NP \quad (3.12)$$

λ_i determines the part of the circulation that is contained in the vortex sheet from the edge to point number i where $i = 1..NP$, with NP the number of panels. λ_{NP} is the part of the circulation contained in the continuous vortex sheet segment. When λ_{NP} is zero, all of the circulation is contained in the point vortex, and we have a single-vortex method, while for λ_{NP} equal to 1 all the circulation is contained in the then infinitely long vortex sheet, and a point vortex representing the vortex core is not present.

Proceeding in time the similarity solution is approached, see figure 3.3. The parameters used for the vortex-sheet calculation are given in table 3.2. Following the initial stage with a smaller fixed angle θ_v , a number of time steps have been performed with larger value of Δs_{max} and θ_{max} , in order to damp spurious initial disturbances in the vortex sheet geometry.

TIME STEP NR.	\mathcal{F}	Δs_{max}	$\Delta \theta_{max}$	θ_v
1 - 250	0.2	0.05	15°	180°
251 - 350	0.2	0.10	20°	1620°
351 - 550	0.2	0.05	15°	1620°
551 - 3550	0.2	0.04	15°	1620°

TABLE 3.2: Parameters used for the vortex sheet solution of the flow around a wedge with $\theta = 90^\circ$, see figure 3.3.

In figure 3.4 the vortex position and strength are given as a function of time. For $t \leq t_1 = 0.1$ the values are given by the force-free single vortex solution (see table 3.1). Clearly, for the steady state solution, the position of the center of vorticity differs significantly from the point vortex position, both for the distance to the edge and for the angle.

For the converged solution obtained at $t = 2.5$, the position of the vortex sheet in the computational and physical plane, dipole distribution and first and second derivative of the dipole distribution along the sheet with respect to the arc length s and the curvature of the sheet, all in the physical plane, are presented in figure 3.5. At the edge the direction of the first derivative of the position vector corresponds with the tangent of the lower side of the wedge. Note that this is not explicitly imposed by the numerical scheme. Application of the Kutta condition corresponds in this case to a vortex sheet leaving the

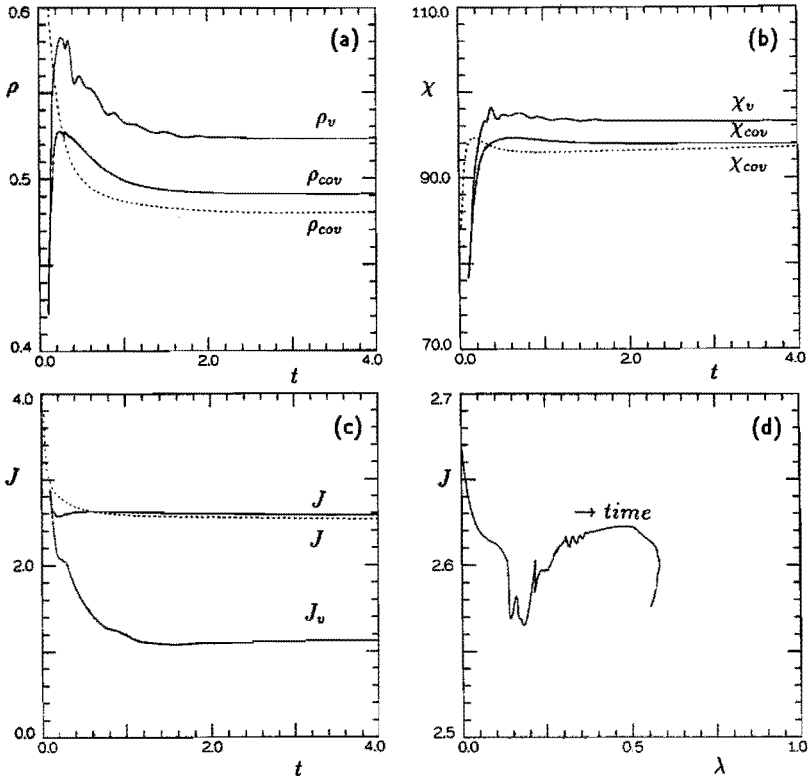


FIGURE 3.4: Vortex position $\omega_v = \rho_v e^{i\chi_v}$, center of vorticity $\omega_{c.o.v.} = \rho_{c.o.v.} e^{i\chi_{c.o.v.}}$, point vortex strength J_v and circulation J , in similarity variables, converge to a steady-state self-similar solution. The force-free single vortex solution given by equation (3.10) with $\Lambda = 2/5$ is used as a start for the convergence process. The scaled arc length λ increases with increasing θ_v . (—) vortex-sheet method (---) vortex blob method (only for the center of vorticity and total circulation).

wedge tangentially. Regions of high curvature k_n correspond with regions of high values of the vortex distribution $\gamma(s)$. Even in the tightly rolled-up region the vortex sheet appears to keep an elliptical shape. At the edge the curvature shows a singular behavior, it *tends to infinity* at the edge. The singular behavior of the vortex sheet near the edge has already been proposed by Graham (1977, 1986) and Clapworthy & Mangler (1974), who proposed that the vortex sheet near the edge should behave as $y_n = Cx_r^{3/2}$, where x_r and y_n are coordinates parallel and normal to the lower side of the wedge, respectively. The vortex-sheet solution appears to confirm this behavior.

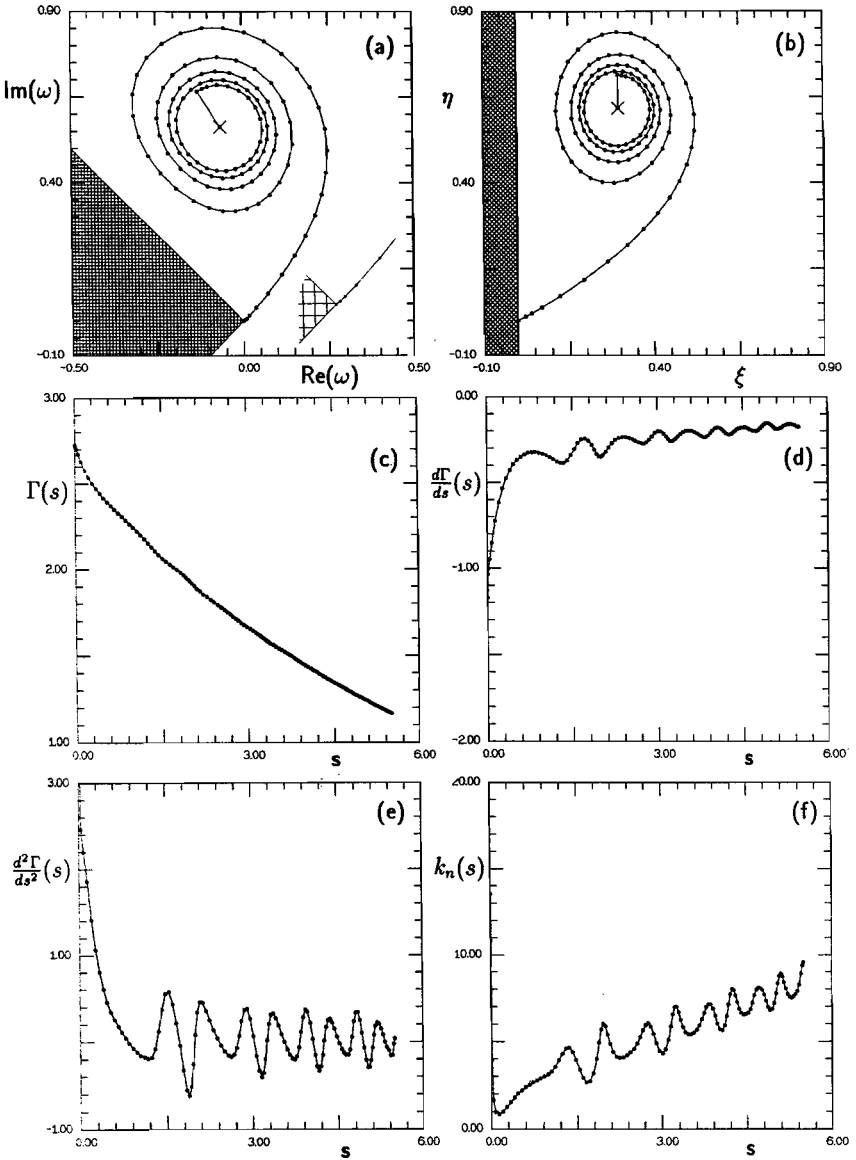


FIGURE 3.5: Quantities at midpoints given as a function of the arc length s along the vortex sheet for the solution presented in figure 3.3 at $t = 2.5$. (a) solution in physical plane, with enlargement of the region near the edge ($\circ =$ edge points of the panels) (b) solution in computational plane (c) dipole distribution $\Gamma(s)$ (d) vortex distribution $d\Gamma(s)/ds = -\gamma(s)$ (e) derivative of vortex distribution $d^2\Gamma(s)/ds^2$ (f) curvature $k_n(s)$

Vortex-blob method

The vortex-blob method, applied to the impulsively started flow around a wedge with interior angle of 90° , requires the specification of a closed region which is much larger than the dimensions of the vortex sheet. It is assumed that at the far-field boundary of this computational region the flow is an undisturbed potential flow, i.e. $\Phi = \Phi_0$.

Each time step a new vortex blob is generated with initial position and strength described by equation (2.106). A fourth-order Runge-Kutta integration method is used to convect the vortex blobs in space.

For the desingularisation of the kernel of the velocity induced by a discrete vortex, the method proposed by Krasny (1986), given by equation (2.46) is used. The value of the desingularisation parameter is chosen to be $\delta = 0.05$, independent of time. However, as time proceeds and the dimension of the vortex system grows, the value of δ decreases relative to the dimensions of the vortex sheet. In scaled coordinates, the limit $t \rightarrow \infty$ corresponds with the limit $\delta \rightarrow 0$.

In figure 3.6, the result of the vortex blob method is given for different values of time, for each time in scaled coordinates. For increasing time the number of turns of the vortex sheet increases, which corresponds to the behavior observed by Krasny (1986) for a decreasing value of δ . In the vortex blob method, a core model is not used to describe the highly rolled-up region of the vortex sheet. Therefore, the solution corresponds to a value $\lambda_{NP} = 1$. The vortex blobs leave the edge approximately tangential to the lower side of the wedge, which corresponds to the behavior observed with the vortex-sheet method. Although the number of turns still increases for $t > 1$, the position of the outer turns is fixed.

In figure 3.4 the center of vorticity and the circulation in scaled coordinates are compared with the results of the vortex-sheet method. From figure 3.4 it can be observed, that for the vortex-blob method a converged solution is obtained for $t \approx 2.5$, and the position of the center of vorticity of the vortex sheet and its circulation are not influenced by the local behavior near the vortex core anymore. If the value of δ is scaled with the distance of the center of vorticity to the edge $r_{c.o.v.}(t)$, it appears that the results become independent of the value of δ for $\delta/r_{c.o.v.} < 0.1$. This corresponds with the influence of δ observed by Krasny (1986). The scaled coordinates of the center of vorticity and the circulation of the *steady state* solution are compared with various methods in table 3.1

Two-vortex method

In the two-vortex method, the initial position of the main vortex is given by the single-vortex solution given by equation (3.10). The complex velocity potential of the attached flow and the point vortex is given by

$$\Phi(\zeta) = \Phi_0(\zeta) + \Phi_v(\zeta) \quad (3.13)$$

with $\Phi_0(\zeta)$ and $\Phi_v(\zeta)$ given by equation (3.2) and (2.87), respectively. The main vortex is convected with the local flow velocity given by equation (2.71) employing a first-order Euler scheme. The position and circulation of the edge vortex is now determined by the similarity solution for the local flow near the edge. Assuming a velocity which is impulsively

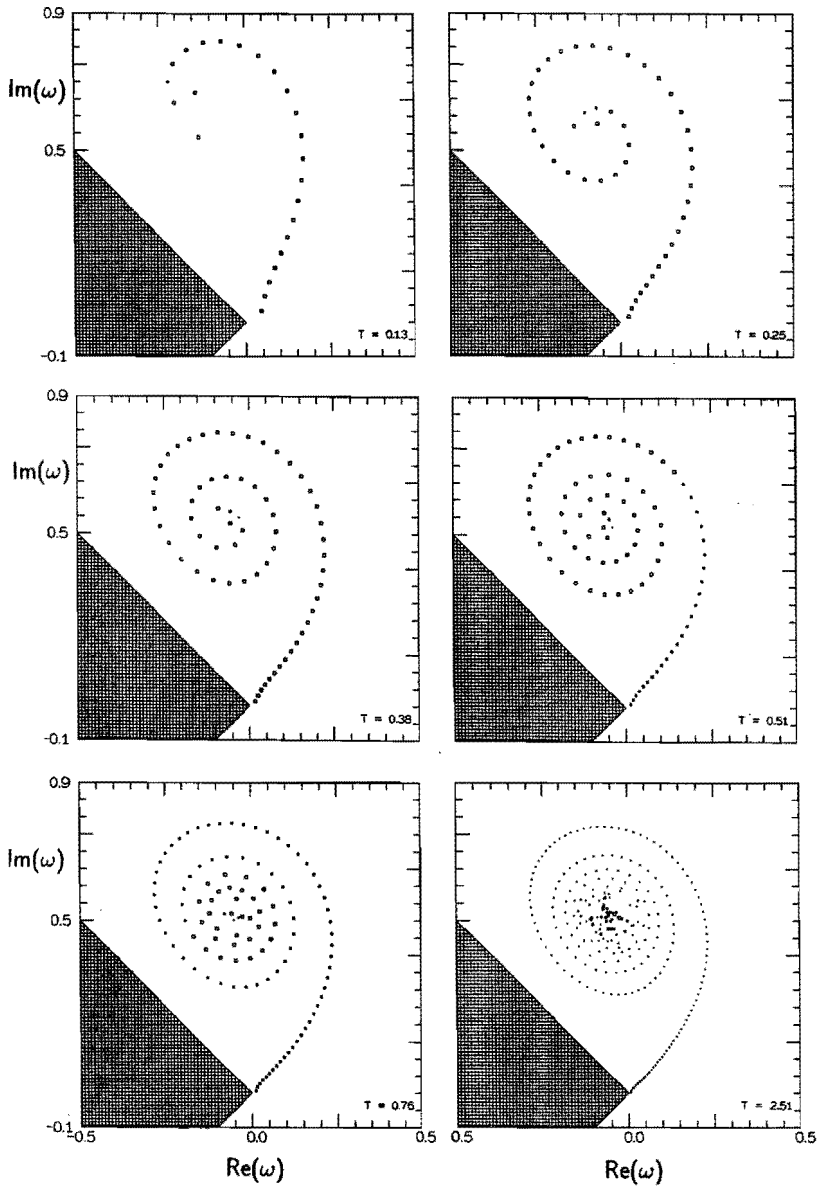


FIGURE 3.6: Development of the vortex sheet computed with the vortex blob method. The vortex sheet geometry is given in similarity coordinates and a steady state self-similar solution is obtained at $t = 2.5$.

increased during each time step, the position of the edge vortex and its strength are given by

$$\begin{aligned} r_e &= \left(\frac{4}{3} \Lambda |B| \Delta t \right)^{3/2} \\ \phi_e &= 0^\circ \\ \Gamma_e &= \frac{4}{3} \pi \Lambda A |B| \Delta t \end{aligned} \quad (3.14)$$

with Λ equal to $2/3$ for the free-vortex method, $2/5$ for the force-free method and $1/3$ for the source-free method. Following the generation of the edge vortex, the convected main vortex and the edge vortex are combined by an amalgamation process. During this amalgamation process the circulation of the new main vortex is the sum of the circulation of the two vortices. For the free-vortex method, the position of the new main vortex is unchanged, while for the force-free method, the new position of the main vortex is the center of vorticity of the two vortices in the physical plane. For the source-free method the new position is equal to the center of vorticity in the computational plane. As the circulation of the edge vortex increases linearly with the time step Δt , the method converges for decreasing time step.

The position of the point vortex and its strength obtained with the two-vortex method are given in table 3.1. For this method the center of vorticity is again identical to the position of the main vortex. Since the vorticity generation is more accurately described compared to the single-vortex method, the results of the two-vortex method are in better agreement with results of the vortex-sheet and the vortex-blob method than the single-vortex method.

Results and discussion

In figure 3.7 the self-similar solutions obtained with the vortex-sheet method and the vortex-blob method are compared with the analytic solutions obtained with the single-vortex methods, the numerical solutions of the force-free two-vortex method and the self-similar solution obtained by Pullin (1978), all in terms of similarity variables.

For the purpose of the comparison of the results of the single- and two-vortex methods with the results of the vortex-sheet and vortex-blob methods, for the discrete vortex methods the streakline emanating from the edge is calculated. The vortex sheet calculated with the other methods is a streakline of the flow.

In the discrete vortex methods the streakline does not contain any vorticity and the velocity is continuous across the streakline. Although the Kutta condition is applied in each method the vortex sheet leaves the edge tangentially, while in the single- and two-vortex method the streakline leaves the wedge symmetrically. In the case of the vortex-sheet method there is a stagnation point at the edge on the upper side of the wedge, while simultaneously the velocity is nonzero on the lower side. In the case of a single-vortex method, there is a stagnation point on both sides of the wedge and the streakline leaves the edge symmetrically. For the converged solution obtained with the force-free two-vortex method, presented in figure 3.7c the Kutta condition is only satisfied if both the main

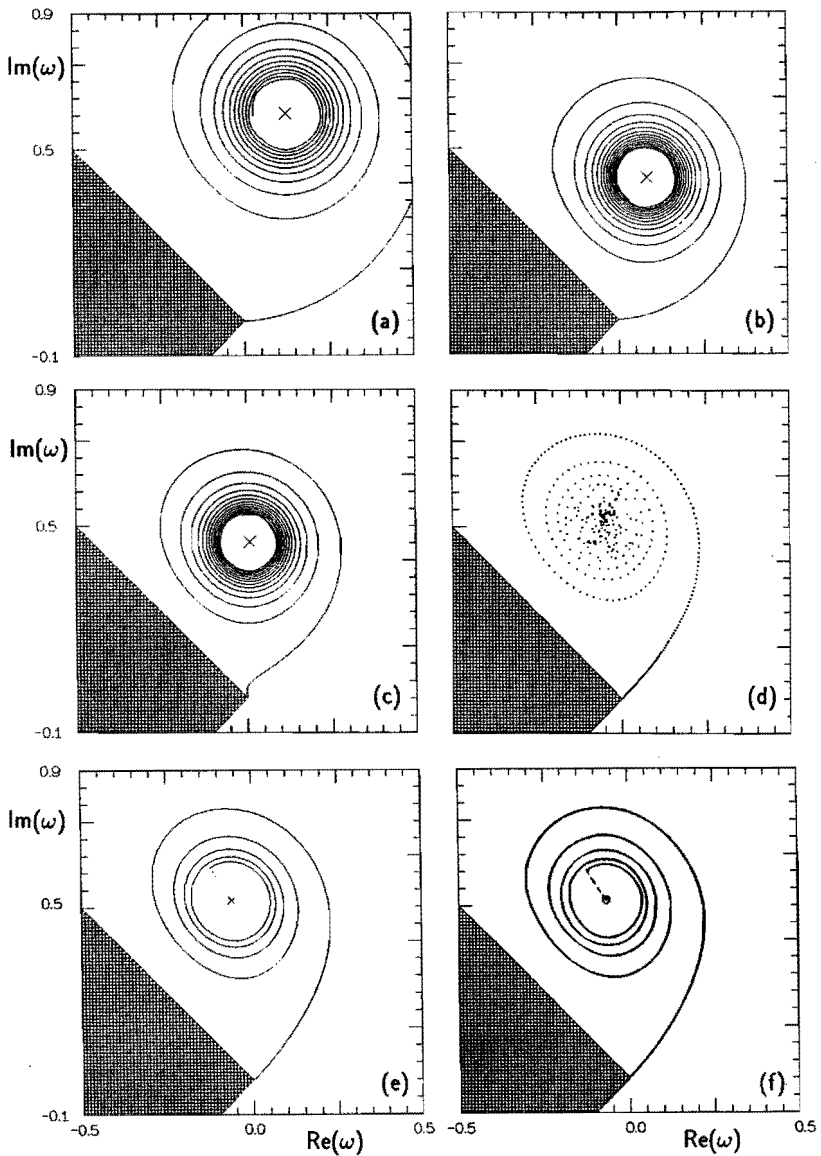


FIGURE 3.7: Comparison of different vortex methods for the impulsively started flow around a wedge. (a) single free-vortex method (b) single force-free vortex method (c) force-free two-vortex method (d) vortex-blob method (e) second-order vortex-sheet method (f) similarity solution obtained by Pullin (1978). In (a-c) the streakline emanating from the edge is given for a comparison with the vortex sheet, present in (d-f).

vortex and the edge vortex are present. Once the two vortices are amalgamated, the Kutta condition is not satisfied anymore and therefore the streakline near the edge does not leave the wedge tangentially.

A more quantitative comparison of the different methods, given in table 3.1, lists the position of the center of vorticity $\omega_{c.o.v.}$ and the circulation J . For the vortex-sheet methods also the position ω_v representing the core of the rolled-up part of the vortex sheet and its circulation J_v can be compared. Although the single-vortex methods are very simple, the center of vorticity and the circulation of the vortex system are fairly well predicted, except for the free single-vortex method. However, the center of vorticity is more accurately predicted by the two-vortex methods, provided that an appropriate amalgamation procedure is used. Both the vortex-sheet method and the vortex-blob method agree fairly well with the self-similar solution of Pullin (1978).

3.2.3 O° Wedge

An interior angle of the wedge θ equal to 0° , corresponds with a flat plate ($n = 1/2$). The flow around a plate differs from the case $\theta > 0^\circ$, because at the edge on either side of the plate a stagnation point is not necessarily present. For the flow around a wedge the limit $\theta \rightarrow 0$ is apparently a nonuniform limit, since for each $\theta > 0$ a stagnation point is present on one side of the wedge. This singular limit has been discussed by Rott (1954), Smith (1966), Graham (1977, 1986) and Pullin (1978).

Single-vortex method

For a comparison of the results of the different vortex methods, we consider the impulsively started flow ($\alpha = 0$) around a plate. The single-vortex solution for this problem is given by equation (3.9), with $n = 1/2$, i.e.

$$\begin{aligned}\rho_v &= \frac{1}{2}\Lambda^{2/3} \\ \chi_v &= 90^\circ \\ J &= \pi\Lambda^{1/3}\end{aligned}\tag{3.15}$$

where $\Lambda = 1, 2/3$ and $1/2$ for the free, force-free and source-free vortex method, respectively. The data are collected in table 3.3. Again, the position of the center of vorticity $\omega_{c.o.v.}$ is equal to that of the point vortex center ω_0 , and the circulation J of the whole vortex system is equal to the point vortex strength J_v .

Vortex-sheet method

The initial position of the point vortex representing the rolled-up part of the vortex sheet is determined by the similarity solution of a force-free single-vortex method, given by equation (3.15) and the initial position of the vortex sheet segment is a flat segment parallel to the plate, with constant circulation distribution equal to $\Gamma(0)$. The initial segment is divided into five panels. The calculation procedure for the vortex sheet roll-up is similar to that of the calculation described for the flow past a 90° -wedge.

METHOD		$\rho_{c.o.v.}$	$\chi_{c.o.v.}$	J	ρ_v	χ_v	J_v
SINGLE VORTEX	<i>free</i> ($\Lambda = 1$)	0.50	90.0°	3.14		see	
	<i>force-free</i> ($\Lambda = 2/3$)	0.38	90.0°	2.74		c.o.v.	
	<i>source-free</i> ($\Lambda = 1/2$)	0.32	90.0°	2.49			
SINGLE PANEL	<i>amalg. vorticity only</i>	0.32	84.0°	2.94		see	
	<i>amalg. z-plane</i>	0.25	84.0°	2.52		c.o.v.	
	<i>amalg. ζ-plane</i>	0.23	84.0°	2.38			
VORTEX SHEET	$\lambda_{NP} = 0.56, \theta_v = 1620^\circ$	0.40	95.8°	2.65	0.42	101°	1.16
PULLIN (1978)	$\lambda_{NP} = 0.53, \theta_v = 1620^\circ$	-	-	2.64	0.42	102°	1.24

TABLE 3.3: Position of center of vorticity $\omega_{c.o.v.} = \rho_{c.o.v.} e^{i\chi_{c.o.v.}}$, circulation J and point vortex position $\omega_v = \rho_v e^{i\chi_v}$ and circulation J_v for different methods. Impulsively started flow ($\alpha = 0$) past a plate with $\theta = 0^\circ$ ($n = 1/2$).

In figure 3.8 results of the vortex-sheet method are presented for the shape of the vortex sheet in similarity coordinates. The vortex sheet leaves the plate tangentially and rolls up into a vortex core, which is positioned nearly perpendicular to the edge of the plate, as predicted by the single vortex solution. The parameters used to obtain the vortex sheet solution are given in table 3.4. The coordinates of the center of vorticity of the vortex-sheet solution and its circulation for the self-similar solution are given in table 3.3. Also in this table the position of the point vortex representing the core region and its circulation are given for the self-similar solution.

For the self-similar solution at $t = 2.5$ the vortex sheet in the computational and physical plane, the dipole strength and its first and second derivative with respect to the arc length s and the curvature as a function of the arc length along the vortex sheet in the physical plane are presented in figure 3.9. Clearly, less panels are present near the edge than in the case of a finite wedge angle since now the derivative of the transformation function, given by equation (3.1), is not singular near the edge.

In the highly rolled-up region, the vortex spiral is still slightly elliptic due to the presence of the plate, but not as much as for the wedge with interior angle of 90° , shown in figure 3.5. Again, the curvature of the vortex sheet shows a singular behavior near the edge, where the curvature tends to infinity, which confirms again the prediction of Clapworthy and Mangler (1974).

The position of the point vortex and its circulation computed with the vortex-sheet method agree with the similarity solution of Pullin (1978). However, the point vortex strength is somewhat higher. In table 3.3 the center of vorticity obtained with the vortex-sheet method is compared with those obtained with single-vortex methods. Again, the free-single vortex method overestimates both the distance of the center of vorticity from the edge and the circulation, while the results of the force-free and the power-free single-vortex methods agree quite reasonably with those of the vortex-sheet method.

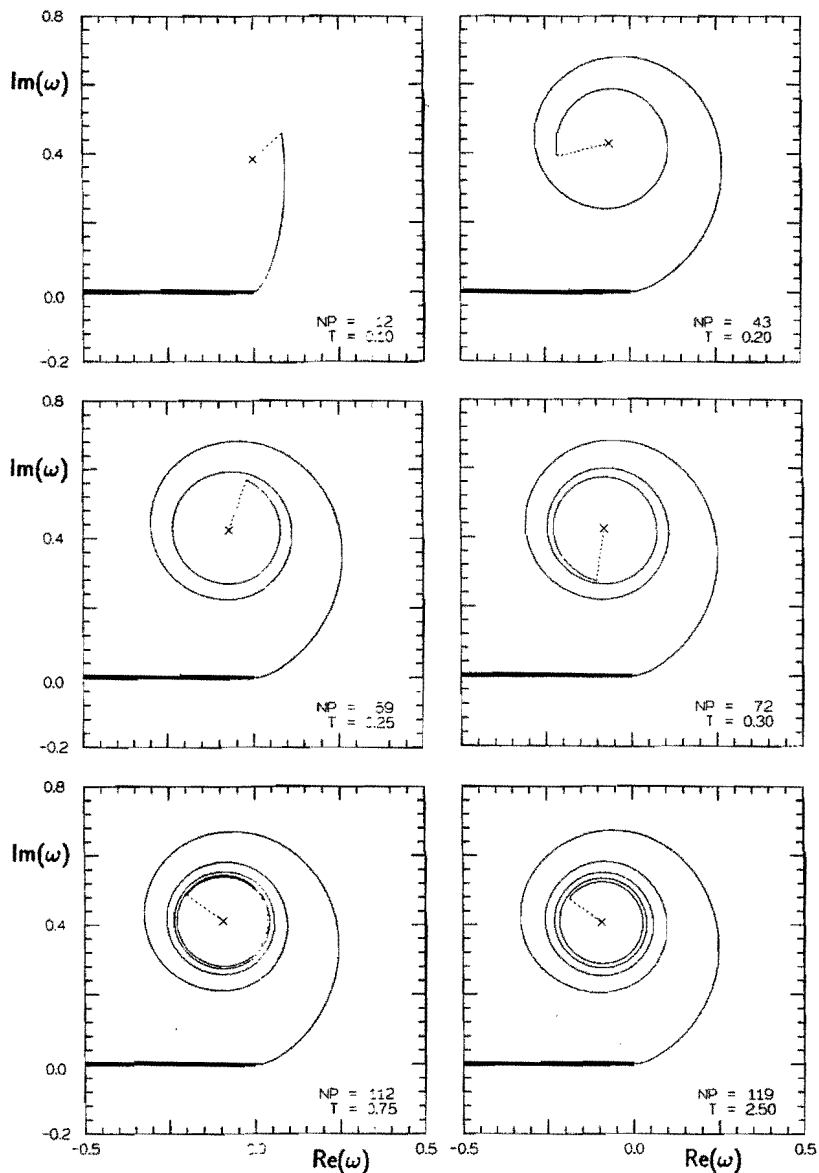


FIGURE 3.8: Separating flow around a flat plate. Development of the vortex sheet computed with the vortex-sheet method. Since the vortex sheet geometry is given in similarity coordinates, a steady state self-similar solution is obtained at approximately $t = 2.5$.

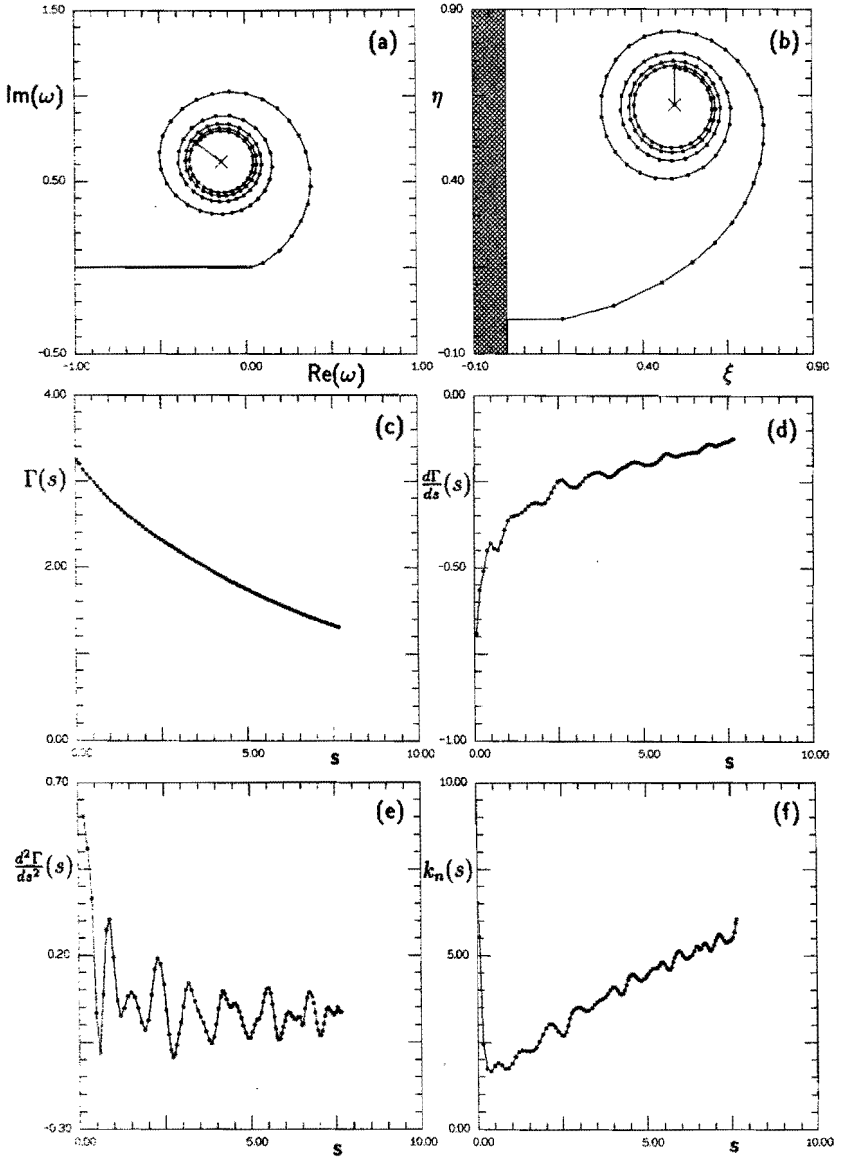


FIGURE 3.9: Quantities at midpoints given as a function of the arc length s along the vortex sheet for the solution presented in figure 3.8 at $t = 2.5$. (a) solution in physical plane (\circ = edge points of the panels) (b) solution in computational plane (c) dipole distribution $\Gamma(s)$ (d) vortex distribution $d\Gamma/ds = -\gamma(s)$ (e) derivative of vortex distribution $d^2\Gamma(s)/ds^2$ (f) curvature $k_n(s)$

TIME STEP NR.	\mathcal{F}	Δs_{max}	$\Delta \theta_{max}$	θ_v
1 - 250	0.2	0.05	15°	180°
251 - 1250	0.3	0.10	15°	1620°

TABLE 3.4: Parameters used for the vortex-sheet solution for the impulsively started flow around a plate with $\theta = 0^\circ$, see figure 3.8.

Single-panel method

In the single-panel method, the vorticity generation near the edge is described by introducing a straight vortex segment with uniform vortex distribution, connected tangentially to the plate. The initial position of the main vortex is given by the single force-free vortex solution given by equation (3.15). The main vortex is convected with the local flow velocity by a second order Runge-Kutta scheme. The edge segment characteristics are obtained from the local flow near the edge, given by equation (2.86) where the velocity potential is given by equation (2.88).

The length of the vortex segment is taken to be a relative small fraction (1 %) of the distance of the main vortex to the edge. This limits the time step of integration during the initial phase of the calculation, according to equation (2.104). The circulation of the segment is given by equation (2.101). The edge segment is amalgamated with the main vortex where the circulation of the newly formed main vortex is equal to the total circulation of the system. The new position of the main vortex depends on the condition for the segment/feeding sheet/point vortex combination, similar to the two-vortex method.

The results of the single-panel method are given in table 3.3 and, similar to the results of the two-vortex method for the flow past a 90° wedge, are in better agreement with the results of the vortex-sheet method than the results of the single-vortex methods.

3.3 STARTING FLOW IN A T-JUNCTION

3.3.1 Introduction

In order to assess the applicability of the different methods for internal flow problems, we consider the inviscid, incompressible starting flow in a two-dimensional T-junction. The T-junction has sharp edges and the width of the side branch is H , see figure 3.10. Since the side branch is closed, the volume flux per unit length in the third dimension is directed through the main pipe with width h . The coordinate z , the volume flux $Q = U_0 h$, time t , circulation Γ , the main pipe width h and the complex velocity potential are non-dimensionalised with U_0 and H according to

$$\begin{aligned}
 z &= z^* H; & t &= t^* H / U_0 \\
 Q &= Q^* U_0 H; & h &= h^* H \\
 \Gamma &= \Gamma^* U_0 H & \Phi &= \Phi^* U_0 H
 \end{aligned} \tag{3.16}$$

In the sequel the non-dimensionalised quantities will be used and the asterisk will be omitted. For the purpose of easily satisfying the boundary conditions on the solid walls

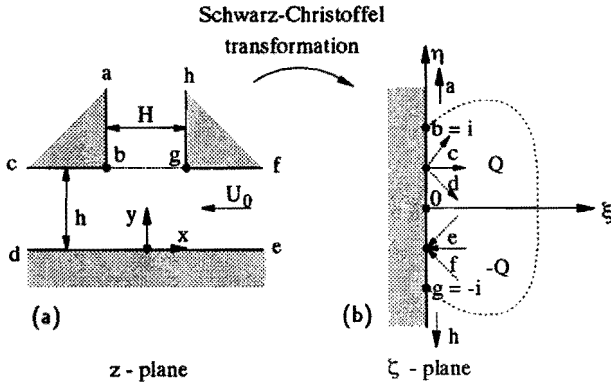


FIGURE 3.10: Conformal mapping of region within a T-junction to a half plane.

the inner part of the T-junction in the physical plane ($z = x + iy$) is mapped to the half-plane $\Re(\zeta) > 0$ a computational plane ($\zeta = \xi + i\eta$) as shown in figure 3.10. This is accomplished by the conformal mapping $z = f(\zeta)$ with

$$f'(\zeta) = \frac{ih \sqrt{\zeta^2 + 1}}{\pi \zeta^2 + a^2} \quad (3.17)$$

with $a = \frac{1}{\sqrt{1+4h^2}} < 1$. The transformation is obtained from equation (3.17) by integration as

$$f(\zeta) = \frac{1}{2} + ih + \frac{i}{\pi} \ln \left(i\zeta + \sqrt{-\zeta^2 - 1} \right) - \frac{h}{\pi} \ln \left(\frac{i\zeta - a}{i\zeta + a} \right) - \frac{2h}{\pi} \ln \left(\frac{\sqrt{(1-a)(i\zeta - 1)} + i\sqrt{(1+a)(i\zeta + 1)}}{\sqrt{(1+a)(i\zeta - 1)} + i\sqrt{(1-a)(i\zeta + 1)}} \right) \quad (3.18)$$

The upstream and downstream edges of the T-junction are mapped onto $\zeta = -i$ and $\zeta = i$, respectively. Infinite upstream ($x = \infty$) is mapped onto $\zeta = -ia$, infinite downstream ($x = -\infty$) is mapped onto $\zeta = ia$. The uniform flow at infinity, with velocity U_0 is generated by a point source of strength $Q = h$ at $\zeta = -ia$ and a sink of equal strength at $\zeta = ia$. The dotted line in figure 3.10 separates the flow in the side branch from the flow in the main pipe, both in the computational plane as well as in the physical plane. The complex velocity potential due to the attached main flow is given by

$$\Phi_0(\zeta) = \frac{h}{\pi} \ln \left(\frac{\zeta + ia}{\zeta - ia} \right) \quad (3.19)$$

where due to the image sources in $\zeta = \pm ia$ the source strength is doubled. As a result of the action of viscosity the flow separates at the sharp upstream edge and vorticity is generated continuously at the edge and convected into the flow field. The flow separation at the downstream sharp edge can usually be neglected, as will be shown by the visualization of the flow inside the T-junction. Therefore in the numerical calculations only flow separation at the upstream edge is taken into account. In the next sections the application of different methods used to describe the flow will be discussed.

3.3.2 Similarity solution near the edge

The different methods used in the previous section to compute the flow around a wedge will now be used to describe the flow with separation in the T-junction. For the initial stage of the development of the flow, when the separated region is still small compared to the side branch width H , the position of the tightly rolled-up vortex sheet and its circulation can be estimated by a self-similar solution of the flow past a wedge with interior angle equal to the included angle of the upstream edge, i.e. $\theta = 90^\circ$. Near the upstream edge ($z = \frac{1}{2} + ih, \zeta = -i$) the transformation function given in equation (3.18) can be approximated by

$$z - \frac{1}{2} - ih = \frac{2\sqrt{2}h}{3\pi(1-a^2)}(-i)^{\frac{3}{2}}(\zeta + i)^{\frac{3}{2}} \quad (3.20)$$

and the expression for the attached-flow velocity potential (3.19) to

$$\Phi_0|_{\zeta \rightarrow -i} = \frac{2iah}{\pi(1-a^2)}(\zeta + i) + \frac{2ah}{\pi(1-a^2)^2}(\zeta + i)^2 + \dots \quad (3.21)$$

Near the upstream edge a self-similar problem of a starting flow past a wedge can be defined according to equation (2.85) and (2.86) with parameters

$$D = \left(\frac{3\pi(1-a^2)}{2\sqrt{2}h} \right)^{2/3} \quad (3.22)$$

$$A = \frac{-2ah}{\pi(1-a^2)} \quad (3.23)$$

$$B = \frac{2ah}{\pi(1-a^2)^2} \quad (3.24)$$

The single vortex self-similar solution for the flow rounding the edge (assume $B = 0$) is given by equation (2.92), and can be written as

$$\Gamma_v = \frac{2}{3}\sqrt{6}\pi AD r_v^{2/3} \quad (3.25)$$

$$z_v = \frac{1}{2} + ih + r_v e^{i\phi_v} \quad (3.26)$$

$$\text{with: } r_v = \left(\frac{|\Lambda|A|D\sqrt{10}t}{9} \right)^{3/4}$$

$$\phi_v = \frac{\pi}{2} + \frac{3}{2} \arcsin \left(\frac{\sqrt{6}}{4} \right)$$

and $\Lambda = 2/3$, $2/5$ and $1/3$ for the free-vortex, for the force-free method and the source-free single-vortex method, respectively.

The single-point-vortex solution determines the initial position of the core and its initial strength in the vortex-sheet method and in the two-vortex method. From now on we will restrict ourselves to the case that main pipe and side branch have equal width so that $h = 1$ and as a result $a = \sqrt{1/5}$.

3.3.3 Comparison of results of different flow methods

Single-vortex method

In the single-vortex method it is assumed that the whole vortex sheet may be represented by a single point vortex at position $z = z_v$ with time-dependent circulation Γ_v . It is mapped to a vortex of equal strength at $\zeta = \zeta_v$ in the transformed plane. To satisfy the boundary condition of zero normal velocity at the solid wall $\xi = 0$, an image vortex of strength $-\Gamma_v$ at $\zeta = -\zeta_v^*$ is introduced.

The circulation of the single vortex is determined by imposing the Kutta condition at the upstream edge $\zeta = -i$. Eliminating the singularity at the upstream edge requires that

$$\left. \frac{d\Phi}{d\zeta} \right|_{\zeta=-i} = 0 \quad (3.27)$$

During the initial stage of the roll-up the flow separation at the edge is only influenced by the local flow velocity and can be obtained from the similarity solution. In that case the initial position of the point vortex and its circulation are approximated by equation (3.26) and (3.25), respectively.

In the free-vortex method, the point vortex is convected with the local velocity, given by equation (2.65), taking into account the singular behavior of the expression for the velocity at the point vortex. In the force-free method, the convection velocity of the vortex is given by equation (2.76). The trajectory of the point vortex can be obtained by integration of the velocity. Each time step the Kutta condition equation (3.27) determines the time-dependent circulation of the vortex. The time-wise integration is performed employing a two-step explicit Runge-Kutta scheme

$$\begin{aligned} \tilde{z}(t + \Delta t) &= z(t) + v(z(t), t) \Delta t \\ z(t + \Delta t) &= z(t) + \frac{1}{2} (v(z(t), t) + v(\tilde{z}(t + \Delta t), t)) \Delta t \end{aligned} \quad (3.28)$$

The trajectory of the point vortex and its circulation are presented in figure 3.11. Also the results of the single-vortex similarity solution near the edge, given by equation (3.25) and (3.26), are given. Similar to the behavior found for the self-similar problem of the flow past a wedge, also for the starting flow in a T-junction, the free-single vortex method overestimates the circulation and the distance of the point vortex to the upstream edge.

In the free-single vortex method, the circulation of the vortex and the distance to the edge increase dramatically when the vortex approaches the downstream edge. This is caused by the dipole-like behavior of the combination of the vortex with its image vortex.

While the vortex convects far from the upstream edge, the circulation of the vortex has to increase fast to satisfy the Kutta condition at the upstream edge. The tangential velocity induced at the upstream edge due to the vortex and its image decreases as $1/r$ when the vortex is near this edge, where r is the distance between the point vortex and the edge, but as $1/r^2$ when the vortex is in the region near the downstream edge. The velocity induced by the image vortex tends to force the vortex into the side branch so that the process is strongly accelerated. This singular and unrealistic behavior of the circulation in the free-vortex method applied to the T-junction has already been observed by Bruggeman (1987). The force-free single-vortex method tends to decrease the amount of vorticity

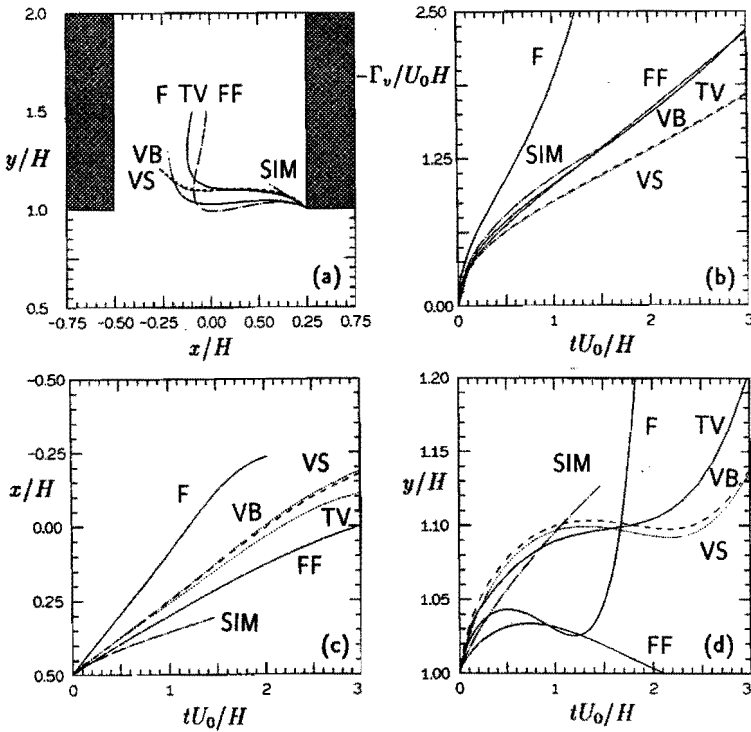


FIGURE 3.11: Trajectory of the center of vorticity of the vortex system and its circulation as a function of time for the impulsively started flow in a T-junction. (....., VS) vortex-sheet method (obtained from figure 3.12) (- - -) vortex-blob method VB (obtained from figure 3.14) (---) single free-vortex method F; (- - - - -) force-free single-vortex method FF; (—) two-vortex source-free method TV; (- - - - -) similarity solution SIM (valid for small times).

generated, and also the velocity of the vortex. However in this method the vortex velocity will become zero when the slip velocity induced on the vortex by the Magnus force balances the local velocity and the right hand side of equation (2.76) vanishes. From figure 3.11 it follows that the force-free vortex method tends to underestimate the vortex velocity while the free vortex method tends to overestimate this velocity. With this latter method, also the circulation is overestimated. The single-vortex method therefore must be rejected as a simple method to describe the vortex formation process in an internal flow such as in a T-junction.

Two-vortex method

In the two-vortex method as discussed in the previous section the circulation of the edge vortex is determined from a similarity solution of the local flow near the upstream edge. The velocity potential due to the main flow and the main vortex at position ζ_v of strength Γ_v is then given by

$$\Phi(\zeta) = \frac{1}{\pi} \ln \left(\frac{\zeta + i\sqrt{1/5}}{\zeta - i\sqrt{1/5}} \right) - \frac{i\Gamma_v}{2\pi} \ln \left(\frac{\zeta - \zeta_v}{\zeta + \zeta_v^*} \right) \quad (3.29)$$

Near the upstream edge the velocity potential due to the attached main flow and the main vortex can be expressed as by

$$\Phi |_{\zeta \rightarrow -i} = -iA(\zeta + i) + B(\zeta + i)^2 + \dots \quad (3.30)$$

$$\text{with : } A = -\frac{\sqrt{5}}{2\pi} + \frac{\Gamma_v}{2\pi} \left(\frac{1}{-i - \zeta_v} - \frac{1}{-i + \zeta_v^*} \right) \quad (3.31)$$

$$B = \frac{5\sqrt{5}}{8\pi} + \frac{i\Gamma_v}{4\pi} \left(\frac{1}{(-i - \zeta_v)^2} - \frac{1}{(-i + \zeta_v^*)^2} \right) \quad (3.32)$$

Because $0 < |A| \ll |B|$ the similarity solution for the edge vortex is given by equation (2.93)

$$\Gamma_e = \frac{4}{3}\pi\Lambda A|B|D^3\Delta t \quad (3.33)$$

$$z_e = \frac{1}{2} + i + r_e e^{i\phi_e} \quad (3.34)$$

$$\text{with : } r_e = \left(\frac{4}{3}\Lambda|B|D^2\Delta t \right)^{\frac{3}{2}}$$

$$\phi_e = 225^\circ$$

with $\Lambda = 2/3$, $2/5$ and $1/3$ for the free-vortex, force-free and source-free methods, respectively. Although the edge vortex does not leave the edge tangentially, and does not accurately describe the vortex sheet near the edge, the shed vorticity is accurately described by equation (3.33) according to Graham (1983).

Each time step the main vortex and the edge vortex are combined by an amalgamation process in which the potential difference between the main pipe and the side branch is not affected and in which the total circulation is conserved. This amalgamation procedure has also been used by Disselhorst & van Wijngaarden (1980) to describe the process of vortex shedding at an open pipe exit with sharp edges. The amalgamation procedure for the T-junction is described by Bastiaans (1991). When the two vortices are near the upstream edge, the amalgamation process is identical to the amalgamation in the computational plane described for the flow around a wedge, equation (2.122). The newly formed vortex at position z_v is then convected with the local flow velocity by a second order explicit Runge-Kutta scheme.

The result of this *source-free* two-vortex method is included in figure 3.11. While the circulation obtained with the two-vortex method corresponds with the result of the force-free single vortex method, the vortex trajectories differ significantly. During the initial phase the circulation of the main vortex and the initial angle of convection correspond to the similarity solution.

Vortex-sheet method

For the vortex-sheet method the similarity solution for the point vortex is used as an initialization for the calculation of the impulsively started flow in a T-junction. In this case, z_v and Γ_v are given by equation (3.26) and (3.25), respectively and the similarity solution is used for $t \leq t_1$. To start off the vortex-sheet method, five panels with a constant circulation $\Gamma(s)$ distribution are attached to the upstream edge along a streakline of the flow. The velocity due to the vortex sheet and the point vortex core in the computational plane is given by equation (2.83) and (2.84), respectively. The derivative of the transformation function $f'(\zeta)$ is given by equation (3.17) and the velocity potential is given by equation (3.11). Since the convection of the vortex system and the Kutta condition are formulated in terms of the coordinates of the computational plane, a transformation of the coordinates to the physical plane is not necessary during the calculation, except for the amalgamation process and for the final result.

With the application of the Kutta condition vorticity is generated at the edge and is convected along the vortex sheet. The vortex sheet starts to increase in length and to wind around the point vortex. During the calculation the angular extent of the vortex sheet is limited to a maximum angle θ_v . An adaptive panel distribution scheme along the vortex sheet is used during the calculation, where the maximum angle subtended by a single panel is $\Delta\theta_{max}$. The time step is determined by allowing a maximum displacement of a fraction \mathcal{F} of each individual panel width. In addition the derivative of the transformation function is not allowed to vary more than 20% on each individual panel.

Figure 3.12 presents the results of the impulsively started flow in a T-junction computed with the vortex-sheet method for $0 < tU_0/H < 3.5$. During this period the vortex sheet grows continuously and reaches the downstream edge. The parameters used for the computations are given in table 3.5.

When the vortex sheet hits the downstream edge the vortex sheet splits into two parts, one convects into the side branch, the other convects into the main pipe. For $tU_0/H = 1.5$

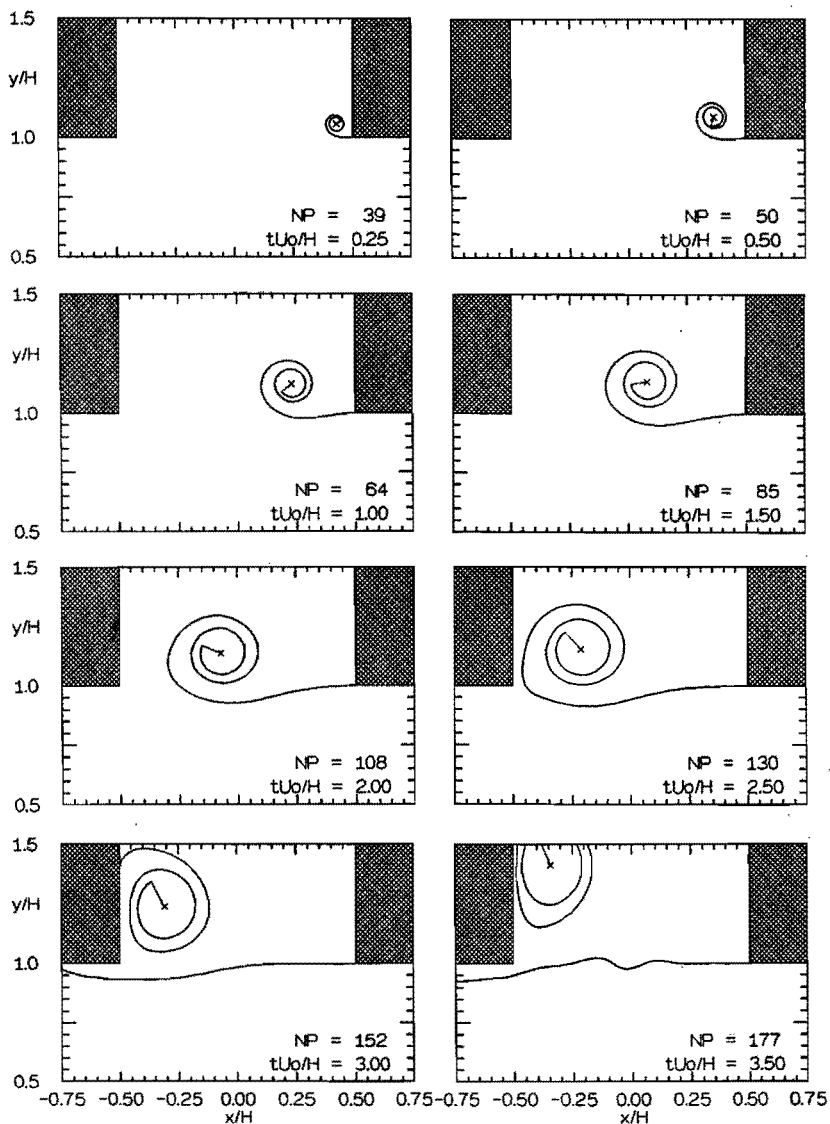


FIGURE 3.12: Impulsively started flow in a T-junction computed with the vortex-sheet method.

TIME STEP NR.	\mathcal{F}	Δs_{max}	$\Delta \theta_{max}$	θ_v
1 - 250	0.2	0.01	20°	225°
251 - 500	0.2	0.02	20°	360°
501 - 1000	0.3	0.05	20°	540°
1001 - 4000	0.3	0.05	20°	900°

TABLE 3.5: Parameters used for the application of the vortex-sheet method to the starting flow in a T-junction, see figure 3.12

and $tU_0/H = 2.5$ the characteristics of the solution of the vortex-sheet method are shown in figure 3.13. At $tU_0/H = 1.5$, the vortex distribution is quite regular, with a local maximum value of the vortex distribution corresponding with a local maximum of the curvature of the sheet. Furthermore, again the vortex sheet leaves the upstream edge tangentially, while the curvature at the edge is infinite, similar to the case of a separated flow around an infinite 90°-wedge. At $tU_0/H = 2.5$, when the vortex sheet nearly hits the downstream edge, the vorticity distribution has a peak value at the point of the sheet closest to the downstream edge, while also the curvature has a maximum value at that point. At $tU_0/H = 3.5$, due to the Kelvin-Helmholtz instability of the straight vortex sheet, vorticity starts to concentrate into rolled-up regions. The wavenumber of this instability is determined by the chosen value of the parameter Δs_{max} of the numerical scheme.

Vortex-blob method

The results obtained with the vortex-blob method with desingularisation parameter $\delta = 0.05$ are presented in figure 3.14. These results show a great resemblance with the results of the vortex-sheet method, except for the instability of the sheet which occurs in the vortex-sheet solution after the initial vortex hits the downstream edge but not in the vortex-blob solution. In the latter solution the instability is determined by the value of the desingularisation parameter δ . For the vortex-blob solution the instability sets in at a later moment in time.

Discussion

To compare the results of the vortex-sheet and vortex-blob method with those of the discrete vortex methods, the center of vorticity and the circulation are included in figure 3.11 as a function of time. The trajectory of the center of vorticity and circulation as a function of time obtained with the vortex-sheet method are similar to those obtained with the vortex-blob method.

In the two-vortex method the computed vortex path and circulation agree well with those computed by the more accurate vortex-sheet and vortex-blob method, primarily as a result of the application of the Kutta condition being enforced by the edge vortex. Therefore the two-vortex method appears to be the most attractive form of a simplified method to describe the vortex shedding process in a T-junction. However, contrary to the

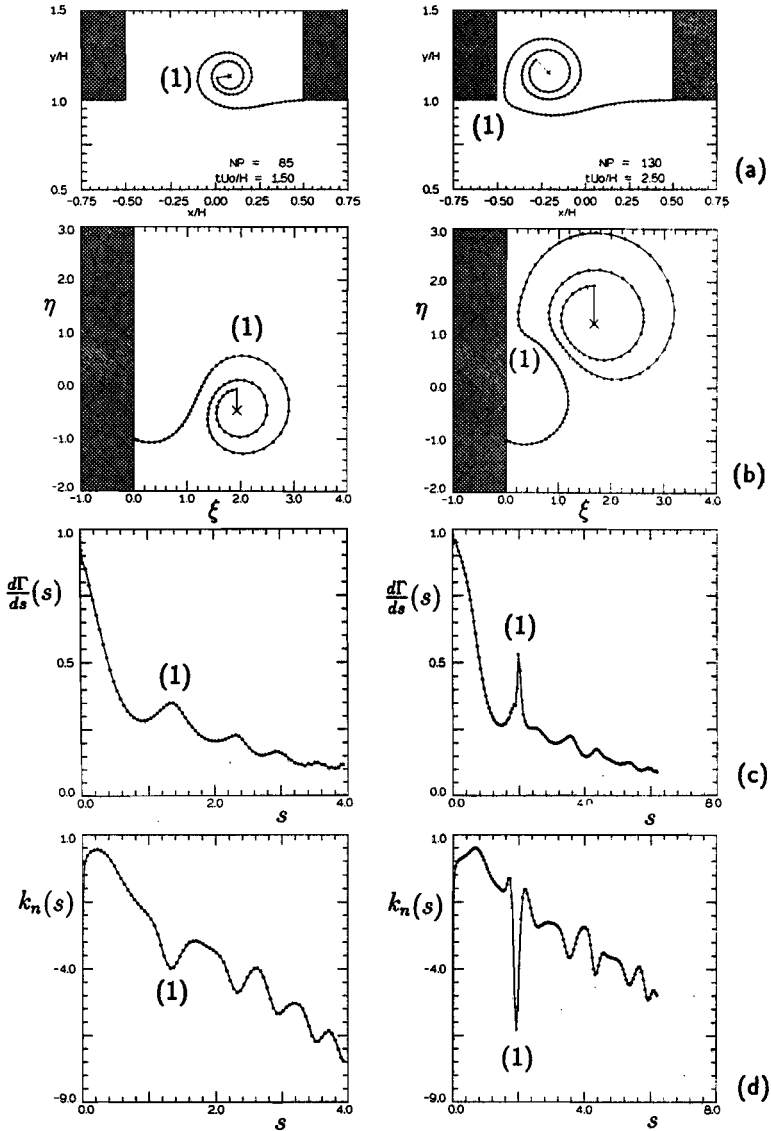


FIGURE 3.13: Characteristics of the vortex-sheet solution presented in figure 3.12 at $tU_0/H = 1.5$ (left column) and $tU_0/H = 2.5$ (right column). (a) solution in physical plane (o denote edge points of the panels) (b) solution in the computational plane (c) vortex distribution $\frac{d\Gamma}{ds}(s) = -\gamma(s)$ (d) curvature $k_n(s)$

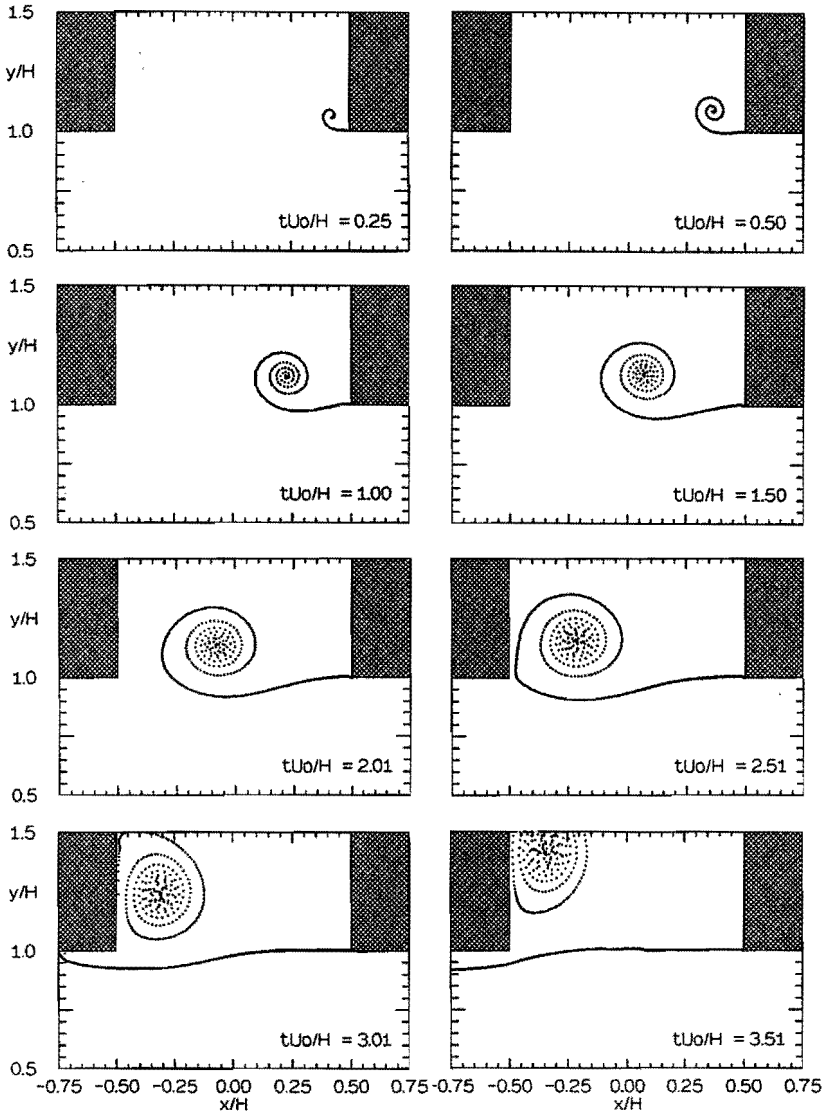


FIGURE 3.14: Impulsively started flow in a T-junction. Results obtained with the vortex-blob method, for $\delta = 0.04$, $\Delta t = 0.005$.

vortex-sheet method, the moment of appearance of a new center of roll-up vortex is an empirical factor in the discrete vortex method.

The moment in time of terminating the amalgamation of vorticity into the main vortex and starting a new main vortex has been discussed by Graham (1977, 1986). It is clear, that when the sign of the vorticity generated changes, a new center of roll-up will develop. However, if the sign of the generated vorticity does not change, Graham (1977, 1986) proposes to start a new vortex when the *rate of vorticity generation is at a minimum*. This criterion is supported by the calculations on the roll-up of a vortex sheet behind an elliptically loaded wing, discussed in chapter 2, where instabilities occurred at the position where $d\Gamma/ds$ is at a minimum.

3.3.4 Experiment

Flow visualization

To verify the numerical results of the convection and roll-up of the vortex sheet an experimental setup has been built to visualize the flow in a T-junction. For the starting flow experiment, a T-junction has been built consisting of square brass pipes of 3.0 cm width H . The side branch has a length of 6.0 cm, which is twice the side branch width. For visualization purposes, part of the side walls of the T-junction are made of glass windows. A starting flow is realized by opening a valve within less than 1 ms.

A pressure difference over the system is obtained by decreasing the pressure in the laboratory with the help of the ventilation system of the building. The room in which the experiment has been carried out has a volume of 40 m^3 , while the laboratory building which is used as a high-pressure supply has a volume of 3600 m^3 . The maximum pressure difference which can be attained in this way is 800 Pa. This pressure difference Δp is measured within 2 Pa by means of a Betz water manometer. The experimental setup is shown in figure 3.15. The high pressure room is connected to the main pipe by a contraction which yields an approximately uniform velocity distribution in the upstream part of the main pipe. The operating pressure during the experiments was close to atmospheric pressure and the temperature close to room temperature (295 K). A standard schlieren method was used to visualize the flow. By injecting CO_2 in the side branch a refractive index variation is created across the shear layer enabling its visualization. A nanolite spark discharge provides a light pulse of about 80 nanoseconds duration. In order to obtain a visualization at a well defined point in time, the nanolite light source can be triggered by a hot wire anemometer, placed just upstream of the side branch. With the hot wire anemometer, the development in time of the main flow velocity is measured after opening the valve. The rise in the velocity with time since the opening of the valve is for different pressure differences given figure 3.16. The measured velocity is compared to the velocity, estimated from integrating the unsteady Bernoulli equation in time for an impulsively increased pressure. The final value of the velocity is equal to the Bernoulli velocity, i.e. $U_{max} = \sqrt{2\Delta p/\rho_0}$, with Δp the initial pressure difference across the valve.

Figure 3.17 shows some results of the flow visualization of the starting flow in the T-junction for three moments in time for different pressure differences $\Delta p = 50, 199$ and 792 Pa. Separation of the flow at the upstream edge causes the formation of a vortex layer.

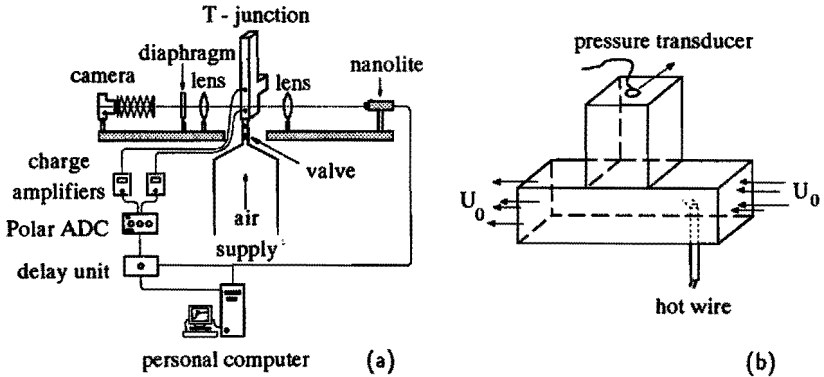


FIGURE 3.15: Experimental setup used for the visualization of the separated flow in a T-junction by a standard schlieren method. (a) schlieren visualization setup (b) measurement of unsteady velocity and pressure inside the T-junction.

Right at the beginning of the motion, the vortex layer rolls up and the shear layer with its vortical structure convects with the local flow velocity in the direction of the downstream edge.

Upon reaching the opposite edge, part of the vortex layer is forced into the side branch, this under influence of the image vorticity in the walls. Under influence of a Kelvin Helmholtz-like instability the not rolled-up part of the vortex sheet in the T-junction starts to distort and finally roll-up in secondary vortices. The instability of the vortex layer is more pronounced when the experiment is performed at a higher pressure difference Δp , i.e. an increased strength of the shear layer and the reduction of its thickness (higher Reynolds number).

Numerical simulation by the vortex-blob method

Using the precise velocity rise as measured with the hot wire anemometer, see figure 3.16, a calculation is performed with the vortex-blob method. The value of the desingularisation parameter δ was estimated from the averaged momentum thickness of the shear layer during the convection towards the downstream edge for the lowest value of the pressure difference ($\delta \approx 2\sqrt{\nu t}/H$). The results of the vortex-blob method for the numerical simulation of the starting flows is presented in figure 3.18. The value of δ is given by 0.10, 0.05 and 0.025 for a pressure difference $\Delta p = 50, 199$ and $792 Pa$, respectively. Due to the decreasing value of δ , the vortex sheet becomes more sensitive to instabilities and forms small substructures in the vortex sheet in a similar manner as observed in the flow visualization.

A comparison of the x -position of the vortex core and of the front of the vortex sheet

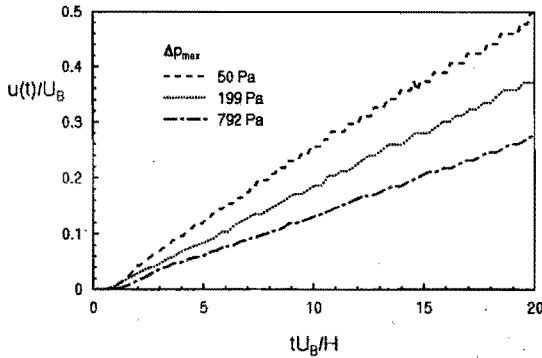


FIGURE 3.16: Main flow velocity in the T-junction. (---) velocity corresponding to $\Delta p = 50 \text{ Pa}$ (.....) $\Delta p = 199 \text{ Pa}$, (- · - · -) $\Delta p = 792 \text{ Pa}$.

is shown in figure 3.19. Here, the upstream edge is taken to be origin. The results of the vortex-blob method agree with the experimental data within the accuracy of the measurement for all three cases. Since in this experiment an external (acoustic) excitation of the vortex sheet is not present the instability most amplified (in absence of shear layer stretching and curvature) is determined by the thickness of the shear layer and flow noise spectra. However, in case the vortex layer is excited by a resonating acoustic field the development of the vortex layer including the periodic formation of centers of roll-up which follows the starting phase results in much larger-scale structures. These structures are not very sensitive to the shear-layer thickness and therefore amenable to simulation based on potential flow models. Chapter 4 is devoted to the case of periodic flow.

3.4 STARTING JET FLOW

3.4.1 Introduction

In the previous section it was shown, that the starting flow in a T-junction can be reasonably described by a two-vortex method, while single-vortex methods appeared to fail in describing the flow. The success of the two-vortex method is due to the fact that the distance from the edge of the center of vorticity of the vortex layer is of the same order of magnitude as the characteristic dimension of the geometry, i.e. the side branch width H . In this section a problem is studied where this is not the case, namely the starting flow out of a nozzle. This problem is studied for two nozzle geometries, one with sharp edges and one with square edges.

Experimental investigations into impulsively started flow for these two-dimensional geometries have been performed by Auerbach (1987) and Blondeaux & Bernardinis (1981).

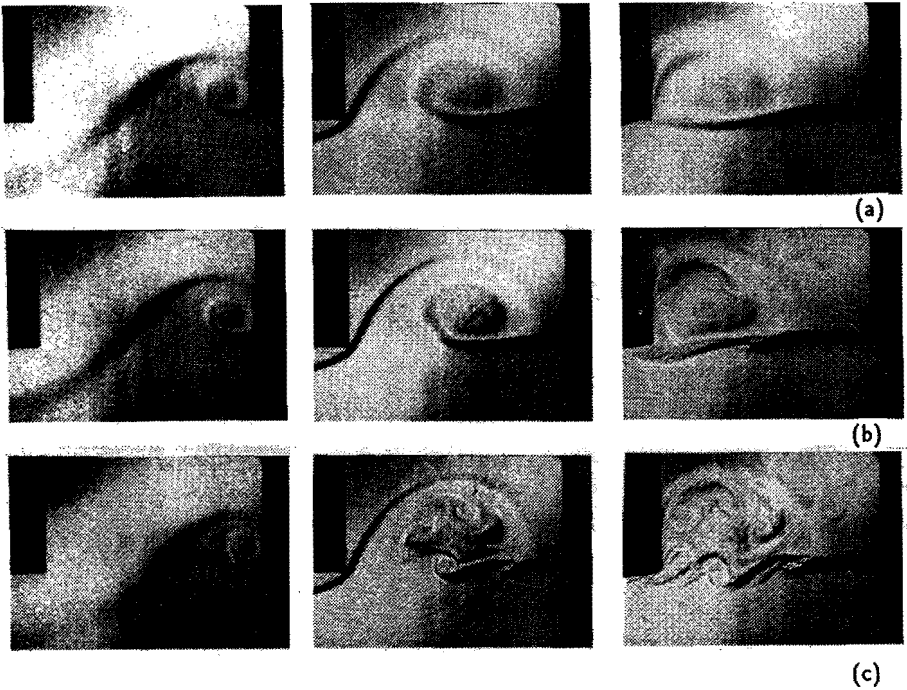


FIGURE 3.17: Starting flow in a T-junction.

(a) flow visualization for $\Delta p = 50 \text{ Pa}$, (b) $\Delta p = 199 \text{ Pa}$, (c) $\Delta p = 792 \text{ Pa}$.

Even during the initial development phase of the vortex layer, Auerbach (1987) found deviations from the similarity solutions describing the local flow around a wedge. This deviation from the similarity solution was also observed in three dimensions experimentally by Didden (1979) and Pullin (1979) and confirmed by numerical simulations of Nitsche (1992).

In this section different vortex methods will be used to compute the development of the solution of this non-similar flow problem and results will be compared with flow visualization. The single-vortex methods will not be considered, since in the previous section it was shown, that these methods are inadequate in describing the behavior of the vortex structure accurately.

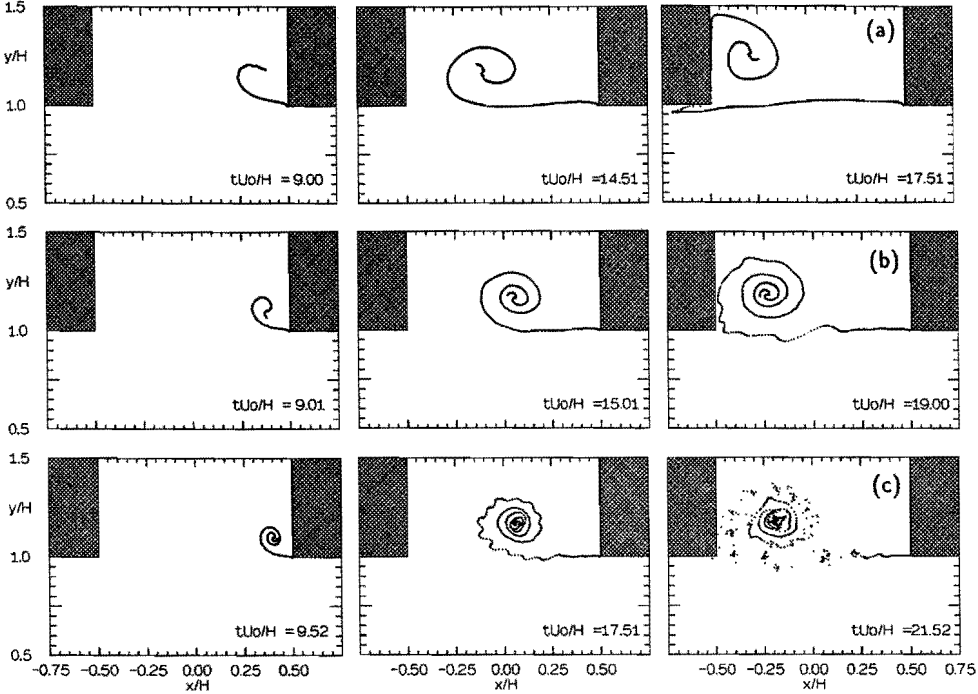


FIGURE 3.18: Numerical simulation of the starting flow in a T-junction, shown in figure 3.17. Vortex-blob solution using the velocity obtained with the hot-wire anemometer, see figure 3.16. (a) $\Delta p = 50 \text{ Pa}$ ($\delta = 0.10$), (b) $\Delta p = 199 \text{ Pa}$ ($\delta = 0.05$), (c) $\Delta p = 792 \text{ Pa}$. ($\delta = 0.025$).

3.4.2 Sharp-edged nozzle

Impulsively started flow

The vortex-sheet and vortex-blob method are used to describe the impulsively started flow at a sharp-edged nozzle. The coordinates and velocity are non-dimensionalised with the channel width H and the velocity U_0 , respectively. Furtheron, only non-dimensionalised values will be given. In both methods symmetry with respect to the channel centerline is assumed.

For the vortex-sheet method a conformal mapping $z = f(\zeta)$ which transforms the flow domain in the physical plane onto the half-space $\Re(\zeta) > 0$ in the computational plane given by $z = f(\zeta)$ with

$$f(\zeta) = \frac{-1}{2\pi}\zeta + \frac{i}{2\pi}\ln(1 - i\zeta) \quad (3.35)$$

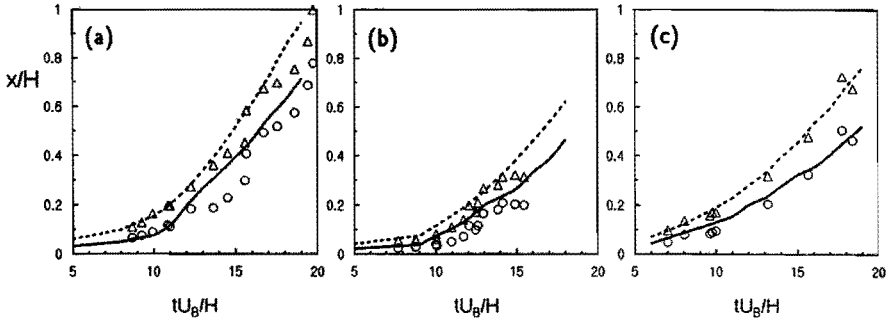


FIGURE 3.19: x -coordinate of the position of the vortex core (x_v) and front (x_f) of the vortex sheet. (—: x_v , - - - : x_f) Vortex-blob method (\circ : x_v , Δ : x_f) data obtained from flow visualization, see figure 3.17. (a) $\Delta p = 50 Pa$ ($\delta = 0.10$), (b) $\Delta p = 199 Pa$ ($\delta = 0.05$), (c) $\Delta p = 792 Pa$ ($\delta = 0.025$).

see figure 3.20.

The nozzle edge at $z = 0$ in the physical plane is mapped onto the origin $\zeta = 0$ in the computational plane, while the mean flow originating from the channel at $z = -i\infty$ corresponds to a point source positioned $\zeta = -i$. The complex velocity potential due to the attached flow is given by

$$\Phi_0(\zeta) = \frac{1}{2\pi} \ln(\zeta + i) \quad (3.36)$$

while the complex velocity potential due to the attached flow, the vortex sheet and point vortex describing the vortex core is given by

$$\Phi(\zeta) = \Phi_0(\zeta) + \Phi_s(\zeta) + \Phi_v(\zeta) \quad (3.37)$$

where $\Phi_0(\zeta)$, $\Phi_s(\zeta)$ and $\Phi_v(\zeta)$ are given by equation (3.36), (2.87) and (3.3), respectively. The initial position of the point vortex in the vortex-sheet method is again obtained from the similarity solution for the local flow at the edge $z = \zeta = 0$ with

$$\begin{aligned} A &= \frac{1}{2\pi}; \quad n = 1/2 \\ B &= \frac{1}{4\pi}; \quad D = 2\sqrt{\pi} \end{aligned} \quad (3.38)$$

The vortex has therefore the initial position $z_v = r_v e^{i\phi_v}$ for $t < t_1$ and circulation Γ_v with

$$\begin{aligned} r_v &= \left(\frac{1}{8} \sqrt{\frac{2}{\pi}} t \right)^{2/3} \\ \phi_v &= \pi \\ \Gamma_v &= \left(\frac{1}{2} \pi t \right)^{1/3} \end{aligned} \quad (3.39)$$

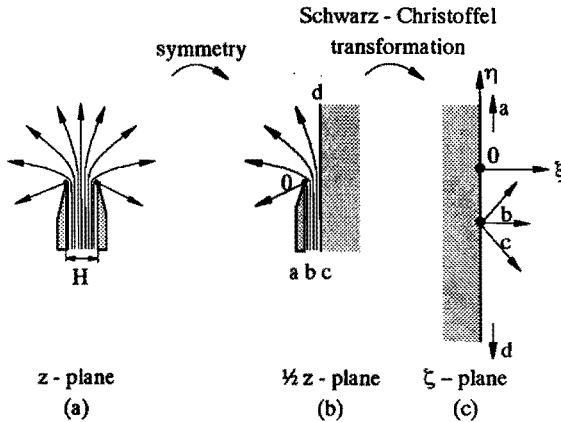


FIGURE 3.20: Conformal mapping of the flow domain of a sharp-edged nozzle onto a half plane. (a) physical plane (b) physical half-plane (c) computational plane

which corresponds to the force-free single-vortex similarity solution for an attached impulsively started flow around the edge. The initial (active) vortex sheet consists of five panels of zero vortex distribution along the streamline originating from the edge. In the computations a second (passive) vortex sheet without a vortex distribution is used to mark the evolution of the front of the fluid which at $t = 0$ was inside the channel.

The development of the vortex-sheet solution is included in figure 3.22, where it is compared with Auerbach's (1987) flow visualization in a water channel with impulsively started flow. The parameters used in the vortex-sheet method are given in table 3.6. It should be noted that the Reynolds number based on the velocity of the main flow and channel width of the experiment by Auerbach (1987) is rather low, i.e. $Re \approx 80$. Therefore, in the experiment the vortex layer is much thicker than the dye suggests.

TIME STEP NR.	\mathcal{F}	Δs_{max}	$\Delta \theta_{max}$	θ_y
1 - 250	0.2	0.05	20°	90°
251 - 750	0.2	0.05	20°	360°
751 - 1250	0.2	0.10	20°	720°
1251 - 6750	0.2	0.15	20°	720°

TABLE 3.6: Parameters used for the vortex-sheet method for the starting flow out of a sharp-edged nozzle, shown in figure 3.22.

Figure 3.22 also includes the results obtained with the vortex-blob method, with a value of the desingularisation parameter $\delta = 0.05$. The symmetrical geometry used for the

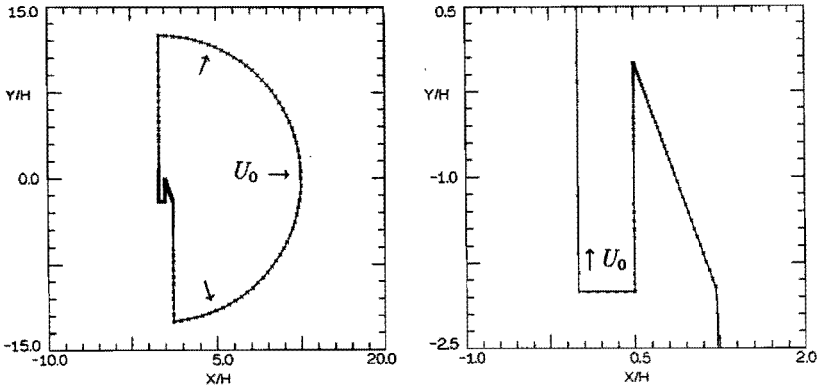


FIGURE 3.21: Panel distribution used for vortex-blob calculation of the outflow at a sharp-edged nozzle. On the axis $x = 0$ a symmetry condition is used.

calculation is shown in figure 3.21. Inside the channel, a uniform flow is imposed, while at the circular far-field boundary, an undisturbed potential outflow is assumed. Note that the geometry used for the vortex-blob method is different from the geometry used for the vortex-sheet method. Figure 3.22 shows that again the results of the vortex-sheet and vortex-blob method are very similar. The different shape found by Auerbach (1987) in the flow visualization is attributed to the viscous effects having a relative large influence at the low value of the Reynolds number of the experiment.

A more quantitative comparison of the results is presented in figure 3.23. The center of vorticity of the vortex sheet, the circulation and the position of the front, all as a function of time are compared with Auerbach's (1987) experimental data and with the similarity solution for a starting flow around the nozzle edge, see equation (3.39), which loses its validity for longer times. The calculated position of the vortex center, position of the front and circulation are almost the same for the vortex-sheet and vortex-blob method. The center of vorticity moves in x -direction according to the similarity solution, while in y -direction the position of the center of vorticity increases linearly in time. This behavior agrees with the prediction by Blondeaux & Bernardinis (1983). They proposed to relate the x -component of the position to the attached flow around the edge, and the y -component to the symmetrical part of the attached flow.

The circulation predicted by this model should increase according to the similarity solution, equation (3.39). This is in agreement with the numerical results presented in figure 3.23. Initially the circulation obtained with the vortex-blob and vortex-sheet method depends on time initially according to the similarity solution, however for longer time, the circulation increases linearly in time as one would expect for a straight jet, with $d\Gamma/dt = \frac{1}{2}U_0^2$.

Auerbach (1987) found for the vortex core trajectory both in y - and x -direction an

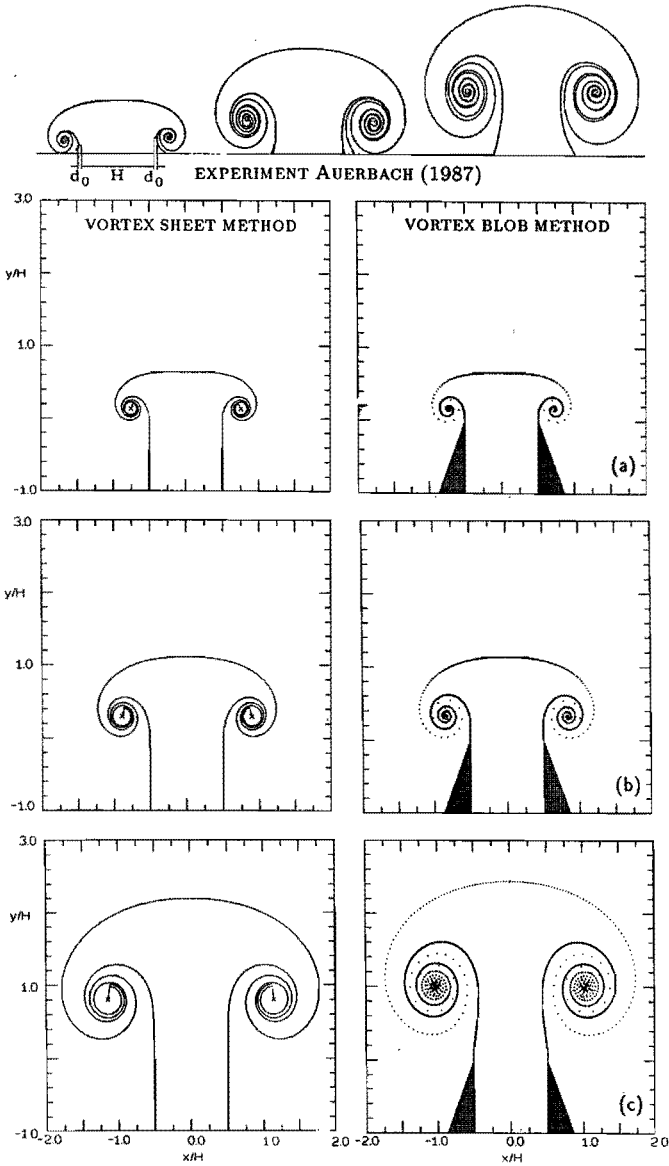


FIGURE 3.22: Impulsively started flow out of a sharp-edged nozzle. The computations have been carried out for half the configuration, imposing symmetry conditions along the line $x = 0$. Numerical simulation: (—) vortex-sheet method ($\Delta s_{max} = 0.05$) (---) vortex-blob method ($\delta = 0.05$) Experiment for $Re = 80$ (Auerbach (1987)). (a-c) are at $t = 1.0, 2.0$, and 5.0 , respectively.

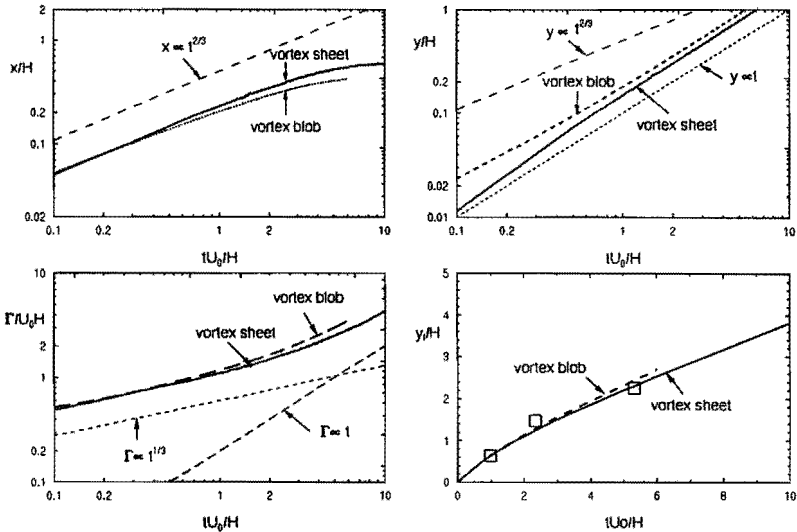


FIGURE 3.23: Position of center of vorticity of the vortex sheet together with its circulation and position of the front for the impulsively started flow out of a sharp-edged nozzle. (\square) experimental data (Auerbach (1987)), see figure 3.22.

increase in time according to the similarity solution, equation (3.39). However, from the present numerical solutions it is clear, that this is not valid for the position of the center of vorticity.

For the three-dimensional case of the starting flow in an unflanged circular pipe, Didden (1979) observed that the axial coordinate of the vortex core does not obey the similarity relation either. Nitsche (1992) showed by numerical simulation that the axial position of the vortex core increases in time according to $t^{3/2}$, which differs from the two-dimensional case. This might be due to the self-induced velocity of the vortex rings, which are formed in the case of the flow out of a circular pipe. This self-induced velocity is not present in the two-dimensional case.

3.4.3 Square-edged nozzle

Impulsively started flow

The flow separation process at the edges of a square-edged nozzle is modeled by using the two-vortex method with an amalgamation procedure, the vortex-sheet and vortex-blob method. It has been assumed that the flanges of the nozzle are infinitely large and that the flow remains symmetrical with respect to the centerline of the channel, so that it suffices to use only one sheet.

For the two-vortex method and the vortex-sheet method, the nozzle geometry is mapped

to the half plane $\Re(\zeta) > 0$, shown in figure 3.24 by the conformal mapping $z = f(\zeta)$, where

$$f(\zeta) = \frac{i\sqrt{i\zeta}}{\pi} - \frac{i}{2\pi} \ln \left(\frac{\sqrt{i\zeta} + 1}{\sqrt{i\zeta} - 1} \right) + 1/2 \tag{3.40}$$

The edge of the nozzle ($z = 0$) is mapped onto the origin $\zeta = 0$ in the computational

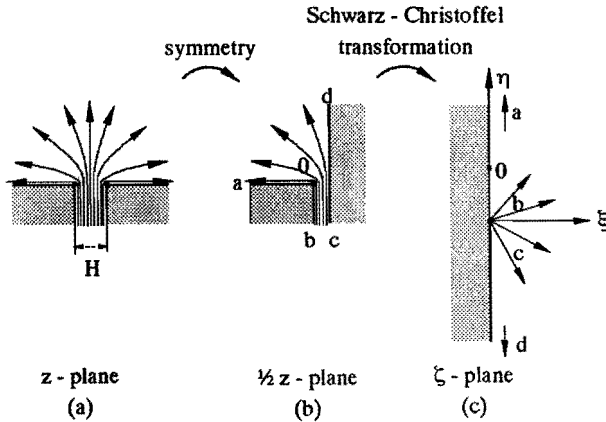


FIGURE 3.24: Conformal mapping of a square-edged nozzle onto a half plane (a) physical plane (b) physical half-plane (c) computational plane.

plane, while the mean flow from the channel, originating at $z = -i\infty$, is mapped onto a point source at $\zeta = -i$. The complex velocity potential of the impulsively started flow is given by

$$\Phi_0(\zeta) = \frac{1}{2\pi} \ln(\zeta + i) \tag{3.41}$$

while the velocity potential of the separated flow is given by equation (3.37). For the vortex-sheet method, the initial position of the point vortex is again obtained from a similarity solution near the edge $z = \zeta = 0$ with

$$\begin{aligned} A &= \frac{1}{2\pi}; \quad n = 2/3 \\ B &= \frac{1}{4\pi}; \quad D = (3\pi)^{2/3} \end{aligned} \tag{3.42}$$

The vortex has therefore the initial position $z_v = r_v e^{i\phi_v}$ for $t < t_1$ and circulation Γ_v with

$$\begin{aligned} r_v &= \sqrt{3\pi} \left(\frac{\sqrt{10}}{45\pi} t \right)^{3/4} \\ \phi_v &= \frac{3}{2} \arcsin \left(\frac{\sqrt{6}}{4} \right) \\ \Gamma_v &= 3\pi \left(\frac{4\sqrt{10}}{270\pi} t \right)^{1/2} \end{aligned} \tag{3.43}$$

which corresponds to the force-free single-vortex similarity solution for an attached impulsively started flow rounding the square-edge. The initial (active) vortex sheet consists of five panels of zero vortex distribution along the streamline originating from the edge. Again, a second (passive) vortex sheet without vortex distribution is used to mark the evolution of the front of the fluid which at $t = 0$ was inside the channel. The method used to describe the vortex sheet development is similar to the vortex-sheet method used for the sharp-edged nozzle. The computed shape of the vortex sheet are presented in figure 3.25. The parameters used to obtain this solution are listed in table 3.7. In the numerical sim-

TIME STEP NR.	\mathcal{F}	Δs_{max}	$\Delta \theta_{max}$	θ_v
1 - 250	0.1	0.025	20°	90°
251 - 350	0.1	0.05	20°	180°
351 - 600	0.1	0.10	30°	360°
601 - 1600	0.2	0.10	20°	540°
1601 - 2600	0.3	0.10	30°	900°
2601 - 6600	0.4	0.10	30°	900°

TABLE 3.7: Parameters used for the vortex sheet solution for the impulsively started flow out of a square-edged nozzle, shown in figure 3.25.

ulation symmetry is assumed, which imposes a zero normal velocity at the symmetry axis. The center of vorticity of the vortex sheet and the circulation are presented in figure 3.27.

In the two-vortex method, the main vortex represents the center of vorticity, while the generation of vorticity is modeled by the edge vortex, which position and circulation is determined by a similarity solution of the separated flow near the edge of the nozzle. The velocity field close to the edge is the sum of the flow induced by the attached main flow and the velocity field induced by the main vortex, similarly to the procedure followed for the case of the starting flow in a T-junction, see section 3.3. In the present case the complex velocity potential is given by

$$\Phi(\zeta)]_{\zeta \rightarrow 0} = -iA\zeta + B\zeta^2 + \dots \quad (3.44)$$

$$\text{with : } A = \frac{1}{2\pi} - \frac{\Gamma_v}{2\pi} \left(\frac{1}{1 - \zeta_v} - \frac{1}{1 + \zeta_v^*} \right)$$

$$B = \frac{1}{4\pi} + \frac{i\Gamma_v}{4\pi} \left(\frac{1}{(1 - \zeta_v)^2} - \frac{1}{(1 + \zeta_v^*)^2} \right)$$

The so found position of the center of vorticity, the position of the front of the contact line and the circulation of the rolled-up vortex layer are compared with the results of the vortex-sheet method in figure 3.27. Both the position of the front and the center of vorticity of the rolled-up vortex sheet obtained with the two-vortex method agree with those of the vortex-sheet method as long as the scale of the vortex sheet is of the order of the width of the channel ($r = \mathcal{O}(H)$), i.e. for $iU_0/H < 2$. For $x > \mathcal{O}(H)$, the velocity at the vortex is overestimated due to the velocity induced by the image vortex distribution in the plane

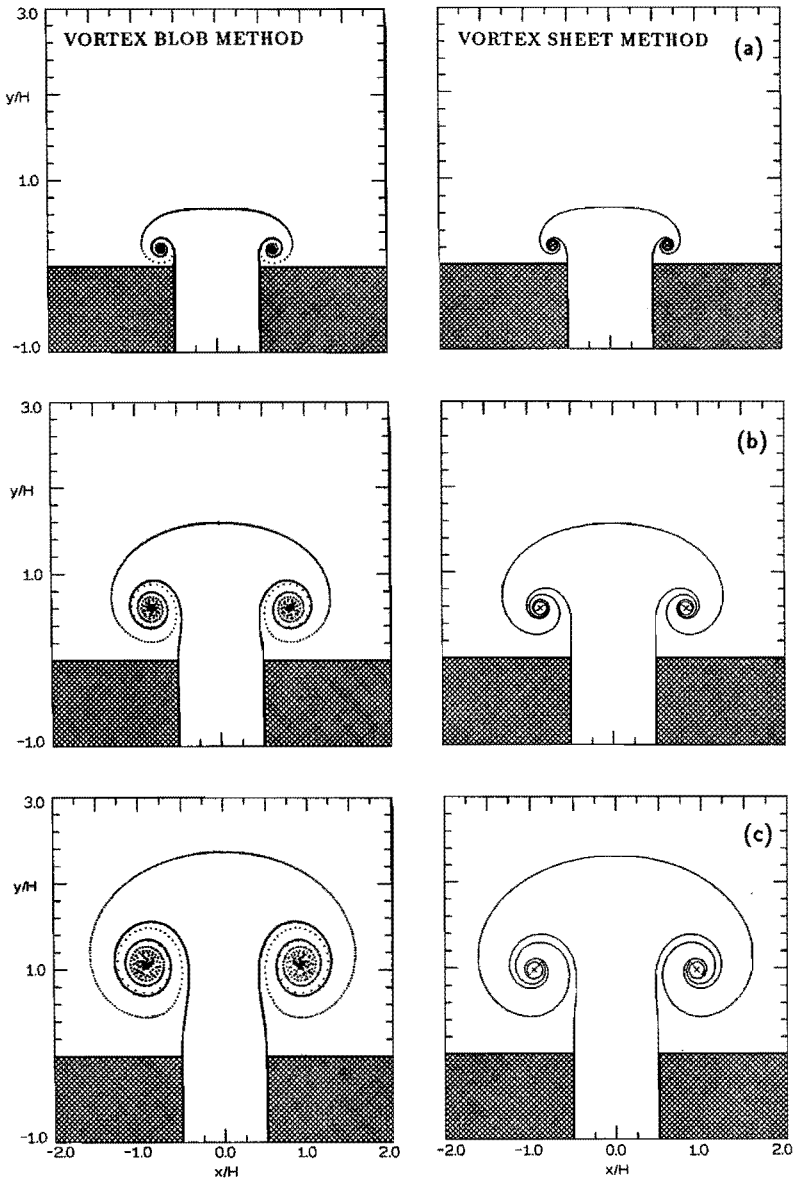


FIGURE 3.25: Numerical simulation of the impulsively started flow out of a square-edged nozzle. The computations have been carried out for half the configuration, imposing symmetry along the line $x = 0$. (\cdots left-hand side) Vortex-blob method ($\delta = 0.10$) ($---$ right-hand side) vortex-sheet method ($\Delta s_{max} = 0.10$). (a-c) are at time $tU_0/H = 1.0, 3.0,$ and 5.0 , respectively.

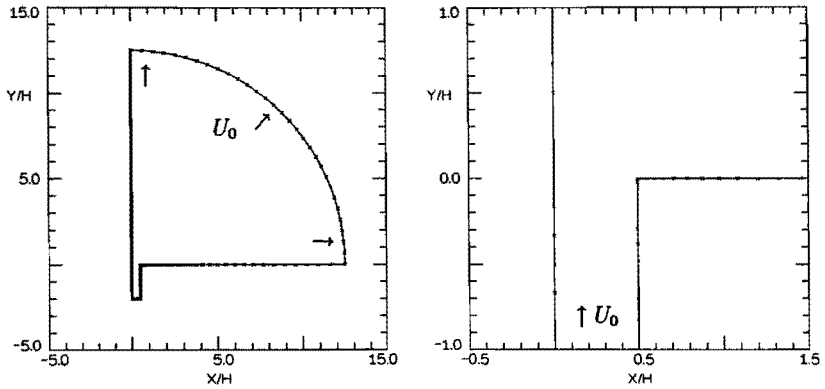


FIGURE 3.26: Panel distribution for the simulation of the flow out of a square-edged nozzle, using the vortex-blob method. On the axis $x = 0$ a symmetry condition is used.

of symmetry. The circulation obtained with the two-vortex method and the one obtained with the vortex-sheet method shows a similar behavior.

The vortex-blob method is also used to describe the impulsively started flow in a nozzle. The geometry used for the boundary-element method is given in figure 3.26. On the circular far-field boundary, a radial, uniform outflow is assumed in the model, with the total flux through the boundary equal to the flux out of the channel. The results, obtained with a value of the desingularisation parameter $\delta = 0.10$ are compared with the vortex-sheet method in figure 3.25. In figure 3.27 the position of the front, the center of vorticity and the circulation of the vortex sheet are compared with the results of the vortex-sheet method and of the two-vortex method.

In contrast to the case of a sharp-edged nozzle, for a square-edged nozzle during the initial development of the sheet both the x - and y -coordinate of the center of vorticity follow the similarity solution given by equation (3.43). Also the circulation increases according to the similarity solution. On a larger time scale, the circulation increases linearly with time according to $d\Gamma/dt = \frac{1}{2}U_0^2$. Although the circulation and center of vorticity obtained with the two-vortex method deviate from the vortex-sheet method for $tU_0/H > 2$, the front position of the vortex sheet is well described by the two-vortex method until $tU_0/H \approx 5$.

3.4.4 Experiment

Flow visualization

In order to validate the numerical simulations, an experimental setup has been built for visualizing the starting flow in a square-edged nozzle. The experimental setup is similar to the setup described in section 3.2 for the T-junction geometry. Instead of the T-junction geometry, a flue organ pipe is used as the basic geometry. The two-dimensional organ pipe

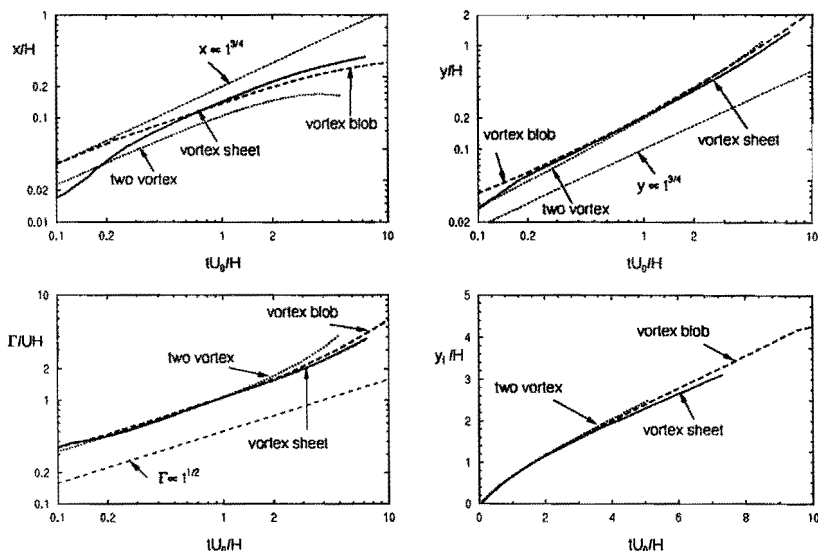


FIGURE 3.27: Position of center of vorticity of the vortex sheet, its circulation and position of the front for the impulsively started flow out of a square-edged nozzle.

geometry, shown in figure 3.28, has a sidewall with length 283.0 mm and is positioned at a distance of 20.0 mm from the flue channel. With this geometry, the transient behavior of a flue organ pipe was studied by Mahu *et al.* (1993), but for the present purpose, the labium and the upper wall of the pipe has been removed resulting into a flanged channel end.

Although the resulting geometry is not symmetric, the flow visualization can be used to study the initial stage of the symmetric vortex sheet development. The height of the flue channel is 1.0 mm. The upper wall of the flue channel has a thickness of 5.0 mm, and as a result, the influence of the finiteness of the upper wall and of the sidewall is expected to be negligible as long as the vortex layer has a scale which is smaller than a few times the channel height.

The unsteady pressure $p_0(t)$ has been measured in the foot of the pipe with an acceleration compensated piëzo electrical gauge (type PCB 116) which is mounted flush in the wall. The pressure gauges have a diameter of 10.0 mm. The signal of the pressure gauge is amplified by a charge amplifier (type Kistler 5007, with bandwidth 0.1 Hz. to 22 kHz.) and transmitted to a digital memory (8 bits, 2048 samples) for further analysis by a Personal Computer. Pressure supply is provided by the ventilation system of the room, like for the starting flow experiments for the T-junction. The velocity at the flue exit $U_0(t)$ is calculated from the pressure in the foot of the channel by using the unsteady Bernoulli equation. The visualization of the flow has been performed by using a standard schlieren method, with a difference in the refractive index provided by injecting CO_2 in the foot of

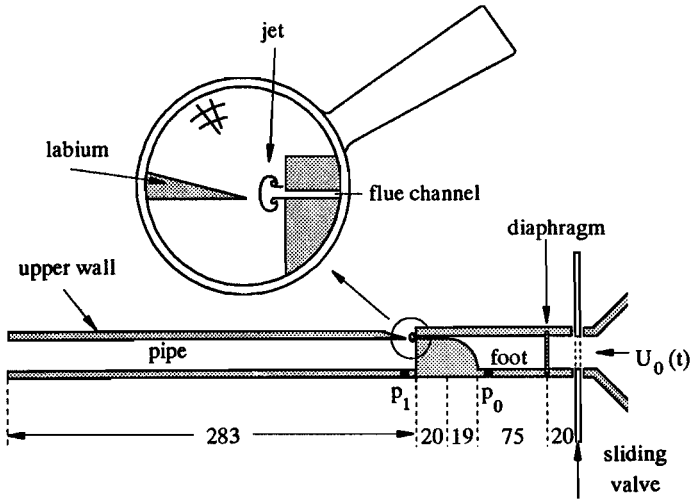


FIGURE 3.28: Organ pipe geometry (dimensions in mm).

the flue channel. The nanolite spark discharge, with a time resolution of 80 ns, is triggered by the pressure rise in the foot, while a delay time can be introduced to obtain a snapshot of the flow at different moments in time. Further details of the experiment can be found in Mahu (1993). In figure 3.29 the visualization of the starting flow in the channel for an initial pressure difference of 250 Pa across the valve is compared with the results for a pressure difference of 750 Pa. Here, time has been non-dimensionalised as $t^* = tU_B/H$, with $U_B = \sqrt{2\Delta p/\rho_{CO_2}}$ the Bernoulli velocity, based on the initial pressure difference Δp across the valve, the density of carbon dioxide in the foot $\rho_{CO_2} = 1.98 \text{ kg/m}^3$ and H the channel height.

The Reynolds number, based on the same quantities is 1360. A deviation from symmetrical flow is observed for dimensionless time $t > 30$, which is assumed to be due to the non-symmetric geometric arrangement. For a pressure difference of $\Delta p = 750 \text{ Pa}$ the corresponding Reynolds number is 2360. For the higher pressure difference, due to the increased Reynolds number, the shear layer thickness decreases, which yields the vortex layer more sensitive to the Kelvin-Helmholtz instability. Due to this instability, small-scale vortices appear in the vortex layer at later times, which are not found in the low-pressure experiment. Deviation from symmetry is observed for $tU_B/H > 40$ when $x/H > 5$. The velocity as a function of time, determined from the pressure difference across the flue channel, is presented in figure 3.30.

For a series of experiments the position of the front of the contact line between the outside air and the CO_2 flowing out of the flue channel and the axial position of the center of the vortex core is presented in figure 3.31 and 3.32, respectively. Only small differences are found for the position of the front for the experiments both at various pressure differences.

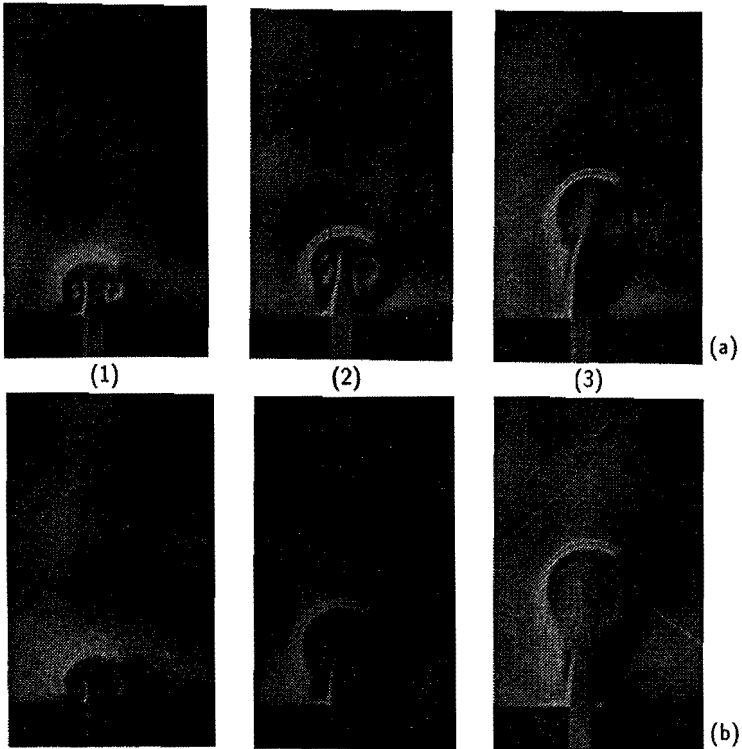


FIGURE 3.29: Flow visualization of the initial behavior of the starting flow from a flanged nozzle. (a) $\Delta p = 250 \text{ Pa}$, $Re = 1360$ (b) $\Delta p = 750 \text{ Pa}$, $Re = 2360$. (1-3) are at time $tU_B/H = 31.2$, 40.8, and 51.0, respectively.

For the position of the center of the rolled-up vortex layer, the differences are larger, in part attributed to the difficulty in determining accurately the position from the flow visualization. Differences between the results at low and high pressure are probably due to viscous effects.

Two limit values of the front position can be deduced, one by assuming that a straight jet is formed; a second one by assuming an attached potential flow. For the straight jet the front position is obtained by integrating the time-dependent velocity in time, i.e.

$$x_{f(\text{jet})} = \int_0^t U_0(t^*) dt^* \quad (3.45)$$

where $U_0(t)$ is given in figure 3.30. The position of the front obtained in this way

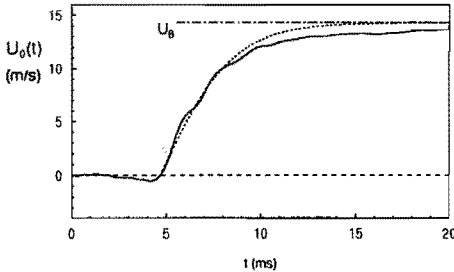


FIGURE 3.30: Main flow velocity, obtained from the pressure difference across the flue channel. (—) experimental data, (---) theoretical velocity for impulsively increased pressure (— · — · — · —) Bernoulli velocity U_B .

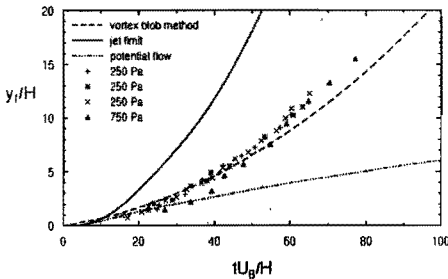


FIGURE 3.31: Position of the front of the contact line for the flow out of a flanged nozzle. Comparison with results of the vortex-blob method.

forms an upper bound, because in reality the flow spreads over a larger region than the width of the nozzle. In the second case the flow does not separate and the front position can be obtained from the trajectory of a tracer starting on the centerline of the channel $dx_{f(pot)}(t)/dt = U(x(t), t)$. This velocity is estimated to be $U(x, t) = U_0(t)/\pi x$, where it has been assumed that the flow originates from a point source at $x = 0$ and spreads over an angle π . This leads to

$$\begin{aligned} x_{f(pot)} &= \sqrt{\frac{2}{\pi} \int_0^t U_0(t^*) dt^*} \\ &= \sqrt{\frac{2}{\pi} x_{f(jet)}} \end{aligned} \quad (3.46)$$

The value obtained from the potential flow is an lower limit for the front position since in reality the flow separates and a jet of finite width is formed. Both limit values for the

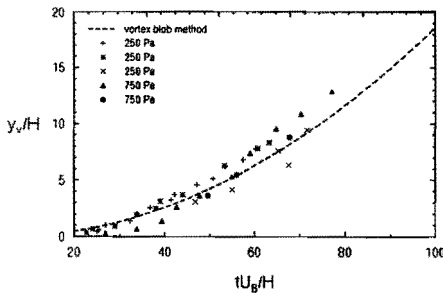


FIGURE 3.32: Position of the center of the vortex core for the flow out of a flanged nozzle. Comparison with results of the vortex-blob method.

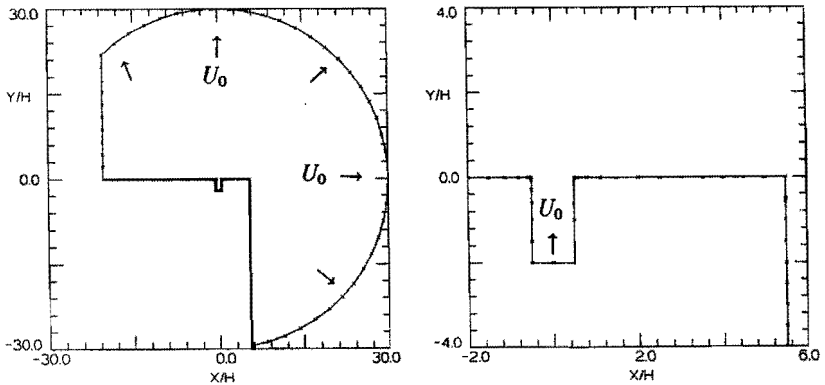


FIGURE 3.33: Panel distribution for the simulation of the flow out of a flue organ pipe in absence of a labium, using the vortex-blob method.

position of the front are shown in figure 3.31. Indeed the experimental data are somewhere between the jet limit and the potential-flow limit.

vortex-blob method

A numerical simulation of the flow for a geometry closely matching that of the experiment has been performed by the vortex-blob method. The panel distribution used for the boundary element method is shown in figure 3.33. On the circular far-field boundary, an undisturbed radial potential outflow is assumed with a total flux equal to that of the uniform inflow over the channel inlet. The value of δ is determined from the value of the momentum thickness θ_m for a fully developed laminar Poiseuille flow in the channel. With $\theta_m = H/15$ we estimate $\delta \approx 4\theta_m/H \approx 0.3$. The results of the numerical simulation by the

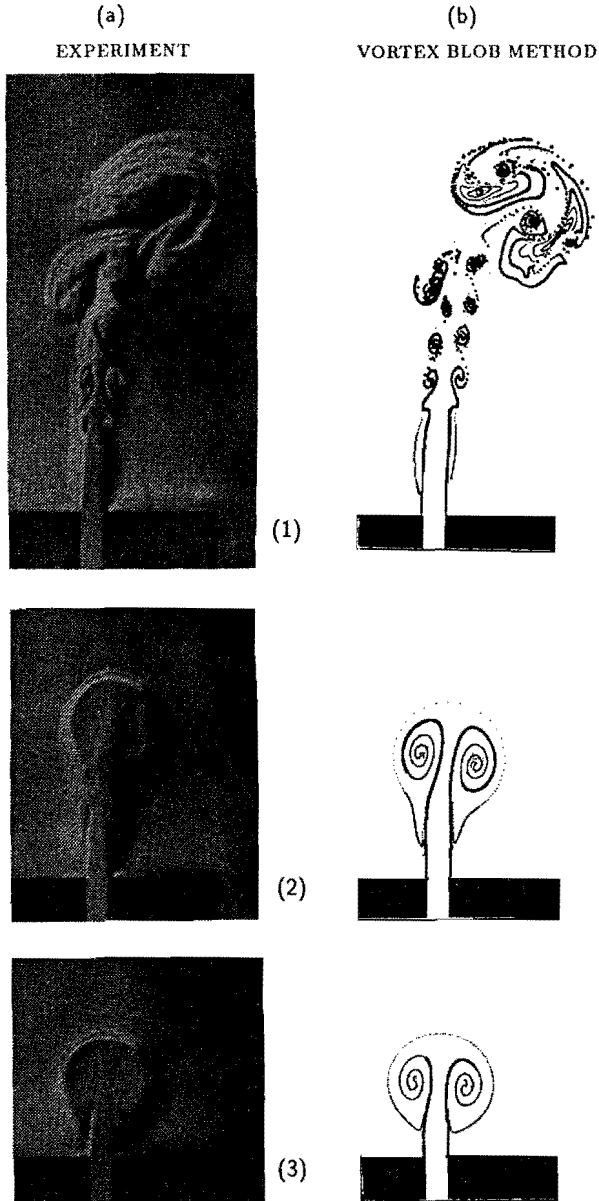


FIGURE 3.34: Starting flow in a flue organ pipe without a labium. (a) flow visualization for $\Delta p = 750 \text{ Pa}$ (b) Numerical simulation with the vortex-blob method ($\delta = 0.3$). (1-3) are at $tU_B/H = 46.3, 56.5$ and 95.3 , respectively

vortex-blob method with $\delta = 0.3$ are compared with the flow visualization for $\Delta p = 750 \text{ Pa}$ for a longer time period in figure 3.34.

The predicted position of the center of the rolled-up vortex layer and that of the front are compared with the experimental data in figure 3.32 and 3.31, respectively. Due to the accurate description of the geometry and the use of the experimentally obtained velocity rise, both the position of the front and that of the vortex center as a function of time are satisfactorily predicted by the vortex-blob method.

3.5 CONCLUSIONS

The starting flow in a number of geometries is simulated by potential flow methods developed in the previous chapter. A single-vortex method usually fails to describe the vorticity generation accurately, as the total circulation of the vortex layer and its velocity of convection is overestimated. If care is taken to describe the generation of vorticity near the sharp edge more accurately, for example by means of an edge vortex or an edge segment, the rate of vorticity generation agrees with more elaborate methods such as the vortex-blob and the vortex-sheet method. However, in these simplified methods still conditions have to be imposed to the point vortex/feeding-sheet combination, in order to obtain a reasonable description of the center of vorticity as the position of the main vortex. The results usually agree with those of other methods and experiments as long as the distance of the main vortex to the vorticity generating edge is of the same order of magnitude as the channel width.

For the generic problem of the flow past a wedge the numerical simulation by a second-order vortex-sheet method has shown, that application of the Kutta condition at the edge results in a vortex sheet which leaves the wedge tangentially, either to the lower or to the upper surface. However, the curvature of the sheet at the edge is infinite, in agreement with predictions by Clapworthy & Mangler (1974).

For the starting flow in a T-junction, a two-vortex method with an appropriate amalgamation procedure can accurately describe the evolution of the circulation of the sheet and the convection of its center of vorticity up to the moment that the vortex sheet collides with the downstream edge. The two-vortex method fails to accurately describe the jet-flow out of a nozzle as soon as the distance of the main vortex to the edge is large compared to the channel height.

For the starting flow out of a sharp-edged nozzle, the time history of the axial coordinate of the center of vorticity of the vortex sheet does not follow the similarity solution for the flow around an isolated wedge of infinite extent. The lateral coordinate and the circulation do follow the similarity solution, at least during the initial period. This deviation for the axial coordinate from the similarity relations has been observed also by Blondeaux & Bernardini (1983) for a two-dimensional sharp-edged channel, and by Didden (1979) for a circular pipe. However, for a circular pipe, the axial coordinate increases in time like $t^{3/2}$, while in two-dimensions it increases like t . This different behavior is probably due to the curvature-dependent self-induced velocity of a vortex ring.

For a two-dimensional square-edged nozzle both the axial and the lateral coordinate obey the similarity solution, as does the circulation of the vortex system.

REFERENCES

- AUERBACH D. (1987) Experiments on the trajectory and circulation of the starting vortex. *J. Fluid Mech.* **183**, 185 - 198.
- BASTIAANS R.J.M. (1991) Vorticity generation at edges. *Internal report R-1121-A* Eindhoven University of Technology (in Dutch)
- BLENDERMANN W. (1969), Der spiralwirbel am translatorisch bewegten kreisbogenprofil; Struktur, bewegung und reaktion. *Schiffstechnik* **16**, 3 - 14.
- BLONDEAUX P. & BERNARDINIS B. DE (1983) On the formation of vortex pairs near orifices. *J. Fluid Mech.* **135**, 111 - 122.
- BROWN C.E. & MICHAEL W.H. (1954) Effect of leading-edge separation on the lift of a delta wing. *J. Aero. Sci.* **21**, 690 - 694.
- BRUGGEMAN J.C. (1987) Flow induced pulsations in pipe systems. PhD thesis Eindhoven University of Technology
- CLAPWORTHY G.J. & MANGLER K.W. (1974) The behavior of a conical vortex sheet on a slender wing near the leading edge. *Royal Aircraft Establishment T.R. 74150*, pp. 1 - 44.
- DIDDEN N. (1979) On the formation of vortex rings: rolling up and production of circulation. *J. Applied Math. & Phys.* **30**, 101.
- DISSELHORST J.H.M & WIJNGAARDEN L. VAN (1980) Flow in the exit of open pipes during acoustic resonance. *J. Fluid Mech.* **99** 2, 293 - 319.
- GRAHAM J.M.R (1977) Vortex shedding from sharp edges. *I.C. Aero report 77-06* pp. 1 - 22.
- GRAHAM J.M.R (1983) The lift on an aerofoil in starting flow. *J. Fluid Mech.* **133**, 413 - 425.
- GRAHAM J.M.R (1986) Application of discrete vortex methods to the computation of separated flows. *Num. Meth. for Fluid Dyn. II* pp. 274 - 302.
- HOEIJMAKERS H.W.M & VAATSTRA W. (1983) A higher order panel method applied to vortex sheet roll-up. *A.I.A.A. Journal* **21** 4, 516 - 523.
- HOWE M.S. (1975) Contributions to the theory of aerodynamic sound, with application to excess jet noise and the theory of the flute. *J. Fluid Mech.* **71** 4, 625 - 673.
- KRASNY R. (1986) A study of singularity formation in a vortex sheet by the point vortex method. *J. Fluid Mech.* **167**, 65 - 93.
- MAHU W.E.A. (1993) Unsteady free jets; Comparison of flow visualizations to potential flow models. internal report R-1204-A Eindhoven University of Technology
- MAHU W.E.A., PETERS M.C.A.M., VERGE M.P., WIJNANDS A.P.J., FABRE B. & HIRSCHBERG A. (1992) Attack transient of a flue organ pipe. *2nd Dutch Conference on Mechanics* Rolduc, The Netherlands
- NITSCHKE M. (1992) Axisymmetric vortex sheet roll-up. PhD Thesis University of Michigan
- PIERCE D. (1961) Photographic evidence of the formation and growth of vorticity behind plates accelerated from rest in still air. *J. Fluid Mech* **11**, 460 - 464.
- PULLIN D.I. (1978), The large scale structure of unsteady self-similar rolled-up vortex sheets. *J. Fluid Mech.* **88** 3, 401 - 430.
- PULLIN D.I. (1979) Vortex ring formation at tube and orifice openings. *Phys. Fluids* **22** 3, 401 - 403.
- PULLIN D.I. & PERRY A.E. (1980) Some flow visualization experiments on the starting vortex. *J. Fluid Mech.* **97** 2, 239 - 255.
- ROTT N. (1954) Diffraction of a weak shock with vortex generation. *J. Fluid Mech.* **1**, 110 - 128.
- SMITH J.H.B (1966) Theoretical work on the formation of vortex sheets. *Prog. Aeron. Sci.* **7**, 35 - 51.

Numerical simulation of periodic flows

Abstract

Acoustically-induced periodic flows are studied both numerically and experimentally. In the presence of an acoustic field only vorticity generation at a sharp edge is a highly nonlinear phenomenon. This phenomenon is studied for a sharp-edged nozzle. Both the low- and high-Strouhal-number limit are considered. In the high-Strouhal-number limit there appears to be a phase shift between the periodic formation of vortex structures and the periodic acoustic velocity field. In the presence of a mean flow the vorticity is convected away from the edge. The periodic vortex formation process is triggered by the acoustic field. For this case the periodic formation of vortex structures in a T-junction and a cross-junction are visualized by means of a schlieren method and simulated numerically by different vortex methods.

4.1 INTRODUCTION

In this chapter the periodic flow involving generation and convection of vorticity in several geometries is simulated for an imposed acoustic velocity field using the vortex methods described in chapter 2.

Vortex shedding from a sharp-edged solid body emerged in an external flow leads to time-varying forces on the body and has been studied extensively during the last decade. For the flow around a cylinder with a square or a rectangular prism cross-section discrete-vortex methods have been used by Clements (1973), Nagano *et al.* (1982) and Sarpkaya & Ihrig (1986). The Strouhal number of the vortex formation process as well as the lift and drag force coefficient are well predicted by the discrete vortex methods. Similar methods have been used by Sarpkaya (1975) and Kiya & Arie (1986) for the periodic vortex formation process associated with the flow about an inclined plate in a steady mean flow. For these problems with a steady uniform onset flow the unsteady character of the vortex formation process is not triggered by an external excitation.

The interaction between an unsteady flow and flow separation for a plate has been studied by Graham (1980) and for an axi-symmetric disc by de Bernardinis *et al.* (1981). The latter studied the flow separation due to an oscillatory potential flow around a disk starting from rest. Although using the discrete vortex method a stable periodic solution was not obtained, the unsteady forces compared well with experimental data. Also for the periodic flow through an axi-symmetric orifice, the pressure difference across the orifice could be accurately predicted.

The periodic vortex shedding from a nozzle, induced by a resonating acoustic field inside a pipe, in absence of a mean flow has been studied by Disselhorst & van Wijngaarden (1978, 1980). Describing the vortex shedding by a multi-point-vortex method a periodic solution could only be obtained for high acoustic Strouhal numbers.

In the limit of high acoustic Strouhal number the acoustic energy loss by vortex shedding could be predicted reasonably well by this method. However, for acoustic Strouhal numbers of order unity, the method failed.

In the presence of a mean flow component the vortices formed can also transfer kinetic energy from the main stream to the acoustic field. This phenomenon has been studied by Welsh & Stokes (1984, 1986) for the vortex shedding from a plate inside a duct and for two plates in tandem in a duct by Stoneman *et al.* (1988). The discrete-vortex approach yields a prediction of the Strouhal number at which self-sustained resonances occur. However, the amplitude of the self-sustained resonance could not be predicted.

Bruggeman *et al.* (1989, 1991) studied the periodic vortex formation in pipe systems with closed side branches where it is the source of self-sustained oscillations. Self-sustained resonances could be obtained in the closed side branches at specific values of the Strouhal number. Using a single-vortex method the Strouhal number at which resonance occurs could be predicted, although the circulation of the vortices and the strength of the aero-acoustic source was overestimated by a factor 3.

In the present numerical analysis of periodic vortex formation, we will consider the case of periodic vortex shedding induced by an imposed periodic acoustic velocity field. The amplitude of the acoustic velocity field will assumed to be constant. The interaction between the velocity field and the acoustic field is considered in chapter 5 for an open pipe termination and in chapter 6 for a pipe system with two closed side branches.

The configurations studied are the following:

- a sharp-edged nozzle, i.e. similar to the configuration studied by Disselhorst & van Wijngaarden (1980)
- a T-junction with sharp edges, studied experimentally by Bruggeman (1987)
- a cross-junction with sharp edges, studied experimentally by Ziada & Bühlmann (1992).

For the periodic flow in a sharp-edged nozzle, the results of the numerical simulation of the flow will be compared with the flow visualization data obtained by Disselhorst (1978). For the T-junction and the cross-junction configuration flow visualization obtained in the present study, at high amplitudes of the acoustic field, will be compared with the results of the numerical simulation. For the T-junction, at moderate acoustic amplitude, the results of the numerical analysis will be compared with Laser Doppler velocity measurements by Bruggeman (1987).

4.2 SHARP-EDGED NOZZLE

4.2.1 Introduction

In this section the periodic flow out of a sharp-edged nozzle of width H is considered. The vortices, formed in the shear layer separating from the sharp edges of the channel, are described employing the discrete vortex methods described in chapter 2 and used in chapter 3 for starting flow problems. The conformal mapping of the geometry of the nozzle is shown in figure 3.20. The velocity of the periodic acoustic flow field is $u_{ac}(t) = \hat{u}_{ac} \sin(\omega t)$, directed into the pipe during the first half period. The acoustic Strouhal number is defined as

$$Sr_{ac} = H/\hat{u}_{ac}T \quad (4.1)$$

where T is the period of oscillation of the acoustic velocity field. In absence of a mean flow the value of the acoustic Strouhal number determines the convection of a vortex structure during a period of the acoustic field. If the Strouhal number is small, and the acoustic velocity is directed outward the separated flow forms a free jet flow, while when the acoustic flow is directed inward the flow forms a jet with a vena-contracta inside the nozzle. For low values of the Strouhal number a quasi-stationary theory can be used. This low-Strouhal-number limit has been extensively studied by Disselhorst (1978) and van Wijngaarden (1968) and will not be discussed here.

On the other hand, if the Strouhal number is high, the vorticity generated convects a distance from the edge small compared to the nozzle width H and the flow can be approximated by the periodic flow around the edge of a single plate in isolation, i.e. neglecting the influence of the opposite nozzle edge. This limit has been studied by Disselhorst & van Wijngaarden (1978, 1980) using a multi-point vortex method.

In the intermediate range of acoustic Strouhal numbers of order one, the vortex structures formed at the opposite edges of the nozzle interact and the complete nozzle geometry has to be considered. For $Sr_{ac} = 2.54$ Disselhorst (1978) visualized the periodic flow using a schlieren method. This case of Strouhal numbers of order unity will be considered first in section 4.2.2, followed by the study of the high-Strouhal-number limit, see section 4.2.3.

4.2.2 Strouhal number of order unity

For the case $Sr_{ac} = 2.54$ the visualization of the periodic flow around the pipe exit by Disselhorst (1978) is shown in figure 4.1. The flow is visualized by schlieren-interferometry which detects gradients in refractive index. The refractive index has been induced by slightly heating the walls. The asymmetry of the flow with respect to the nozzle edge is due to the influence of the vortex layer at the opposite nozzle edge. The arrows denote the total velocity measured by means of a hot-wire (visualized at $t/T = 0.71$). The estimated position of the core center during one period of the rolled-up part of the vortex layer is presented in figure 4.2 for the two vortex structures which are present in the flow visualization. The first vortex structure (denoted in figure 4.2 by a \times) is generated when the acoustic velocity is directed into the channel, while the second vortex structure (denoted in figure 4.2 by a \circ) contains vorticity of opposite sense and is generated when the acoustic

velocity is directed out of the channel. At the end of each period the two vortices with opposite circulation form a dipole which moves away from the edge.

The axial and lateral coordinate of the estimated vortex core centers of the two vortex structures are presented in figure 4.3. From this figure it is clear that a new vortex structure is generated before the acoustic velocity changes sign, both for the first and for the second vortex. The vortices are generated approximately $0.1 T$ ahead of the change in acoustic velocity. This is due to the velocity induced by the vortex generated during the previous half period. A new vortex is generated when the sum of the acoustical velocity and the velocity induced by the vorticity changes sign at the edge.

For the numerical simulation of the periodic flow in the sharp-edged nozzle the geometry used is identical to the one used for the calculation of the starting flow in a sharp-edged nozzle, shown in figure 3.20 and 3.21, in which symmetry of the flow with respect to the centerline of the channel has been assumed.

Single-vortex method

Using a single-vortex method, all the vorticity generated at the edge is concentrated in a single point with, at each point in time, the circulation of the point vortex determined by the Kutta condition. This implies that the circulation of the vortex decreases to zero when the acoustic velocity decreases to zero and changes sign. Subsequently a new vortex is formed at the edge when the velocity changes sign. As a result in this method only a single vortex is present at any point in time. Depending on the conditions for the feeding sheet/ point vortex combination in this method the velocity of the point vortex is given by the local flow velocity at the vortex position given by equation (2.65), or by the value that follows from the conditions given by equation (2.76) for the force-free method or (2.80) for the source-free method.

For the force-free single-vortex method the trajectory of the vortex during one period is presented in figure 4.2. The asymmetry of the vortex trajectory is due to the influence of the vortex generated at the opposite edge of the nozzle. The vortex leaves the edge approximately perpendicular to the edge according to the similarity solution of the local separating flow near the edge (see section 3.2.3). The comparison of these results with the experimental data obtained by Disselhorst (1978) shows that for this case the single-vortex method does not accurately predict the vortex path. This is because in reality the vortices do not disappear within half a period of the acoustic field and therefore influence the formation and convection of the other vortices.

In figure 4.4 the circulation of the vortex system is shown. For the free-vortex method, the circulation is overestimated compared to the force-free method while for both methods the total circulation of a vortex system can decrease and is zero when the acoustic flow vanishes.

Single-panel method

It is expected that, for Strouhal numbers of order unity, vorticity generated at the beginning of an acoustic period influences the formation of a new vortex during the second half period

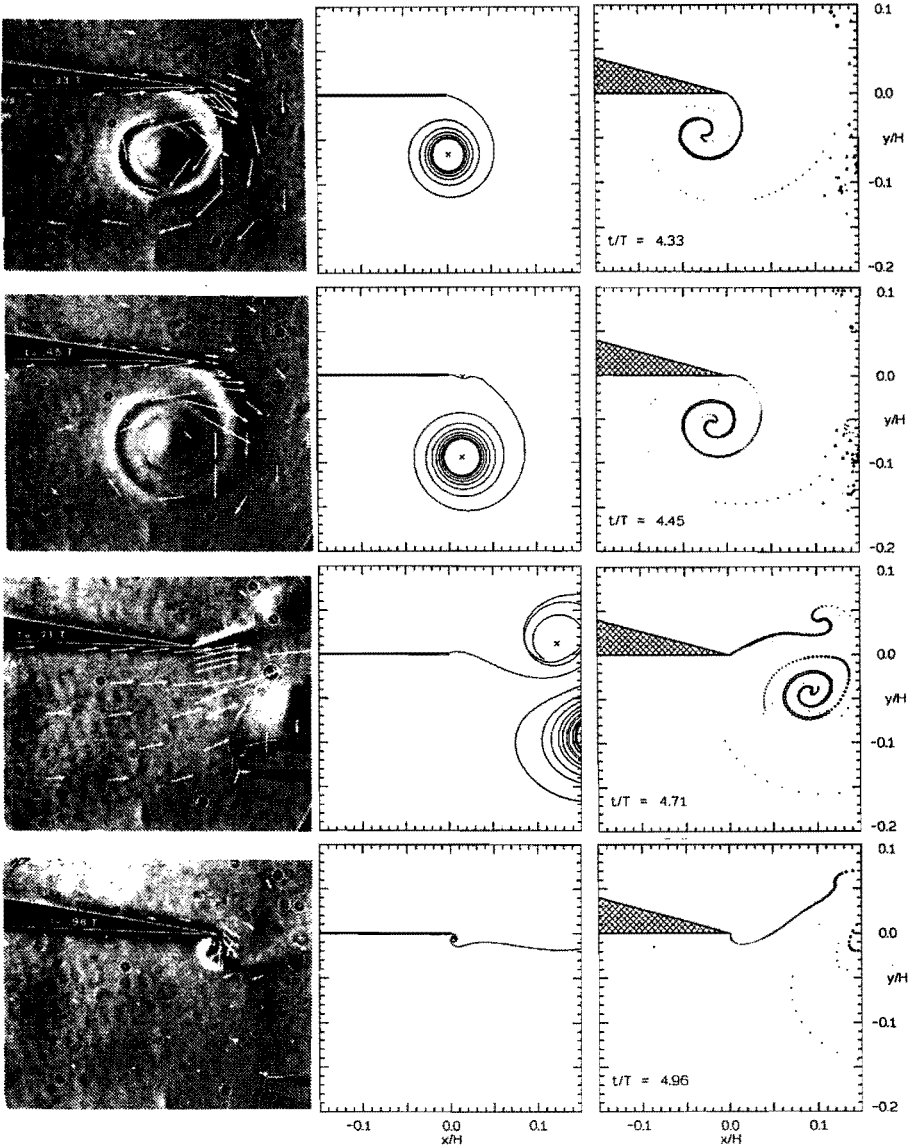


FIGURE 4.1: Periodic flow out of a sharp-edged nozzle. $Str_{ac} = 2.54$
 (a) Flow visualization by a schlieren method by Disselhorst (1978) (b)
 numerical simulation by the single-panel method, (—) streakline of the
 flow (c) numerical simulation by the vortex-blob method ($\delta = 0.04$) (Shown
 is the periodic solution at $t/T = 0.33, 0.45, 0.71$ and 0.96 , respectively)

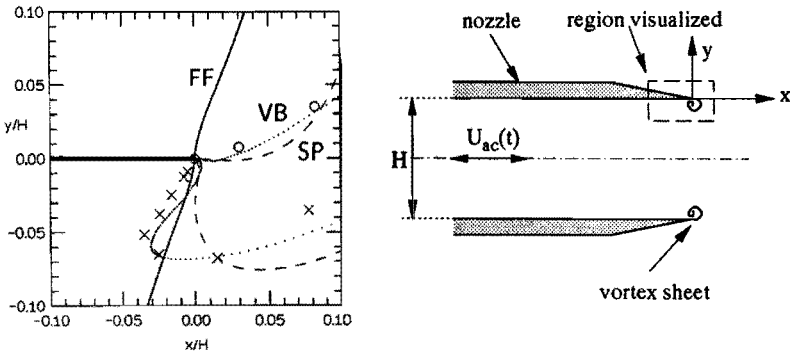


FIGURE 4.2: Positions of center of vorticity during one period of acoustic oscillation using different methods. $Sr_{ac} = 2.54$ (—) force-free single-vortex method (FF) (---) single-panel method (SP) (.....) vortex-blob method (VB) ($\delta = 0.04$). Vortex core for first (x) and second (o) vortex structure, obtained from flow visualization by Disselhorst (1978), presented in figure 4.1.

of the acoustic field. It is therefore important to take into account the influence of vortex structures generated during the previous half period of the acoustic flow. This has been accomplished by using the single-panel method, in which also the vorticity generation at the nozzle edge is described more accurately (see section 2.2.5). In the method the vorticity convected away from the edge is represented by a point vortex at position z_v (ζ_v in the computational plane) with circulation Γ_v .

The initial position of this main vortex is given by the similarity solution for a force-free single vortex describing the flow past an infinite plate. A straight vortex segment of length S_z with a uniform vortex distribution γ_z in the physical (z -)plane and connected tangentially to the edge represents the vorticity generated during the current time step. The length of the segment and its circulation are given by equation (2.104) and (2.101), respectively. The flow in the proximity of the edge ($\zeta = 0$) is described by the following parameters

$$z = \left(\frac{\zeta}{D}\right)^{1/n} \quad (4.2)$$

$$\Phi(\zeta)|_{\zeta \rightarrow 0} = -iA\zeta + B\zeta^2 + \dots$$

$$\text{with } \begin{cases} n = 1/2; & A = -\frac{u_{ac}(t)}{2\pi} + \frac{\Gamma_v}{2\pi} \left(\frac{1}{\zeta_v} + \frac{1}{\zeta_v^*}\right) \\ D = 2\sqrt{\pi}; & B = -\frac{u_{ac}(t)}{4\pi} + \frac{i\Gamma_v}{4\pi} \left(\frac{1}{\zeta_v^2} - \frac{1}{\zeta_v^{*2}}\right) \end{cases}$$

which represents the flow past a semi-infinite plate.

Each time step a new edge segment is generated and subsequently amalgamated with

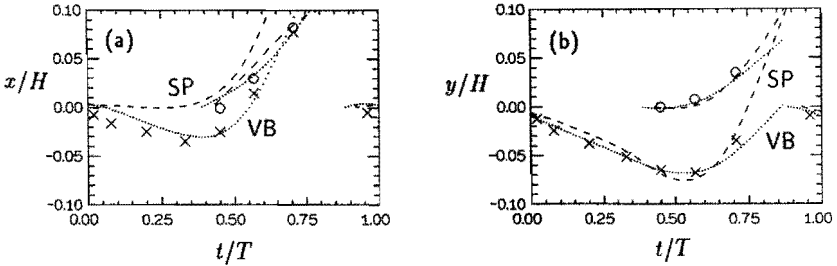


FIGURE 4.3: Position of the vortex center of the vortex sheet, formed at the sharp-edged nozzle during one period of acoustic oscillation. (a) axial coordinate (b) lateral coordinate $Str_{ac} = 2.54$ (---) single-panel method (SP) (.....) vortex-blob method (VB) ($\delta = 0.04$). Vortex core for first (\times) and second (\circ) vortex structure, obtained from flow visualization by Disselhorst (1978), presented in figure 4.1.

the main vortex to form a new main vortex with circulation equal to the total circulation of the system. The new main vortex is placed at the position determined by the requirement that the velocity potential far in- and outside the channel is not modified by the amalgamation. This amalgamation procedure was proposed by Disselhorst & van Wijngaarden (1978, 1980). It turns out that by using such an amalgamation procedure the new position of the main vortex is slightly different from the center of vorticity of the combination of point vortex and vortex segment.

The main vortex is then convected with the local flow velocity by a two-step Runge Kutta method. The time step is chosen such that the length of the edge segment remains a fraction ($\approx 1\%$) of the distance of the main vortex to the edge. At the moment in time that the circulation of the edge segment is opposite to the circulation of the main vortex, the circulation of the main vortex is frozen and a next main vortex is introduced starting at the edge.

Since the circulation of the edge segment depends on the factor A rather than on the acoustic velocity only (see equation (4.2)), the newly formed vortex generally appears before the acoustic velocity changes sign. The resulting phase shift between the period of vortex generation and the acoustic field depends on the distance of the main vortex to the edge after one period and as a result depends on the acoustic Strouhal number. This phase shift has indeed been observed in the experiments by Disselhorst (1978) and cannot be described by single-vortex methods, as discussed in the previous section.

In figure 4.2 the computed trajectory of the main vortex during one period of the acoustic field is compared with the results of the force-free single-vortex method. It is clear that the vortex trajectories of the first and second vortex are more accurately described by the single-panel method than by the single-vortex method. From the circulation of the main vortices, given in figure 4.4, it can be observed that new vortex structures are introduced at $t/T \approx 0.4$ and ≈ 0.9 , which corresponds to the experimental observation by Disselhorst (1978), see figure 4.1.

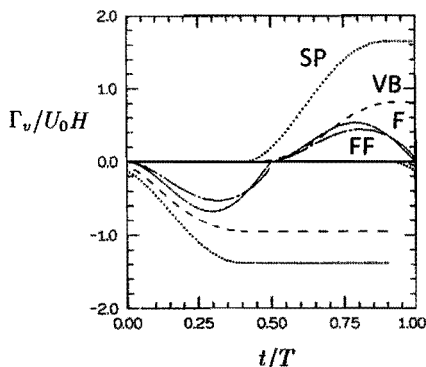


FIGURE 4.4: Variation with time of the circulation of the separate vortex structures generated at a sharp-edged nozzle during one period of the acoustic oscillation for different vortex methods. $Sr_{ac} = 2.54$ (—) free single-vortex method (F) (- · - · -) force-free single-vortex method (FF) (- - -) vortex-blob method (VB) ($\delta = 0.04$) (·····) single-panel method (SP).

In order to compare the results of the single-panel method with the results of the flow visualization experiments by Disselhorst (1978), the streaklines emanating from the nozzle edge have been calculated by introducing each time step a passive tracer particle at the nozzle edge, which subsequently is convected with the local flow velocity. The streakline obtained in this way can be compared directly with the visualization of the flow in the experiment, which shows a streakline of the flow. The difference with the streakline obtained by numerical simulation is that the real vortex layer is a streakline which contains vorticity. In view of the simplicity of the theory, the comparison in figure 4.1 of the flow visualization with the results of numerical simulation shows a remarkable resemblance.

A more quantitative comparison with the flow visualization is presented in figure 4.3. The computed position of the center of vorticity of each vortex structure is compared with the position of the vortex core, obtained from flow visualization during one period of the acoustic flow. For the axial position of the vortex center a small difference is found. Just like found with the single-panel method, the main vortex does not convect towards the channel (which is observed experimentally during the first half period of the acoustic field). For the lateral coordinate, the agreement between the computed position of the vortex center and the position seen in the experiment is satisfactory, both for the first and for the second vortex.

The acoustic energy absorption due to vortex formation obtained from the single-panel method by using the vortex sound theory by Howe (1975) has been presented in Peters & Hirschberg (1993).

Vortex-blob method

For the vortex-blob method the computational region is equal to that used for the starting flow out of a sharp-edged nozzle, shown in figure 3.21. At the pipe entrance a periodic flow is imposed with a flux equal to the total flux at the circular boundary of the computational region. The results of the vortex-blob method are included in figure 4.1.

The solution shown is the result during the fourth period of the acoustic field, when the solution has become periodic. The value of the desingularisation parameter $\delta = 0.04$ has been estimated from the value of the unsteady boundary layer thickness occurring in the experiment by Disselhorst (1978), $\delta \approx 4\sqrt{\nu/\omega/H}$. Variation of the value by a factor two up or down does not change the behavior of the vortex formation in a global sense. The size of the markers denoting the position of the vortex blobs is linearly related to the circulation of the vortex blob, while a \square and \triangle denote negative and positive circulation, respectively. At $t/T = 0.45$ the vortex sheet leaving the edge has positive circulation while in the vortex core the circulation is negative. At $t/T = 0.57$ the first part of the vortex sheet is unstable and a new vortex core is formed. Both vortex structures with circulation of opposite sense then convect away from the edge as a vortex pair (*dipole*).

The position of the center of vorticity for both structures is compared with the results of the single-vortex method and the single-panel method in figure 4.2 and is given as function of time in figure 4.3. The position of the center of vorticity obtained by using the vortex-blob method is in agreement with the estimated position of the vortex center from the flow visualization.

The circulation of both vortex structures is included in figure 4.4. The circulation of the vortex structures is overestimated by the single-panel method compared to the vortex-blob method. From the circulation it is clear that also for the vortex-blob method a new vortex starts to be formed before the acoustic velocity changes sign. The vorticity generated at the edge changes sign at $t/T \approx 0.4$ and ≈ 0.9 , which is in agreement with the single-panel method. For this value of the Strouhal number the total amount of vorticity generated during one period of oscillation is negative. This is due to the asymmetry of the flow induced by the vorticity shed at the other nozzle edge.

4.2.3 High Strouhal number

For high values of the acoustic Strouhal number the vortex layer remains even in closer vicinity of the edge of the nozzle, and is less influenced by the vorticity generated at the other edge than for Strouhal numbers of order unity. In this case the periodic flow out of a channel can be simplified to the periodic flow around an isolated semi-infinite plate. This generic problem was studied numerically by Disselhorst & van Wijngaarden (1980) using a multi-point vortex method. If the nondimensionalized coordinates and circulation are scaled by the acoustic Strouhal number according to $z^* = Sr_{ac}^{2/3}z/H$ and $\Gamma^* = Sr_{ac}^{1/3}\Gamma/\hat{u}_{ac}H$, the solution presented in scaled coordinates becomes independent of the Strouhal number.

The periodic flow past a wedge is simulated by the vortex-blob method using the geometry shown in figure 4.5. On the boundaries attached to the wedge a periodic flow is imposed, while the far field boundary corresponds to a streamline of the attached potential

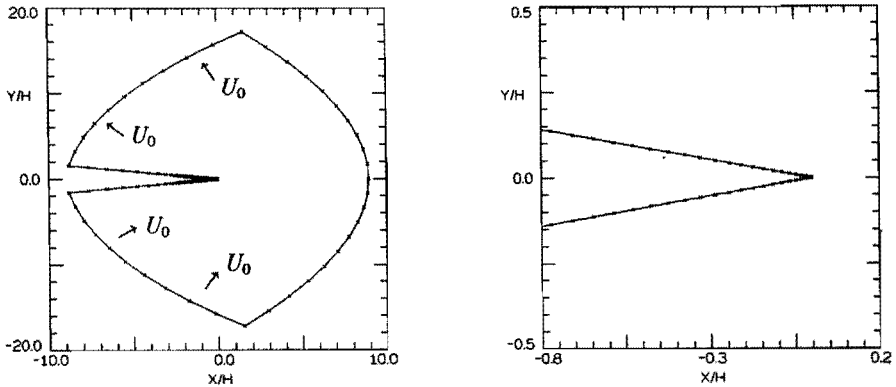


FIGURE 4.5: Panel distribution used for the periodic flow past a wedge with interior angle of 20° using the vortex-blob method.

flow, which is assumed to be unaffected by the flow separation near the edge. On this boundary, a zero normal velocity is imposed. The solution, obtained with the vortex-blob method with $\delta = 0.04$ after four periods of the acoustic field is presented in figure 4.6. For the periodic solution the vortices formed during the first and second period of the acoustic field form a dipole which leaves the edge in the direction along the centerline of the wedge. Finally, a von Kármán vortex street appears with alternating vortex structures of positive and negative circulation. The subsequently formed vortices have equal in strength, but opposite circulation.

The trajectory of the center of vorticity and the circulation, obtained with the vortex-blob method during four periods, are presented in figure 4.7 and figure 4.8, respectively. Initially, vortex trajectory is asymmetric and the circulation of the first and second vortex structure are not equal. This is due to the influence of the initial transients, i.e. the vortex structure formed when the flow is started is not influenced by vorticity generated earlier, which is the case for the vortex formation at later moments in time¹.

After four periods a symmetric solution is obtained for the vortex trajectory while the circulation of the vortex system becomes periodic. From the variation of the circulation with time, shown in figure 4.8, it is clear that for the periodic solution vorticity of opposite sign is generated before the acoustic velocity changes sign, namely at $t/T = 0.375$ and 0.875 of each cycle. This is because for the high Strouhal number case during one period the vorticity remains in the vicinity of the edge, i.e. influences strongly the generation of vorticity.

When the high-Strouhal number solution of the periodic flow around a wedge is compared with the solution for $Str_{ac} = 2.54$, obtained by taking the full geometry of the nozzle

¹During the first period of oscillation the amplitude of the acoustic velocity field was varied, in order to increase the convergence of the solution to a periodic flow solution.

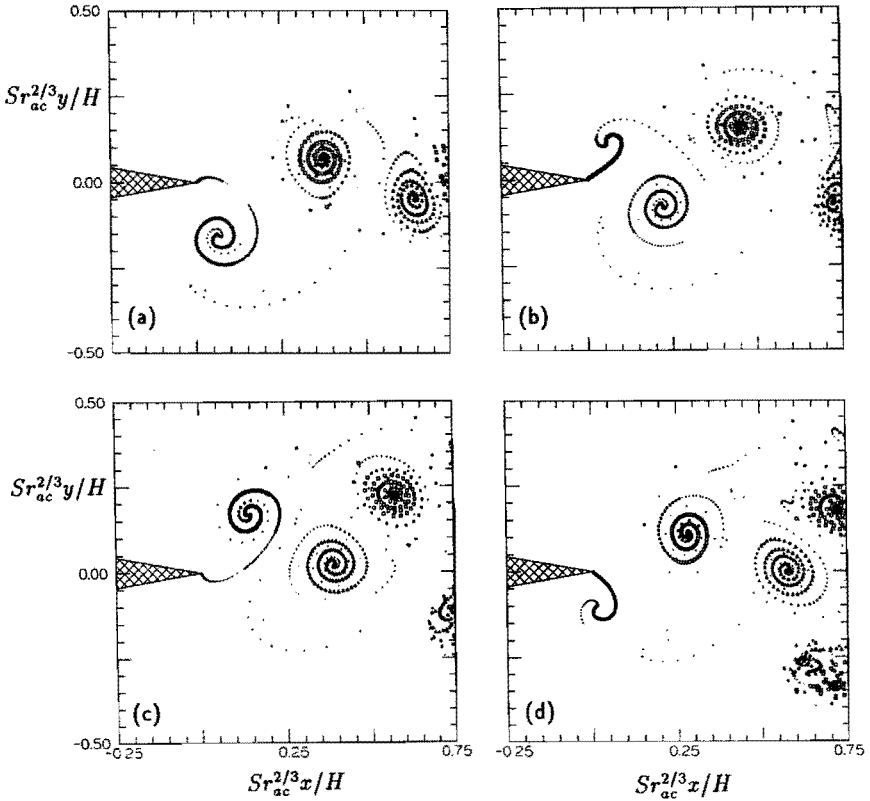


FIGURE 4.6: *Periodic flow past a semi-infinite wedge with interior angle 20° . Numerical simulation by the vortex-blob method ($\delta = 0.04$) (The periodic solution is shown in (a-d) at $t/T = 2.50, 2.75, 3.00$ and 3.25 , respectively)*

into account, it can be observed, that for $Sr_{ac} = 2.54$ the circulation of the vortex system and the trajectory of the center of vorticity of each vortex structure can be predicted reasonably well by the high-Strouhal number solution, i.e. the flow around an isolated wedge.

However, the **asymmetry** with respect to the edge in the vortex formation observed at in- and outflow and the difference in circulation, generated during in- and outflow can only be explained by taking the full geometry of the nozzle into account. For even lower values of the acoustic Strouhal number the asymmetry is more pronounced, since in such a case a free jet flow is observed at outflow and a jet with vena-contracta is formed at inflow.

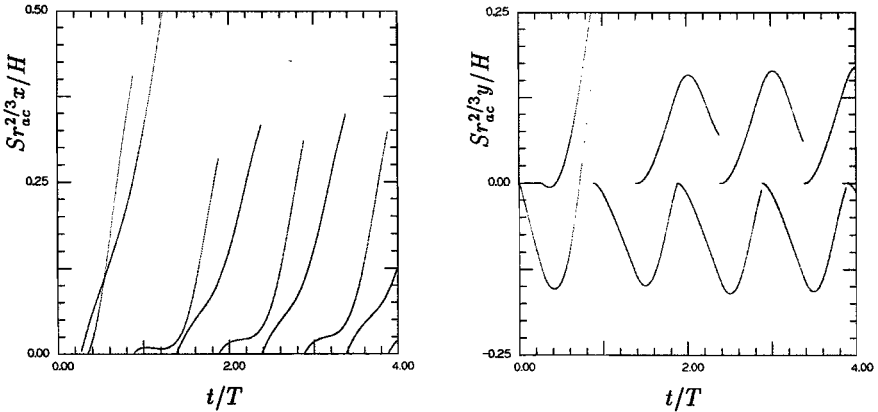


FIGURE 4.7: Trajectory of center of vorticity for vortex structures with positive (—) and negative (---) circulation, during four periods of the acoustic velocity field around a wedge. Vortex-blob method ($\delta = 0.04$). (a) scaled axial coordinate (b) scaled lateral coordinate.

4.3 PERIODIC FLOW IN A T-JUNCTION

4.3.1 Introduction

The vortex formation process induced in a channel with a T-junction by an imposed periodically varying acoustic velocity field superimposed on a main flow will be studied in this section. The present study is restricted to the case of a constant mean flow moving through the main pipe and a time-dependent acoustic field which is resonating between the closed side branch and the downstream part of the channel. The periodic flow in the T-junction can be produced in an experimental setup if the main pipe with a closed side branch terminates downstream of the T-junction as an open pipe (with sharp edges or with a horn). In this case the acoustic velocity field resonates between the open end and the closed side branch.

By connecting a horn to the channel exit the pipe system forms a resonator with a high quality factor. In such a configuration amplitudes of the acoustic field of $\hat{u}_{ac}/U_0 \approx 0.6$ can be reached. If the main pipe has a sharp-edged open exit the acoustic amplitude \hat{u}_{ac}/U_0 is typically of $\mathcal{O}(0.1)$.

The relevant nondimensionalized parameters of this problem are the nondimensionalized amplitude of the acoustic velocity field \hat{u}_{ac}/U_0 and the Strouhal number Hf/U_0 . For pipe systems in acoustic resonance the Strouhal number is of order one (Bruggeman (1987)). The amplitude of the acoustic field may vary from low amplitude ($\hat{u}_{ac}/U_0 \ll 1$) to moderate amplitude ($\hat{u}_{ac}/U_0 = \mathcal{O}(M)$) and high amplitude ($\hat{u}_{ac}/U_0 = \mathcal{O}(1)$). This sub-division was proposed by Bruggeman (1987).

The instability of the vortex sheet emanating from the upstream edge of the T-junction

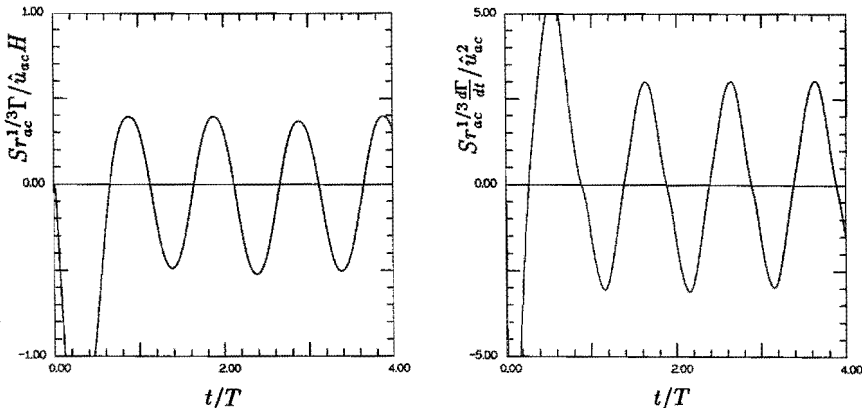


FIGURE 4.8: Circulation and its time-derivative for the vortex system during four periods of the acoustic velocity field around a wedge. Vortex-blob method ($\delta = 0.04$) (a) scaled circulation (b) scaled derivative of the circulation with respect to time.

is triggered by the acoustic field. The disturbance is amplified while it is convected downstream and a coherent vortex structure is formed, which at low and moderate amplitudes hits the downstream edge. At low and moderate amplitudes Bruggeman (1984) observed that a new vortex structure is formed at the upstream edge each time the acoustic pressure at the end of the closed side branch attains its minimum value. This corresponds with a change in the direction of the acoustic velocity field; the direction of the acoustic velocity changes from out of the side branch to into the side branch.

However, for the high-amplitude case, i.e. $\hat{u}_{ac}/U_0 = \mathcal{O}(1)$, it will be shown that the point in time that a vortex structure appears will shift to an earlier point in time, in the same way as observed in the previous section for the periodic flow in a sharp-edged nozzle.

In the single-vortex and two-vortex method the time at which the formation of a new vortex structure starts is an input parameter for the numerical analysis which must be determined experimentally or estimated on theoretical grounds. In the vortex-sheet and vortex-blob method the vortex sheet has retained its inherent tendency Kelvin-Helmholtz instability which will induce the formation of a new vortex structure. As a result these latter two methods do not require the specification of an input parameter to reach a periodic solution for a given value of the Strouhal number and of the acoustic amplitude.

In section 4.3.2 a visualization of the periodic flow in a T-junction will be presented for three different amplitudes, corresponding approximately with the low, moderate and high amplitude cases. In section 4.3.3 different vortex methods, described in chapter 2, will be used to describe the periodic flow in a T-junction for the high-amplitude case. The results of the periodic solution obtained with different methods will be compared.

In section 4.3.4 a comparison of the periodic flow in a T-junction for the solution obtained with the vortex-blob method and Laser Doppler velocity measurements of Bruggeman (1987) will be presented.

4.3.2 Flow visualization

The periodic formation of a vortex structure is visualized using the experimental setup shown in figure 4.9. The experimental setup differs from the setup for the starting flow experiment in a T-junction in the scale of the experiment which is now somewhat larger, with a side branch width $H = 0.06\text{m}$. Since the flow is periodic, a stroboscopic observation

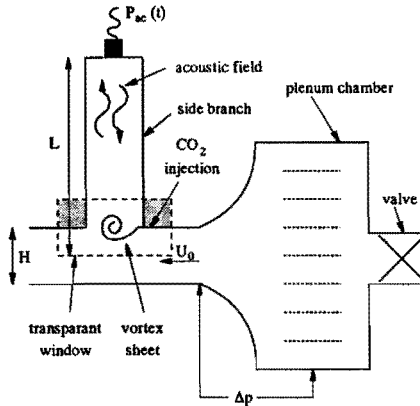


FIGURE 4.9: Experimental setup used for the flow visualization of periodic vortex formation in a T-junction by a schlieren method. (square cross section $H = 0.06\text{ m}$)

of the flow becomes possible with by a video recording. The nanolite light source is made to generate a light pulse each time that the acoustic pressure at the end of the closed side branch exceeds a certain value. An additional delay between the trigger signal and the nanolite pulse can be introduced in order to obtain a visualization at a different moment in the oscillation period.

The difference in refractive index necessary for the schlieren technique is obtained by injecting CO_2 near the upstream edge. In some experiments instead of CO_2 a mixture of 50% Ar and 50% Ne has been used. This mixture has a density and speed of sound close to that of air, however the refractive index is different. Therefore, the acoustic behavior of the pipe system is not changed by introducing this mixture in the flow field.

The main flow is produced by air flowing from a settling chamber with square cross section, width 0.35 m, into the pipe through a smooth contraction, placed one side branch width ahead of the T-junction. This keeps the upstream boundary layer as thin as possible. The magnitude of the velocity of the main flow is calculated from the measured pressure difference across the contraction, using the stationary Bernoulli equation. The amplitude of the acoustic velocity field at the junction is estimated from the acoustic pressure amplitude, measured at the end of the closed side branch by assuming a standing wave inside the side branch, i.e. leading to $\hat{u}_{ac} = \hat{p}_{ac}/\rho_0 c_0$. The maximum value of the main flow that can be reached is $U_0 \approx 50\text{ m/s}$. The experiments have been performed at atmospheric pressure

and room temperature ($T_0 = 295K$).

In figures 4.10, 4.11 and 4.12 the results of the flow visualization are shown for a low-amplitude case $\hat{u}_{ac}/U_0 = 0.08$ with $Sr = 0.44$, a moderate-amplitude case $\hat{u}_{ac}/U_0 = 0.23$ with $Sr = 0.39$ and for a high-amplitude case $\hat{u}_{ac}/U_0 = 0.62$ with $Sr = 0.29$, respectively. The acoustic pressure, measured at the end of the closed side branch for the various experiments is presented in figure 4.13. The time indicated in the flow visualization is the time relative to the time $0.25 T$ before the pressure measured at the end of the closed side branch is zero and is going from a negative to a positive value. For low amplitudes of the acoustic field, $t = 0$ corresponds to a minimum value of the acoustic pressure at the end of the side branch. However, since for high acoustic amplitudes the position of the minimum in acoustic pressure is strongly influenced by the presence of strong higher harmonics (see figure 4.13), $t = 0$ corresponds to the minimum value of the fundamental harmonic of the acoustic pressure in this case.

For the lowest-amplitude case, the shear layer is only slightly disturbed by the acoustic field and only a small coherent vortex structure is formed, which convects at about a constant speed $U_c \approx 0.4 U_0$ from the upstream to the downstream edge of the T-junction. The pulsation amplitude is not very stable. The pressure pulsation amplitude measured at the end of the side branch is fluctuating approximately 10% in value.

For the moderate-amplitude case a more pronounced spiral vortical structure is formed. Furthermore, the vortex layer bends into the side branch during the first half period, when the acoustic flow is directed into the side branch, and bends back into the main pipe during the second half period when the acoustic field is directed out of the side branch. For low and moderate amplitudes the formation of a new vortex structure starts when the pressure attains its minimum ($t = 0$), which was also observed by Bruggeman (1987).

However, for the high-amplitude case a new vortex structure appears at an earlier instant, namely at the time the acoustic pressure changes from a positive to a negative value. It will be shown that this is due to the inherent instability of the shear layer. For the high-amplitude case the vorticity distribution of the shear layer is strongly influenced by the acoustic velocity field. At $t = 0.75T$ the acoustic velocity and the velocity induced by the vorticity distribution in the T-junction cancel exactly the velocity around the edge due to the main flow U_0 . At this moment we expect a stagnation point at the edge. The vortex layer is leaving the edge along its bisector and no vorticity is generated at the sharp edge. Due to the high amplitude of the acoustic field the vortex layer convects deep into the side branch during the first half-period of the acoustic oscillation. During the second half period of the acoustic oscillation the vorticity is convected into to main pipe.

The Strouhal number at which the system resonates is found to decrease with the maximum amplitude, which reflects the low convection velocity of the vortex when it is convected deep into the side branch. Furthermore it is observed that at the downstream edge flow separation is negligible, even for the high-amplitude case. For an increasing acoustic amplitude the acoustic pressure signal measured at the end of the side branch shown, shown in figure 4.13, starts to contain more uneven higher harmonics. A list of amplitudes of the harmonics is given in table 4.1.

For low and moderate amplitudes the higher harmonics have an amplitude of at most 4% of the amplitude of the fundamental mode. For the high-amplitude case a value of 9%

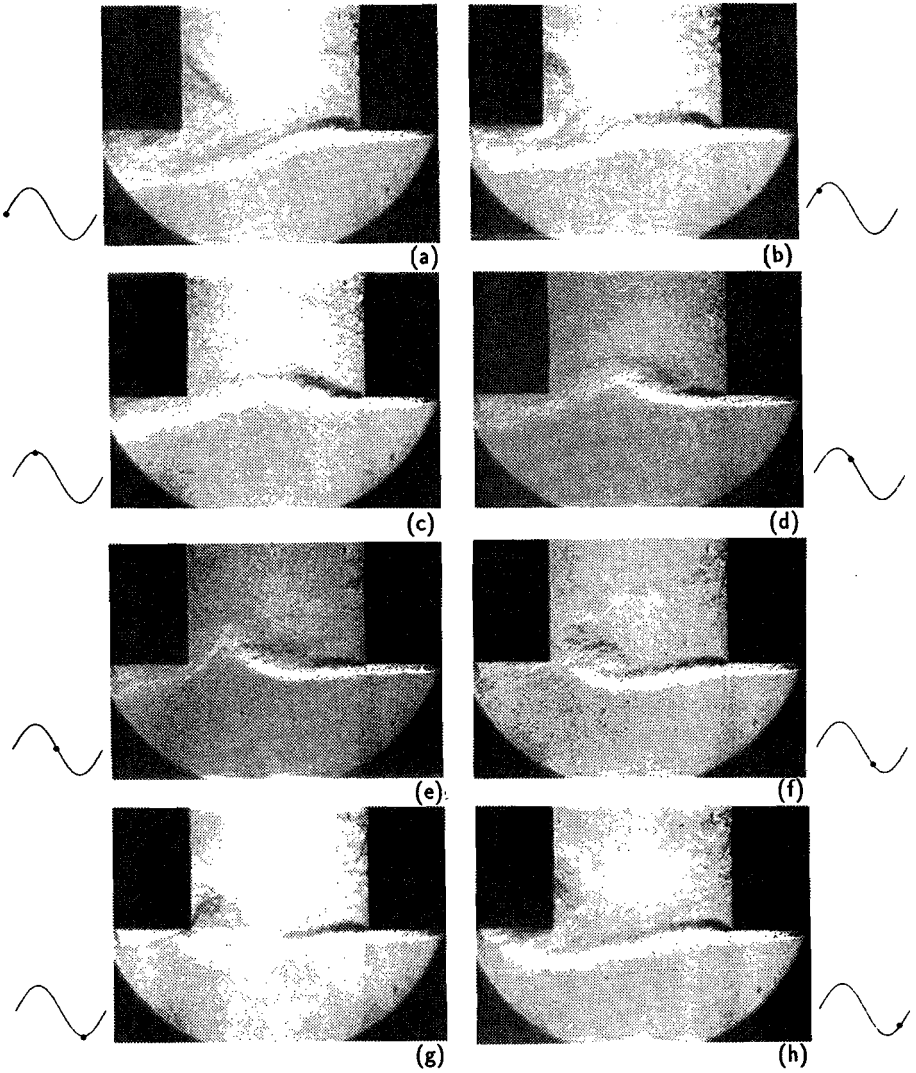


FIGURE 4.10: Flow visualization of periodic vortex formation in a T-junction for a low amplitude acoustic field, $\hat{u}_{ac}/U_0 = 0.08$ with $Sr = 0.44$, $U_0 = 29.3$ m/s, $f = 217.6$ Hz. (a) - (h) are at $t/T = 0.03, 0.12, 0.23, 0.33, 0.47, 0.61, 0.75$, and 0.92 , respectively.

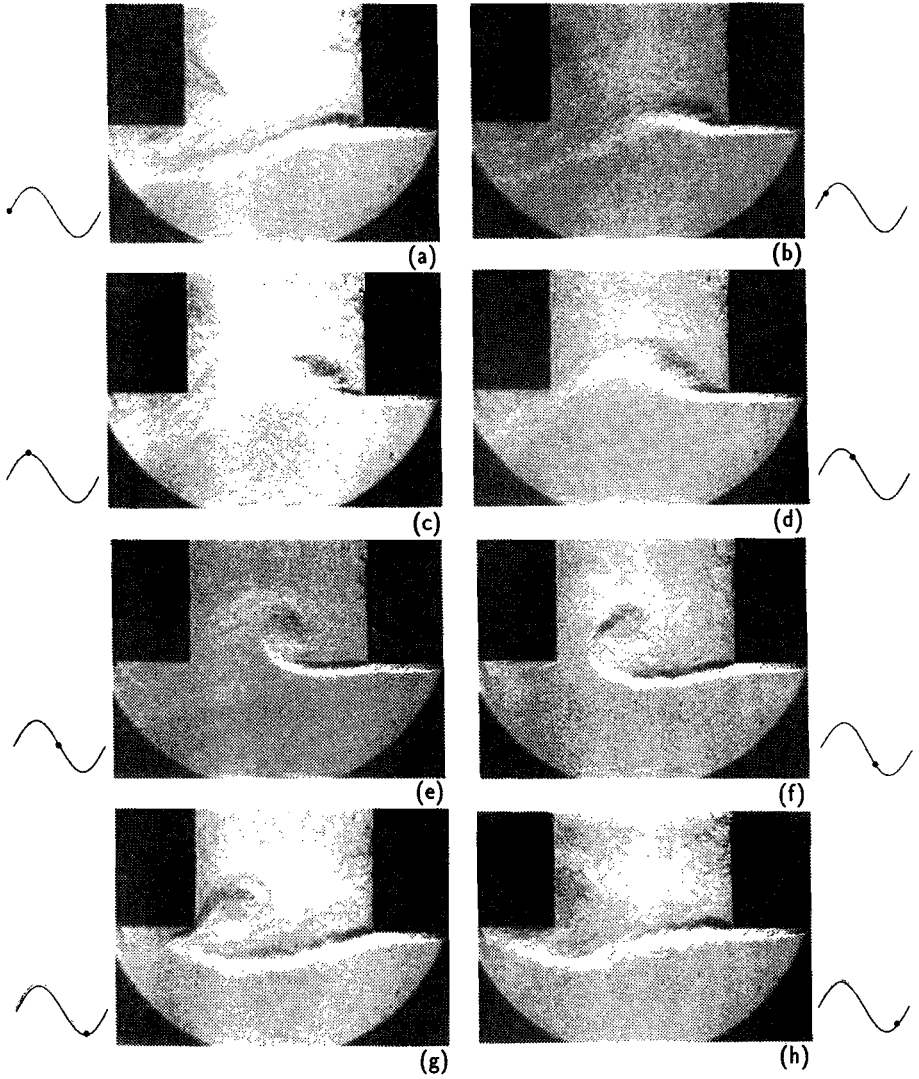


FIGURE 4.11: Flow visualization of periodic vortex formation in a T-junction for a moderate amplitude acoustic field, $\hat{u}_{ac}/U_0 = 0.23$ with $Sr = 0.39$, $U_0 = 34.1$ m/s, $f = 218.5$ Hz. (a) - (h) are at $t/T = -0.01, 0.12, 0.24, 0.34, 0.49, 0.60, 0.75,$ and 0.88 , respectively.

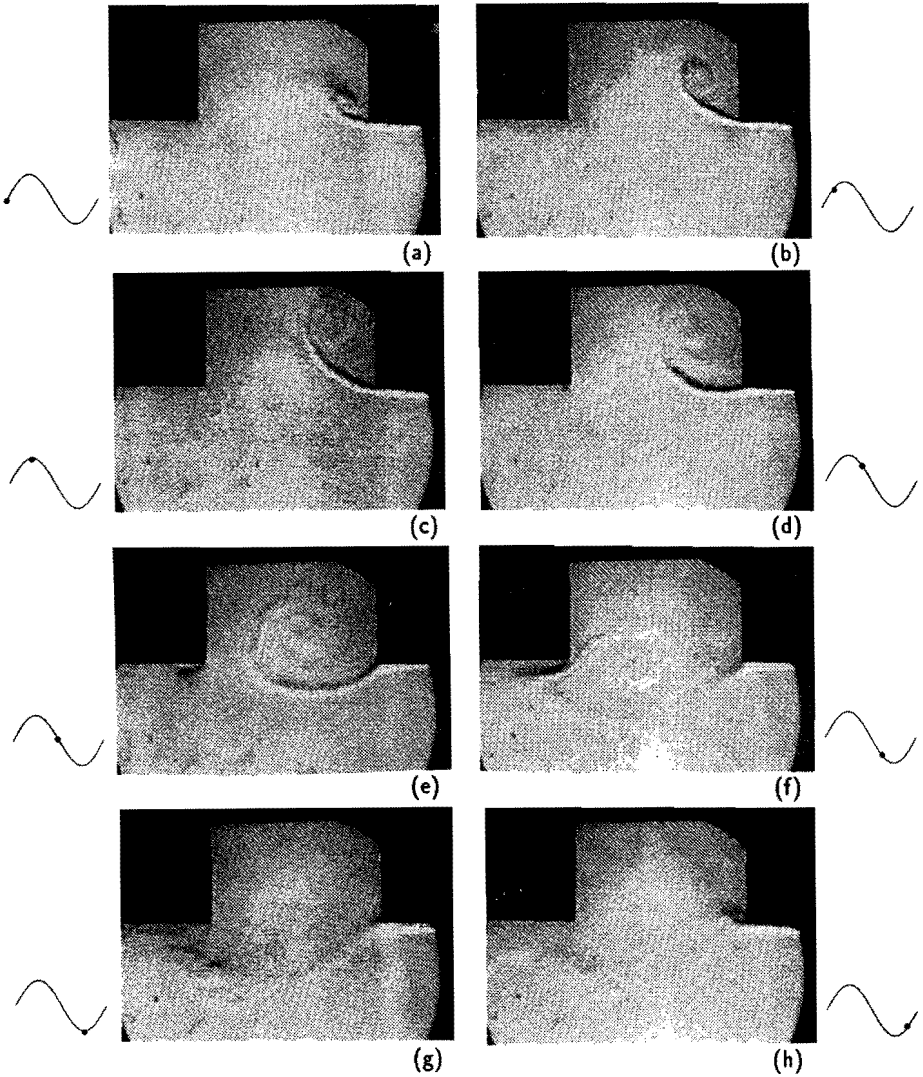


FIGURE 4.12: Flow visualization of periodic vortex formation in a T-junction for a high amplitude acoustic field, $\hat{u}_{ac}/U_0 = 0.62$ with $Sr = 0.29$, $U_0 = 45.9$ m/s, $f = 222.5$ Hz. (a) - (h) are at $t/T = 0.07, 0.19, 0.32, 0.44, 0.56, 0.69, 0.82,$ and 0.94 , respectively.

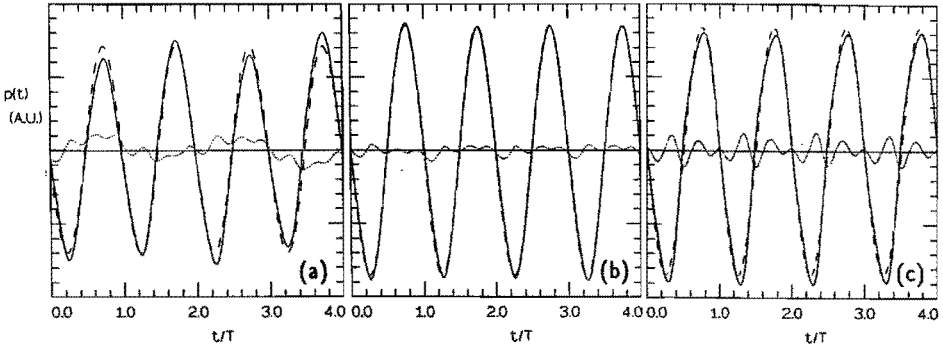


FIGURE 4.13: Comparison of acoustic pressure signal measured at the end of the closed side branch with the fundamental harmonic in the pressure signal. (—) pressure signal (---) fundamental harmonic (·····) difference between pressure signal and fundamental harmonic.

- (a) low-amplitude case $\hat{u}_{ac}/U_0 = 0.08$ with $Sr = 0.44$, see figure 4.10
 (b) moderate-amplitude case $\hat{u}_{ac}/U_0 = 0.23$ with $Sr = 0.39$, see figure 4.11
 (c) high-amplitude case $\hat{u}_{ac}/U_0 = 0.62$ with $Sr = 0.29$, see figure 4.12.

\hat{u}_{ac}/U_0	Sr	M	$f_1(\text{Hz})$	A_2	φ_2	A_3	φ_3	A_4	φ_4
0.08	0.44	0.09	217.6	0.028	-197°	0.040	63°	0.003	-103°
0.23	0.39	0.10	218.5	0.024	-67°	0.026	-53°	0.002	-87°
0.62	0.29	0.13	222.5	0.059	-56°	0.089	-75°	0.007	-133°

TABLE 4.1: Magnitude A_j and phase shift φ_j of higher harmonics relative to the fundamental harmonic contained in the pressure signals for the periodic flow in a T-junction, presented in figure 4.13.

is reached. For the high-amplitude case the presence of strong higher harmonics causes a significant shift in time ($\approx 0.06 T$) of the position of the minimum of the acoustic pressure. Therefore, for a proper comparison with experimental data of the results of the numerical simulation of an harmonically varying flow, the time has been determined relative to the zero-crossing of the pressure, which is not strongly influenced by the higher harmonics.

4.3.3 Numerical simulation at high acoustic amplitudes

For the case of a high acoustic amplitude, shown in figure 4.12, the flow predicted by different vortex methods will be compared to the flow visualization. In the comparison of the results of different vortex methods for the impulsively starting flow in chapter 3 it was shown that the single-vortex methods cannot describe the vortical flow in a T-junction.

Therefore the two-vortex method, described in section 2.2.5, will be used for the numerical simulation of the periodic vortex formation in a T-junction. The results of the simple method will be compared with results obtained by the more elaborate methods, i.e. the vortex-sheet method and the vortex-blob method.

The complex velocity potential due to the irrotational main flow and the acoustic flow is for the periodic flow problem given in nondimensionalised quantities by

$$\Phi_0(\zeta) = \frac{1}{\pi} \left[\ln \left(\frac{\zeta + i/\sqrt{5}}{\zeta - i/\sqrt{5}} \right) + \hat{u}_{ac} \sin(2\pi Sr t) \ln(\zeta - i/\sqrt{5}) \right] \quad (4.3)$$

The main flow is mapped to a source of strength 1 in $\zeta = -i/\sqrt{5}$ and a source of strength -1 in $\zeta = i/\sqrt{5}$. The acoustic source of strength $u_{ac}(t)/U_0$ is positioned at $\zeta = i/\sqrt{5}$ in the computational plane, i.e. far downstream in the main pipe. The acoustic source in the side branch is mapped to infinity in the computational plane, so that it does not appear in above expression. The acoustic velocity field contributes to the potential flow around the edge as described by equation (3.31) and (3.32). The parameters A and B are in presence of an acoustic velocity field slightly modified.

Two-vortex method

In the two-vortex method the main vortex, representing the center of vorticity of the vortex sheet, and the edge vortex, describing the generation of vorticity, are amalgamated each time step by a procedure in which the difference in velocity potential between the side branch and the downstream part of the main pipe is conserved. A new main vortex is formed each time the acoustic velocity changes sign, i.e. changes from going out of to going into the side branch. The results of the method are presented in figure 4.14, again in the form of the streakline emanating from the upstream edge.

The differences between the results of the two-vortex method and those of the flow visualization are caused by the simplified description of the vortex sheet and the uncertainty in the moment of the formation of a new vortical structure. In the present application of the two-vortex method it has been assumed that a new vortex structure is formed at $t = 0$. However, for this high acoustic amplitude the flow visualization indicates that a new vortex starts approximately $0.2 T$ earlier. From figure 4.15 it appears, that this corresponds approximately to the point where $d\Gamma/dt = 0$, with $d^2\Gamma/dt^2 > 0$. This criterion for the formation of a new vortex structure has been proposed by Graham (1977).

The influence of this empirically determined phase shift of the start of a new vortex on the results of the two-vortex method is studied in figure 4.15. This figure shows the trajectory of the center of vorticity during one period of the periodic solution. The time of formation of a new vortex structure appears to have a strong influence on the trajectory of the center of vorticity during the first half period of the oscillation. During the second half period of oscillation the influence is small.

Vortex-sheet method

The numerical simulation of the periodic flow at high acoustic amplitude in a T-junction, obtained with the vortex-sheet method are presented in figure 4.16. The parameters used to

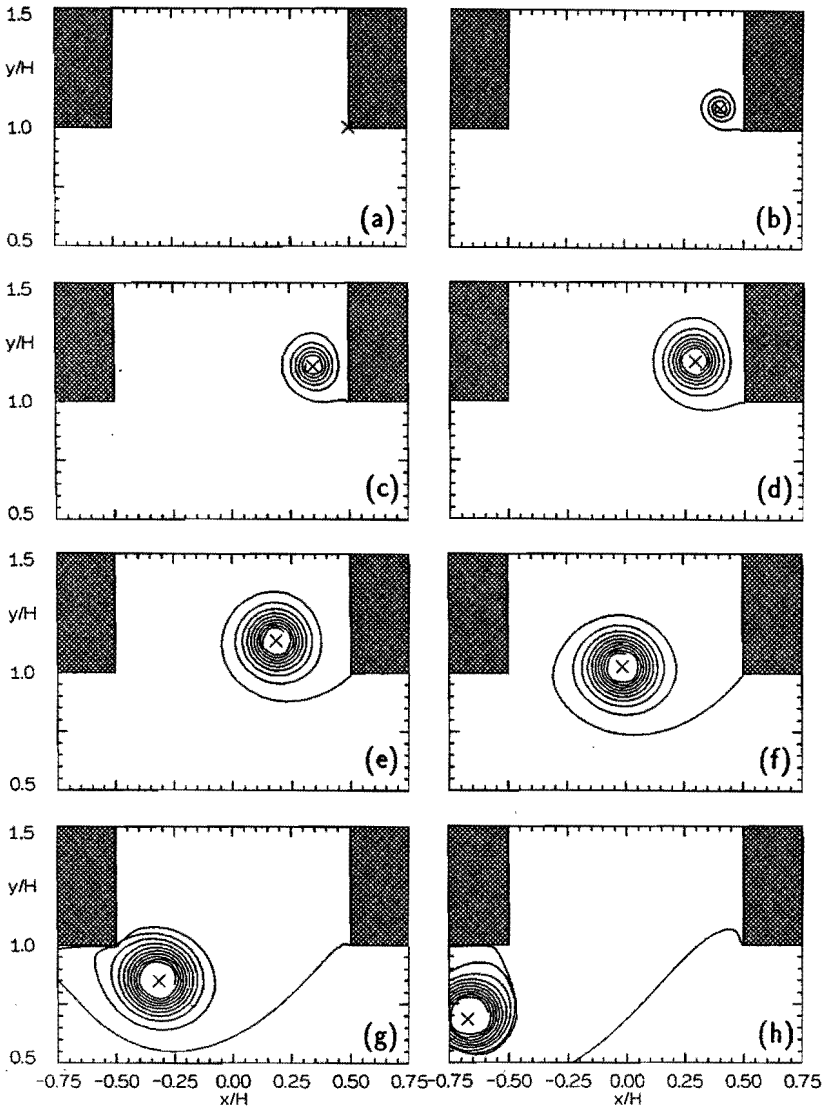


FIGURE 4.14: Numerical simulation of periodic vortex formation in a T-junction. High-amplitude acoustic field, $\hat{u}_{ac}/U_0 = 0.62$ with $Sr = 0.29$. Results of the two-vortex method with a streakline emanating from the upstream edge. A new vortex is generated each time the pressure is at minimum ($t = 0$). (a) - (h) are at $t/T = n/8$, with $n = 0 \dots 7$, respectively.

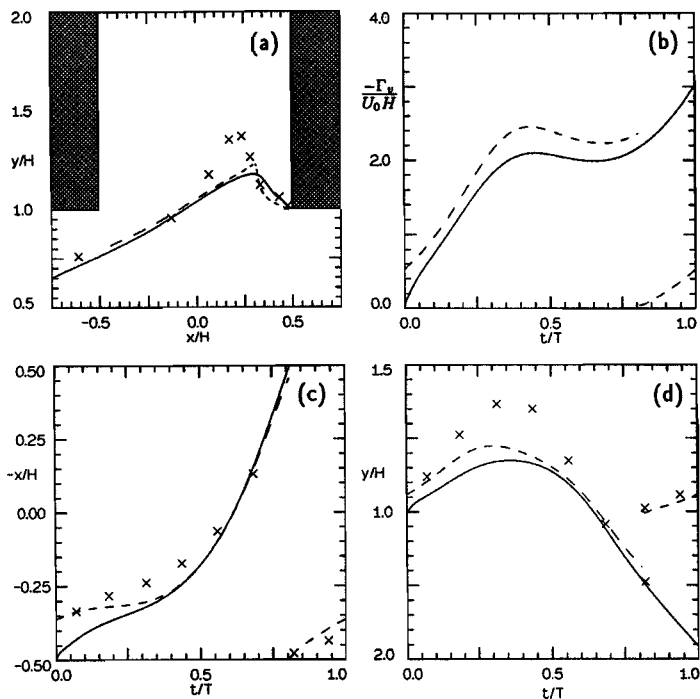


FIGURE 4.15: Periodic solution of the trajectory of the center of vorticity during one period of the acoustic field in a T-junction. High-amplitude acoustic field, $\hat{u}_{ac}/U_0 = 0.62$ with $Sr = 0.29$. Results of the two-vortex method. (—) Start of vortex formation at $t = 0$ (---) Start of vortex formation at $t = -0.2T$ (x) point vortex position estimated from flow visualization, shown in figure 4.12. (a) vortex trajectory (z_v) (b) circulation Γ_v (c) x -coordinate of center of vorticity (d) y -coordinate of center of vorticity.

obtain the periodic solution are given in table 4.2. Initially, in the first period of oscillation, the vortex is formed at $t = 0$, the start of the computation, but due to the instability of the vortex sheet, a second center of roll-up is formed before the acoustic velocity changes sign. This agrees with the flow visualization of figure 4.12.

All circulation contained in the part of the vortex sheet connecting the first center of roll-up to the newly formed vortex core is convected towards the centers of roll-up and at $t/T = 0.125$ this part of the vortex sheet contains hardly any circulation. The coordinates of the center of vorticity of the vortex sheet, and its circulation during the first three periods of oscillation are given in figure 4.17. In this figure, also the estimated

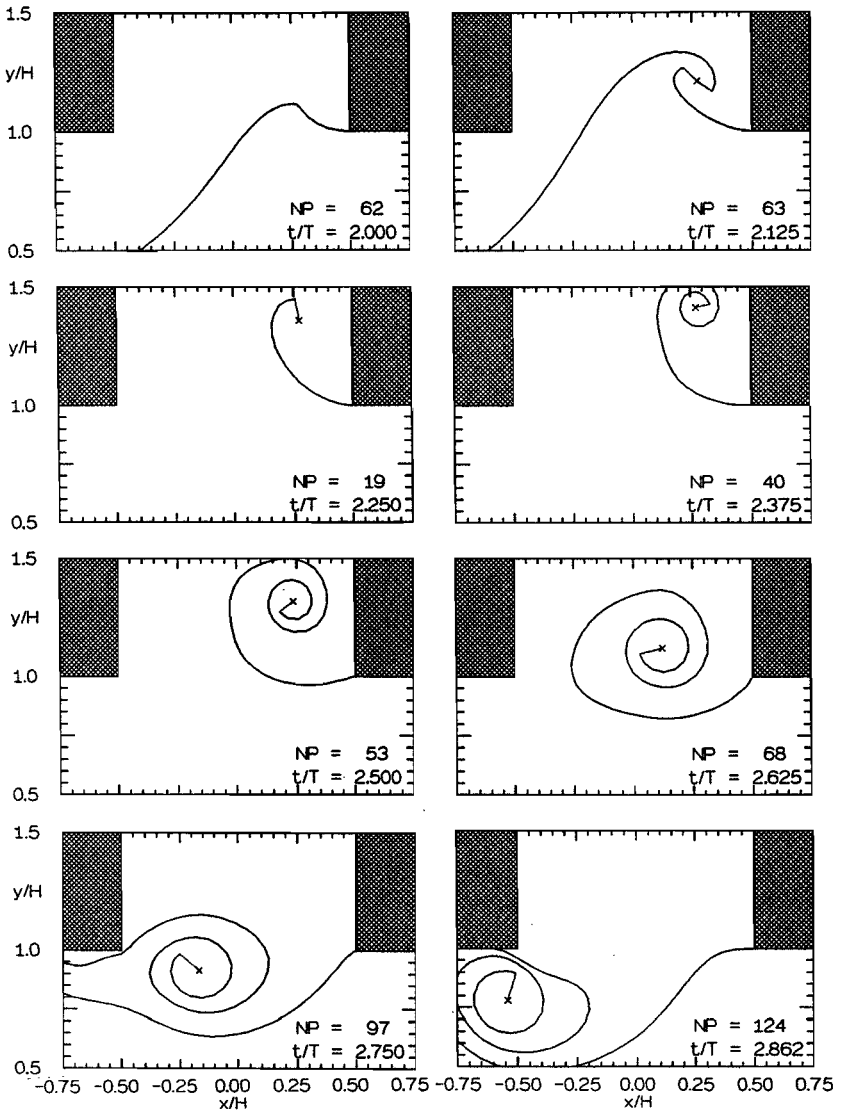


FIGURE 4.16: Numerical simulation of periodic vortex formation in a T-junction. High-amplitude acoustic field, $\hat{u}_{ac}/U_0 = 0.62$ with $Sr = 0.29$. Results of the vortex-sheet method ($\Delta s_{max} = 0.10$). The main flow and acoustic flow have been started at $t = 0$. (NP denotes the number of particles used to describe the system state).

TIME STEP NR.	t/T	\mathcal{F}	Δs_{max}	$\Delta \theta_{max}$	θ_0
1 - 350	0.007	0.2	0.01	20°	225°
351 - 600	0.019	0.2	0.04	20°	360°
601 - 1100	0.084	0.3	0.05	20°	540°
1101 - 2100	0.436	0.2	0.10	20°	900°
2101 - 3100	0.753	0.1	0.10	20°	900°
3101 - 3465	0.876	0.2	0.10	15°	900°
<i>split segment</i>					
3466 - 3470	0.877	0.2	0.10	20°	900°
3471 - 4220	1.167	0.2	0.10	20°	360°
4221 - 4470	1.241	0.2	0.10	20°	270°
<i>remove first segment</i>					
4471 - 5470	1.700	0.2	0.10	20°	900°
5471 - 5970	1.797	0.2	0.10	20°	900°
5971 - 6220	1.917	0.2	0.10	40°	900°
6221 - 6320	1.944	0.2	0.10	20°	900°
6321 - 6570	2.013	0.2	0.10	10°	45°
6570 - 6820	2.023	0.2	0.10	10°	5°
<i>split segment</i>					
6821 - 6825	2.024	0.2	0.10	20°	900°
6826 - 7575	2.236	0.2	0.10	20°	270°
<i>remove first segment</i>					
7576 - 8575	2.716	0.2	0.10	30°	900°
8576 - 8825	2.861	0.2	0.10	30°	900°
8826 - 8925	2.941	0.1	0.10	20°	45°
8926 - 9175	3.041	0.2	0.10	15°	45°

TABLE 4.2: Parameters used for the simulation of the periodic flow in a T-junction with the vortex-sheet method, see figure 4.16.

position of the vortex core obtained from the flow visualization shown in figure 4.12 is given. There is a large difference between the results of the first period of oscillation and the results of the periodic solution. This difference is due to the different moment in time of the start of the formation of a new vortex.

The vortex-sheet method obtains a periodic solution within three periods of oscillation, and a new vortex structure is formed at $t/T \approx 0.8$ and again at $t \approx n + 0.8 T$, with n an integer number. In the two-vortex method the moment of generation of a new vortex structure has been imposed to be at $t/T = (n + 0.8)$.

In figure 4.18 the geometry, the vortex distribution and the curvature of the vortex sheet are given for two different points in time: at $t/T = 2.74$ when the vortex sheet hits the downstream edge, and at $t/T = 2.02$ when a new center of roll-up appears near the upstream edge. The vortex distribution for the periodic solution at $t/T = 2.74$ is comparable with the vortex distribution for an impulsively started flow at $tU_0/H = 5$ in figure 3.13. A peak value of the vortex distribution and the curvature occurs at the

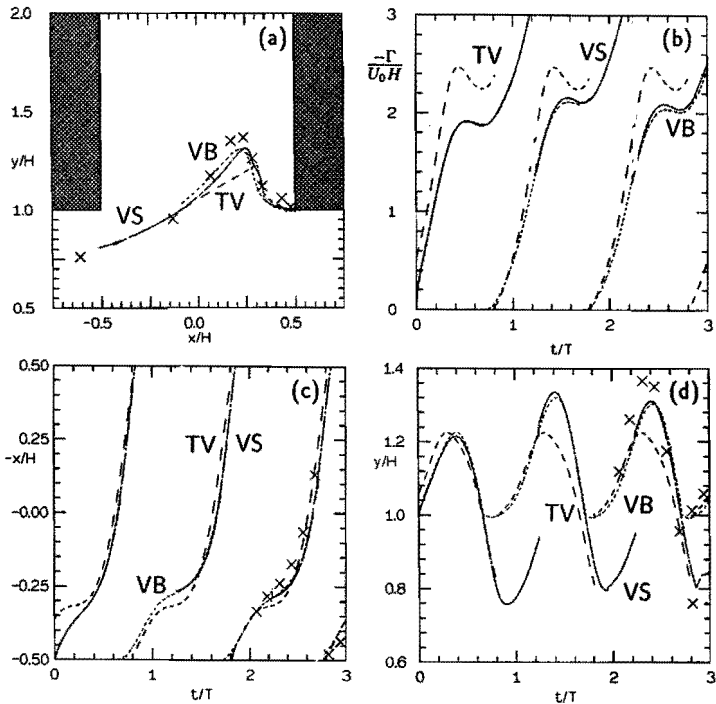


FIGURE 4.17: Position of the center of vorticity and circulation of the vortex sheet during three periods of the acoustic field in a T-junction. High amplitude acoustic field, $\hat{u}_{ac}/U_0 = 0.62$ with $Sr = 0.29$. (—) vortex-sheet method (VS), see figure 4.16; (⋯⋯) vortex-blob method (VB), see figure 4.19; (---) two-vortex method (TV), see figure 4.14 (vortex is formed at $t/T = -0.2$); (x) position of vortex core estimated from flow visualization shown in figure 4.12.

points on the sheet close to the downstream edge. However, for the present case the vortex distribution is negative on part of the vortex sheet, while it is always positive in the case of the starting flow. Furthermore, for the high-amplitude case the circulation is mainly concentrated in the last part of the rolled-up vortex sheet, while in absence of an acoustic field the circulation is more evenly distributed along the sheet.

At $t/T = 2.02$, nearly all the circulation is concentrated in the point vortex at the end of the vortex sheet, and the sheet hardly contains any circulation, except at the beginning of the sheet where a new vortex is formed. In this new center of roll-up the curvature of the sheet shows a singular behavior.

That most of the circulation is contained within the point vortex is partly due to the

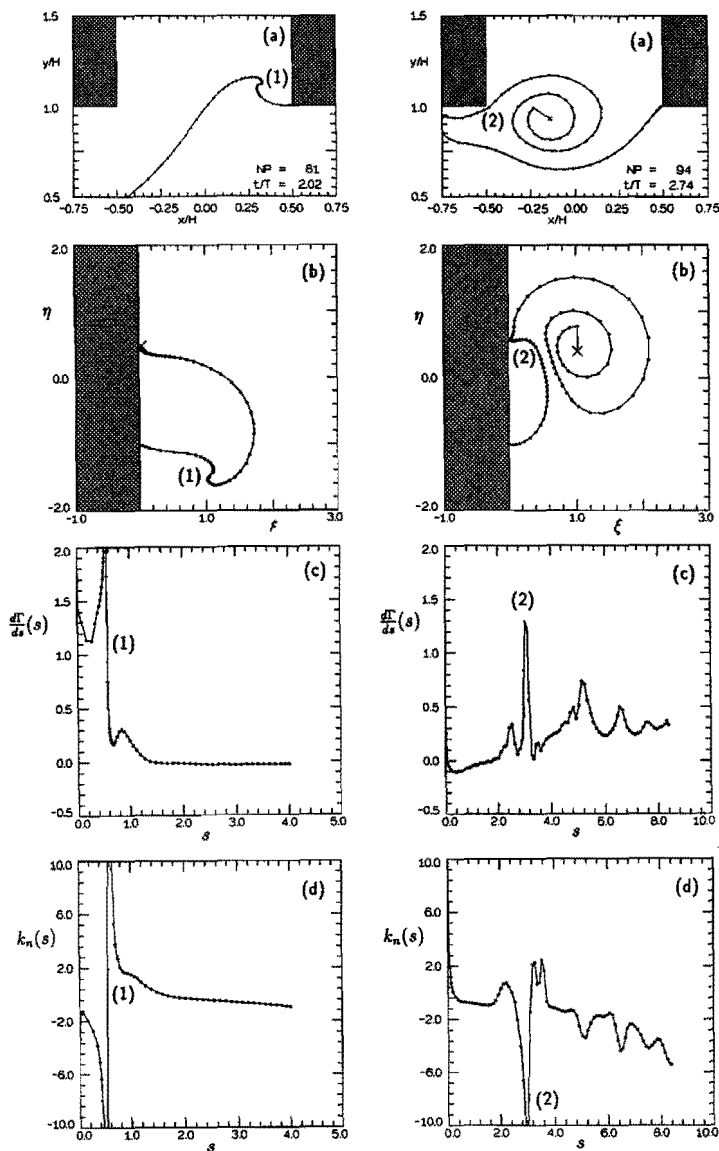


FIGURE 4.18: Details of the results obtained with the vortex-sheet method, presented in figure 4.16, at $t/T = 2.02$ and $t/T = 2.74$. (a) solution in physical plane (\circ denote edge points) (b) solution in the computational plane (c) vortex distribution $d\Gamma/ds = -\gamma(s)$ (d) curvature $k_n(s)$

vortex sheet being cut-off in order to avoid problems when the sheet approaches the point $\zeta = i/\sqrt{5}$ in the computational plane too closely. This point corresponds to a point far inside the downstream part of the main pipe.

Vortex-blob method

Finally, the vortex formation process in a T-junction has been simulated by the vortex-blob method. The main flow and the acoustic flow have been started at $t = 0$ and a vortex blob is generated each time step. The periodic solution obtained for a value of the desingularisation parameter $\delta = 0.10$ is shown in figure 4.19. The value of δ is chosen on the basis of the estimated average momentum thickness of the vortex layer in the T-junction as measured in absence of pulsations by Bruggeman (1987). Changing this value by a factor two up or down does not change the overall values as for example the position of the center of vorticity and the circulation. However, the roll-up of the newly formed vortex close to the upstream edge is influenced by the value of δ . Since the shear layer thickness in the experiment is initially smaller than the average value, the vortex sheet rolls-up more slowly in the results of the vortex-blob method than in the flow visualization.

In the vortex-sheet method a curvature-dependent panel distribution scheme is used, which decreases the panel size at parts of the sheet with high curvature. As a result the roll-up of the first part of the sheet is more accurately described by the vortex-sheet method than by the vortex-blob method, as can be observed from a comparison of figure 4.19 with figure 4.16. In the periodic solution, obtained within three periods, a new vortex is formed at $t/T \approx (n + 0.8)$, where n is an integer number, which again agrees with the results of the vortex-sheet method and the flow visualization shown in figure 4.12.

The position of the center of vorticity and the circulation obtained by the vortex-blob method are included in figure 4.17. The results of the simple two-vortex method agree with those of the vortex-sheet method and the vortex-blob method for the periodic solution if in the two-vortex method the moment of vortex formation is adjusted with the experimentally observed or by the vortex-sheet and vortex-blob method predicted phase shift ($\Delta t \approx -0.2T$). The results of the two-vortex method agree with those of the vortex-sheet and vortex-blob method for the high-amplitude case because the main part of the circulation contained in the vortex system is concentrated around the vortex core, and a two-vortex method is a fair approximation for such a vortex distribution.

4.3.4 Moderate acoustic amplitude

Bruggeman (1987) studied experimentally the periodic vortex formation in a setup with two side branches. In the experiment the side branches have a length of $0.645m$ and are placed at a distance of $1.26 m$ apart. This configuration forms a resonator with the acoustic field resonating between the two side branches with few losses due to radiation and friction. The maximum amplitude of the resonance was obtained for a main flow velocity of $U_0 = 20.5 m/s$ and for a Strouhal number of $Sr = 0.38$. Bruggeman (1987) obtained a maximum acoustic amplitude $\hat{u}_{ac}/U_0 = 0.17$. From the visualization of the flow the trajectory of the vortex core was determined during one period of the acoustic oscillation. Also Laser Doppler Anemometry (L.D.A.) velocity measurements were performed and the

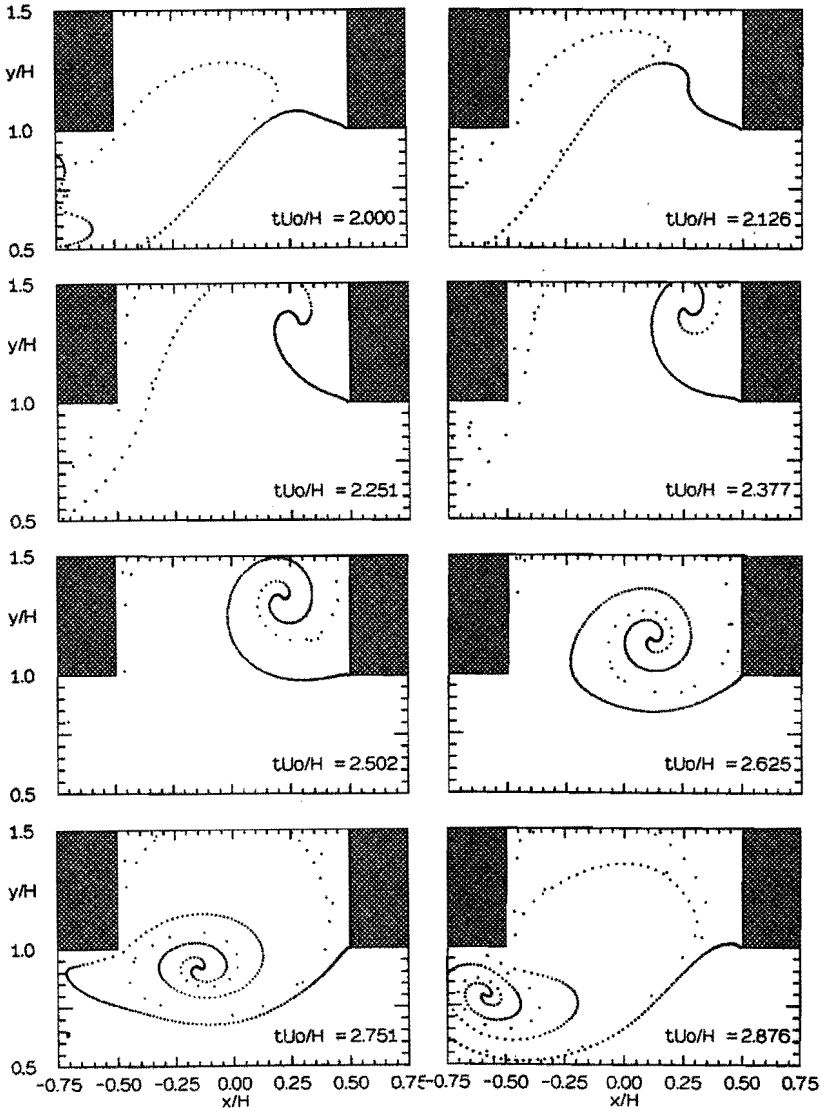


FIGURE 4.19: Numerical simulation of periodic vortex formation in a T-junction. High-amplitude acoustic field, $\hat{u}_{ac}/U_0 = 0.62$ with $Sr = 0.29$. Vortex-blob method ($\delta = 0.10$, $\Delta t = 0.01$). The main flow and acoustic flow have been started at $t = 0$.

time-dependent velocity in the x -direction along the main pipe axis was obtained at specific positions in the T-junction.

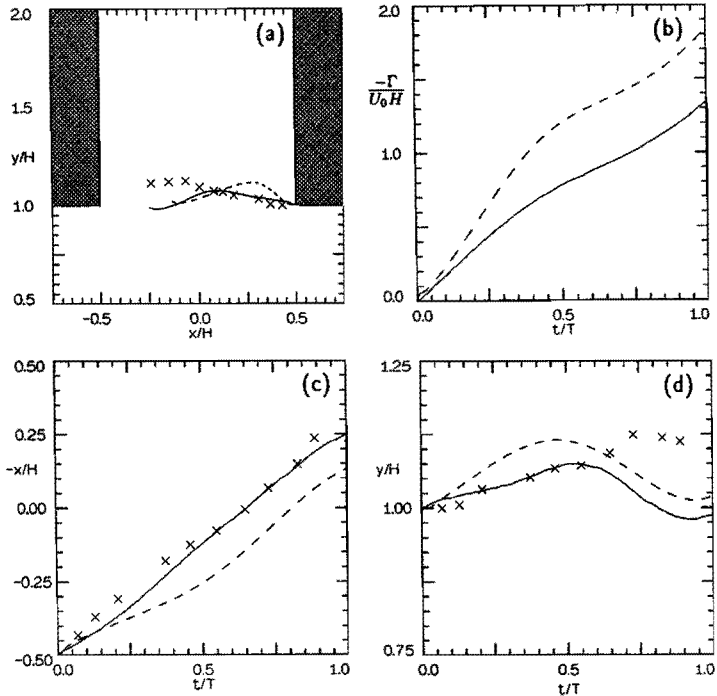


FIGURE 4.20: Position of the center of vorticity and circulation of the vortex sheet for the periodic flow in a T-junction. Moderate-amplitude acoustic field, $\hat{u}_{ac}/U_0 = 0.17$ with $Sr = 0.38$. (---) two-vortex method (vortex formation at $t/T = 0$) (—) vortex-blob method ($\delta = 0.10$), (x) position of vortex core measured by Bruggeman (1987). (a) trajectory of center of vorticity (b) circulation (c) x -coordinate of center of vorticity (d) y -coordinate of center of vorticity

Simulating the periodic vortex formation by a vortex-blob method for these conditions resulted in a periodic solution within three periods of oscillation. The position of the center of vorticity computed by the vortex-blob method is compared in figure 4.20 with the measured position of the vortex core by Bruggeman (1987). The vortex core convects in the x -direction with approximately a constant velocity: $u_c/U_0 \approx Sr$. This corresponds to a travel time of the vortex core from the up- to the downstream edge equal to the acoustic period.

The difference between the results of the vortex-blob method and the experimental

results during the second half-period of the acoustic field is expected to be due to fact that from the flow visualization only the position of the vortex core can be determined, while for the vortex-blob method only the center of vorticity is determined. The position of center of vorticity and that of the vortex core can differ considerably, specially at low acoustic amplitudes.

In contrast to the high amplitude case, it follows from figure 4.17 that for the moderate amplitude case the convection velocity is approximately constant and the circulation increases approximately linearly in time during one period of oscillation. This is due to the small influence the acoustic velocity field has on the convection and generation of vorticity at low and moderate amplitudes. In contrast to the high amplitude case a new vortex structure is formed at the beginning of each cycle of the acoustic field, i.e. at $t/T \approx 0$.

The position of the vortex center obtained from the two-vortex method is also given in figure 4.20. Even for the periodic solution the y -component of the position of the center of vorticity and the circulation are somewhat overestimated by the two-vortex method. This is expected to be due to the vorticity being evenly distributed along the vortex sheet for moderate amplitudes, a vortex distribution which cannot be handled properly by the two-vortex method.

In figure 4.21 the time-dependent velocities in x -direction at various positions in the T-junction computed with the vortex-blob method are compared with the results of the L.D.A. measurements by Bruggeman (1987). After two periods the predicted amplitude of the velocity signal agrees within 10% with the experimental data. Also the phase of the fluctuations are reasonably well predicted by the vortex-blob method.

4.4 PERIODIC FLOW IN A CROSS-JUNCTION

4.4.1 Introduction

In a pipe system with a *single* closed side branch, acoustic resonance of low and moderate amplitude have been realized by Bruggeman *et al.* (1987, 1991). Acoustic resonances with high acoustic amplitude can be obtained if *two* closed side branches are placed in a tandem configuration twice the side branch length or an other even multiple of this distance apart. Bruggeman (1987) measured for the double side branch setup with rounded-off edges a maximum acoustic amplitude of $\hat{u}_{ac}/U_0 = 0.6$. The highest amplitudes are to be expected if the distance between the side branches is smallest and the side branches are positioned opposite to each other. In this case the resonating acoustic field has a wavelength equal to approximately four times the length of the side branches.

Such a cross-junction geometry has been studied experimentally by Ziada & Bühlmann (1993). They studied the influence on the pulsation amplitude of the length of the side branches, the amplitude of the mean flow and the ambient pressure. In section 4.4.2, a visualization of the flow in a cross-junction at high acoustic amplitude will be presented. The vortex formation process will be described numerically by using the two-vortex method and the vortex-blob method, see section 4.4.3. The aero-acoustic behavior of such a configuration will be discussed in chapter 6. In this chapter the acoustic velocity field obtained from the acoustic pressure signal by assuming standing waves in the pipe system is simply

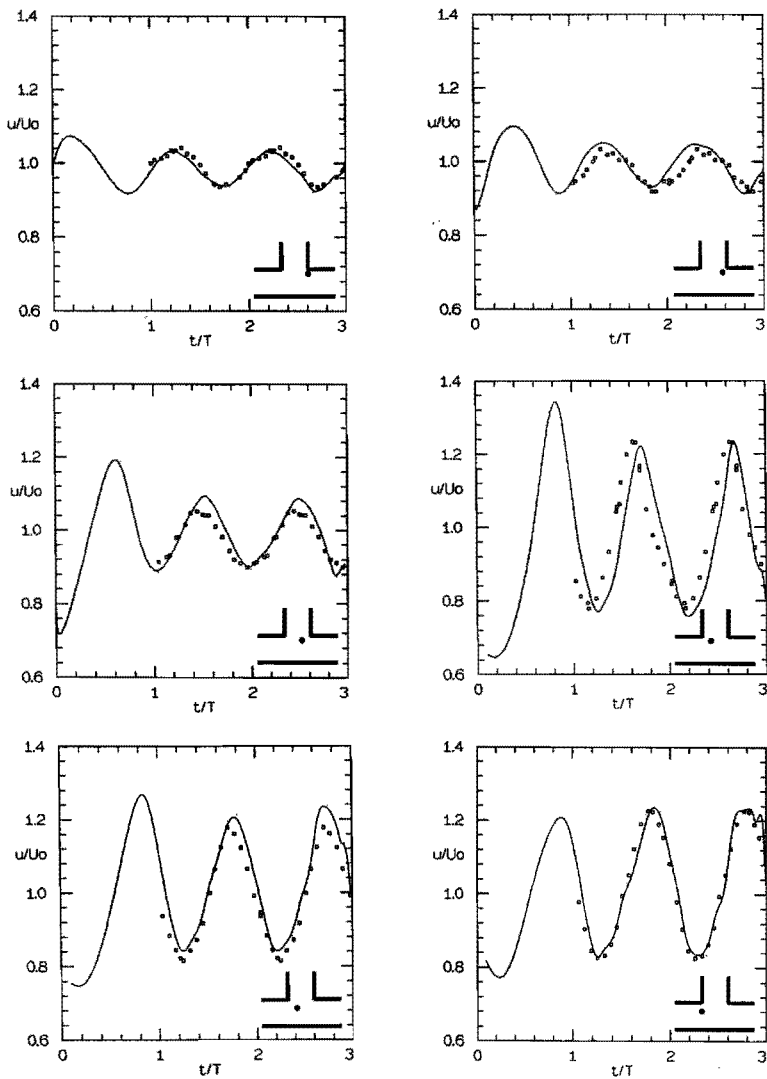


FIGURE 4.21: Velocity in x -direction at a number of locations in the T-junction. Periodic vortex formation for a moderate-amplitude acoustic field, $\hat{v}_{ac}/U_0 = 0.17$ with $Sr = 0.38$. Results of the vortex-blob method ($\delta = 0.10$), (\square) L.D.A. measurements by Bruggeman (1987)

superimposed on the mean velocity field.

4.4.2 Flow visualization

The experimental setup used to visualize the flow in a cross-junction is similar to the setup used to visualize the periodic flow in a T-junction, see figure 4.9. In order to obtain the necessary difference in refractive index a mixture of 50% *Ne* and 50% *Ar* is injected at the upstream edge. In a setup with two closed side branches of equal length ($L = 0.564$ m), opposite to each other and perpendicular to a square main pipe ($H = 0.06$ m), a maximum resonance occurs for mean flow velocity of $U_0 \approx 35$ m/s.

The visualization of the periodic flow at resonance is presented in figure 4.22. At resonance conditions, the Strouhal number has a value $Sr = 0.27$ while the amplitude of acoustic velocity is $\hat{u}_{ac}/U_0 = 0.76$. The acoustic pressure, measured at the end of the closed side branch, is given in figure 4.23a. The corresponding acoustic velocity in the source region can be obtained by assuming a standing wave pattern between the closed side branches. Only the uneven harmonics of the pressure contribute to the acoustic velocity in the source region. The resulting acoustic velocity in the cross-junction, obtained if three harmonics are taken into account, is shown in figure 4.23b.

For this high-amplitude resonance the acoustic pressure and velocity signal are not a pure harmonic signal due to the presence of strong higher harmonics. The amplitude and phase of the higher harmonics compared to those of the fundamental mode are given in table 4.3. Similar to the high-amplitude case for a T-junction the largest amplitude of a higher harmonic is approximately 10% of that of the fundamental mode.

At the two upstream edges free shear layers with vorticity of opposite sign are generated. The flow is periodic and there is a phase shift of half a period between the formation of a center of roll-up in the two vortex layers. Because the vortex formation in the shear layer emanating from the upper and lower edge is identical but for a phase shift of half a period, only the shear layer from the upper edge is visualized. Similarly to the high-amplitude periodic vortex formation in a T-junction and in a nozzle, a new vortex structure is formed before the beginning of a new period of the acoustic field. At the present high acoustic amplitude the vorticity generated at the upstream edge is initially convected into the side branch. When the acoustic velocity field changes sign the vorticity turns back towards the main pipe and eventually the vortex structure is convected with the main stream.

\hat{u}_{ac}/U_0	Sr	M	$f_1(Hz)$	A_2	φ_2	A_3	φ_3	A_4	φ_4
0.76	0.27	0.10	156.3	0.054	103°	0.090	54°	0.047	-79°

TABLE 4.3: Magnitude A_j and phase shift φ_j of higher harmonics relative to the fundamental harmonic contained in the pressure signals for the periodic flow in a cross-junction, presented in figure 4.23.

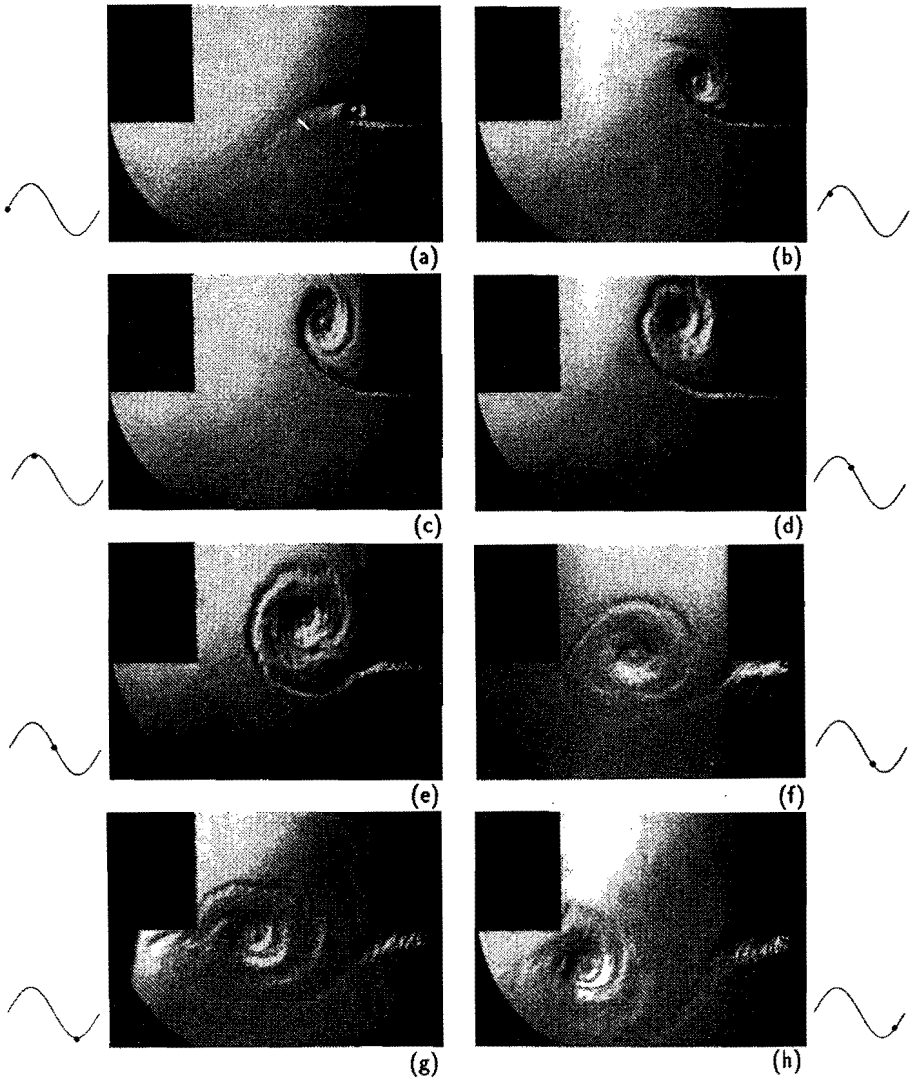


FIGURE 4.22: Flow visualization of periodic vortex formation in a cross-junction. High-amplitude acoustic field $\hat{v}_{ac}/U_0 = 0.76$ with $Sr = 0.27$, $U_0 = 35.0$ m/s, $f = 156.3$ Hz. (a) - (h) are at $t/T = 0.09, 0.23, 0.34, 0.48, 0.58, 0.70, 0.75$ and 0.85 , respectively.

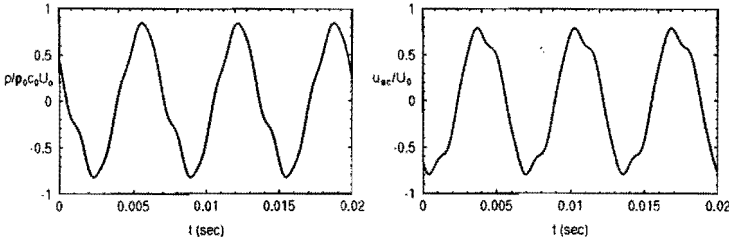


FIGURE 4.23: Acoustic pressure signal measured at the end of the closed side branch in a cross-junction geometry and corresponding acoustic velocity signal in the source region. High-amplitude acoustic field, $\bar{u}_{ac}/U_0 = 0.76$ with $Sr = 0.27$, see flow visualization in figure 4.22.

4.4.3 Numerical simulation

Two-vortex method

For the numerical simulation of the periodic flow in a cross-junction with the two-vortex method, the cross-junction is mapped onto a computational half-plane $\Re(\zeta) > 0$. This is accomplished by the transformation for a T-junction $z = f(w)$, given in equation (3.18), in combination with the transformation $w = g(\zeta)$ with

$$g(\zeta) = \frac{a}{2} \left(\zeta - \frac{1}{\zeta} \right) \quad (4.4)$$

where $a = 1/\sqrt{1+h^2}$, with h the width of the main pipe, nondimensionalised with the width of the side branch H . With this transformation the lower part of the cross-junction ($\Im(z) < 0$) is mapped to the inner part of the semi-circle $|\zeta| < 1$, $\Re(\zeta) > 0$, while the upper part of the cross junction is mapped to the outer part of the unit circle $|\zeta| > 1$, $\Re(\zeta) > 0$. For a cross-junction where the width of the main pipe is equal to that of the side branch, the value $h = 1$ and as a result $a = 1/\sqrt{2}$. The edges of the cross-junction in the physical plane at $z/H = \pm 1/2 \pm i/2$ are mapped to the points in the computational plane with $w = \pm i(1 \pm \sqrt{2})$ as shown in figure 4.24. The derivative of the transformation function $z = f(g(\zeta))$ is given by

$$\frac{dz}{d\zeta} = \frac{-2\sqrt{\zeta^2 + b^2}\sqrt{\zeta^2 + c^2}}{\zeta(\zeta^2 + 1)} \quad (4.5)$$

where $b = \sqrt{2}-1$ and $c = \sqrt{2}+1$. The acoustic velocity field originating from the lower side branch at $z \rightarrow -i\infty$ is mapped to a point source in the computational plane positioned at $\zeta = 0$, while the acoustic flow originating from the upper side branch is mapped to infinity in the computational plane.

The main flow originating from the pipe segment at the right side of the cross-junction at $z \rightarrow \infty$ and vanishing into the pipe segment on the left side at $z \rightarrow -\infty$ is mapped onto point sources of opposite strength at $\zeta = -i$ and $\zeta = i$, respectively.

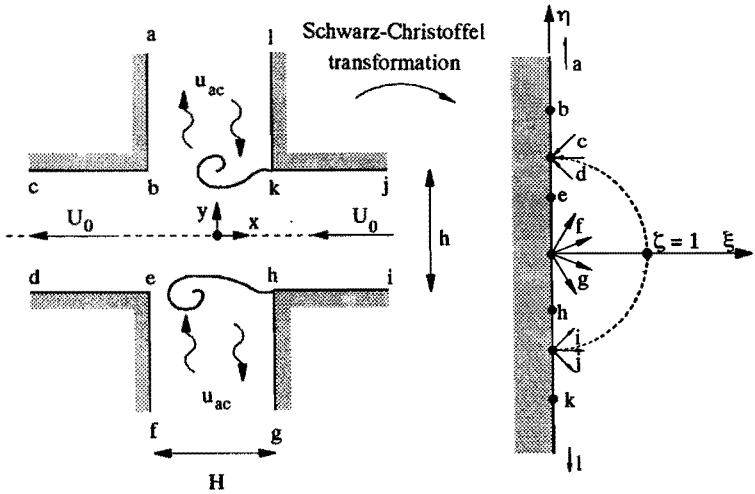


FIGURE 4.24: Conformal mapping of the flow in a cross-junction to the flow in a half plane. (a) physical flow domain (b) computational domain.

The complex velocity potential of the attached flow is in the computational plane, in nondimensionalized coordinates, given by

$$\Phi_0(w) = \frac{\hat{u}_{ac} \sin(2\pi S r t)}{\pi} \ln(\zeta) + \frac{1}{\pi} \ln \left(\frac{\zeta + i}{\zeta - i} \right) \quad (4.6)$$

Since vorticity is generated at both upstream edges, at position $\zeta = -i(\sqrt{2} \pm 1)$ in the computational plane, two main vortices with time varying circulation are present during each period of calculation. In the two-vortex method the initial position of the main vortices is determined by the similarity solution of the flow in the region near the upstream edges $\zeta = -i(\sqrt{2} \pm 1)$. The circulation of the two initial vortices is obtained from the Kutta condition applied at the upstream edges

$$\left. \frac{d\Phi}{d\zeta} \right|_{\zeta = -i(\sqrt{2} \pm 1)} = 0 \quad (4.7)$$

where $\Phi(\zeta)$ is the complex velocity potential in the computational plane with contributions due to the mean flow, the acoustic velocity field and the vortices. Because in the flow visualization separation of the flow at the downstream edges ($\zeta = i(\sqrt{2} \pm 1)$) is not observed, the flow at the downstream edges is assumed to remain attached.

Each time step the main vortices are convected with the local flow velocity obtained from equation (2.65) and the transformation function (4.5). Subsequently the edge vortex is generated at the upstream edges, which strength and position follow from the local flow near the upstream edges, by using the local similarity solution. Each edge vortex is combined with the associated main vortex through an amalgamation procedure in which

the potential far inside the side branches is conserved. A similar amalgamation procedure has been used for the simulation of the periodic flow in a T-junction and for the periodic flow in a nozzle.

For moderate acoustic amplitude, a new main vortex is started when the acoustic velocity field changes from going out of the side branch to going into the side branch. As a result, there is a phase shift of half a period between vortex formation at the upper and that at the lower edge. The position of the center of vorticity and the circulation for the periodic solution for a moderate acoustic amplitude $\hat{u}_{ac}/U_0 = 0.3$ with $Sr = 0.4$ are shown in figure 4.25. The vortex trajectories of the two vortices are geometrically symmetric, but there is a phase shift of half a period between the time of formation of the two vortices.

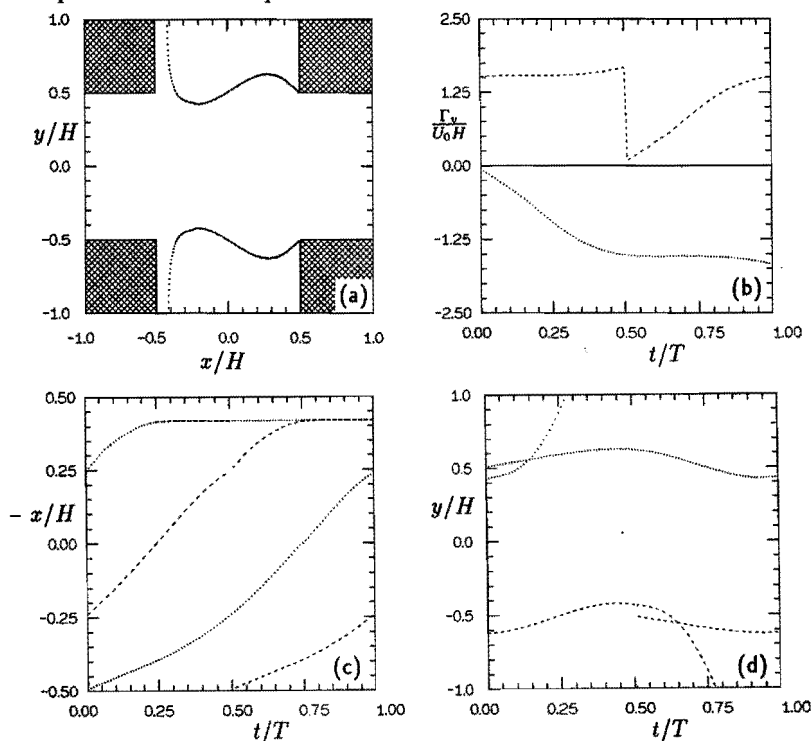


FIGURE 4.25: Position of center of vorticity and circulation as a function of time for the periodic flow in a cross-junction. Moderate-amplitude acoustic field, $\hat{u}_{ac}/U_0 = 0.3$ with $Sr = 0.4$. Results of two-vortex method (a) trajectory of main vortices z_v (b) circulation Γ_v (c) x -coordinate of vortex trajectory (d) y -coordinate of vortex trajectory (\cdots) main vortex shed at upper upstream edge ($---$) main vortex shed at lower upstream edge.

For high acoustic amplitudes the flow visualization showed that near an edge a new vortex structure appears in the shear layer before the acoustic velocity changes sign. Since this is an empirical parameter for the two-vortex method, the method is less suited for this case.

Vortex-blob method

The high-amplitude periodic vortex formation has been simulated by the vortex-blob method. At $t = 0$, the mean and acoustic flow have been started and two vortex structures are formed simultaneously at the upstream edges. Due to the instability of the vortex sheet, a new vortex structure is formed each period near both edges, however not simultaneously but with a shift of half a period. The latter can be understood by realizing that for a single side branch each period a new vortex structure starts to be formed when the acoustic waves start to move into the side branch. Since for the specified geometry considered here this condition occurs half a period apart in the two opposite side branches the formation of a new vortex structure has a phase shift of half a period.

The periodic solution obtained with the vortex blob method for $Sr = 0.27$ and $\hat{u}_{ac}/U_0 = 0.76$ is shown in figure 4.26. To obtain this result only the fundamental mode of the acoustic velocity has been imposed. It has been verified that a numerical simulation including two higher harmonics shows only minor differences in the trajectory of the center of vorticity.

The size of the markers is linearly related to the circulation of the vortex blob at the marker position, while the type of marker is related to the sign of its circulation ($\Delta =$ negative, $\square =$ positive). From the results of the numerical simulation presented in figure 4.26 it is clear that for high acoustic amplitudes, the circulation is nonuniformly distributed along the vortex sheet and most of the vorticity is concentrated near the center of the vortex spiral. At $t/T = n + 0.25$, when the acoustic velocity reaches a maximum value and is directed into the upper side branch, vorticity of negative sign is generated at the lower upstream edge and the vortex sheet leaves the edge tangentially to the wall of the side branch.

In figure 4.27 the position of the center of vorticity and the circulation for each individual vortex structure are compared with the estimated position of the vortex core from the experimental data in figure 4.22. During the initial stage of the computation the position of the center of vorticity and that of the vortex core follow the similarity law for the impulsively started flow around a 90° wedge. From the similarity solution for the impulsively started flow around a 90° wedge we obtain $\Gamma \sim t^{1/2}$ and as a result $d\Gamma/dt \sim t^{-1/2}$ which is singular for $t \rightarrow 0$, which explains the singular behavior of $d\Gamma/dt$ during the initial stage of the computation.

However, for the periodic solution the trajectory of the center of vorticity leaves the edges tangentially, while the position of the vortex core agrees with the experimental data. If we define the moment of formation of a new vortex as the moment that $d\Gamma/dt = 0$ with $d^2\Gamma/dt^2 > 0$, we observe that a new vortex is formed at $t/T \approx n + 0.3$ and $n + 0.8$, which is $\approx 0.2 T$ before the acoustic wave starts to move into the side branches. This agrees with the results of the flow visualization at high acoustic amplitude (see figure 4.22) and with

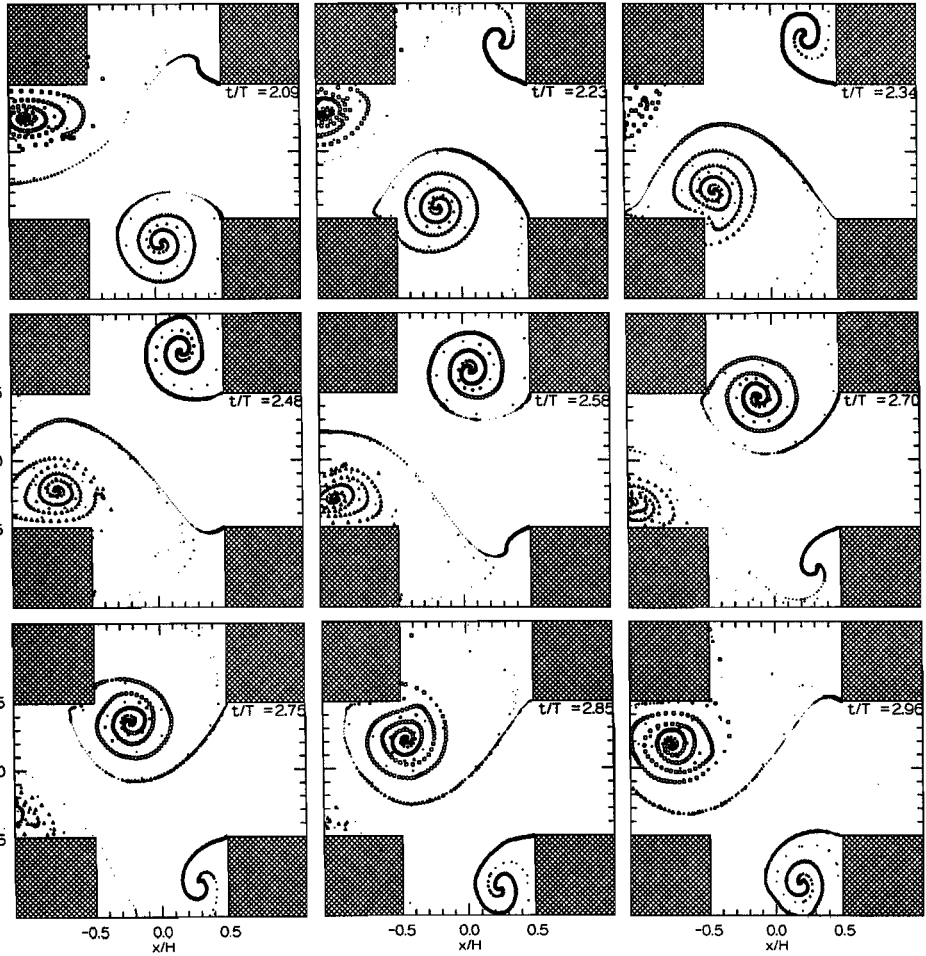


FIGURE 4.26: Numerical simulation of periodic vortex formation in a cross-junction. High-amplitude acoustic field, $\hat{u}_{ac}/U_0 = 0.76$ with $Sr = 0.27$. Results of the vortex-blob method ($\delta = 0.10$). The mean and acoustic flow have been started at $t = 0$.

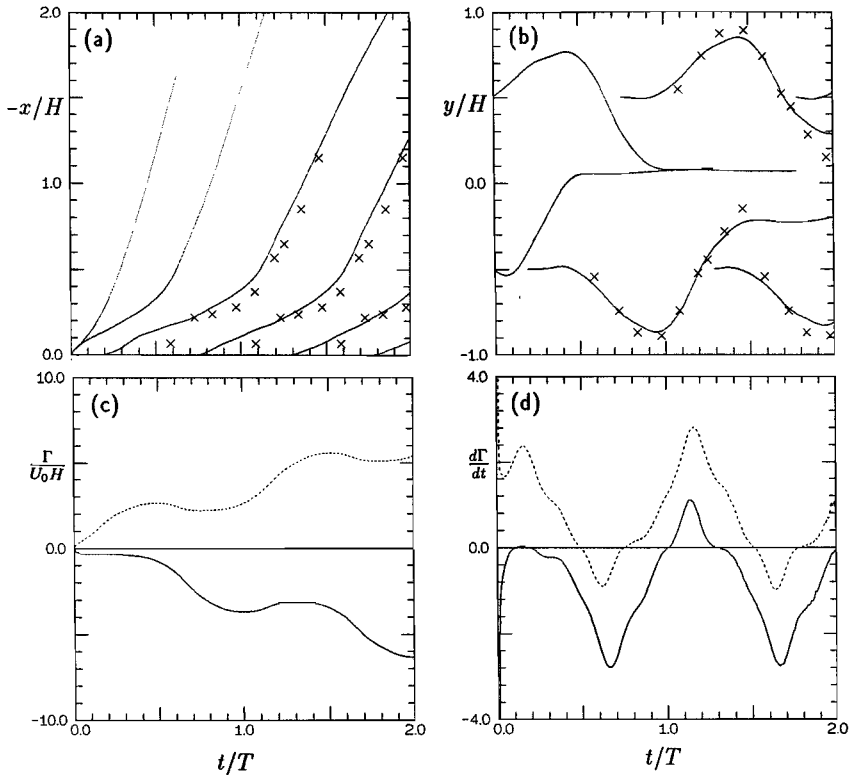


FIGURE 4.27: Trajectory of center of vorticity and circulation of the vortex sheet for the periodic flow in a cross-junction. High-amplitude acoustic field, $\hat{u}_{ac}/U_0 = 0.76$ with $St = 0.27$. (\times position of vortex core obtained from the flow visualization shown in figure 4.22) (a) x -coordinate of center of vorticity (b) y -coordinate of center of vorticity (c) circulation (d) increase of circulation (—) vortex formed at upper upstream edge (.....) vortex formed at lower upstream edge.

the results obtained at high amplitudes in a T-junction (see figure 4.12) and in a nozzle at high acoustic Strouhal numbers (see figure 4.1 and 4.8).

4.5 CONCLUSIONS

In this chapter the periodic vortex formation in the shear layer associated with the flow separation at sharp edges and triggered by an externally imposed periodic acoustic velocity field has been studied, both with or without a main stream. In the presence of a main flow field it is found that at low acoustic amplitudes the moment of formation of a vortex

structure is equal to the moment the acoustic velocity changes sign. In that case the acoustic velocity field triggers the inherent Kelvin-Helmholtz instability of straight vortex sheets with a nearly uniform vortex distribution. The initial disturbance grows while it is convected along the shear layer from the upstream edge in the direction of the downstream edge with a nearly constant velocity.

The formation of a vortex structure and its circulation are only slightly influenced by the value of the acoustic amplitude. Comparison of the results computed by the vortex-blob method and results of Laser Doppler velocity measurements carried out in a T-junction at moderate acoustic amplitude shows that the vortex-blob method describes the periodic vortex formation process accurately.

For high acoustic amplitudes, the periodic vortex formation shows a phase shift with respect to the acoustic velocity field of approximately $-0.2 T$, both for the flow in a T-junction as well as for the flow in a cross-junction. The formation of a new vortex structure is in this case not only determined by the acoustic flow field, but mainly by the vorticity distribution in the vortex layer. For high acoustic amplitudes the vorticity is distributed highly nonuniformly along the shear layer, i.e. most of the vorticity is concentrated in the region near the vortex core. In case the amplitude of the acoustic velocity is of the same order (not necessarily higher) than the velocity of the mean flow even vorticity of opposite sign can be present in the vortex layer.

Due to the concentration of vorticity in small areas a two-vortex method can describe the periodic vortex formation at high amplitudes quite well. In the two-vortex method the moment of vortex formation is an input parameter, which has to be obtained from flow visualization or from numerical results of a more sophisticated method. Both the vortex-sheet method and the vortex-blob method can be used for this purpose.

In absence of a mean flow the problem is always nonlinear and also in this case vortices start to be formed before the acoustic velocity changes sign. The vortex formation at a sharp-edged nozzle could be accurately described by the vortex-blob method. Due to the absence of a mean flow vortices remain close to the nozzle-edge during an acoustic period and, in view of the simplicity of the method a single-panel method, assuming that a new vortex is formed when the increase of circulation changes sign, also gives reasonable results.

REFERENCES

- BERNARDINIS B. DE, GRAHAM J.M.R. & PARKER K.H. (1980) Oscillatory flow around disks and through orifices. *J. Fluid Mech.* **102**, 279 - 299.
- BRUGGEMAN J.C. (1987) Flow induced pulsations in pipe systems. PhD thesis Eindhoven University of Technology
- BRUGGEMAN J.C., HIRSCHBERG A., DONGEN M.E.H. VAN, WIJNANDS A.P.J. & GORTER J. (1989) Flow induced pulsations in gas transport systems: analysis of the influence of closed side branches. *J. Fluids Eng.* **111**, 484 - 491.
- BRUGGEMAN J.C., HIRSCHBERG A., DONGEN M.E.H. VAN, WIJNANDS A.P.J. & GORTER J. (1991) Self-sustained aero-acoustic pulsations in gas transport systems: experimental study of the influence of closed side branches. *J. Sound & Vibr.* **150** 3, 371 - 393.

- CLEMENTS R.R. (1973) An inviscid model of two-dimensional vortex shedding. *J. Fluid Mech.* **57** 2, 321 - 336.
- DISSELHORST J.H.M. (1978) Acoustic resonance in open tubes. PhD thesis Twente University of Technology
- DISSELHORST J.H.M & WIJNGAARDEN L. VAN (1980) Flow in the exit of open pipes during acoustic resonance. *J. Fluid Mech.* **99** 2, 293 - 319.
- GRAHAM J.M.R (1977) Vortex shedding from sharp edges. *I.C. Aero report 77-06* , pp. 1 - 22.
- GRAHAM J.M.R (1980) The forces on sharp-edged cylinders in oscillatory flow at low Keulegan-Carpenter numbers. *J. Fluid Mech.* **97** 1, 331 - 346.
- HOWE M.S. (1975) Contributions to the theory of aerodynamic sound, with application to excess jet noise and the theory of the flute. *J. Fluid Mech.* **71** 4, 625 - 673.
- KIYA M. & ARIE M. (1977) An inviscid numerical simulation of vortex shedding from an inclined flat plate in shear flow. *J. Fluid Mech.* **82** 2, 241 - 253.
- NAGANO S., NAITO M. & TAKATA H. (1982) A numerical analysis of two-dimensional flow past a rectangular prism by a discrete vortex model. *Computers and Fluids* **10** 4, 243 - 259.
- PETERS M.C.A.M. & HIRSCHBERG A. (1993) Acoustically induced periodic vortex shedding at sharp-edged open channel ends: Simple vortex models. *J. Sound & Vibr.* **161** 2, 281 - 299.
- SARPKAYA T. (1975) An inviscid model of two-dimensional vortex shedding for transient and asymptotically steady separated flow over an inclined plate. *J. Fluid Mech.* **68** 1, 109 - 128.
- SARPKAYA T. & IHRIG C.J. (1986) Impulsively started steady flow about rectangular prisms: Experimental and discrete vortex analysis. *J. Fluids Eng.* **108**, 47 - 54.
- STOKES A.N. & WELSH M.C. (1986) Flow-resonant sound interaction in a duct containing a plateII: square leading edge. *J. Sound & Vibr.* **104** 1, 55 - 73.
- STONEMAN S.A.T, HOURIGAN K., STOKES A.N. & WELSH M.C. (1988) Resonant sound caused by flow past two plates in tandem in a duct. *J. Fluid Mech.* **192**, 455 - 484.
- WELSH M.C. & STOKES A.N. (1984) Flow-resonant sound interaction in a duct containing a plate, part I: Semi-circular leading edge. *J. Sound & Vibr.* **95** 3, 305 - 323.
- WIJNGAARDEN L. VAN (1968) On the oscillations near and at resonance in open pipes. *J. Eng. Math.* **11** 3, 225 - 240.
- ZIADA S. & BÜHLMANN E.T. (1992) Self-excited resonances of two side-branches in close proximity. *J. Fluids & Structures* **6**, 583 - 601.

The aeroacoustic behavior of an open pipe¹

Abstract

The propagation of plane acoustic waves in smooth pipes and their reflection at open pipe terminations have been studied experimentally. The accuracy of the measurements is determined by comparison of experimental data with results of linear theory for the propagation of acoustic waves in a pipe with a quiescent fluid. Considered are the damping and the reflection at an unflanged pipe termination.

In the presence of a fully developed turbulent mean flow the measurements of the damping confirm the results of Ronneberger & Ahrens (1977). In the high-frequency limit the quasi-laminar theory of Ronneberger (1975) predicts accurately the convective effects on the damping of acoustic waves. For low frequencies a simple theory combining the rigid plate model of Ronneberger & Ahrens (1977) with the theoretical approach of Howe (1984) yields a fair prediction of the influence of turbulence on the shear stress. The finite response time of the turbulence near the wall to the acoustic perturbations has to be taken into account in order to explain the experimental data. The model yields a quasi-stationary limit of the damping which does not take into account the fundamental difference between the viscous and thermal dissipation observed for low frequencies.

Measurements of the nonlinear behavior of the reflection properties for unflanged pipe terminations with thin and thick walls in absence of a mean flow confirm the theory of Disselhorst & van Wijngaarden (1980), for the low frequency limit. It appears however that a two-dimensional theory as proposed by Disselhorst & van Wijngaarden (1980) for the high frequency limit underestimates the acoustical absorption by vortex shedding by a factor 2.5. The measured influence of wall thickness on the reflection properties of an open pipe end confirms the linear theory of Ando (1969). In the presence of a mean flow the end correction δ of an unflanged pipe end varies from the value of the high Strouhal number limit $\delta/a = 0.61$, with a the pipe radius, which is equal to the value in absence of a mean flow given by Levine & Schwinger (1948) of $\delta/a = 0.61$, to a value of $\delta/a = 0.19$ in the low Strouhal number limit which is close to the value of $\delta/a = 0.26$ predicted by Rienstra (1983).

The pressure reflection coefficient is found to agree with the theoretical predictions by Munt (1977, 1990) and Cargill (1982b) in which a full Kutta condition is

¹accepted for publication in the Journal of Fluid Mechanics; M.C.A.M. PETERS, A. HIRSCHBERG, A.J. REIJNEN & A.P.J. WIJNANDS, *Damping and reflection coefficient measurements for an open pipe at low Mach and low Helmholtz numbers.*

included. The accuracy of the theory is fascinating in view of the dramatic simplifications introduced in the theory. For a thick-walled pipe end and a pipe terminated by a horn the end correction behavior is similar. It is surprising that the nonlinear behavior at low frequencies and high acoustic amplitudes in absence of mean flow does not influence the end correction significantly.

The aero-acoustic behavior of the pipe end is dramatically influenced by the presence of a horn. In the presence of a mean flow the horn is a source of sound for a critical range of the Strouhal number.

The high accuracy of the experimental data suggests that acoustic measurements can be used for a systematic study of turbulence in unsteady flow and of unsteady flow separation.

5.1 INTRODUCTION

In duct systems, which are part of complex flow distribution systems, used for example by the Netherlands gas distribution company (N.V. Nederlandse Gasunie) to distribute gas under high pressure, acoustic excitation can be caused by compressors or flow instability. In particular we study the coupling between periodic vortex shedding and acoustic standing waves. To be able to predict for a given geometry the conditions at which resonant acoustic oscillations occur and to estimate the amplitude of such a resonance, knowledge is required of the quality factor of the resonator. This quality factor is determined by amongst others the reflection coefficient of the acoustic waves at the end of the resonator, the damping of the acoustic waves by visco-thermal losses in the boundary layer and the interaction of acoustic waves with a turbulent mean flow. Typical for industrial conditions are low frequencies, low mean flow velocities and very high Reynolds numbers.

In this paper an open pipe with various types of pipe terminations is studied. A plane acoustic pressure wave of complex-valued amplitude \hat{p}_+ and a reflected wave of complex-valued amplitude \hat{p}_- are traveling inside the pipe in positive and negative direction, respectively. The reflection coefficient $R = \hat{p}_-/\hat{p}_+$ at an open pipe end is easily obtained with a two-microphone method as described by Abom & Boden (1986, 1988). In the original method the wave numbers of the plane acoustic waves are assumed to be known. These wave numbers are calculated from the damping coefficient according to Kirchhoff (1868), see Davies (1988), Abom & Boden (1986, 1988). A major advantage of the two-microphone method is that data can be obtained for very low Helmholtz numbers (Peters *et al.* (1992)), at which the standing wave method does not yield accurate results (Alfredson & Davies (1970)).

In order to increase the accuracy of the measurements the two-microphone method is extended to a multi-microphone method which enables the simultaneous measurement of the wave numbers and the reflection properties. In this way, also the damping α_{\pm} of acoustic waves traveling in the pipe has been determined.

The parameters characterizing the problem are the Mach number $M = U_0/c_0$, the Helmholtz number $ka = \omega a/c_0$, the mean flow Strouhal number¹ $St_0 = \omega a/U_0$ which is

¹Note that in this chapter the Strouhal number is based on the radian frequency ω , rather than the frequency f , as used in the previous chapters

equal to ka/M and the acoustic Strouhal number $St_{ac} = \omega a/\hat{u}_{ac}$. Here, a is the inner radius of the pipe, ω the radian frequency of the acoustic waves inside the pipe, U_0 is the mean volume flow divided by the pipe cross-sectional area πa^2 and c_0 is the speed of sound, while \hat{u}_{ac} is the amplitude of the acoustic velocity at the open end of the pipe. Table 5.1 gives an overview of the main theoretical and experimental results obtained during the last decades for the magnitude $|R|$ of the reflection coefficient, its phase φ expressed as the so-called end correction $\delta = \frac{\varphi - \pi}{2\omega/c_0}$ and the damping α_{\pm} .

Many theoretical results have been obtained for the reflection of acoustic waves at an open pipe end with sharp edges (e.g. Levine & Schwinger (1948)), as well as for the influence on the reflection properties of: wall thickness (e.g. Ando (1969)); mean flow (e.g. Munt (1977, 1990), Cargill (1982a,b), Rienstra (1983) and Howe (1979a)); and vortex shedding (e.g. Disselhorst & van Wijngaarden (1980)). However, accurate experimental data are not available for cases with both a low Mach number and a low Helmholtz number. In many cases experimental results are given in terms of transmission losses (e.g. Bechert (1980) and Cummings & Eversman (1983)). Typical scatter in reported data, as for example by Alfredson & Davies (1970), Abrishaman (1977), Ingard & Singhal (1975), Davies *et al.* (1980) and Abom & Boden (1986, 1988) of the reflection of plane acoustic waves at an open pipe end amounts to 3% in $|R|$ and 20% in the end correction δ .

Without a mean flow accurate predictions for the reflection coefficient and end correction for a sharp-edged pipe end are given by Levine & Schwinger (1948). For low Helmholtz numbers $ka < 0.5$, the work of Ando (1969) indicates that in a quiescent fluid there is no significant influence of the wall thickness at the pipe end on the magnitude of the reflection coefficient. However, Ando (1969) also predicted a significant increase of the end correction δ with increasing wall thickness, δ rising to the value of the end correction for a flanged pipe end given by Nomura *et al.* (1960).

There is little information on the dependence of the reflection coefficient on the ratio \hat{u}_{ac}/U_0 of the amplitude of the acoustic velocity \hat{u}_{ac} at the pipe end and the mean flow velocity U_0 in presence of a mean flow nor on the ratio of the acoustical displacement and the pipe radius $St_{ac} = \omega a/\hat{u}_{ac}$ in absence of mean flow. Some experimental work on the nonlinear behavior of pipe ends and diaphragms on the reflection characteristics at high acoustic amplitudes has been described in terms of quasi-stationary models by Ingard & Ising (1967), van Wijngaarden (1968), Bechert (1980), Cummings & Eversman (1983) and Cummings (1984). For a quiescent fluid a prediction for the acoustic energy absorption by vortex shedding was calculated in the limit $St_{ac} \gg 1$ by Disselhorst & van Wijngaarden (1980) using a two-dimensional description of the flow.

In presence of a mean flow the reflection coefficient R and damping α are strongly influenced by the Mach number. The influence of the Mach number on the reflection properties was studied using a linear theory, including a Kutta condition at the pipe end, by Munt (1977, 1990). The theory of Munt (1977) and other theories, based on this basic theory assume a uniform main flow (plug flow) and infinitely thin shear layers as boundaries for the jet. The shear layer oscillations induced by the acoustic perturbations are growing exponentially as they are convected away from the edges of the pipe end. Obviously after a few hydrodynamic wave lengths it is questionable whether linear theory is still applicable. Hence the validity of the theory is not obvious. Furthermore the theory should only be

valid when the thickness of the acoustic boundary layer is large compared to that of the main flow boundary layer at the pipe exit.

The theory of Munt (1990) predicts that the reflection coefficient $|R|$ can exceed unity within a critical range of the Helmholtz number. Cargill (1982a,b) and Rienstra (1983) analyzed the problem for the case of low Strouhal number ($Sr_0 = ka/M$), and found a similar behavior for the magnitude of the reflection coefficient in case the Kutta condition was imposed at the edges of the pipe end, but a significantly different behavior for the solution in which Kutta condition was not imposed. For the latter solution the magnitude of the reflection coefficient in the low Strouhal number limit is equal to $|R| = (1 - M)/(1 + M)$ which corresponds with the reflection of all of the acoustic energy at the pipe end.

Rienstra (1983) was also able to predict a low-Strouhal-number limit for the end correction in the presence of a low-Mach-number mean flow. It is common practice (e.g. Davies (1988)) to assume that for an unflanged pipe termination the presence of a mean flow has no effect on the ratio of the end correction δ and the pipe radius a ($\delta/a = 0.6133$, see Levine & Schwinger (1948)), i.e. for low Strouhal numbers it has the same value as for high Strouhal numbers. However, the low-Strouhal-number theory of Rienstra (1983) predicts a much lower value, namely of $\delta/a = 0.2554$.

For the high-Strouhal-number limit, Rienstra (1983) and Howe (1979a) derived that the end correction indeed approaches the value ($\delta/a = 0.6133$) found in absence of a mean flow component. For small but finite Mach numbers Howe (1979a) found a correction factor, which is a function of the Mach number, which has to be applied to the end correction found without a mean flow. In the intermediate region of $Sr_0 = \mathcal{O}(1)$ Cargill (1982b) states that there is no simple approximate analytical expression for δ/a . There are some indications for the nonuniform behavior of δ/a for low Mach numbers and low Helmholtz numbers. For example, the experimental data of Davies *et al.* (1980) indicate a decrease of the end correction δ as a result of nonzero mean flow. However, in the latter investigation the different cases of $Sr_0 \rightarrow 0$ and $Sr_0 \rightarrow \infty$ have not been distinguished.

Powell (1951), Wilson *et al.* (1970) and Hirschberg *et al.* (1988) have shown that the presence of a horn at the end of the pipe may have a spectacular influence on the aero-acoustic behavior of an open pipe termination. For a critical range of the Strouhal number the value of the energy reflection coefficient defined as $R_E = |R|^2(1 - M)^2/(1 + M)^2$ exceeds unity. We will present some additional data, in particular on the end correction.

In a quiescent fluid a theoretical expression for the damping coefficient α is given by Kirchhoff (1868) for the case the acoustic boundary layer is thin compared to the pipe radius. A general theory for low-frequency-plane wave propagation in pipes can be found in Tijdeman (1975). In the presence of a mean flow the damping coefficient for the acoustic waves traveling in upstream direction is different from the one for waves traveling in the downstream direction. This convective effect on the damping of acoustic waves has been studied by Ronneberger (1975). Ronneberger (1975) proposes a quasi-laminar theory taking the turbulent mean flow velocity profile into account, but neglecting the dissipation due to the interaction of the turbulent stresses and the acoustic field.

An important parameter appears to be the ratio of the thickness $\delta_{ac} = \sqrt{2\nu/\omega}$ of the acoustic boundary layer and the thickness $\delta_l \approx 10\nu/\sqrt{\tau_0/\rho_0}$ of the viscous sublayer of the turbulent mean flow boundary layer. Here, ν is the kinematic viscosity, ρ_0 is the density

of the fluid and τ_0 is the mean wall shear stress. If the ratio is small $\delta_{ac} \ll \delta_l$, the damping of acoustic waves is not influenced by the turbulent stresses, and a general agreement between the quasi-laminar theory of Ronneberger (1975) and the experimental data has been demonstrated by Ronneberger & Ahrens (1977). For very large values of the ratio δ_{ac}/δ_l , a quasi-stationary theory has been proposed by Ingard & Singhal (1974).

A theory including the nonuniform turbulent eddy viscosity is proposed by Howe (1979b), and extended in a later paper by the same author, Howe (1984). Howe's theory (1984) predicts satisfactorily the global features of the damping coefficient α_{\pm} . However, the difference between the experimental data obtained by Ronneberger & Ahrens (1977) and the results of the theory of Howe (1984) is still quite large, of the order of 20%. Furthermore the theory of Howe (1979b, 1984) is based on a two-dimensional flat-plate approximation and does not yield a finite quasi-stationary limit of the damping at low frequencies. Intuitively the ratio δ_{ac}/δ_l is expected to be crucial for the validity of the assumptions of plug-flow and Kutta condition in the model of Munt (1977). These assumptions correspond to the limit $\delta_{ac}/\delta_l \ll 1$. For this reason, reflection coefficient measurements have been carried out over a wide range of values of this parameter, i.e. $0.2 < \delta_{ac}/\delta_l < 3$.

The purpose of the present investigation is to obtain accurate data of the reflection coefficient R and the damping α_{\pm} for low Helmholtz numbers ka , low Mach numbers M , this for a wide range of Strouhal numbers $Sr_0 = ka/M$ and Sr_{ac} . In this region of parameters very few experimental data exist (see table 5.1) though this region is of special interest for practical applications. Differences between the various theoretical predictions for R and α_{\pm} are relatively small in this range of the parameters. Therefore a high accuracy of the experimental data is required to validate the predictions of the theoretical models.

In section 5.2 the experimental setup will be described as well as the extension of the two-microphone method to a multi-microphone method. The accuracy of the method is checked by comparison of experimental data, obtained in absence of a mean flow, with predictions.

The damping of acoustic waves due to viscous and thermal forces, the influence of a nonzero mean flow and turbulence will be discussed in section 5.3, where also experimental data on the damping coefficient α is presented.

In section 5.4 the acoustic properties of an open pipe end in absence of mean flow is studied. The influence of the pipe end geometry on the reflection characteristics of a pipe end is determined and compared with theories found in the literature for low- and high-amplitude acoustic fields, respectively. Finally the influence of a mean flow on the reflection properties of an open pipe end is discussed in section 5.5.

5.2 SETUP AND EXPERIMENTAL PROCEDURE

5.2.1 Setup

The measurements have been carried out in a horizontal steel tube of 6 m length and inner radius $a = 15.013$ mm. The wall thickness of the tube is $d_0 = 5.00$ mm. The inner pipe wall has a surface roughness of less than $0.1\mu\text{m}$, which in all the applications considered

AUTHOR	TH.	EXP.	R	δ	α	ka	M	Sr ₀	Sr _{ac}
MUNT (1977, 1990)	×	-	×	-	-	VAR.	< 1	VAR.	≫ 1
RIENSTRA (1983)	×	-	×	×	-	< 1	< 1	≪ 1	≫ 1
CARGILL (1982a,b)	×	-	×	-	-	< 1	< 1	≪ 1	≫ 1
ANDO (1969)									
LEVINE & SCHWINGER (1948)	×	-	×	×	-	VAR.	0	-	≫ 1
NOMURA <i>et al.</i> (1960)									
KIRCHHOFF (1868)									
TIJDEMAN (1975)	×	-	-	-	×	VAR.	0	-	≫ 1
HOWE (1979b,1984)	×	-	×	×	×	< 1	< 1	≫ 1	≫ 1
RONNEBERGER (1975)									
RONNEBERGER & AHRENS (1977)	×	×	-	-	×	VAR.	< 1	VAR.	≫ 1
INGARD & SINGHAL (1974, 1975)	×	×	×	-	×	< 3.5	< 0.5	VAR.	≫ 1
DISSELHORST <i>et al.</i> (1980)	×	×	×	-	-	< 1	0	-	VAR.
INGARD & ISING (1967)									
BECHERT (1980)									
CUMMINGS & EVERSMAN (1983)	×	×	×	-	-	VAR.	< 1	VAR.	< 1
CUMMINGS (1984)									
ALFREDSON & DAVIES (1970)									
ABRISHAMAN (1977)									
DAVIES (1980)	-	×	×	×	-	> 0.1	< 0.2	> 1	≫ 1
ABOM & BODEN (1986, 1988)									
PETERS <i>et al.</i> (1992)	-	×	×	×	-	< 0.3	< 0.2	VAR.	VAR.

TABLE 5.1: Summary of existing theoretical and experimental results for the reflection and damping of acoustic waves in an open pipe. (var.) corresponds with a continuous range of values.

here corresponds to an hydraulically smooth surface. A very thin coating of oil was present in order to avoid possible corrosion of the tube. The experimentally determined friction coefficient agreed within the accuracy of the volume flow measurement (0.5%) with the one that follows from Prandtl's law for the friction of a tube with hydraulically smooth walls (Schlichting (1968)).

The open pipe end is placed in the middle of a large room ($20 \times 16 \times 9m^3$), 0.66 m above a rigid floor. The nearest wall is at 6 m distance. The four different types of pipe end geometries studied in this paper are given in figure 5.1.

- The first type of geometry, shown in figure 5.1a, approximating the unflanged pipe termination with thin walls, studied by Levine & Schwinger (1948), Munt (1977, 1990) and others, has a sharp edge with a bevel angle of 20° .
- The second type of geometry given in figure 5.1b is an unflanged pipe end with thick walls, with the thickness d comparable with the thickness d_0 of the pipe wall. Two

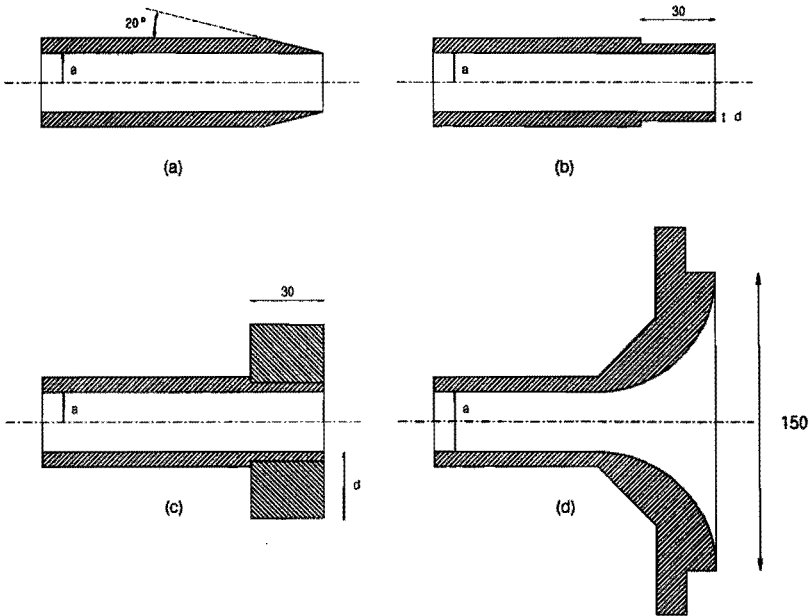


FIGURE 5.1: Pipe end geometries used for the experiments (dimensions in mm). (a) sharp edged pipe end. (b) thick-walled pipe end with wall thickness d of the order of d_0 . (c) thick-walled pipe end with wall thickness d much larger than d_0 . (d) circular horn with radius of curvature $r = 4a$.

values of the wall thickness d at the pipe end were chosen, one for which the ratio of inner to outer radius $a/(a + d) = 0.85$ and a second one for which this quantity equals 0.70, each corresponding with geometries studied by Ando (1969).

- Experiments with pipe end wall thicknesses d larger than the pipe radius a , i.e. $d/a = 4/3$ and $20/3$, i.e. with the type of pipe end geometry given in figure 5.1c, were carried out to obtain values for the end correction for conditions close to those of a flanged pipe end.
- Finally a pipe end with a circular horn with radius of curvature r equal to $4a$, shown in figure 5.1d, was studied. This geometry is a reasonable approximation for the human lips in a position used for human whistling.

In the absence of a mean flow, the acoustic excitation is provided by a loudspeaker enclosed in a box with a hole of radius a at both sides of the box. One of the holes is placed at a distance 1 mm from the pipe entrance. By closing the remaining gap with flexible

tape, the possible influence of acoustical streaming on the high amplitude measurements was checked. No significant influence was observed. Mechanical contact between the pipe and the excitation is avoided by placing these elements on two independent frames. To avoid the transfer of mechanical vibrations from the loudspeaker to the pipe via the floor the frame supporting the pipe is placed on 6 rubber strips. In order to obtain an optimal signal to noise ratio, the measurements were performed at frequencies corresponding to acoustic resonances of the pipe/excitation combination. Measurements of the reflection coefficient at a closed pipe end have confirmed that there is no significant effect of pipe wall vibrations on the results of the measurements.

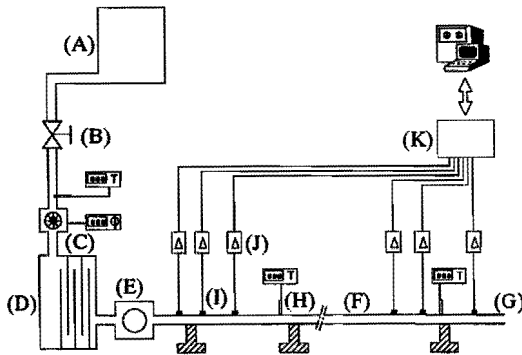


FIGURE 5.2: Experimental setup (A) high pressure supply (B) valve (C) flow meter (Instomet Q-66) (D) reverberation chamber (E) siren (F) steel tube (inner radius $a = 0.015013$ m) (G) pipe end geometry (H) wall temperature measurement (I) pressure transducers (type PCB 116 A) (J) charge amplifiers (type Kistler 5007) (K) data acquisition system (HP 3656 S)

In the presence of a mean flow, the acoustic pulsations are provided by a siren (see figure 5.2) which is, in the frequency range considered ($10\text{Hz} < f < 1000\text{Hz}$), a much more efficient sound source than the loudspeaker. A bypass allows a variation of the ratio of the amplitude of the acoustic velocity \hat{u}_{ac} at the open pipe end and the mean flow velocity U_0 in the range $0.01 < \hat{u}_{ac}/U_0 < 0.5$. When the siren and the pipe are detached to allow the mean flow to escape through the gap between the two devices, the siren can be used to excite a pipe with a closed end. This allows the comparison of the reflection coefficient at a closed pipe end obtained by excitation with the loudspeaker with that obtained with the siren. High-amplitude acoustic fields could easily be obtained using the siren as a sound source, which however can induce significant temperature variations along the pipe.

The present investigation is limited to low and intermediate values of the acoustic amplitude. When the siren was rigidly attached to the pipe, with an open side branch to

deflect the mean flow, a small but significant deviation of the reflection coefficient of the closed pipe end was found (0.5 %) for those frequencies corresponding to the mechanical resonance frequencies of the setup. With a gap of about 1 cm between the siren and the pipe end the mechanical contact was avoided and the effect of the mechanical vibration on the reflection coefficient became negligible. Since the measurements for a closed pipe end are much more sensitive to small errors than measurements for an open pipe end, this implies that the siren does not induce significant vibrations in the pipe walls. However, in order to ensure that wall vibrations do not affect the data the siren and the pipe were detached and the gap was closed with flexible plastic tape.

The speed of sound c_0 is calculated from the wall temperature T_w measured at various positions in the pipe. The variation of the temperature along the tube is about 0.1°C , which corresponds with the uncertainty in its measurement. Using a 0.2 mm thermocouple placed across the tube, it was verified that the stagnation temperature of the flow did not differ more than 0.2°C from the wall temperature under the conditions considered ($M < 0.1$). The flow temperature T was calculated by assuming a recovery factor, i.e. $T = T_w(1 - 0.18M^2)$ corresponding to a turbulent boundary layer on a plane surface according to Ronneberger (1975). The speed of sound was estimated by interpolation of the data found in the CRC Handbook on Chemistry and Physics (Weast (1976)). For measurements without a mean flow the speed of sound c_0 is corrected for the humidity of the air. For the experiments with mean flow the air is provided by a high pressure supply (60 bar) and is dry (dewpoint -40°C).

The mean flow velocity U_0 is calculated from the volume flow obtained with a calibrated turbine meter (type Instromet Q-66). The uncertainty in the measurement of U_0 is about 0.5%. The measured U_0 is corrected for the difference in pressure and temperature between the pipe exit and the flow meter position. The calibration of the turbine meter was checked by a comparison of the measured mean velocity with the value obtained from the profile for a fully-developed turbulent pipe flow where the centerline velocity was measured by a Prandtl tube. Also a comparison with data obtained with an orifice meter showed that the measured mean velocity is accurate within 0.5 %.

The mean static pressure in the pipe was measured using a Wallace & Tiernan manometer with a measurement accuracy of 50 Pa. The atmospheric pressure was determined with a mercury manometer with an error of less than 100Pa . The acoustic pressure in the pipe is measured by means of acceleration compensated piezo-electrical gauges (type PCB 116 A). These gauges have a diameter of 10.3 mm. Because the diameter of the gauges is large compared to the pipe radius, the gauges cannot be mounted flush in the pipe wall. The installation of the gauges in the wall of the pipe is shown in figure 5.3. A channel (3.5 mm diameter and 1.5 mm long) connects the pipe with a cylindrical cavity (10.5 mm diameter and 0.5 mm deep) in front of the surface of the pressure gauge. Calibration of the installed gauge involving a reference pressure gauge mounted flush in a closed pipe end yields a correction on the gauge readings for the influence of the gauge installation units.

The pipe consists of separate segments on which the individual pressure gauges are mounted. By interchanging these pipe segments, different positions of the microphones are obtained. As will be shown in the next section, the accuracy of the measured data depends on the relative position of the gauge with reference to the standing wave pattern in the

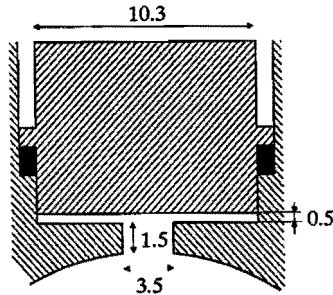


FIGURE 5.3: Configuration of the pressure gauges in the pipe wall (dimensions in mm).

pipe and hence on the frequency considered. As a rule of the thumb, one of the gauges used for the determination of the reflection coefficient must be placed close to a pressure node. In the case of an open pipe end the first microphone is placed about three diameters from the pressure node at the pipe end. At this position a plane wave approximation yields an accurate description of the acoustic flow field.

The proximity of the first microphone to the pressure node at the open pipe end implies that measurements will be accurate for a continuous range of frequencies. One of the microphones has to be positioned at a pressure node, which implies that when a closed pipe end is considered, or when data obtained at a location further down the pipe is considered (for example for the measurement of damping), full accuracy of the data is only achieved for discrete frequencies.

The position x_i , measured from the pipe end, of the microphone i was determined with an accuracy of 0.1 mm. Measurements for a closed pipe end confirm, that the acoustical position of the gauge corresponds with the geometrically determined position of the gauge. The signals from the microphones are amplified by means of charge amplifiers (Kistler type 5007, bandwidth $0.1\text{ Hz} < f < 22\text{ kHz}$) and transferred for further analysis to a HP 3565S data acquisition system (dynamic range 80 dB, phase accuracy 0.1 degree, linearity 0.1 dB). Using FFT analysis (frequency discretisation 0.004 Hz, using a Hanning window), the transfer functions H_{ij} between microphones at position x_i and x_j were obtained. Only data with a coherence equal to one within the accuracy of the measurement (10^{-4}) were used. Each measurement was repeated three times.

The reproducibility of the measurements appears to be determined by the analog/digital converter (13 bit). The accuracy of the measurements is mainly limited by the accuracy of the calibration of the pressure gauges. Because the measurement for the case of the closed pipe end is very sensitive to small errors in the calibration, these measurements were used to adjust the calibration obtained with the procedure described above. In this refinement the damping coefficient in a quiescent fluid obtained from the measurement data was used which was close to the value predicted by Kirchhoff (1868).

Because the measurements were carried out with simultaneous reading up to six microphones, independent reflection coefficient data could be obtained. Data were checked on their sensitivity to systematic errors due to the uncertainties in the calibration. Suspect data, showing errors more than 0.5% as a result of the uncertainties in the calibration, were rejected. In general, data obtained with different microphone pairs agreed within 0.1%. Typical reproducibility of the data is of the order of 0.05% or better. The largest systematic errors observed are due to the room acoustics and will be discussed further.

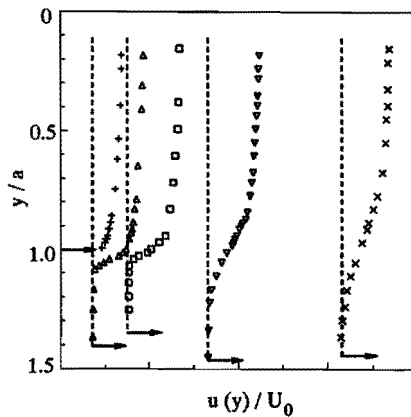


FIGURE 5.4: Velocity profile measured close to a flanged circular pipe end. The arrow denotes the mean velocity in the pipe (41 m/s). Measurements presented are obtained at a distance (+) $x = -0.2 a$, (Δ) $x = 0.15 a$ (\square) $x = 0.7 a$ (∇) $x = 1.9 a$ (\times) $x = 3.9 a$ from the pipe end.

5.2.2 Mean flow conditions

As the test section of the pipe was always placed more than 100 pipe diameters downstream of the siren, a fully developed turbulent mean flow was achieved in all experiments. The mean velocity profile close to the pipe end was measured by means of a constant temperature hot wire of $5\mu\text{m}$ diameter and 6 mm length. The average velocity inside the pipe was approximately 41 m/s, which is close to the maximum velocity used in all experiments. The measured velocity profiles in the shear layer of the free jet at a flanged pipe end are presented in figure 5.4. The momentum thickness of the free shear layer increases linearly with x , the distance to the pipe end.

For the steady flow in a pipe segment, terminated by a horn, for the flow conditions considered the separation point depends strongly on the Reynolds number. This effect is measured by means of a pressure recovery factor, defined by $C_D = \Delta p / \frac{1}{2} \rho_0 U_0^2$, where Δp is the pressure difference between a point just inside the pipe in front of the horn and a

point in the far field outside. This pressure recovery factor is presented in figure 5.5. It can be related to an effective diameter D_j of the free jet by $C_D = 1 - (2a/D_j)^4$, where a uniform velocity profile in the jet has been assumed and the Bernoulli equation has been used. The maximum pressure recovery factor found in this manner is $C_D = 0.3$, which is equivalent to a maximum increase of the jet width by about 10%.

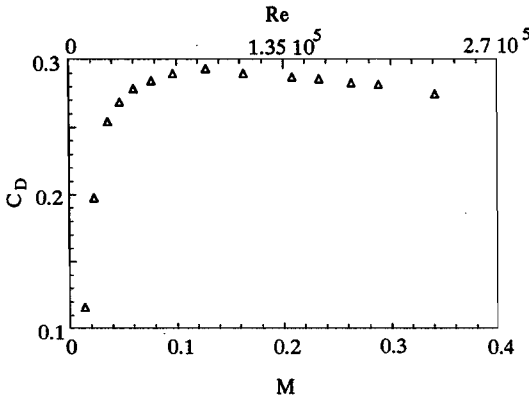


FIGURE 5.5: Pressure recovery factor for the steady flow in the horn, shown in figure 5.1d.

5.2.3 Determination of reflection coefficient and the damping

Using the measured transfer functions H_{ji} between the microphone at position x_j and the reference microphone at position x_i close to the open pipe end ($x = 0$), the reflection coefficient R of the open pipe end and the complex-valued wave numbers k_+ and k_- , of the in positive and negative direction traveling acoustic waves, can be determined. The underlying analysis is based on the assumption that the acoustic field can be described in terms of plane waves for which $p(x, t) = \hat{p}(x)e^{i\omega t}$ with

$$\hat{p}(x) = \hat{p}_+ e^{-ik_+ x} + \hat{p}_- e^{ik_- x} \quad (5.1)$$

where \hat{p} is the complex-valued amplitude of the acoustic pressure $\hat{p}(x)$ and ω is radian frequency. The imaginary parts of the wave numbers $\Im(k_{\pm})$ correspond to the negative of the damping coefficients α_{\pm} of the waves

$$\alpha_{\pm} = -\Im(k_{\pm}) \quad (5.2)$$

When the wave numbers k_{\pm} and the transfer function $H_{ji} = \hat{p}(x_j)/\hat{p}(x_i)$ are known, the complex-valued reflection coefficient $R(x)$ at position x , defined as

$$R(x) = \hat{p}_- e^{ik_- x} / \hat{p}_+ e^{-ik_+ x} \quad (5.3)$$

can be calculated from

$$R(x) = \frac{H_{ji}e^{-ik_+(x_i-x)} - e^{-ik_+(x_j-x)}}{e^{ik_-(x_j-x)} - H_{ji}e^{ik_-(x_i-x)}} \quad (5.4)$$

where k_{\pm} is assumed to be independent of the position x . If the wave numbers k_{\pm} are known, the reflection coefficient can be determined by the two-microphone method described by Abom & Boden (1986, 1988). The reflection coefficient at the pipe end $R(0)$ will be denoted by R . If the wave numbers k_{\pm} are unknown as well, a multi-microphone method can be used. When four microphones are used, three independent pairs of microphones can be selected. From equation (5.4) a set of three nonlinear complex-valued equations is obtained with R , k_+ and k_- as complex-valued unknowns, which has to be solved iteratively. When more than four microphones are used, a nonlinear regression procedure can be used to solve the resulting set of overdetermined nonlinear equations (e.g. Ronneberger & Ahrens (1977)).

The procedure used for the experiments presented in this paper is based on the concentration of microphones into *two clusters*. The first cluster of microphones is placed near the pipe end. The second cluster is placed at a distance from the open pipe end which is much larger than the microphone spacing within a cluster. The first cluster is used to determine the reflection coefficient $R(x_i)$ at position x_i of the microphone, closest to the pipe end. The second cluster is used to calculate the reflection coefficient $R(x_j)$ at position x_j of the microphone of the second cluster placed in a **pressure node**. (This last condition determines the values of frequencies at which the experiments are carried out.) Under these conditions $R(x_i)$ and $R(x_j)$ appear to be most insensitive to random errors, calibration errors and other systematic errors. It was found that the values of $R(x_i)$ and $R(x_j)$ calculated using equation (5.4) for both clusters is rather insensitive to the precise value of k_{\pm} as long as the microphones in each cluster are placed closer than a quarter of the acoustic wavelength apart. When a theoretical value is used for k_{\pm} , an accurate first approximation for $R(x_i)$ and $R(x_j)$ can be obtained. From these values of the reflection coefficient an accurate first guess for the damping coefficient α_{\pm} can be determined from the imaginary part of the individual complex values of k_+ and k_- obtained from

$$\begin{aligned} e^{-ik_+\Delta x_{ij}} &= H_{ij} \left(\frac{1 + R(x_j)}{1 + R(x_i)} \right) \\ e^{ik_-\Delta x_{ij}} &= H_{ij} \left(\frac{1 + R(x_j)}{1 + R(x_i)} \right) \frac{R(x_i)}{R(x_j)} \end{aligned} \quad (5.5)$$

where $\Delta x_{ij} = x_i - x_j$ is the distance between the microphones at the position x_i and x_j . In principle, because there is a mean pressure gradient along the pipe, the Mach number M and wave numbers k_{\pm} depend on the position x . Using the correction procedure proposed by Ronneberger & Ahrens (1977) this effect was estimated, but it appeared to be negligible for our experimental conditions ($M \leq 0.1$). Therefore here it is assumed that M and k_{\pm} are independent of position x . The complex-valued average wavenumber can be obtained by averaging k_+ and k_- , i.e. $k_0 = (k_- + k_+)/2$ or directly from

$$\frac{R(x_i)}{R(x_j)} = e^{2ik_0\Delta x_{ij}} \quad (5.6)$$

This procedure can either be repeated, using the new values of the wavenumbers k_{\pm} to recalculate $R(x_i)$ and $R(x_j)$, or one can use a general nonlinear solver procedure to determine R , k_+ and k_- from the signals of two pairs of microphones (one pair in each cluster). It turned out that both procedures converged rapidly towards the same result.

Typical accuracy in $|R|$ using the two-microphone method with theoretical estimates for the wavenumbers k_{\pm} is better than 0.2% for $ka < 0.1$ and 0.3% for $0.1 < ka < 0.3$. The typical absolute accuracy in the corresponding δ is about 0.03 a. For the multi-microphone method the accuracy could be increased to 0.1% for $|R|$, and to $\pm 0.02 a$ uncertainty for δ . The accuracy of the wavenumber k_{\pm} is 2 % for the imaginary part and 0.02 % for the real part. The reproducibility was found to be better than 0.05 % for $|R|$ and 0.5 % for δ and $\Im(k_{\pm})$. This accuracy was confirmed by measurements without a mean flow, which will be described in the following sections.

The energy reflection coefficient R_E is defined as the ratio of the intensity of the reflected and that of the incident acoustic energy at the pipe end. The energy reflection coefficient R_E is related to the pressure reflection coefficient R by (Mechel (1965))

$$R_E = |R|^2 \left(\frac{1 - M}{1 + M} \right)^2 \quad (5.7)$$

where $M = U_0/c_0$ is the Mach number, averaged over the duct cross section.

5.2.4 Influence of the acoustics of the room

The influence of the rigid floor on the reflection coefficient of the open pipe end is taken into account by assuming a point source below the floor, at the mirror-imaged location of the pipe end, of strength equal to the acoustic volume flow at the pipe end. This image source represents the reflection of the acoustic field at the floor. Free field conditions are assumed above the floor, i.e. reflections at the ceiling and the side walls are not taken into account. Since the nearest wall is at 6 m direct reflections at this wall are assumed to be negligible. The correction to the reflection coefficient and end correction due to the presence of the floor, in the low frequency approximation, is given by (Disselhorst & van Wijngaarden (1980))

$$\begin{aligned} |R_{f1}| - |R| &= -\frac{(ka)^2}{4kH} \sin(2kH) \\ \delta_{f1} - \delta &= \frac{a^2}{8H} \cos(2kH) \end{aligned} \quad (5.8)$$

where H is the distance of the pipe to the floor and $|R_{f1}|$ and δ_{f1} are the reflection coefficient and end correction measured in the presence of the floor, respectively. $|R|$ and δ are the values for the latter two quantities for free field conditions. For low Helmholtz numbers, i.e. $ka < 0.3$, the corrections in our experiments (with $H = 660\text{mm}$ and $a = 15.013\text{ mm}$) are

less than 0.2% for an open pipe end. Nevertheless it has been applied to all data presented here.

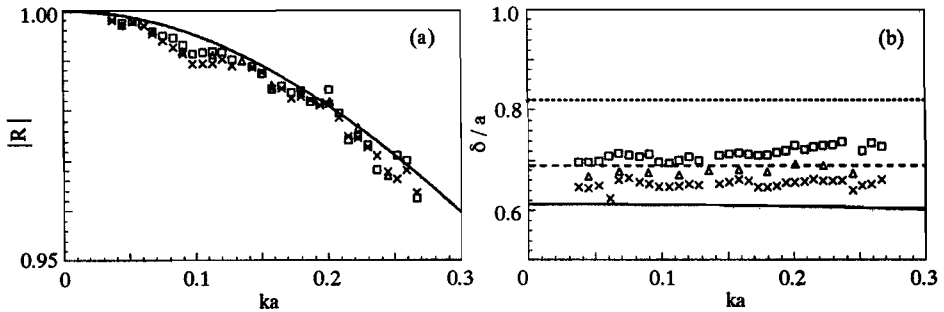


FIGURE 5.6: Influence of wall thickness on the reflection coefficient for an open pipe end without a mean flow at low acoustic amplitudes ($Sr_{ac} > 20$) as a function of the Helmholtz number ka . Influence of room resonances is observed mainly for $ka \approx 0.1$. A two-microphone method, using an experimentally determined value of the damping α_0 , close to the value given by equation (5.10) is used.

Microphone positions : $x_1 = -86.8$ mm, $x_2 = -224.5$ mm. (\times) sharp edges, $a/(a+d) = 1.00$, (Δ) thick walls, $a/(a+d) = 0.85$, (\square) $a/(a+d) = 0.70$. (a) Absolute value of the reflection coefficient $|R|$ (b) End correction δ ——— Levine & Schwinger (1948) for $a/(a+d) = 1.00$ and Ando (1969) for $a/(a+d) = 0.85$. - - - - - Ando (1969) for $a/(a+d) = 0.70$ Nomura et al. (1960) for $a/(a+d) = 0.0$.

Figure 5.6 compares the reflection coefficient $|R|$ and end correction δ obtained with a two-microphone method, in absence of a mean flow, with the theoretical results of Levine & Schwinger (1948) for an unflanged pipe end with thin walls, and the theory of Ando (1969) for pipes with finite wall thickness d . It is found that the data for $|R|$ obtained from the present measurements agree within 0.5 % with the theoretical data, while the data for δ obtained from the experiments agree within 5 % with the corresponding theoretical data.

The data presented in figure 5.6 have been obtained for small values of the acoustic displacement \hat{u}_{ac}/ω compared to the pipe radius a . This condition can be expressed in terms of an acoustic Strouhal number $Sr_{ac} = \omega a/\hat{u}_{ac}$. The data of figure 5.6 have been obtained for conditions such that $Sr_{ac} > 20$. For acoustic Strouhal numbers in this range there is no significant nonlinear behavior to be expected.

The main systematic difference between the reflection coefficient obtained from the measured data and the theoretical ones occurs around $ka = 0.1$. It is expected that this apparent systematic error of about 0.5 % is due to the resonance of the large room in which the experiments have been carried out.

5.3 DAMPING

In section 5.3.1 to 5.3.3 the existing theories and data on damping of plane waves in smooth pipes will be discussed. New data obtained with the multi-microphone method described in the previous section is presented in section 5.3.4.

5.3.1 Damping in absence of mean flow

Visco-thermal damping of acoustic waves in a quiescent medium in pipes has been studied by Kirchhoff (1868), Rayleigh (1896) and Tijdeman (1975). In the low frequency approximation ($ka \ll 1$) and for high shear numbers ($Sh = a\sqrt{\omega/\nu} \gg 1$, where ν is the kinematic viscosity of the medium) the wave number can be approximated by

$$k = \frac{\omega}{c_0} \left(1 + \frac{1-i}{\sqrt{2}} \frac{1}{Sh} \left(1 + \frac{\gamma-1}{\sqrt{Pr}} \right) - \frac{i}{Sh^2} \left(1 + \frac{\gamma-1}{\sqrt{Pr}} - \frac{1}{2} \gamma \frac{\gamma-1}{Pr} \right) \right) \quad (5.9)$$

where γ and Pr are the ratio of the specific heats, also known as Poisson's ratio and the Prandtl number, respectively. In the experiments described in this paper $ka < 0.3$ while $Sh > 30$. For air $Pr = 0.71$ and $\gamma = 1.4$. The density ρ_0 of air was taken from Weast (1976). For the dynamic viscosity of air $\mu = \rho\nu$ the data given by Touloukian *et al.* (1975) was used. As a result, the temperature dependence of the kinematic viscosity of dry air is given by $\nu = A + B(T - T_{ref})$, with T the absolute temperature of the air inside the pipe, $A = 1.51 \cdot 10^{-5} \text{ m}^2/\text{s}$, $B = 9.2 \cdot 10^{-8} \text{ m}^2/\text{sK}$ and $T_{ref} = 293.16 \text{ K}$. The first correction to ω/c_0 which is inversely proportional to the shear number corresponds to the solution given by Kirchhoff (1868), which also changes the phase velocity of the acoustic plane waves. The second term, i.e. the Sh^{-2} term, is a correction of the damping obtained by Kirchhoff (1868) and was obtained by Ronneberger (1975) from the exact expression given in Tijdeman (1975). The result is valid for $Sh > 20$ and within 0.01% in agreement with the low-frequency solution obtained by Tijdeman (1975).

The damping in a quiescent fluid is given by the negative of the imaginary part of equation (5.9), i.e.

$$\alpha_0 = \frac{\omega}{c_0} \left(\frac{1}{\sqrt{2}Sh} \left(1 + \frac{\gamma-1}{\sqrt{Pr}} \right) + \frac{1}{Sh^2} \left(1 + \frac{\gamma-1}{\sqrt{Pr}} - \frac{1}{2} \gamma \frac{\gamma-1}{Pr} \right) \right) \quad (5.10)$$

Although the Sh^{-2} term in equation (5.10) is usually neglected in literature (e.g. Davies (1988), Morse & Ingard (1968), Pierce (1989)) in our experiments it can attain values of 2% of the first term. Hence this correction should be taken into account in view of the accuracy (1%) which is to be achieved in the measurement of the damping.

The dissipation is dominated by the viscothermal losses at the walls. The viscothermal losses in the bulk of the flow are given by Pierce (1989) as

$$\alpha_{bulk} = \frac{\omega (ka)^2}{c_0 2Sh^2} \left(\frac{4}{3} + \frac{\mu_b}{\mu} + \frac{\gamma-1}{Pr} \right) \quad (5.11)$$

where μ_b is the bulk viscosity which is approximately 0.6μ . This contribution to the damping is two orders of magnitude smaller than the losses in the boundary layer and will

be neglected. The contributions due to relaxation processes can be accounted for by an enhanced bulk viscosity $\Delta\mu_b$ and can, for air at room temperature with 20% humidity be approximated by

$$\Delta\mu_b = \frac{\rho_0 c_0^2}{\pi^2} \sum_{i=1}^2 \frac{(\alpha_i \lambda)_{max}}{f_i} \frac{f_i^2}{f^2 + f_i^2} \quad (5.12)$$

where $(\alpha_i \lambda)_{max}$ is the maximum absorption per wavelength associated with the i -type relaxation process and f_i is the relaxation frequency (Pierce (1989), chapter 10). For air, we find for O_2 , $i = 1$, $f_1 = 12500 Hz$, $(\alpha_1 \lambda)_{max} = 0.0011$ and for N_2 , $i = 2$, $f_2 = 173 Hz$, $(\alpha_2 \lambda)_{max} = 0.002$. For low frequencies $f < 200 Hz$, the contribution of the relaxation processes to the damping in the bulk of the flow dominates the other contributions given in equation (5.11). However, for the present experimental setup, the damping in the bulk of the flow is still less than 1% of the damping in the boundary layer and is therefore neglected.

5.3.2 Convective effects

The wave numbers for up- and downstream propagating acoustic waves are influenced by the mean flow velocity U_0 , defined as the volume flux divided by the pipe cross-section. For a uniform mean flow, neglecting damping, it is found that

$$k_{\pm} = \frac{\omega/c_0}{1 \pm M} \quad (5.13)$$

where $M = U_0/c_0$ is the Mach number of the mean flow. The effect of a non uniform laminar mean velocity distribution on the damping coefficient was studied by Ronneberger (1975). By taking into account the turbulent mean velocity profile Ronneberger (1975) solved the linearized equations for mass, momentum and energy conservation for a pipe flow. In this quasi-laminar theory the acoustic effect of the turbulent mixing was neglected. When the acoustic boundary layer thickness $\delta_{ac} = \sqrt{2\nu/\omega}$ is small compared to the thickness of the viscous sublayer $\delta_l \approx 10\nu/v^*$ of a turbulent pipe flow (where $v^* = \sqrt{\tau_0/\rho_0}$ is the friction velocity), the quasi-laminar theory is expected to describe the damping of the acoustic waves quite accurately.

To first order approximation the damping coefficient is independent of the mean flow velocity distribution, but depends only on the mean flow Mach number, i.e. according to (Ronneberger (1975))

$$\frac{\alpha_-}{\alpha_+} = \left(\frac{1+M}{1-M} \right)^2 \frac{\frac{1}{(1-M)^2} + \frac{\gamma-1}{\sqrt{Pr}}}{\frac{1}{(1+M)^2} + \frac{\gamma-1}{\sqrt{Pr}}} \quad (5.14)$$

which is valid for the region where $\delta_{ac} < \delta_l$. Using a two-dimensional flow model Howe (1984) found an alternative result which for $\delta_{ac} < \delta_l$ is given by

$$\frac{\alpha_-}{\alpha_+} = \frac{\frac{1}{(1-M)^2} + \frac{\gamma-1}{\sqrt{Pr}}}{\frac{1}{(1+M)^2} + \frac{\gamma-1}{\sqrt{Pr}}} \quad (5.15)$$

Since Howe's (1984) theory is more approximate than the one used by Ronneberger (1975), we expect the result given by Ronneberger (1975) to be more accurate for $\delta_{ac} < \delta_l$.

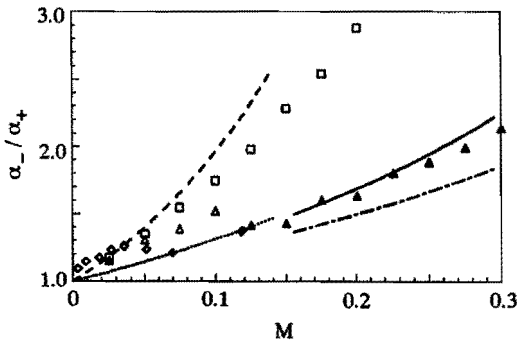


FIGURE 5.7: Influence of Mach number on the damping coefficient in upstream (α_-) and downstream (α_+) direction.

(Δ) $f = 630$ Hz, (\square) $f = 3350$ Hz : data Ronneberger & Ahrens (1977). (\diamond) $f = 135$ Hz present data obtained with a multi-microphone method with microphones at positions $x_1 = -86.8$ mm, $x_2 = -347.8$ mm, $x_3 = -385.3$ mm, $x_4 = -4550.3$ mm, $x_5 = 4601.2$ mm, $x_6 = -5093.7$ mm. Data corresponding to values for which $\delta_{ac}/\delta_l > 1$ are presented by filled markers. Theory for $\delta_{ac}/\delta_l < 1$: - - -: quasi-laminar theory Ronneberger (1975), equation (5.14). : Howe (1984), equation (5.15). For $\delta_{ac}/\delta_l \gg 1$: - - - - - : Ingard & Singhal (1974), equation (5.17). — : Howe (1984), equation (5.18).

In figure 5.7 the data of Ronneberger & Ahrens (1977) for the damping coefficients are given as a function of the Mach number. The data were obtained by varying the Mach number keeping the frequency constant (630 Hz (Δ) and 3350 Hz (\square)). For the region, where $\delta_{ac}/\delta_l < 1$, the data are given by open symbols, while the other data are given as solid symbols. Included in figure 5.7 are the two theoretical results given by equations (5.14) and (5.15). For $\delta_{ac}/\delta_l < 1$, the quasi-laminar theory of Ronneberger (1975) describes the convective effects quite accurately. However, for the region where turbulence affects the acoustic damping $\delta_{ac}/\delta_l \gg 1$ a strong deviation from the theory of Ronneberger (1975) is observed. Note that equation (5.14) is only a first approximation of the quasi-laminar theory of Ronneberger (1975). Comparison with the full quasi-laminar solution can be found in Ronneberger & Ahrens (1977). The effect of turbulence on the acoustic damping properties will be described in the next part of this section.

5.3.3 Influence of turbulence

In the presence of a turbulent mean flow the damping of acoustic waves is influenced by the action of the turbulent stresses if the acoustic boundary layer thickness δ_{ac} is larger than that of the laminar sublayer δ_l . The effect of turbulence can be described in first-order approximation by adding to the kinematic viscosity an eddy viscosity, which is nonuniform

over the pipe cross-section. The eddy viscosity is small compared to the kinematic viscosity for distances from the wall (y) small compared to the thickness of the viscous sublayer δ_l . For $y > \delta_l$, i.e. in the logarithmic region of the turbulent boundary layer, the eddy viscosity increases approximately linearly with the distance from the wall.

Using van Driest hypothesis (see Schlichting (1968)) for the calculation of the eddy viscosity, Ronneberger & Ahrens (1977) derived a model for the damping of acoustic waves by a turbulent mean flow. From their experimental data three different regions in terms of the relative thickness of the acoustic boundary layer could be distinguished.

1. For low values of the ratio δ_{ac}/δ_l , the damping of acoustic waves is not influenced by the turbulent shear stress and is accurately described by the quasi-laminar theory of Ronneberger (1975) (figure 5.7). This findings fully agree with the observation that the eddy viscosity is small in the viscous sublayer.
2. For large values of δ_{ac}/δ_l the damping was found to increase linearly with the acoustic boundary layer thickness. In this case the damping is mainly the result of the turbulent mixing in the bulk of the flow.
3. For a value of the ratio δ_{ac}/δ_l of order one, at a critical Mach number, a minimum in the damping was observed by Ronneberger & Ahrens (1977). This minimum is lower than the value predicted by the quasi-laminar theory. Hence Ronneberger & Ahrens (1977) conclude that the damping appears to be reduced by the presence of turbulence.

This reduction of damping has been explained by Ronneberger & Ahrens (1977) as being the result of the destructive interference at the wall of the shear waves generated by the acoustic field with the shear waves reflected at the edge of the viscous sublayer by the strong variation of the eddy viscosity. For critical ratios of the acoustic boundary layer thickness and the thickness of the laminar sublayer, this destructive interference is maximal which results in the observed minimum in the damping.

Using the eddy viscosity model of van Driest (Schlichting (1968)), Ronneberger & Ahrens (1977) could not predict the minimum in the damping. In their model the damping coefficient $\alpha_0 = \lim_{M \rightarrow 0} \alpha_{\pm}$ was always larger than the damping in a quiescent fluid. Using a model for the eddy viscosity in which the eddy viscosity depends linearly on the distance from the wall and in which the eddy viscosity is neglected within the viscous sublayer Howe (1984) did predict a minimum of the damping coefficient α_0 . However, the minimum in α_0 does not appear at the correct value of δ_{ac}/δ_l and the interference effect is severely underestimated.

Even the simplified 'rigid plate' model, proposed by Ronneberger & Ahrens (1977), assuming an infinitely large eddy viscosity, which certainly overestimates the reflection of the shear wave at the edge of the viscous layer does not predict the correct δ_{ac}/δ_l at which the minimum in the damping occurs, nor the correct value of the minimum itself. Using the thickness of the laminar sublayer δ_l as a parameter to shift the position of the minimum to the observed value of δ_{ac} at minimum, the minimum in the damping is underestimated by a factor of two.

Because the shear wave decays rapidly with the distance from the wall y a deep minimum suggests reflections from a distance from the wall smaller than the value of δ_l used in the existing theories. To obtain a destructive interference one should then have an additional phase shift during the reflection. This phase shift might be related to 'memory' effects of turbulence. Hence in spite of the fact that Ronneberger & Ahrens (1977) assume these memory effects to be negligible a theory neglecting these effects does apparently not explain the experimental data available.

More recently Ronneberger (1991) estimated that the time scale involved in the memory effects of turbulence is of the order of $t_m = 100\nu/v^{*2}$. This corresponds to the acoustic period if $\omega^+ = \omega\nu/v^{*2} = 2\pi/100$. This appears to be a value of the same order of magnitude as the value of ω^+ , where the damping approaches a minimum ($\omega^+ \approx 0.01$) in the experiments of Ronneberger & Ahrens (1977).

If the rigid plate model proposed by Ronneberger & Ahrens (1977) is extended by including a phase shift of $\omega t_m = 100\omega^+$ due to the reflection at the edge of the viscous sublayer ($y = \delta_l$), the shear stress at the wall τ_0 is given by

$$\frac{\tau_0}{\tau_{Stokes}} = \frac{1 + e^{-2(1+i)(\delta_l^+/\delta_{ac}^+) - 200i/\delta_{ac}^{+2}}}{1 - e^{-2(1+i)(\delta_l^+/\delta_{ac}^+)}} \tag{5.16}$$

where the superscript + denotes values nondimensionalised with the kinematic viscosity ν and the friction velocity v^* and $\tau_{Stokes} = \frac{\mu(1+i)}{\delta_{ac}^+} \hat{u}_{ac} e^{i\omega t}$ is the shear stress for a Stokes boundary layer in absence of a mean flow. If the value of δ_l^+ is adjusted to fit the low frequency quasi-steady limit, a value of $\delta_l^+ = 12.5$ is obtained.

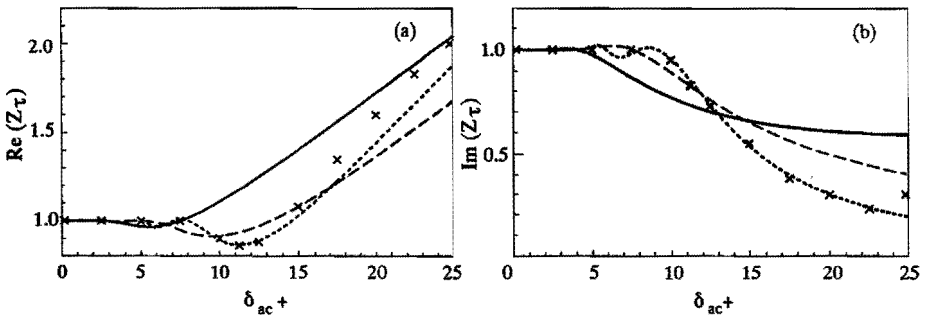


FIGURE 5.8: Influence of turbulence on the shear stress impedance, $Z_\tau = (1 + i)\tau_0/\tau_{Stokes}$. (a) real part $\Re(Z_\tau)$, (b) imaginary part $\Im(Z_\tau)$. (x) experimental data Ronneberger & Ahrens (1977). (.....) rigid-plate model ($\delta_l^+ = 15$), Ronneberger & Ahrens (1977, (---) rigid-plate model with memory effects ($\delta_l^+ = 12.5$), equation (5.16), (—) model Howe (1984) ($\delta_l^+ = 7$).

In figure 5.8 the experimental data of Ronneberger & Ahrens (1977) for the wall shear stress impedance $Z_r = (1+i)\tau_0/\tau_{Stokes}$ in presence of a turbulent mean flow are compared with the results of the rigid plate model of Ronneberger & Ahrens (1977) with $\delta_l^+ = 15$, the theoretical result of Howe (1984) with $\delta_l^+ = 7$ and the modified rigid-plate model with $\delta_l^+ = 12.5$ in which a phase shift due to memory effects of turbulence is taken into account. Figure 5.8 clearly shows that memory effects can be responsible for the differences between the results of existing theories and the experiments. The result given in equation (5.16), obtained by including memory effects into the simple rigid plate model, considerably increases the correlation between theory and the experiment. This is rather surprising since the rigid-plate model is a very approximate model of the interaction of the acoustic shear wave with the turbulent flow away from the wall.

The decrease of the wall shear stress observed by Ronneberger & Ahrens (1977) agrees with more recent data on the wall shear stress reported in Mankbadi & Liu (1992) and Louis & Isabey (1992), although the data presented there show a large scatter, in particular in the region where $\delta_{ac}/\delta_l > 1$.

For high values of the ratio δ_{ac}/δ_l the two-dimensional approximation of the boundary layer used by Howe (1979b, 1984) is not valid anymore, because the acoustic boundary layer thickness then becomes of the order of the radius of the pipe ($Sh \approx 1$). From the experimental data of Ronneberger & Ahrens (1977) a quasi-stationary behavior is obtained for $\delta_{ac}/\delta_l > 2$. The two-dimensional theory of Howe (1984) does not have such a quasi-stationary limit for $\delta_{ac}/\delta_l \rightarrow \infty$ in its present form. This is a severe drawback which calls for further theoretical study.

Ingard & Singhal (1974) have derived a quasi-stationary theory for the damping in the region where δ_{ac}/δ_l is large. In their theory the damping coefficient is given by

$$\frac{\alpha_{\pm}}{\alpha_k} = \frac{\delta_{ac}^+ \sqrt{\psi/2} (1 + \frac{Re}{2} \frac{\partial \ln(\psi)}{\partial Re})}{1 + \frac{\gamma-1}{\gamma Pr}} \quad (5.17)$$

where α_k is the damping in a quiescent fluid according to Kirchhoff (1868) and is given by the first term in equation (5.10). In equation (5.17) Re is the Reynolds number, based on the mean flow velocity and the pipe diameter and ψ is the turbulent friction factor. For smooth pipes ψ can be obtained from Prandtl or Blasius equations (see Schlichting (1968)). For high Reynolds numbers ψ depends only weakly on the Reynolds number. The expression given by Howe (1984) can be simplified for the limit of $\delta_{ac}/\delta_l \gg 1$ to

$$\frac{\alpha_{-}}{\alpha_{+}} = \frac{\frac{1}{(1-M)^2} + \frac{\gamma-1}{Pr}}{\frac{1}{(1+M)^2} + \frac{\gamma-1}{Pr}} \quad (5.18)$$

which differs slightly from equation (5.15) by the dependence of the Prandtl number. In figure 5.7 in the region where $\delta_{ac}/\delta_l > 1$ the convective effects can be compared with the experimental data of Ronneberger & Ahrens (1977) for a frequency of 630 Hz. In this region the theory of Howe (1984) is found to give a more accurate prediction of the convective effects than the theory of Ingard & Singhal (1974).

Ingard & Singhal (1974) obtained a frequency dependence of the damping α_{\pm} by simply adding Kirchhoff's damping α_k without mean flow to α_{\pm} given by equation (5.17). This is

certainly a very crude approach which is not justified by existing experimental data.

A quasi-stationary limit for the damping coefficient can also be obtained from the rigid plate model, proposed by Ronneberger & Ahrens (1977), which, using the two-dimensional theory of Howe (1984), results in

$$\frac{\alpha_{\pm}}{\alpha_k} = \frac{\delta_{ac}^+ \frac{1}{(1 \pm M)^2} + \frac{\gamma-1}{Pr}}{\delta_t^+ \left(1 + \frac{\gamma-1}{\sqrt{Pr}} \right)} \quad (5.19)$$

For $\delta_t^+ = 12.5$ the value of the damping is reasonably close to the result of Ingard & Singhal (1974), given by equation (5.17). However the theory of Ingard & Singhal (1974) neglects the influence of thermal convection and corresponds to an isothermal solution. The convective effects and the frequency dependence of equation (5.19) are in much better agreement with the experimental data. However, it should be noted that at the moment no well established theory is present for describing the convective effects in the quasi-stationary limit.

5.3.4 Experimental results

Using the multi-microphone method the damping coefficient for plane waves traveling in a pipe in a quiescent fluid have been determined for a setup consisting of a pipe with a closed end. The reflection coefficient of the closed pipe end is $R(x_c) = 1$, while a reflection coefficient $R(x_j)$ was obtained with two pairs of microphones $\pm 3.5m$ from the closed end. From equation (5.6) the average wavenumber k_0 , and as a result the damping could be determined accurately.

The damping coefficient $\bar{\alpha}$ obtained for the acoustic waves is presented in figure 5.9. The damping coefficient is normalized with the theoretical value for the damping α_0 in absence of mean flow for high shear numbers (equation (5.10)). The data obtained with the different microphone pairs agree within the experimental accuracy ($\pm 2\%$) of $\bar{\alpha}$. Figure 5.9 shows that the damping is within the range of the required accuracy for the present measurements, i.e. the damping is about 0.7% larger than the value predicted by equation (5.10). This small systematic deviation can partially be explained by the viscosity in the bulk of the flow, given by equation (5.11) and (5.12), which is of the order of 0.6% of α_0 due to relaxation processes.

For the measurements without mean flow, presented in section 5.4, the data obtained with the two-microphone method were post-processed by using the experimentally determined value of the damping.

The damping of acoustic waves in a turbulent mean flow was obtained in two ways: at constant Helmholtz number by varying the Mach number, $0.01 < M < 0.1$, and at constant Mach number by varying the Helmholtz number. The Helmholtz number has been varied between $0.01 < ka < 0.06$, because in this range the microphone calibration is most accurate. In figure 5.10 the damping coefficient for waves traveling in up- and downstream direction are shown as a function of the Mach number at constant frequency ($f = 88Hz$).

The damping is nondimensionalised with the value in absence of mean flow (equation (5.10)). For high Mach numbers a strong increase of damping is observed as the damping

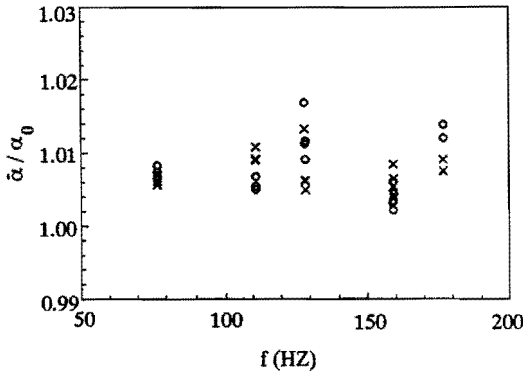


FIGURE 5.9: Damping coefficient in absence of mean flow, nondimensionalised with the value given by equation (5.10). A multi-microphone method is used with microphones at positions $x_1 = -7.5$ mm, $x_2 = -3426.0$ mm, $x_3 = -3476.8$ mm.

(o) : $(\bar{\alpha}/\alpha_0)$ obtained from $R(0) = 1, R(x_2)$ and H_{12} ,

(x) : $(\bar{\alpha}/\alpha_0)$ obtained from $R(0) = 1, R(x_3)$ and H_{13}

tends towards a quasi-stationary limit. The damping in up- and downstream direction are different due to the presence of a mean flow.

The average wave number k_0 can be obtained accurately from the multi-microphone method according to equation (5.6), while the different values of the up- and downstream wave numbers, obtained from equation (5.5), are more sensitive to calibration errors. Therefore average values k_0 are presented in figure 5.11 rather than data for k_{\pm} extrapolated to zero Mach number in the way as proposed by Ronneberger & Ahrens (1977). For low Mach numbers ($M < 0.1$), the difference between k_0 and $\lim_{M \rightarrow 0} k_{\pm}$ is of the order of M^2 .

Figure 5.11a presents the average damping coefficient $\bar{\alpha} = \frac{1}{2}(\alpha_- + \alpha_+)$, normalized with the value α_0 in absence of a mean flow, given in equation (5.10), as a function of δ_{ac}^+ . The experimental data are again obtained in two ways: at constant frequency by varying the Mach number, and at constant Mach number by varying the frequency. Within the experimental accuracy (2% in $\Im(\bar{k})$) the different data sets collapse onto a single curve. The data agree with the real part of the averaged wall impedance

$$Z = \lim_{M \rightarrow 0} \frac{k_0 - \frac{\omega/c_0}{1-M^2}}{-i\alpha_0} \quad (5.20)$$

which is equal to a weighted sum of the shear stress impedance Z_{τ} and the impedance of the heat conduction wave Z_q . In the region where $\delta_{ac}/\delta_l \approx 1$ the damping decreases significantly to a value about 4 % smaller than the damping for the case without mean flow. In the region just before that ($\delta_{ac}^+ \approx 7$) the damping increases slightly ($\pm 3\%$) which

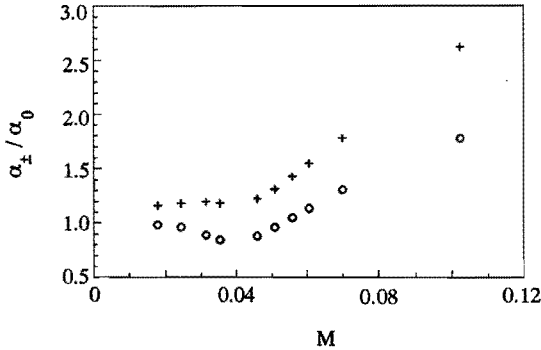


FIGURE 5.10: Damping coefficient α_{\pm}/α_0 as a function of Mach number M for constant Helmholtz number $ka = 0.0242$. Multi-microphone method with microphones at positions $x_1 = -112.5\text{mm}$, $x_2 = -3531.0\text{mm}$, $x_3 = -3581.8\text{mm}$, $x_4 = -3732.0\text{mm}$ at a pipe, terminated by a sharp edge with $a/(a+d) = 1.00$. (o) : α_-/α_0 , (+) : α_+/α_0

is clearly seen in the enlargement in figure 5.11a. Although the data of Ronneberger & Ahrens (1977) are obtained from an extrapolation of results obtained at finite Mach number to results for zero Mach number, the difference with the average damping is less than 2% for $M < 0.1$. In the present investigation experimental data could be obtained for a value of δ_{ac}^+ twice the maximum value obtained by Ronneberger & Ahrens (1977). In this region a change in the quasi-stationary behavior is found. A similar behavior is also observed in figure 5.11b, which shows the imaginary part of the averaged wall impedance Z . For $\delta_{ac} < 25$, this parameter decreases towards a value of 0.4, which was also obtained by Ronneberger & Ahrens (1977), but a small increase is found for $\delta_{ac} > 25$.

The convective effect on the damping expressed in the form α_-/α_+ is given in figure 5.7 for a constant frequency of 135 Hz. Indeed the present low frequency data are reasonably in agreement with the earlier data at higher frequencies (630 Hz, 3350 Hz) of Ronneberger & Ahrens (1977), and clearly exhibit the convective effect for the different regions where $\delta_{ac}/\delta_l \gg 1$ and $\delta_{ac}/\delta_l \ll 1$.

5.4 OPEN PIPE END IN A QUIESCENT FLUID

5.4.1 Influence of pipe end geometry

In this section the linear behavior of an open pipe end in a quiescent fluid is considered. The linear behavior is found for low amplitudes of the acoustic velocity field ($\hat{u}_{ac}/c_0 \ll 1$ and $Sr_{ac} = \omega a/\hat{u}_{ac} \gg 1$).

Analytical results are in general limited to either an unflanged thin-walled open pipe

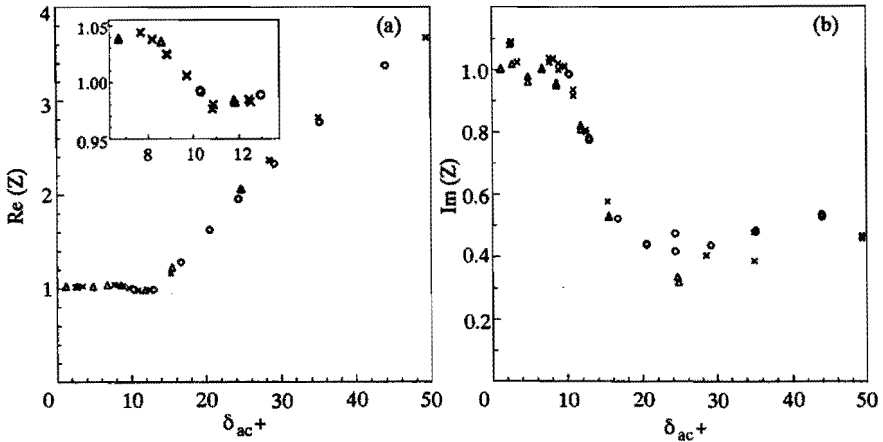


FIGURE 5.11: Averaged wall impedance Z obtained from the averaged wavenumber k_0 . (a) $\Re(Z) = \bar{\alpha}/\alpha_0$ as a function of δ_{ac}^+ with an enlargement of the region near the minimum in damping.

(b) $\Im(Z) = (k_0 - \frac{\omega}{c_0} \left(\frac{1}{1-M^2} \right)) / (-i\alpha_0)$ as a function of δ_{ac}^+ . Variable Mach number: (Δ): $ka = 0.0371$, (\circ): $ka = 0.0121$.

Variable Helmholtz number: (\times): $M = 0.011, 0.042$ and 0.107 .

in free space, or a pipe with an infinitely large hard baffle (flanged pipe end). The theory further neglects the influence of viscosity, which corresponds to the limit of high shear numbers ($Sh \gg 1$).

Because our emphasis is on low Helmholtz numbers ($ka \ll 0.3$) the acoustic field in the pipe can be described in terms of plane waves. Furthermore, in this limit the reflection coefficient can be determined by assuming incompressible flow. At a distance r_1 from the pipe end for which $r_1/a \gg 1$ but $kr_1 \ll 1$, the flow at r_1 can be described by the incompressible flow generated by a point source. Matching the volume flow at the pipe exit with the volume flow at r_1 , and matching the acoustical energy fluxes yields the absolute values of the reflection coefficient at the pipe end, namely

$$|R| = 1 - \frac{(ka)^2}{2} \quad (5.21)$$

for $ka < 0.2$ for an unflanged pipe end and

$$|R| = 1 - (ka)^2 \quad (5.22)$$

for $ka < 0.2$ for a flanged pipe end. The difference between these low frequency approximations and the more accurate expressions derived by Levine & Schwinger (1948) for an unflanged thin walled pipe end, by Ando (1969) for an unflanged thick walled pipe end

and by Nomura *et al.* (1960) for a flanged pipe end are of the order of the experimental accuracy (0.5%). In figure 5.6 the reflection coefficients determined from the present measurements are given for an unflanged pipe end with different values of the wall thickness ($a/(a+d) = 0.70, 0.85$ and 1.00), and compared with the exact theory of Levine & Schwinger (1948). It is indeed found from figure 5.6a that in the low frequency limit the shape of the pipe end does not influence the magnitude $|R|$ of the reflection coefficient, as suggested earlier by Bechert (1980).

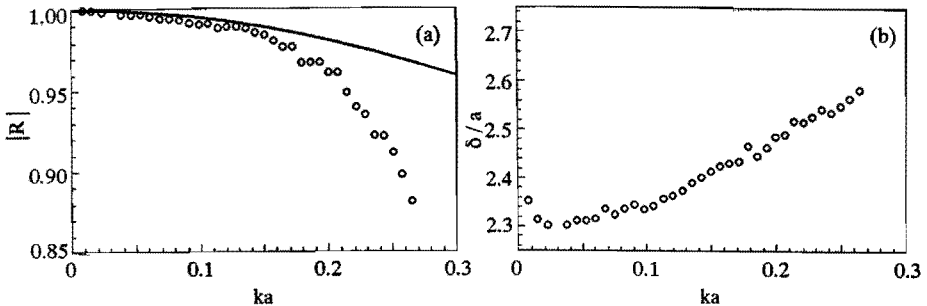


FIGURE 5.12: (a) Pressure reflection coefficient $|R|$ and (b) end correction δ for a pipe terminated by a horn, in absence of a mean flow as a function of the Helmholtz number ka at low acoustic amplitude.

(\circ) : Data obtained with a two-microphone method with microphones at positions $x_1 = -117.6\text{mm}$, $x_2 = -255.3\text{mm}$ using an experimentally determined value of α_0 .

— : Theory for an unflanged pipe end by Levine & Schwinger (1948).

Figure 5.12 shows the reflection coefficient for a pipe terminated by a horn, with a radius of curvature equal to twice the pipe diameter (see figure 5.1d). Also for this configuration the theory for the unflanged pipe end appears to be valid for the magnitude $|R|$ of the reflection coefficient, at least up to $ka = 0.15$. For higher frequencies the radiation is considerably enhanced by the horn. At $ka = 0.1$ a small influence of room resonances is observed similar to what has been noted for an unflanged pipe end in figure 5.6a.

In contrast with the reflection coefficient $|R|$ the end correction δ strongly depends on the geometry of the pipe end. The end correction is a measure for the inertia of the acoustic flow around the pipe end. This effect is determined by the local flow within a region with length scale of the order of the pipe radius. Hence as far as $|R|$ is concerned, an unflanged pipe with a thick wall will behave like any other unflanged pipe if the wall thickness is small compared to the wavelength of the acoustic field. If the wall thickness is larger than the pipe radius the end correction δ of an unflanged, thick-walled pipe is close to that of a flanged pipe end. Indeed, as predicted by Ando (1969), an increase of the end correction from the value predicted by Levine & Schwinger (1948) for an unflanged thin walled pipe end is observed, i.e.

$$\delta/a = 0.6133 - 0.1168(ka)^2 \quad (5.23)$$

for $ka < 0.5$ towards the end correction for a flanged pipe end predicted by Nomura *et al.* (1960)

$$\delta/a = 0.8217 - 0.367(ka)^2 \quad (5.24)$$

for $ka < 0.5$. Figure 5.6b shows the end correction determined from the present measurements for an unflanged pipe end with thin ($a/(a+d) = 1.0$) and thick ($a/(a+d) = 0.70, 0.85$) walls. For a pipe end with wall thickness $a/(a+d) = 0.70$ the influence of the wall thickness on the end correction observed in figure 5.6b agrees with the theoretical data given by Ando (1969). The theoretical data given by Ando (1969) for $a/(a+d) = 0.85$ would imply a negligible influence of the wall thickness d on the end correction δ for $ka < 0.3$. However, the experimental results show a significant increase of δ for this value of the wall thickness. Because the theoretical end correction of Ando (1969) for $a/(a+d) = 0.85$ is substantially different from the experimentally determined values we think that this discrepancy is due to an error in the representation of the theoretical data, rather than a fundamental difference between the theory and experiment.

The end correction data for a pipe terminated by a horn is presented in figure 5.12b. The end correction (defined relative to the end of the straight pipe and therefore much larger) shows a gradual increase ($\pm 13\%$) with an increasing Helmholtz number ($0 < ka < 0.3$).

Using a one-dimensional approximation for the acoustic flow in the horn the end correction of the horn can be estimated to be $\delta/a = 1.92$, while a value close to 2.3 is found from the experiment. This indicates that the end correction of a horn is dominated by the inertia of the acoustic flow within the horn.

5.4.2 Nonlinear losses

The most significant nonlinear effect observed in the present experiments is the effect of the unsteady separation of the acoustic flow at the pipe end and the formation of vortices associated with the separation of the flow. This occurs when the amplitude of the acoustic displacement is large compared to the pipe radius, i.e. for conditions where the acoustic Strouhal number $St_{ac} = \omega a / \hat{u}_{ac}$ is small.

This nonlinear behavior of the acoustics of a pipe end causes a strong increase in the absorption of sound since part of the acoustic energy is transferred into the kinetic energy of the vortices which is subsequently dissipated by friction. The nonlinearity was studied by Bechert (1980) and Cummings & Eversman (1983) for a pipe which ends into a nozzle and by Ingard & Ising (1967) and Cummings (1984) for a flanged pipe end with an orifice plate at the exit.

For an unflanged pipe end, without mean flow, both with sharp and with rounded edges, the nonlinear behavior was studied extensively by Disselhorst & van Wijngaarden (1980). For high acoustic Strouhal numbers the vortices formed at the pipe end remain in the vicinity of the edges where they have been generated. Under these conditions, the

vorticity generation and convection process can be described qualitatively by a locally two-dimensional potential flow model, employing for example a discrete vortex method as proposed by Disselhorst & van Wijngaarden (1980). Peters & Hirschberg (1993) have shown that similar results can be obtained using a method with a single point vortex which carries the circulation in combination with a vortex segment attached to the edge, which takes care of the vorticity generation.

In contrast with the method of Disselhorst & van Wijngaarden (1980) the single vortex method predicts an acoustic energy absorption which is a factor 2.5 lower than the value observed experimentally for a sharp-edged pipe end. Comparison of the results of the two-dimensional flow method with flow visualization in a two-dimensional flow by Disselhorst & van Wijngaarden (1980) and with more detailed calculations based on a vortex blob method indicate that the flow model is fairly accurate. The discrepancy between the calculated and the measured value of the absorption is thought to be due to the translation of the two-dimensional results into equivalent three-dimensional situation. The procedure proposed by Disselhorst & van Wijngaarden (1980) is based on matching the acoustic potential flow. This procedure neglects the contribution of the vortex filament curvature on the self-induced velocity in the three-dimensional case.

In the case of a free vortex ring with a core radius corresponding to δ_{ac} this would result in an underestimation of the vortex velocity by a factor of three. Since the vortex ring velocity depends only weakly on the core radius this effect is only weakly dependent on the frequency.

For low Strouhal numbers a quasi-steady theory, like the one described by Disselhorst & van Wijngaarden (1980), can be used in which during that part of the period of the acoustic field with a positive velocity a jet-line outflow is assumed and during the remainder of the period the flow is characterized by the formation of a vena-contracta-type of inflow with a turbulent recovery region. For the acoustic power absorbed by the vortices, nondimensionalised with $\frac{1}{2}\rho_0\hat{u}_{ac}^3\pi a^2$ and averaged over a period of the acoustic oscillation, it is found that

$$\bar{P}_{ac}^* = \frac{\bar{P}_{rad}}{\frac{1}{2}\rho_0\hat{u}_{ac}^3\pi a^2} = \beta Sr_{ac}^{\frac{1}{2}} \quad (5.25)$$

for $Sr_{ac} \gg 1$, where a star denotes nondimensionalised quantities and

$$\bar{P}_{ac}^* = \frac{2c_d}{3\pi} \quad (5.26)$$

for $Sr_{ac} \ll 1$. The parameter c_d is determined by the geometry of the pipe end and is equal to 2 for a thin-walled unflanged pipe end and equal to 13/9 for a flanged pipe. Disselhorst & van Wijngaarden (1980) determined the parameter β by means of numerical simulation and found values between 0.6 and 1.0, depending on the number of point vortices used to describe the roll-up of the free shear layer. Using a simpler flow model, but the same procedure to translate the two-dimensional results into equivalent three-dimensional ones, Peters & Hirschberg (1993) found a value of $\beta = 0.2$.

The power loss due to vortex formation and radiation of acoustic energy at the pipe end, averaged over a period, can be determined experimentally from the reflection coefficient

using the relation (see Cargill (1982a))

$$\bar{P} = \frac{\pi a^2}{2\rho_0 c_0} (|p_+|^2 - |p_-|^2) \quad (5.27)$$

for an open end in a quiescent fluid. The amplitude of the acoustic velocity \hat{u}_{ac} at the open pipe end can be obtained from $|p_+ - p_-| = \rho_0 c_0 \hat{u}_{ac}$. For low Helmholtz numbers ka the theoretical reflection coefficient for a sharp-edged pipe end without vortex formation is given by equation (5.21). The acoustic power loss by radiation is then given by

$$\bar{P}_{rad}^* = \frac{1}{4} ka Sr_{ac} \quad (5.28)$$

For low Helmholtz numbers the power loss by radiation is negligible compared to the nonlinear losses given by equation (5.25), as long as

$$Sr_{ac} \ll (ka)^{-\frac{3}{2}} \quad (5.29)$$

Employing equation (5.27) the total loss of acoustic energy was determined from the pressure reflection coefficient at the pipe exit and the amplitude of the pressure signal at a pressure transducer.

For three frequencies (27 Hz, 54 Hz and 84 Hz) the acoustic Strouhal number was varied by changing the amplitude of the acoustic velocity \hat{u}_{ac} . For these frequencies the Helmholtz number is very small ($ka = 0.0074$, 0.0145 and 0.0230 , respectively), so that the condition for neglecting the radiation losses, given by equation (5.29), is certainly justified.

Figure 5.13a compares the experimental data for the nondimensionalised acoustic power loss by vortex shedding with the predictions of Disselhorst & van Wijngaarden (1980), given by equation (5.25) and (5.26). Also included in figure 5.13a are data obtained by Disselhorst & van Wijngaarden (1980) from measurements of the quality factor of a resonating open pipe. Our measured data present an independent check for the theory.

It is interesting to note that the high amplitude data ($Sr_{ac} \ll 1$) agree better with the theory than the original data of Disselhorst & van Wijngaarden (1980). From figure 5.13a it is concluded, that a quasi-stationary limit for the nonlinear power absorption is found which for $Sr_{ac} \ll 1$ is very close to the value from the theory proposed by Disselhorst & van Wijngaarden (1980). For lower acoustic amplitudes ($Sr_{ac} \gg 1$) the locally two-dimensional approximation of the vortex shedding proposed by Disselhorst & van Wijngaarden (1980) predicts the functional dependence on Sr_{ac} of the acoustic power. A fair agreement is found for a value $\beta = 0.5$. Hence with $\beta = 0.5$ equation (5.25) can be used as a fit of the data for $Sr_{ac} \gg 1$.

A change in the dependence on Sr_{ac} of \bar{P}_{ac}^* is observed around $Sr_{ac} = 10$. This is apparently related to the increasing asymmetry in the flow pattern during inflow and outflow of the acoustic field, observed by Disselhorst & van Wijngaarden (1980) in their flow visualization at $Sr_{ac} \approx 10$.

An advantage of the measurement of the reflection coefficient over the measurement of the quality factor of the resonating pipe as performed by Disselhorst & van Wijngaarden (1980) to determine the energy absorption by vortex formation, is that with the present

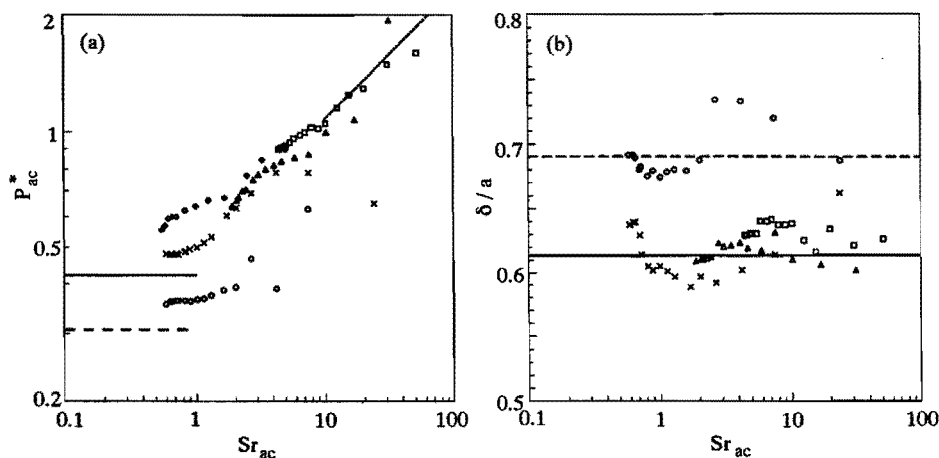


FIGURE 5.13: Acoustic amplitude dependence of (a) the nondimensionalised acoustic power loss \bar{P}^* and (b) end correction δ/a in absence of mean flow for an open pipe end with sharp edges or thick walls. Two-microphone method with microphones at positions $x_1 = -86.8$ mm, $x_2 = -224.7$ mm using an experimentally determined value of α_0 .

sharp edges: $a/(a+d) = 1.00$. (\times) $ka = 0.00742$, (Δ) $ka = 0.0145$, (\square) $ka = 0.0230$, (\circ) data Disselhorst & van Wijngaarden (1980). thick walls: $a/(a+d) = 0.70$. (\circ) $ka = 0.00742$.

Theory (a): — : quasi-stationary theory for ($a/(a+d) = 1.00$) (equation (5.26)); \cdots : high frequency limit for $\beta = 0.5$. - - - - : quasi-stationary theory for ($a/(a+d) = 0.70$) (equation (5.26)). (b): — : end correction for ($a/(a+d) = 1.00$) (Levine & Schwinger (1948)). - - - - : end correction for ($a/(a+d) = 0.70$) (Ando (1969)).

method also the influence of the nonlinear behavior on the end correction can be determined. From the end correction data shown in figure 5.13b it is observed that δ/a varies only slightly with the acoustic Strouhal number. In the high amplitude limit ($Sr_{ac} \ll 1$) a slight increase (10%) is found relative to the linear behavior and a local increase of about 5% is observed around $Sr_{ac} \approx 1$. This rather small influence of flow separation on the end correction is quite surprising when compared to the spectacular effect of a nonzero mean flow on the end correction which will be discussed in the following section.

The same experiments were also performed for a pipe end with thick walls, for which $d/(a+d) = 0.70$. The results are included in figure 5.13b. Similarly to the behavior of a sharp-edged pipe end, for a pipe end with thick walls a quasi-stationary limit of the acoustic power absorption is found, which agrees with the predicted value given in equation (5.26) for a flanged pipe. However, a strong dip is observed in the acoustic power absorption at a value of the acoustic Strouhal number close to $Sr_{ac} = 5$. For this Strouhal number the

vortices formed at the sharp edge of the pipe end travel during one period of the acoustic field over a distance of the order of the wall thickness d .

This effect is similar to the gain in acoustical energy for the case of a horn with a mean flow, which will be discussed in the next section. This effect can also be associated with the phenomenon of pipe tone and may play a significant role in the acoustical behavior of tone holes in woodwinds like a clarinet for which at resonance $Sr_{ac} \approx 1$.

The end correction is found to agree with the theory of Ando (1969) for a thick-walled pipe exit with $a/(a+d) = 0.70$ and it shows only a slight influence of the acoustic amplitude for $Sr_{ac} \ll 1$ and $Sr_{ac} \approx 1$.

5.5 OPEN PIPE END WITH MEAN FLOW

5.5.1 Unflanged pipe termination

A linear theory for the reflection of plane acoustic waves at a thin-walled, unflanged pipe end has been derived by Munt (1977). The results have been obtained in the form of integral equations which have been solved numerically by Munt (1990). In the presence of a uniform subsonic mean flow (plug flow) and for low acoustic amplitudes ($\hat{u}_{ac}/U_0 \ll 1$) the linear theory predicts the pressure reflection coefficient at the pipe end as a function of the Helmholtz number ka and as a function of the mean flow Mach number M .

In the theory of Munt a Kutta condition is assumed to apply at the edges of the pipe end, which implies a finite velocity and pressure at the edges. In that case an acoustic disturbance of the jet corresponds to a transfer of acoustic energy into the kinetic energy of the vortical disturbances of the jet shear layers. Munt (1990) found that the magnitude of the pressure reflection coefficient approaches a value of 1.0 for all Mach numbers if the Helmholtz number approaches zero, i.e.

$$\lim_{ka \rightarrow 0} |R| = 1, \text{ for all } M \quad (5.30)$$

The acoustic power loss P is according to Cargill (1982a) given by

$$P = \frac{\pi a^2 |\hat{p}_+|^2}{\rho_0 c_0} ((1+M)^2 - |R|^2 (1-M)^2) \quad (5.31)$$

which for the limit $ka \rightarrow 0$ can be approximated as

$$\lim_{ka \rightarrow 0} P = \frac{\pi a^2 |\hat{p}_+|^2}{\rho_0 c_0} 4M \quad (5.32)$$

irrespective of the frequency. For $M > 0$, P is always positive.

For intermediate Helmholtz numbers and for $M > 0$ the pressure reflection coefficient reaches a maximum value which lies above 1.0. Cargill (1982b) found that this maximum value appears at a Strouhal number of $Sr_0 \approx \pi$. The energy reflection coefficient R_E as given by equation (5.7) remains less than 1.0 for all values of the Helmholtz number ka .

For low Helmholtz numbers ka and low Mach numbers M approximate but closed-form solutions of the theory of Munt (1990) have been derived by Cargill (1982a,b) and by

Rienstra (1983). Both Cargill (1982) and Rienstra (1983) distinguish the case that a Kutta condition is not imposed and the case that a full Kutta condition is imposed at the sharp edge of the pipe exit, the latter corresponding to the case used by Munt (1977, 1990). For the reflection coefficient Cargill (1982b) found the following expressions for $ka \ll 1$

$$\begin{aligned} |R|_{NK} &\approx \left(\frac{1+M}{1-M} \right) \left(1 - \frac{(ka)^2}{2} \right) \\ |R|_K &\approx \left| \frac{(1+M)g-1}{(1-M)g+1} \right| \left(1 - \frac{(ka)^2}{2} \right) \end{aligned} \quad (5.33)$$

where $g = (g_1 + ig_2)/M$ and g_1 and g_2 are functions of the Strouhal number $Sr_0 = ka/M$ defined in Cargill (1982b). The indices NK and K denote the results for the cases without and with a Kutta condition imposed, respectively. The frequency dependence of the reflection coefficient corresponds to the low frequency behavior in absence of mean flow given by equation (5.21). For $0 < M \ll 1$ the convective correction factor for $|R|$ can be written as

$$|R| = (1 + M\mathcal{A}) \left(1 - \frac{(ka)^2}{2} \right) \quad (5.34)$$

where the amplification factor $\mathcal{A}_{NK} = 2$ and $\mathcal{A}_K = 2 - \frac{2g_1}{g_1^2 + g_2^2}$. \mathcal{A}_K varies continuously between $\mathcal{A}_K = 0$ for $Sr_0 \rightarrow 0$ and $\mathcal{A}_K = 0.90$ for $Sr_0 \rightarrow \infty$. It is found from equation (5.33) that

$$\begin{aligned} \lim_{ka \rightarrow 0} |R|_K &= 1 \\ \lim_{ka \rightarrow 0} |R|_{NK} &= \frac{1+M}{1-M} \end{aligned} \quad (5.35)$$

The latter result for $|R|_{NK}$ agrees with the result for the flow through the pipe with zero net acoustic power, given by equation (5.31), because without a Kutta condition imposed at the pipe edges no vortical disturbances are produced.

For the Kutta/No Kutta condition cases Rienstra (1983) confirmed the above limits in the behavior of the reflection coefficient. In addition he obtained an expression for the end correction. Rienstra (1983) also found a nonuniform behavior of the end correction for $ka \ll 1, M \ll 1$. For low frequencies ka , in the limit of vanishing mean flow $M \rightarrow 0$, with $Sr_0 = ka/M \rightarrow \infty$, the end correction attains the same limiting value as found by Levine & Schwinger (1948) in absence of mean flow, i.e.

$$\lim_{M \rightarrow 0, Sr_0 \rightarrow \infty} \delta/a = 0.6133 \quad (5.36)$$

For small but finite Mach number and very low frequencies Rienstra (1983) found

$$\lim_{ka \rightarrow 0, Sr_0 \rightarrow 0} \delta/a = 0.2554\sqrt{1-M^2} \quad (5.37)$$

Davies *et al.* (1980) indeed report that the end correction depends strongly on the frequency. However, since the end correction is presented as a function of the Helmholtz

number ka , rather than as a function of the Strouhal number Sr_0 , the differences in the end correction yield an apparent scatter of the obtained values. In addition, the limit of low Strouhal number is not reached because the data reported by Davies *et al.* (1980) and the data reported by Munt (1990) have been obtained for $ka > 0.1$ and $M < 0.3$.

In the present experiments our attention has been focussed on the range of the Helmholtz number $0 < ka < 0.06$. By varying the Mach number in the range $0.01 < M < 0.2$ the range of Strouhal numbers covered is $0.05 < Sr_0 < 6$. Here we note that Rienstra (1983) did not expect that the low Strouhal number limit of the end correction could experimentally be obtained for any reasonable value of ka and M .

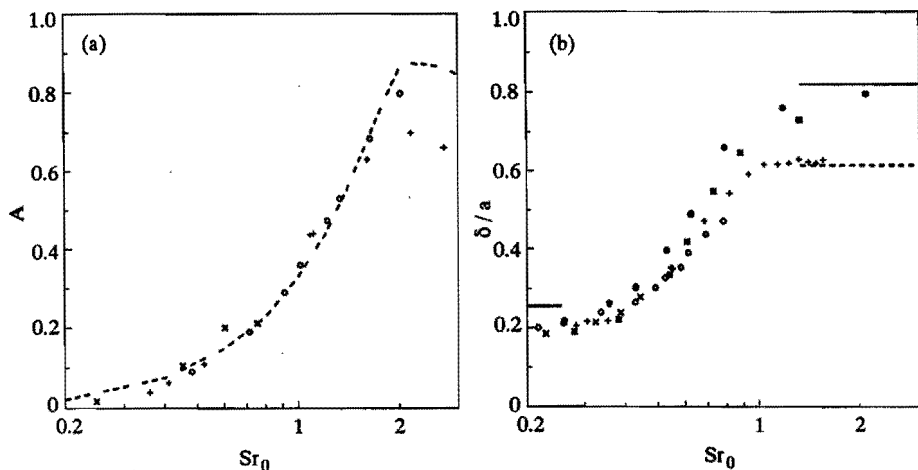


FIGURE 5.14: Pressure reflection coefficient $|R| = (1 + MA)(1 - \frac{1}{2}(ka)^2)$ expressed in terms of the amplification factor A and end correction δ for an open pipe end in presence of a mean flow at low acoustic amplitudes. Two-microphone method with microphone positions $x_1 = -51.8$ mm, $x_2 = -189.5$ mm.

sharp edges: (\circ) $M = 0.052$, $\hat{u}_{ac}/U_0 \approx 0.1$; ($+$) $M = 0.017$, $\hat{u}_{ac}/U_0 \approx 0.3$; Multi-microphone method with microphone positions $x_1 = -86.9$ mm, $x_2 = -239.3$ mm, $x_3 = -290.1$ mm, $x_4 = -782.4$ mm, $x_5 = -1925.5$ mm. sharp edges: (\times) $M = 0.002$, $\hat{u}_{ac}/U_0 \approx 0.1$. thick walls ($*$) $d/a = 4/3$, $M = 0.02$, $\hat{u}_{ac}/U_0 \approx 0.1$; (\bullet) $d/a = 20/3$, $M = 0.01$, $\hat{u}_{ac}/U_0 \approx 0.1$.

(a) Amplification factor A as a function of Strouhal number ($Sr_0 = ka/M$)
 - - - - - : A_K , ($A_{NK} = 2$) Cargill (1982b)

(b) End correction δ/a as a function of Strouhal number ($Sr_0 = ka/M$)
 unflanged pipe end: - - - - - : Levine & Schwinger (1948) ($M = 0$)
 and Howe (1979a) for ($Sr_0 \rightarrow \infty$); — : Rienstra (1983) for ($Sr_0 \rightarrow 0$).
 flanged pipe end: $\cdots\cdots$: Nomura *et al.* (1960) ($M = 0$).

Figure 5.14 presents the amplification factor \mathcal{A} appearing in the expression for the convective factor of the pressure reflection coefficient (equation(5.34)) and the end correction, both as a function of the Strouhal number for three different Mach numbers. The data obtained for these three Mach numbers collapse onto Cargill's (1982b) and Rienstra's (1983) predictions if a Kutta condition is imposed at the pipe edge.

For the various Mach numbers the maximum value of the reflection coefficient is found to agree with the data predicted by Cargill (1982b), which is $Str_0 \approx \pi$. Also the data for the end correction, presented in figure 5.14b, collapse onto a single curve when presented as a function of the Strouhal number. For high Strouhal numbers a limiting value is found which is independent of the Mach number, while for low Strouhal number a limiting value $\delta/a = 0.19$ is found. The latter value is close to the limit $0.2554\sqrt{1 - M^2}$ predicted by Rienstra (1983). The Mach number dependence predicted by Rienstra (1983), see equation (5.37), could not be verified experimentally, since this Mach number dependence is for $M < 0.1$ is within the scatter in the data ($\pm 0.02 a$ in δ).

For low Strouhal numbers the difference between the predicted and the experimental value of the end correction might be due to the interaction between the unsteady and the stationary boundary layers as described by Howe (1979a). As noted by Howe (1979a) the assumption of a uniform flow, made by Munt (1977, 1990), Cargill (1982b) and Rienstra (1983) is only valid if the thickness of the unsteady boundary layer ($\sqrt{2\nu/\omega}$) is large compared to the characteristic length of the gradients in the shear layers of the jet leaving the pipe exit. In a turbulent pipe flow this characteristic length scale is the thickness of the laminar sublayer δ_l . In our experiments δ_{ac}/δ_l varied between 0.2 and 3. In this range a transition was observed from a weak coupling between the turbulent flow and the acoustic field towards a strong coupling in the damping of acoustic waves in a turbulent flow. A breakdown of the validity of the plug-flow model of Munt (1977) could be expected for $\delta_{ac}/\delta_l \ll 1$. It is therefore surprising that the experimental data do not show any deviation from the theoretical results from Munt (1990) in this region.

It is also surprising that even a low Mach number mean flow affects the end correction significantly ($> 60\%$), while as shown in figure 5.13b, nonlinearities involving the formation of free jets affect the end correction only slightly ($< 10\%$).

5.5.2 Thick-walled pipe end and horn

For the thick-walled pipe terminations, illustrated in figure 5.1c, the end correction is presented in figure 5.14b. For a wall thickness of $d/a = 4/3$ the end correction for a high Strouhal number equals the value of the end correction without mean flow. For low Strouhal numbers the value $\delta/a = 0.19$ is found, which is equal to the value obtained for the end correction of an unflanged pipe termination at low Strouhal numbers.

For a very thick-walled pipe end, with $d/a = 20/3$, it is shown in figure 5.14b that the end correction as a function of the Strouhal number has a similar appearance as for an unflanged pipe end with thinner walls. For low Strouhal numbers the end correction seems to be independent of the wall thickness of the pipe end. The value for high Strouhal numbers is generally found to agree with the end correction without mean flow. For an increasing thickness of the wall at the pipe end the end correction for a flanged pipe

termination (equation (5.24), given by Nomura *et al.* (1960)) is obtained.

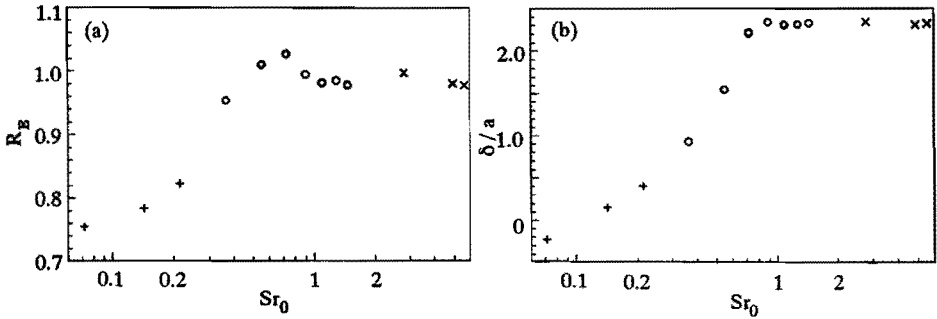


FIGURE 5.15: (a) Energy reflection coefficient R_E and (b) end correction δ for a horn as a function of the Strouhal number $Sr_0 = ka/M$. Multi-microphone method with microphones at positions $x_1 = -91.8$ mm, $x_2 = -577.8$ mm, $x_3 = -628.8$ mm, $x_4 = -4769.3$ mm, $x_5 = -4964.3$ mm, $x_6 = -6066.8$ mm. (+) $M = 0.107$, $\hat{u}_{ac}/U_0 \approx 0.1$, (o) $M = 0.042$, $\hat{u}_{ac}/U_0 \approx 0.1$, (x) $M = 0.011$, $\hat{u}_{ac}/U_0 \approx 0.1$.

The influence of the mean flow on the energy reflection coefficient R_E of a pipe terminated by a horn with radius of curvature equal to $r = 4a$ is shown in figure 5.15a for the mean flow Mach numbers $M = 0.011$, 0.042 and 0.107 . From a comparison with the pressure reflection coefficient obtained in the absence of the mean flow, see figure 5.12, it is observed that the reflection coefficient is dramatically influenced by the mean flow.

The most striking effect is that for a limited range of Strouhal numbers around $Sr_0 \approx \pi a/r$, the energy reflection coefficient R_E exceeds a value of 1.0. This indicates that the horn is a source of sound. For a horn such a behavior has been reported earlier by Powell (1951) who analyzed the radiated field and by Hirschberg *et al.* (1988) for different geometries of the horn using a two-microphone method. This feature has also been studied by Wilson *et al.* (1971) in connection with human whistling.

Also for the closely related Whistler nozzle configuration a similar behavior was found by Hirschberg *et al.* (1988), who explained the sound production in terms of vortex sound. Like in the 'Whistler nozzle', studied by Selerowicz *et al.* (1991) and Hirschberg *et al.* (1988), the horn presents a significant acoustical energy production when the travel time of vortices across the horn matches a number of acoustic oscillation periods. The acoustic energy production at $Sr_0 \approx \pi a/r$ corresponds to the first hydrodynamic mode. A second, less pronounced maximum at $Sr_0 \approx 2\pi a/r$ corresponds to the second hydrodynamic mode. This behavior is an indication for a strong coupling (Kutta condition) between the acoustic field and the vortical field near the separation point, this in spite of the rather smooth curvature of the wall.

The influence of the mean flow on the end correction is presented in figure 5.15b. The end correction is measured with the end of the pipe of radius a as reference ($x = 0$).

The end correction is dramatically influenced by the mean flow, in a similar manner as found for the unflanged pipe end presented in figure 5.14b. Similarly to the case of the unflanged pipe the value for high Strouhal numbers corresponds to the data obtained at low amplitudes in the absence of a mean flow (figure 5.12b). For low values of Sr_0 a strong influence of the Mach number on δ is observed. The end correction decreases from the value without a mean flow and for low Helmholtz numbers ($\delta/a = 2.3$) towards a negative value. This unexpected behavior of the end correction can not be explained intuitively and calls for further theoretical analysis. It is also interesting to note that a horn has a more strongly pronounced nonlinear behavior than an unflanged pipe for $\hat{u}_{ac}/U_0 \approx 0.5$ (Peters *et al.* (1992, 1993)).

5.6 CONCLUSIONS

An multi-microphone measurement technique has been described utilized to obtain accurate values of the reflection coefficient $|R|$ (0.1 %), end correction δ ($\pm 0.02 a$) and the damping coefficient α_{\pm} (2%) of plane acoustic waves in an open pipe termination for $ka < 0.3$ and $M < 0.2$.

The influence of the room resonances on the measured reflection coefficient $|R|$ is less than 0.2% for $ka < 0.1$ and less than 0.5% for $0.1 < ka < 0.3$. In the absence of a mean flow and for low amplitudes of the acoustic field the present experimental data for $|R|$, δ and α_0 determined for a closed pipe end and an open sharp-edged pipe end agree with the values provided by the theories proposed by Levine & Schwinger (1948) for $|R|$ and δ , and of the damping α_0 obtained from the solution proposed by Tijdeman (1975).

Our data on the influence of the wall thickness on $|R|$ and δ agree with the predictions derived by Ando (1969). For low frequencies $ka \ll 1$ the influence of the wall thickness on the reflection coefficient $|R|$ is found to be negligible. This is in agreement with the conclusion of Bechert (1980), that for low frequencies the exact shape of the pipe exit should not affect $|R|$. However, the end correction δ is strongly influenced by the wall thickness.

For high amplitudes of the acoustic field the influence of vortex formation, earlier predicted by Disselhorst & van Wijngaarden (1980) is confirmed. For low Strouhal numbers Sr_{ac} , based on the amplitude of the acoustic velocity, a quasi-stationary limiting value for the absorbed acoustic power is obtained. For high Strouhal numbers a locally two-dimensional model of the vortex shedding at the pipe end is used to predict the variation with the Strouhal number of the acoustic power absorption. Application of a two-dimensional model for the vortex shedding process at the end of a circular pipe, as proposed by Disselhorst & van Wijngaarden (1980), yields a prediction of the power absorption which is a factor 2.5 lower than the measurements. This difference might be due to a fundamental problem with the translation from a two-dimensional flow theory to a corresponding equivalent three-dimensional case.

For the high amplitude behavior of a pipe end with thick walls an indication was found that for certain values of the Strouhal number Sr_{ac} based on the acoustic velocity and the wall thickness the vortices formed at the pipe end can also transform part of their kinetic energy back into acoustic energy. This behavior is expected to be significant in tone holes

of reed woodwinds for which at resonance $Sr_{ac} = \mathcal{O}(1)$.

For an unflanged pipe end we were able to determine the influence of the mean flow on the behavior of a sharp-edged pipe termination in a low amplitude acoustic field. For $M \ll 1$ and $ka \ll 1$ the values predicted by Munt (1990) and Cargill (1982a,b) for the reflection coefficient and the value predicted by Howe (1979a) and Rienstra (1983) for the end correction all agree with the values found in the present experiments. For the reflection coefficient our data confirm the theory of Munt (1990) and Cargill (1982) and therefore imply indirectly that the Kutta condition has to be imposed at the pipe end. It is surprising that the plug-flow model of Munt (1977) applies so well to a fully developed turbulent mean flow even for values δ_{ac}/δ_l as low as 0.2. It is shown that the end correction depends mainly on the Strouhal number Sr_0 based on the mean flow velocity and that for low Strouhal number the end correction tends to the value of $\delta/a = 0.19$, which is close to the value of $\delta/a = 0.2554$, predicted by Rienstra (1983). For high Strouhal numbers Sr_0 the end correction agrees with the theoretical value of $\delta/a = 0.6133$ as predicted by Howe (1979a) and Levine & Schwinger (1948). The value of $\delta/a = 0.19$ found for low Strouhal numbers was also obtained for a thick-walled pipe end with $d/a = 4/3$ and for one with $20/3$. A negative value of the end correction was obtained for a pipe terminated by a horn. For all the pipe end geometries studied the value of the end correction at high Strouhal numbers agreed with the value obtained without a mean flow. In addition of a mean velocity field the aero-acoustic behavior of a horn is also considerably affected in the region where $Sr_0 \approx \pi a/r$. In a critical range of Sr_0 near this value the energy reflection coefficient R_E exceeds unity.

The influence of the mean flow on the damping coefficient was found to be accurately described by the quasi-laminar theory of Ronneberger (1975) in the region where the ratio $\delta_{ac}/\delta_l < 1$ and by the theory of Howe (1984) in the region where $\delta_{ac}/\delta_l > 1$. The influence of turbulence on the wall shear stress impedance could qualitatively be described by the rigid plate model, proposed by Ronneberger & Ahrens (1977), which in the present study has been modified to include memory effects of turbulence.

The multi-microphone method is found to be a very useful tool to obtain accurate quantitative data on the effect of vortex formation on the aeroacoustic behavior of a pipe termination. Furthermore, it is thought that the influence of imposed unsteadiness on turbulent shear stress can be obtained more accurately using the multi-microphone method than using alternative methods.

REFERENCES

- ABOM, M. & BODEN, H. (1988) Error analysis of two microphone measurements in ducts with flow. *J. Acoust. Soc. Am.* **83**, 2429 - 2438.
- ABRISHAMAN, M. (1977) Effect of flow on the acoustic impedance of a duct exit. *Noise and Fluid Engineering, Proceedings Winter Annual Meeting AMSE, Atlanta, Georgia*, 171 - 177.
- ANDO, Y. (1969) On the sound radiation from semi-infinite circular pipe of certain wall thickness. *Acustica* **22**, 219 - 225.
- ALFREDSON, R.J. & DAVIES, P.O.A.L. (1970) The radiation of sound from an engine exhaust. *J. Sound & Vibr.* **13** 4, 389 - 408.

- BECHERT, D.W. (1980) Sound absorption caused by vorticity shedding, demonstrated with a jet flow. *J. Sound & Vibr.* **70**, 389 - 405.
- BODEN, H. & ABOM, M. (1986) Influence of errors on the two-microphone method for measuring acoustic properties in ducts. *J. Acoust. Soc. Am.* **79**, 541 - 549.
- CARGILL, A.M. (1982a) Low-frequency sound radiation and generation due to the interaction of unsteady flow with a jet pipe. *J. Fluid Mech.* **121**, 59 - 105.
- CARGILL, A.M. (1982b) Low frequency acoustic radiation from a jet pipe - a second order theory. *J. Sound & Vibr.* **83**, 339 - 354.
- CUMMINGS, A. & EVERSMA, W. (1983) High amplitude acoustic transmission through duct terminations: theory. *J. Sound & Vibr.* **91**, 503 - 518.
- CUMMINGS, A. (1984) Acoustic nonlinearities and power losses at orifices. *A.I.A.A. Journal* **22**, 6, 786 - 792.
- DAVIES, P.O.A.L., BENTO COELHO, J.L. & BHATTACHARYA, M. (1980) Reflection coefficients for an unflanged pipe with flow. *J. Sound & Vibr.* **72**, 543 - 546.
- DAVIES, P.O.A.L. (1987) Plane wave reflection at flow intakes. *J. Sound & Vibr.* **115**, 560 - 564.
- DAVIES, P.O.A.L. (1988) Practical flow duct acoustics. *J. Sound & Vibr.* **124**, 91 - 115.
- DISSELHORST, J.H.M. & WIJNGAARDEN, L. VAN (1980) Flow in the exit of open pipes during acoustic resonance. *J. Fluid Mech.* **99**, 293 - 319.
- HIRSCHBERG, A., BRUGGEMAN, J.C., WIJNANDS, A.P.J. & MORGENSTERN, M. (1988) The whistler nozzle and horn as aero-acoustic sound sources in pipe systems. *Proceedings of the Institute of Acoustics* **10**, 3, 701-708.
- HOWE, M.S. (1979a) Attenuation of sound in a low Mach number nozzle flow. *J. Fluid Mech.* **91**, 209 - 229.
- HOWE, M.S. (1979b) The interaction of sound with low Mach number wall turbulence, with application to sound propagation in turbulent pipe flow. *J. Fluid Mech.* **94**, 729 - 744.
- HOWE, M.S. (1984) On the absorption of sound by turbulence and other hydrodynamic flows. *IMA J. Appl. Math.* **32**, 187 - 209.
- INGARD, U. & ISING, H. (1967) Acoustic nonlinearity of an orifice. *J. Acoust. Soc. Am.* **42**, 1, 6 - 17.
- INGARD, U. & SINGHAL, V.K. (1974) Sound attenuation in turbulent pipe flow. *J. Acoust. Soc. Am.* **55**, 535 - 538.
- INGARD, U. & SINGHAL, V.K. (1975) Effect of mean flow on the acoustic resonance of an open-ended duct. *J. Acoust. Soc. Am.* **58**, 788 - 793.
- KIRCHHOFF, G. (1868) Über den Einfluss der Wärmeleitung in einem Gase auf die Schallbewegung. *Pogg. Ann.* **134**, 6, 177 - 193.
- LEVINE, H. & SCHWINGER, J. (1948) On the radiation of sound from an unflanged circular pipe. *Physical Review* **73**, 383 - 406.
- LOUIS, B. & ISABEY, D. (1992) Interaction of oscillatory and constant turbulent flows in airway-like tubes during impedance measurement. *Submitted to J. Appl. Phys.*
- MANKBADI, R.R. & LIU, J.T.C. (1992) Near-wall response in turbulent shear flows subjected to imposed unsteadiness. *J. Fluid Mech.* **238**, 55-71.
- MECHEL, F., SCHILZ, W. & DIETZ, J. (1965) Akustische Impedanz einer luftdurchströmten Öffnung. *Acustica* **15**, 199 - 206.
- MORSE, P.M. & INGARD, K.U. (1968) *Theoretical Acoustics*. McGraw-Hill book company.

- MUNT, R.M. (1977) The interaction of sound with a subsonic jet issuing from a semi-infinite cylindrical pipe. *J. Fluid. Mech.* **83**, 609 - 640.
- MUNT, R.M. (1990) Acoustic transmission properties of a jet pipe with subsonic jet flow: I, the cold jet reflection coefficient. *J. Sound & Vibr.* **142**, 413 - 436.
- NOMURA, Y., YAMAMURA, I. & INAWASHIRO, S. (1960) On the acoustic radiation from a flanged circular pipe. *J. Phys. Soc. Japan* **15** 3, 510 - 517.
- PETERS, M.C.A.M., HIRSCHBERG, A., KONIJNENBERG, J.A., HUIJSMANS, F.J.J., LEEUW, R.W. DE, OP DE BEEK, S.S. & WIJNANDS, A.P.J. (1992) Experimental study of the aeroacoustic behavior of an open pipe termination at low Mach numbers and low Helmholtz numbers. *DGLR/AIAA Paper 92-02-055* 14th Aeroacoustics Conference Aachen, Proceedings Vol. **1**, 350 - 355.
- PETERS, M.C.A.M. & HIRSCHBERG, A. (1993) Acoustically induced periodic vortex shedding at sharp edged open channel ends: simple vortex models. *J. Sound & Vibr.* **161** 2, 281 - 299.
- PETERS, M.C.A.M., HIRSCHBERG, A. & WIJNANDS, A.P.J. (1993) The aero-acoustic behavior of an open pipe exit. *Conference Proceedings Noise '93* St. Petersburg, G.O.S. **6**, 191 - 196.
- PIERCE, A.D. (1989) Acoustics, an introduction to its physical principles and applications. McGraw-Hill book company, New York.
- POWELL, A. (1951) A Schlieren study of small scale air jets and some noise measurements in two-inch diameter air jets. *ARC 14726 FM 1694*
- RAYLEIGH (1896) The theory of sound. Vol II, 2nd ed., The Macmillian Company, pp. 319 - 326.
- RIENSTRA, S.W. (1983) A small Strouhal number analysis for acoustic wave-jet flow-pipe interaction. *J. of Sound & Vibr.* **86**, 539 - 556.
- RONNEBERGER, D. (1975) Genaue Messung der Schalldämpfung und der Phasengeschwindigkeit in durchströmten Rohren im Hinblick auf die Wechselwirkung zwischen Schall und Turbulenz. *Habilitationsschrift Mathematisch-Naturwissenschaftliche Fakultät der Universität Göttingen*
- RONNEBERGER, D. & AHRENS, C. (1977) Wall shear stress caused by small amplitude perturbations of turbulent boundary-layer flow: an experimental investigation. *J. Fluid Mech.* **83** 3, 433 - 464.
- RONNEBERGER, D. (1991) Response of wall turbulence to imposed unsteadiness. *Euromech Colloquium 272*, Aussois, France.
- SCHLICHTING, H. (1968) Boundary Layer Theory. McGraw-Hill Book Company, New York.
- SELEROWICZ, W.C., SZUMOWSKI, A.P. & MEIER, G.E.A. (1991) Self-excited compressible flow in a pipe-collar nozzle. *J. Fluid Mech.* **228**, 465-485.
- TJDEMAN, H. (1975) On the propagation of sound in cylindrical tubes. *J. Sound & Vibr.* **39** 1, 1 - 33, also as NLR Report MP 74004 U.
- TOULOUKIAN, Y.S., SAXENA, S.C. & HESTERMANS, P. (1975) Thermophysical properties of matter.
- WEAST, R.C. (1976) Handbook of Chemistry and Physics. 57th edition CRC Press Florida.
- WIJNGAARDEN, L. VAN (1968) On the oscillations near and at resonance in open pipes. *J. Eng. Math.* **11** 3, 225 - 240.
- WILSON, J.A., BEAVERS, G.S., DE COSTER, M.A., HOLGER, D.K. & REGENFUSS, M.D. (1971) Experiments on the fluid mechanics of whistling. *J. Acoust. Soc. Am.* **50**, 366 - 372.

The aeroacoustic behavior of pipe systems with two closed side branches

Abstract

High-amplitude acoustic pulsations occur in pipe systems in which the acoustic energy can accumulate in resonant modes. The aero-acoustic source strength is determined from a numerical simulation of the periodic flow for a pipe system consisting of a main pipe and two closed side branches in tandem or opposite to each other. Together with an estimate of the acoustic energy loss in the pipe system due to visco-thermal action an equilibrium amplitude of the acoustic resonance is predicted, which for a low-amplitude acoustic field is in fair agreement with the experimental data.

At high acoustic amplitudes non-linear deformation of the waves generates higher harmonics. The even harmonics are efficiently radiated which results in a considerable damping due to radiation.

The influence of the length of the side branches, the mean flow velocity, pipe cross-section geometry and ambient pressure on the pulsation amplitude is studied experimentally. Also the influence of the geometry of the edges in the junction on the pulsations is discussed. For rounded edges acoustical amplitudes \hat{u}_{ac}/U_0 larger than unity are observed and nonlinear wave deformation results in weak shock formation.

6.1 INTRODUCTION

Analysis of field cases of flow-induced pulsations by the Netherlands Gasunie indicated that closed side branches were the origin of the most severe pulsation problems. In some cases it caused damage to the pipe system. After some preliminary laboratory experiments at Gasunie a systematic study in collaboration with Eindhoven University of Technology¹ has been undertaken. The main results of this study are described in the thesis by Bruggeman (1987).

In pipe systems with closed side branches severe acoustic resonances have also been observed in laboratory experiments by amongst others Ingard & Singhal (1976), Baldwin & Simmons (1986) and Jungowski *et al.* (1989). A single closed side branch is a perfect reflector of plane acoustic waves if the length of the side branch is equal to an odd number times a quarter of the wave length of the acoustic field. However, since as pointed out by Bruggeman (1987) a single side branch is not a resonator strong pulsations are not to be expected ($\hat{p}_{ac}/\rho_0 c_0 U_0 < 0.1$).

¹Gasdynamics/Aeroacoustics group of the department of Physics

The pulsations can become much stronger in a pipe system in which an acoustic resonator is present since in that case acoustic energy can accumulate. Such is the case in for example a pipe system with two closed side branches placed a distance $L_3 = 2mL$ apart, where m is an integer number.

Different geometries for a pipe system with two closed side branches (for $m = 0, 1$) in which flow-induced acoustic resonances can occur are shown in figure 6.1. In the

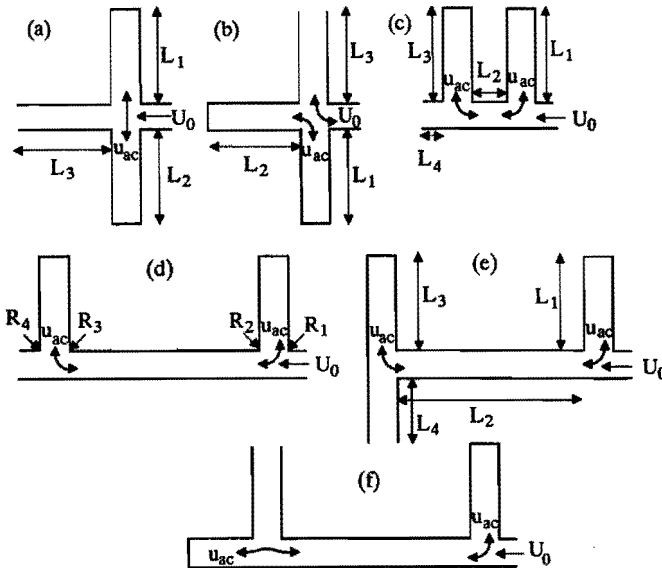


FIGURE 6.1: Geometries of a pipe system with two closed side branches in which resonances can occur. (a) co-axial branches, with cross-junction (b) two closed side branches under right angle, with diverted mean flow (c) tandem branches ($m = 0$) with T-junctions (d) tandem branches ($m = 1$) and horizontal mean flow (e) tandem branches ($m = 1$) and downward diverted mean flow (f) tandem branches ($m = 1$) and horizontal second side branch and upward diverted mean flow. Only the geometries shown in (a) and (c,d) are studied in this chapter, since in these geometries the highest amplitude pulsations are observed.

geometries considered there is a constant main flow with velocity U_0 from right to left. Superimposed is an acoustic velocity field resonating between the two closed side branches. Assuming a standing wave pattern in the resonator, dominated by the first mode, the amplitude of the resonating acoustic velocity field \hat{u}_{ac} measured at the junction is related

to the acoustic pressure amplitude \hat{p}_{ac} according to $\hat{u}_{ac} = \hat{p}_{ac}/\rho_0 c_0 U_0$, where \hat{p}_{ac} is measured at the end of the closed side branch. This relation has to be corrected for high amplitudes of the acoustic field, when due to non-linear wave propagation in the side branches higher harmonics are formed and the pressure signal is strongly distorted by the presence of these higher harmonics. The order of magnitude of \hat{u}_{ac}/U_0 observed in experiments is given for each configuration in figure 6.1.

Since the low- and moderate-amplitude case has already been studied both experimentally and theoretically by Bruggeman (1987) and others, in this chapter we will address geometries in which a high-amplitude acoustic field is resonating ($\hat{p}_{ac}/\rho_0 c_0 U_0 = \mathcal{O}(1)$).

The quality factor of the resonator is defined as the ratio of the total acoustic energy content and the loss of acoustic energy, both per period of the acoustic field. It is determined by the loss of acoustic energy through two effects; the damping of the acoustic waves by viscous forces and heat conduction in the boundary layer of the pipe flow; and by radiation of the acoustic energy into the main pipe. An additional radiation loss can be caused by vibrations of the pipe walls. The radiation losses into the main pipe are smallest when the length of the side branches is approximately $(n + \frac{1}{2})\frac{1}{2}\lambda$ and the distance between the side branches is approximately $m\frac{1}{2}\lambda$, where m and n take integer values and λ is the wavelength of the resonating acoustic field².

As a result the highest quality factor of the resonator is expected for the pipe geometry with two side branches opposite to each other, further called the *cross-junction geometry*, see figure 6.1a ($m = n = 0$), or for the geometry with tandem branches with the distance between the branches much smaller than the acoustic wavelength, further called the *double T-junction geometry*, see figure 6.1c (also $m = n = 0$).

These configurations have been studied experimentally by Ziada & Bühlmann (1992) for pipes with circular cross-section. They indeed observed that for a cross-junction geometry with sharp edges pulsations with $\hat{u}_{ac}/U_0 \approx 0.3$ could be obtained. Ziada & Bühlmann (1992) also observed that with increasing length of the side branches the amplitude of the higher modes could attain a higher pressure amplitude than the fundamental mode. This phenomenon will be discussed further in section 6.6.

Experiments for double T-junction geometries with a distance of half a wavelength between the branches or more ($m \geq 1$) have been performed by Bruggeman *et al.* (1987, 1989). On the basis of the value of the amplitude of the acoustic field \hat{u}_{ac}/U_0 Bruggeman *et al.* (1987, 1989) distinguished three cases:

- for small amplitudes ($\hat{u}_{ac}/U_0 < 10^{-3}$) the growth of disturbances in the shear layer can be described by linearized theory.
- for moderate pulsation amplitudes ($10^{-3} < \hat{u}_{ac}/U_0 < 10^{-1}$) the linear theory is valid for the initial disturbance of the shear layer only. At a later stage, due to nonlinear effects, coherent vortex structures are formed which limit the amplification of the perturbations in the shear layer.

The rate of generation of vorticity and the convection of the vorticity are not strongly influenced by the acoustic velocity field. Bruggeman (1987) showed that at these

²Here the end corrections $\delta = \mathcal{O}(H)$ of the side branches at the junctions are neglected since the effect is small as long as the side branches are long compared to the pipe width H .

moderate amplitudes the strength of the dipole sound source is independent of the amplitude of the acoustic field.

- for high pulsation amplitudes ($\hat{u}_{ac}/U_0 = \mathcal{O}(1)$) the vortex layer rolls up instantaneously into a coherent vortical structure. The generation and convection of vorticity are strongly influenced by the acoustic velocity field. As a result also the strength of the dipole sound source depends on the amplitude of the acoustic field.

Jungowski *et al.* (1989) studied the influence of the variation of the ratio between the diameter of the side branch and that of the main pipe. Stronger pulsations were observed if the diameter of the side branches was decreased relative to the diameter of the main pipe.

Baldwin & Simmons (1986) studied the effect of the geometry of the edges of the junction for a single side branch configuration. They concluded that in a geometry with sharp edges the highest pulsation amplitudes can be expected.

Bruggeman *et al.* (1987, 1991) also studied the influence of the sharpness of the edges of the junctions. For circular pipes with diameter D the amplitude of the acoustic oscillations in a tandem side branch geometry increased significantly (up to a factor 5) when the edges were rounded with a radius of curvature $R = 0.2 D$. By extrapolation of a series of experiments with increasing ambient pressure Bruggeman (1987) estimated the maximum pulsation amplitude in a double T-junction geometry ($m = 1$) with rounded edges to be $\hat{u}_{ac}/U_0 = 0.6 \pm 0.1$, this in absence of friction losses.

The present chapter presents additional experimental data for different double-side-branch geometries as well as a comparison of the predicted strength of the sound source in the resonant acoustic field with experimental data. The strength of the source can be obtained from the model of the periodic flow in the cross-junction or T-junction, described in chapter 4. For a given value of the amplitude of the acoustic field the source strength is determined by applying the vortex sound theory of Powell (1964) and Howe (1975). The results for a T-junction and a cross-junction will be presented in the next section.

At low frequencies ($kH \ll 1$) the losses due to radiation into the main pipe are negligible in case m and n have integer values. In the present investigation rigid walls are assumed and radiation via the pipe walls is not taken into account.

At low amplitudes the acoustic field can be fairly well described by a single mode resonating between the side branches (see figure 4.13a) and only the acoustic energy losses due to friction and heat conduction at the pipe walls have to be estimated. This energy loss is determined in section 6.3.

At high amplitudes the acoustic waves steepen while traveling inside the side branches due to nonlinear effects. As a result acoustic energy from the fundamental mode is converted to higher harmonics and is effectively radiated into the main pipe for the even harmonics which do not correspond to resonant modes of the pipe system. This type of acoustic energy loss is discussed in section 6.4.

In section 6.5 it is shown how a balance between the aeroacoustic energy source and the energy losses determine the equilibrium amplitude of the resonant acoustic field. For a cross-junction a comparison with experimental data is given in section 6.6. In section 6.6

also the influence of the pipe cross section geometry (circular or square) and the sharpness of the edges in the junctions on the aeroacoustics is discussed.

6.2 DETERMINATION OF AERO-ACOUSTIC SOURCE STRENGTH

The mechanism of the flow-induced pulsations is the coupling between the vorticity, generated at the sharp edges of the junction and the resonant acoustic field. Due to this interaction, kinetic energy of the main stream and the irrotational flow induced by the vorticity is transferred to the acoustic field and the other way around. The theory underlying the phenomenon has been described by Powell (1964) and Howe (1975). For a low Mach number, isentropic flow the first-order approximation of the instantaneous rate of energy transferred from the mean flow to the acoustic field is given by (see chapter 2)

$$P(t) = - \iiint_V \rho_0 (\vec{\omega} \times \vec{v}) \cdot \vec{u}_{ac} dV \quad (6.1)$$

The value of $P(t)$ will be referred to as the instantaneous rate of acoustic energy production by the aeroacoustic source. From this equation it is clear that the acoustic energy source strength depends on the acoustic velocity $\vec{u}_{ac}(\vec{x}, t)$, the total velocity $\vec{v}(\vec{x}, t)$ and the vorticity $\vec{\omega}(\vec{x}, t)$ present in the flow field. Only the non-acoustic part of the total flow field, i.e. the mean flow field and the flow induced by vorticity contribute to the integral. For periodic pulsations, i.e. oscillations with stationary amplitude, the net strength of the aeroacoustic source $\langle P \rangle$ is obtained upon averaging $P(t)$ over one period of the acoustic velocity field.

The potential-flow solution for the periodic flow in a T-junction or a cross junction, described in chapter 4, allows for vorticity in the vortex sheet only. This implies that the acoustic energy can be obtained by performing the integration in equation (6.1) along the vortex sheet. The instantaneous and net acoustic energy source strength will be presented in dimensionless form using the total kinetic energy of the mean flow $\rho_0 U_0^3 A$ as a reference, where A is the cross-sectional area of the side branch.

6.2.1 Double T-junction geometry

In a double T-junction geometry like shown in figure 6.1c-f two source regions are present in which the vorticity generated at the sharp edges interacts with the resonating acoustic velocity field. The difference between the various T-junctions is the direction of the mean flow and of the acoustic flow. This is not only important for the generation and convection of vorticity but it has also a strong influence on the strength of the aeroacoustic energy source. In this section the source strength is determined in a T-junction with a main flow from right to left through the main pipe. We consider two cases; an acoustic velocity field coming out of the side branch and going into either the up- or downstream part of the main pipe. This describes the flow which is present in tandem side branches, shown in figure 6.1c,d and the flow in the upstream T-junction in figure 6.1e,f.

Figure 6.2 shows the instantaneous strength of the aeroacoustic sound source in a T-junction, obtained with the different numerical methods employed in chapter 4 to simulate

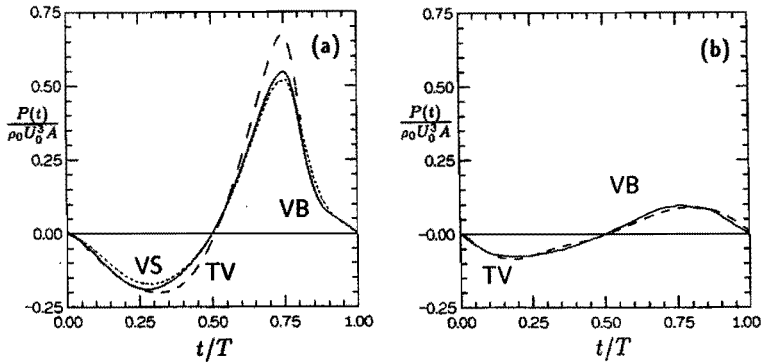


FIGURE 6.2: Instantaneous energy source strength in a T-junction with an acoustic field resonating between the side branch and the downstream part of the main pipe.

(a) High-amplitude acoustic field, $\hat{u}_{ac}/U_0 = 0.62$ with $Sr = 0.29$.

(b) Moderate-amplitude acoustic field, $\hat{u}_{ac}/U_0 = 0.17$ with $Sr = 0.38$.

Results obtained from the numerical simulations presented chapter 4. (---) two-vortex method TV (see figure 4.14) (·····) vortex-sheet method VS (see figure 4.16) (—) vortex-blob method VB (see figure 4.19 and 4.20).

the periodic flow. Here the acoustic field resonates between the closed side branch and the downstream part of the main pipe. The Strouhal number used is $Sr = 0.29$ while the amplitude of the acoustic field is $\hat{u}_{ac}/U_0 = 0.62$, corresponding to the values found in the high-amplitude flow visualization experiment shown in figure 4.12.

Since the periodic solutions obtained with the vortex-sheet and vortex-blob method are very similar the instantaneous source strengths obtained from the results of both methods are approximately equal. Apparently the vortex structures which are convected in downstream direction into the main pipe do not contribute to the acoustic source strength, given by equation (6.1), since the convection velocity \vec{v} of such a vortex structure is parallel to the velocity of the acoustic field \vec{u}_{ac} . These vortex structures are taken into account in the vortex-blob method, but in the vortex-sheet method they are removed when convected a certain distance into the downstream part of the main pipe.

It turns out that also the simple two-vortex method yields an accurate prediction of the source strength. Apparently, concentrating the spatial distribution of vorticity into a discrete vortex at the center of vorticity of the actual distribution of vorticity does not affect the source strength, at least not for this case. This is probably due to the circumstance that in reality for a high-amplitude acoustic field the vorticity rapidly concentrates into highly rolled-up region. For such vorticity distributions the two-vortex method yields a satisfactory approximation.

Figure 6.2 also presents the source strength obtained from results of the periodic flow

presented in figure 4.20, obtained by the two-vortex method and the vortex-blob method for the moderate-amplitude case $\hat{u}_{ac}/U_0 = 0.17$ with $Sr = 0.38$. For this moderate-amplitude periodic flow the rate of vorticity generation is approximately constant and the vorticity is nearly uniformly distributed along the shear layer. For this case the two-vortex method does not give an accurate description of the vorticity distribution. However, figure 6.2b shows that even in this case global characteristics such as the source strength are still reasonably accurately determined by the simple two-vortex method compared to the results of the vortex-blob method. This validates the single-vortex models used by Nelson *et al.* (1983) and Bruggeman (1987) to estimate the aeroacoustic source strength at moderate and high amplitudes.

The dependence of the strength of the aeroacoustic sound source on the amplitude of the acoustic velocity field can be determined by solving the periodic flow problem for a range of values of \hat{u}_{ac}/U_0 . However, for a variation of the acoustic amplitude also the Strouhal number at which in the experiment the resonance is at maximum pulsation amplitude varies. For a moderate-amplitude resonance the Strouhal number is approximately 0.4, which decreases to 0.3 for a high-amplitude acoustic resonance.

In the present study the periodic flow in a T-junction, in the presence of an acoustic field resonating between the side branch and the downstream part of the main pipe, is simulated numerically for a number of acoustic amplitudes, all for a fixed value of the Strouhal number. For the moderate-amplitude case the Strouhal number was taken to be $Sr = 0.4$, while for the high-amplitude case the Strouhal number was taken to be $Sr = 0.3$. The results obtained with the vortex-blob method for a T-junction with an acoustic field resonating between the side branch and the downstream part of the main pipe are shown in figure 6.3.

For moderate acoustic amplitudes the net source strength increases linearly with the acoustic amplitude. This can be explained as follows. For moderate amplitudes of the acoustic velocity field both the vorticity generated and the convection velocity of the vorticity are independent of the amplitude of the acoustic field. Both are completely determined by the mean flow U_0 . Only the instant of the formation of a new vortex structure in the shear layer is determined by the frequency of the acoustic field. Since the acoustic velocity field is described by an irrotational potential flow in the T-joint, the instantaneous acoustic power generation given by equation (6.1) depends linearly on the acoustic amplitude.

For acoustic amplitudes larger than about 0.3, both the rate of vorticity generation and the convection of the vorticity is strongly influenced by the acoustic field and the net source strength increases nonlinearly with the acoustic amplitude.

In a double-side-branch setup two T-junctions and therefore also two aero-acoustic sources are present. In the upstream side branch the acoustic velocity field is resonating between the side branch and the downstream part of the main pipe, in the downstream side branch the acoustic velocity field is resonating between the side branch and the upstream part of the main pipe. The strength of the respective sources in the T-junction of the upstream and that in the downstream positioned side branch have to be added to obtain the overall aeroacoustic energy source strength. The phase relation between the aeroacoustic sources is determined by the resonating acoustic field.

The instantaneous strength of the aeroacoustic source for the two side branches is

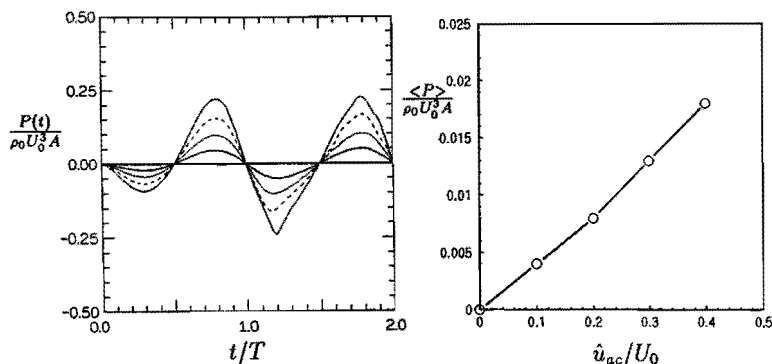


FIGURE 6.3: Instantaneous and net energy source strength $\langle P \rangle$ in a T-junction with an acoustic field resonating between the side branch and the downstream part of the main pipe. The Strouhal number is fixed to $Sr = 0.4$ for a moderate-amplitude acoustic field. Results obtained from a numerical simulation of the flow by the vortex-blob method ($\delta = 0.10$). Acoustic amplitude \hat{u}_{ac}/U_0 : (—): 0.1, (⋯⋯): 0.2, (---): 0.3, (- - -): 0.4.

presented in figure 6.4 for high values of the acoustic amplitude. The Strouhal number is taken to be constant $Sr = 0.3$ for this high-amplitude case. Only results obtained with the vortex-blob method are presented. The desingularisation parameter δ used for the calculation of the flow was chosen to be $\delta = 0.10$. It was checked, that a variation of this value by a factor two up or down did not affect the net source strength.

From the data presented in figure 6.4 it is clear that in the upstream side branch the production of acoustic energy is large during the second half period of the acoustic field, while for the downstream side branch the energy absorption is large during the first half period of the acoustic field. As a result for $\hat{u}_{ac}/U_0 > 0.5$ the sound source in the upstream T-junction gives a net production, while in the downstream T-junction the sound source gives a net absorption. This difference between the two T-junctions was qualitatively explained by Bruggeman (1987) as a result in the difference of the acoustic velocity between the up- and downstream edges of the T-junctions. For the upstream positioned side branch the acoustic velocity at the downstream edge of the T-junction is approximately 3 times larger than the acoustic velocity at the upstream edge. The opposite is the case for the T-junction of the downstream positioned side branch. From figure 6.4 it becomes clear that the instantaneous source strength increases approximately linearly with the acoustic amplitude, except at the downstream edge of the second side branch. While the initial absorption increases with increasing amplitude the production is only slightly influenced by an increase in the amplitude of the acoustic velocity field. In the second side branch

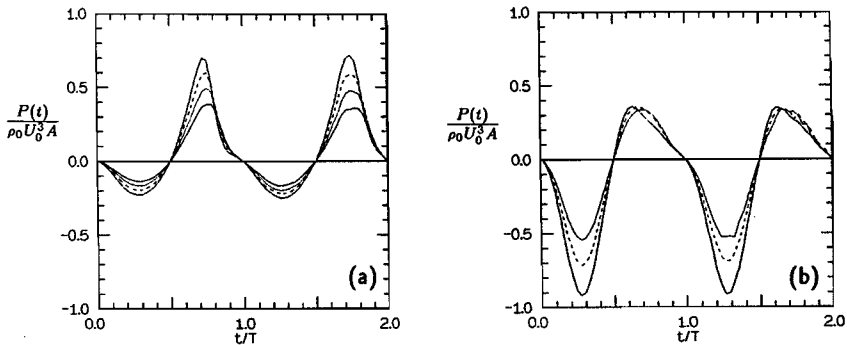


FIGURE 6.4: Instantaneous energy source strength $P(t)$ in a geometry with tandem branches. (a) T-junction with an acoustic field resonating between the side branch and the downstream part of the main pipe ($0.5 \leq \hat{u}_{ac}/U_0 \leq 0.8$). (b) T-junction with an acoustic field resonating between the side branch and the upstream part of the main pipe ($0.6 \leq \hat{u}_{ac}/U_0 \leq 0.8$). Acoustic amplitude varied with Strouhal number fixed ($Sr = 0.3$). Results obtained from the numerical simulation with the vortex-blob method ($\delta = 0.10$). Acoustic amplitude \hat{u}_{ac}/U_0 : (—): 0.5, (.....): 0.6, (---): 0.7, (-·-·-): 0.8.

the net source strength is therefore negative.

The net source strengths for the up- and downstream T-junction are presented in figure 6.5. For moderate acoustic amplitudes the Strouhal number is fixed to $Sr = 0.4$, while for high acoustic amplitudes the Strouhal number is taken to be $Sr = 0.3$ in accordance with the experimentally observed value of the Strouhal number at resonance conditions. The net source strength in the upstream T-junction is for moderate amplitudes equal to that presented in figure 6.3. The net source strength of the downstream branch is negative for $\hat{u}_{ac}/U_0 > 0.45$. The overall source strength of the system with tandem branches is equal to the sum of the two contributions. It is zero for an acoustic amplitude of $\hat{u}_{ac}/U_0 \approx 0.65$. This limits the amplitude of the acoustic field which can be obtained in an ideal resonator with a tandem side branches (in absence of other sound sources). This phenomenon is in literature often referred to as the *vortex damping mechanism*.

The amplitude at which a zero net source strength is predicted can be realized only if losses due to radiation and damping of acoustic waves are negligible, i.e. in practice the equilibrium amplitude will be lower. In the next sections the source strength and acoustic energy losses occurring in the cross-junction geometry will be discussed further in detail.

The maximum amplitude which can be obtained in a pipe system with tandem branches is considerably lower than the corresponding value for a resonator with a single side branch with an acoustic field resonating between the side branch and the downstream part of the

main pipe³ and also, as will be shown in the next section for a cross-junction configuration with co-axial branches.

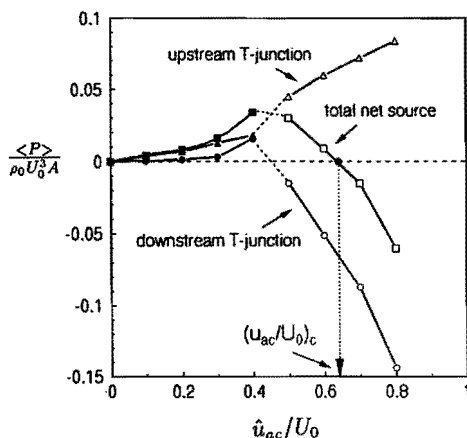


FIGURE 6.5: Net energy source strength $\langle P \rangle$ in a geometry with tandem branches. The Strouhal number is fixed at $Sr = 0.4$ for moderate acoustic amplitudes $\hat{u}_{ac}/U_0 \leq 0.4$ (represented with filled markers) and at $Sr = 0.3$ for high acoustic amplitudes $\hat{u}_{ac}/U_0 \geq 0.5$ (represented with open markers). Results are obtained from a numerical simulation of the flow by the vortex-blob method ($\delta = 0.10$). (Δ) upstream T-junction (\circ) downstream T-junction (\square) net source strength of the double side branch system

6.2.2 Cross-junction geometry

In a pipe system with co-axial side branches, i.e. a cross-junction geometry (see figure 6.1a), the aeroacoustic source strength can be determined from the periodic solution of the flow as described in chapter 4. For this geometry the acoustic velocity field is resonating between the closed side branches and in contrast to the acoustic flow in a T-junction at any instant the local amplitude of the acoustic velocity at the up- and downstream edges of the cross-junction are equal in magnitude. The instantaneous source strength is due to the interaction of the two vortex sheets emanating from the upstream edges of the cross junction with the acoustic field. It can be determined from equation (6.1).

Figure 6.6 shows the instantaneous source strength $P(t)$ for the periodic flow in a cross junction for $Sr = 0.3$ and the acoustic amplitude \hat{u}_{ac}/U_0 varied from 0.1 up to 0.8. The instantaneous source strength is obtained from the periodic flow solutions using the vortex-blob method again with $\delta = 0.10$. The vortex sheets emanating from the upper

³For instance in a pipe system with a single closed side branch and a circular horn, connected to the open end of the main pipe (see e.g. Hirschberg *et al.* (1989)).

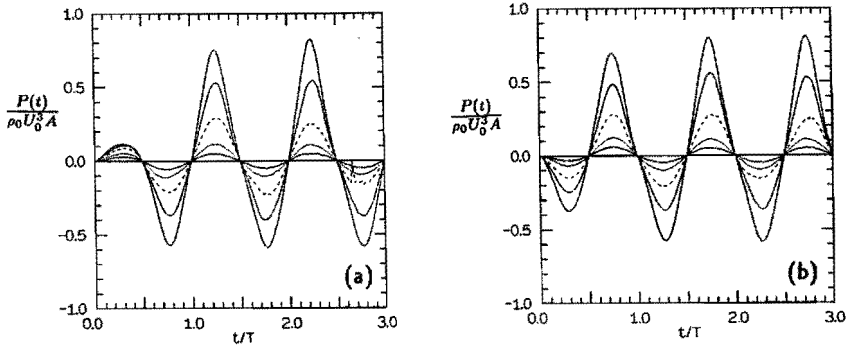


FIGURE 6.6: Instantaneous source strength in a cross-junction. The amplitude of the acoustic field is varied while the Strouhal number is kept fixed to $Sr = 0.3$. Results of the vortex-blob method (see for example figure 4.26 with $\delta = 0.10$). Acoustic amplitude \hat{u}_{ac}/U_0 : (—) : 0.1, (.....) : 0.2, (---) : 0.4, (-·-·-) : 0.6, (— · — · —) : 0.8. (a) vortex sheet emanating from the upper upstream edge (b) vortex sheet emanating from the lower upstream edge.

and lower upstream edge are aeroacoustic sources of opposite sign and their contribution to the instantaneous source strength is equal in magnitude but 180° out of phase. The net source strength per period of each of the two vortex sheets is therefore equal⁴. The sum of the two source strengths is presented in figure 6.7 for different acoustic amplitudes.

Again the calculations have been performed at two values of the Strouhal number, namely $Sr = 0.3$ and $Sr = 0.4$, this in order to check the sensitivity of the net source strength to the value of the Strouhal number. The behavior of the net source strength is similar to that found for the upstream T-junction, see figure 6.5. The linear behavior of the source strength is valid until $\hat{u}_{ac}/U_0 \approx 0.2$, which is comparable to the behavior found for a T-junction.

Along the curve corresponding to $Sr = 0.3$ the source strength attains a maximum value for an acoustic amplitude of $\hat{u}_{ac}/U_0 \approx 0.8$. For higher values of the amplitude of the acoustic velocity field the net source strength decreases. This effect has also been predicted by Bruggeman (1987) who suggested that during the first half period of the acoustic velocity field the absorption of acoustic energy increases stronger with the amplitude of the acoustic field than the production during the second half period. As a result, the net source strength can decrease for $\hat{u}_{ac}/U_0 > 0.8$. This behavior is similar to that of the net source strength found for a T-junction with an acoustic velocity field across the downstream edge, see figure 6.3.

For moderate amplitudes of the acoustic velocity field $\hat{u}_{ac}/U_0 < 0.2$ the net source strength obtained with a fixed value of the Strouhal number of 0.4 is larger than the source

⁴This is an independent check of the accuracy of the numerical solution.

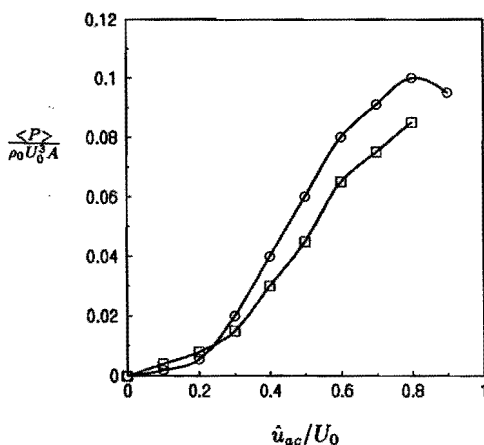


FIGURE 6.7: Net energy source strength $\langle P \rangle$ in a cross-junction at different acoustic amplitudes. Results from numerical simulation of the flow by the vortex-blob method ($\delta = 0.10$). (\square) $Sr = 0.4$, (\circ) $Sr = 0.3$.

strength obtained for $Sr = 0.3$. The opposite behavior is found for a high amplitude acoustic field. This corresponds with the observed behavior, that the Strouhal number at which maximum pulsation occurs shifts from $Sr \approx 0.4$ for moderate-amplitude pulsations towards $Sr \approx 0.3$ for high-amplitude pulsations.

Since for the flow in a cross-junction both vortex sheets are aero-acoustic sources of sound the maximum amplitude which can be reached for negligible acoustic energy losses is much higher than the critical amplitude of $(\hat{u}_{ac}/U_0)_c \approx 0.65$ found for a tandem T-junction geometry.

6.3 ESTIMATE OF ACOUSTIC ENERGY LOSS BY FRICTION AND HEAT CONDUCTION

Because the Helmholtz number is small ($He \ll 1$), radiation losses into the main pipe will be negligible for the resonating modes of the pipe configuration for which parameters m and n take an integer value. Non-resonating modes of the pipe system are radiated effectively into the main pipe. At low acoustic amplitudes the energy losses are mainly due to viscous forces acting on the pipe walls and heat conduction to the walls. In the closed side branches the mean flow velocity is zero and for Shear numbers $Sh_H = H\sqrt{\omega/\nu} \gg 1$ the damping of acoustic pressure waves due to visco-thermal action can be approximated by (Tijdeman (1975))

$$\alpha_0 = \frac{L_A}{4Ac_0} \sqrt{2\omega\nu} \left(1 + \frac{\gamma - 1}{\sqrt{Pr}} \right) \quad (6.2)$$

where L_A and A are the perimeter and cross-sectional area of the pipe segment, respectively. The value of $4A/L_A$ is equal to the pipe width H for a square pipe and equal to the diameter

D for a circular pipe. The damping in the bulk of the flow is neglected since the damping coefficient in the bulk of the flow is much smaller than α_0 in the low frequency region considered here.

In the present experiments the Shear number has a minimum value of approximately 50. The standing wave pattern of the resonating acoustic field in the pipe system can be thought of as a superposition of two plane waves traveling in opposite direction, each with pressure amplitude $\hat{p}_{\pm} = \frac{1}{2}\hat{p}_{ac}$. The amplitude of the intensity of these waves is in absence of damping equal to $|I_+| = |I_-| = \hat{p}_{ac}^2/8\rho_0c_0$. The intensity of both waves is damped exponentially while traveling up or down the side branch with damping coefficient $2\alpha_0$ if the mean flow is zero. For a nonzero mean flow the damping coefficient is given by $2\alpha_+$ and $2\alpha_-$ for the down- and upstream traveling wave, respectively.

The values of the damping coefficients in up- and downstream direction α_{\pm} can be obtained from the experimental data presented in chapter 5, e.g. see figure 5.10 and figure 5.11. For low Mach numbers and high frequencies the parameter δ_{ac}^+ will be less than 15 and the damping coefficients do not deviate too much from the value in absence of a mean flow, except for a Doppler shift. Therefore, the influence of mean flow on the damping can in this region be neglected.

In that case the total energy loss averaged over one period in a closed side branch of length L can be approximated by

$$\langle P_{loss} \rangle = \left(\frac{\hat{p}_{ac}^2}{2\rho_0c_0} \right) \alpha_0 LA \quad (6.3)$$

where we have used that in the present experiments $2\alpha_0L \ll 1$. The total power loss by visco-thermal action can be expressed, in nondimensionalized form, as

$$\frac{\langle P_{loss} \rangle}{\rho_0 U_0^3 A} = \left(\frac{\hat{p}_{ac}}{2\rho_0 U_0^2} \right) \left(\frac{\hat{u}_{ac}}{U_0} \right) \alpha_0 L \quad (6.4)$$

where it has been used that for a standing wave pattern in the resonator $\hat{p}_{ac} = \rho_0 c_0 \hat{u}_{ac}$. For a pipe system with co-axial branches the total power loss by friction and heat conduction can be obtained by summing the power loss of the two individual side branches and the damping in the pipe section between the branches.

6.4 NONLINEAR EFFECTS AT HIGH ACOUSTIC AMPLITUDE

For high amplitudes of the acoustic velocity field the acoustic waves are distorted by nonlinear effects during propagation into the side branches. Due to nonlinear steepening of the waves higher harmonics are generated in the resonator, which can either correspond to modes of the pipe system which do not radiate into the main pipe (uneven harmonics), or modes which are efficiently radiated into the main pipe (even harmonics). The amplitude of each of the higher harmonics depends on the ratio between the acoustic pressure amplitude \hat{p}_{ac} and the ambient pressure p_0 , which is related to the amplitude of the acoustic velocity field by $\hat{p}_{ac}/p_0 \approx \gamma \hat{u}_{ac}/U_0$, where γ is the ratio of specific heats ($\gamma = 1.4$ for air).

The energy transfer between the fundamental mode and higher harmonics is for a simple wave described by Pierce (1989)⁵. It depends on the shock formation length \bar{x} , which for a simple wave can be estimated from

$$\bar{x} \approx \frac{2\rho_0 c_0^2}{(\gamma + 1)k\hat{p}_{ac}} \quad (6.5)$$

The energy transfer from the fundamental mode to the higher harmonics depends on the value of $\sigma = x/\bar{x}$. For a simple wave it is given by

$$\sigma = \frac{\gamma + 1}{2\gamma} kx \frac{\hat{p}_{ac}}{p_0} \quad (6.6)$$

and by using the relations $\gamma p_0 = \rho_0 c_0^2$ and $\hat{p}_{ac} \approx \rho_0 c_0 \hat{u}_{ac}$ we obtain

$$\sigma \approx \frac{\gamma + 1}{2} kxM \frac{\hat{u}_{ac}}{U_0} \quad (6.7)$$

For small values of σ the amplitude of the fundamental mode decreases according to

$$\hat{p}_1 = \hat{p}_{ac} \left(1 - \frac{\sigma}{8}\right) \quad (6.8)$$

while the amplitude of the second harmonic increases according to

$$\hat{p}_2 = \hat{p}_{ac} \frac{\sigma}{2} \quad (6.9)$$

Assuming that during one period of the acoustic field the fundamental mode with wave number $k = \pi/2L$, generated by the aeroacoustic source at the junction, travels a distance L towards the side branch, the amplitude of the second harmonic at the closed end of the side branch is equal to

$$\hat{p}_2 = \hat{p}_{ac} \frac{\gamma + 1}{8} \pi M \frac{\hat{u}_{ac}}{U_0} \quad (6.10)$$

In a low frequency approximation, the second harmonic is totally radiated into the main pipe since it has a pressure maximum at the junction. Therefore it will be assumed that all the energy contained in the second harmonic is lost by radiation. Applying this theory to the experimental data obtained for a single side branch (figure 4.13 and table 4.1) and for co-axial branches (figure 4.23 and table 4.3) shows that the predicted amplitudes of the second harmonic given in table 6.1 agree reasonably with the experimentally observed values. Apparently the assumption of the presence of a simple wave causes an overestimate of the value of σ for a high-amplitude acoustic field.

The maximum value of σ obtained in our experiments for a high-amplitude acoustic field is approximately $\sigma \approx 0.12$. For such values of σ acoustic energy is mainly transferred from the fundamental mode to the second harmonic. The acoustic energy transferred to the third harmonic is much smaller, but since the third harmonic is also a non-radiating mode of the pipe system the energy of the third harmonic can accumulate. Therefore it

⁵Chapter 11, 'Nonlinear effects in sound propagation'.

\hat{u}_{ac}/U_0	M	$(A_2/A_1)_{exp}$	$(A_2/A_1)_{th}$
0.08	0.09	0.028	0.007
0.23	0.10	0.024	0.021
0.62	0.13	0.059	0.076
0.76	0.10	0.054	0.071

TABLE 6.1: Amplitude of second harmonic relative to the fundamental mode contained in the pressure signals. Comparison of data predicted by equation (6.10) for a simple wave model with experimental data for the periodic flow in a T-junction and cross-junction, presented in figure 4.13 and 4.23, respectively.

may occur in the measured pressure signal at the closed end of the side branch that the amplitude of the third harmonic can become comparable to the amplitude of the second harmonic (see table 4.1 and 4.3).

For $\sigma < 0.2$ the net acoustic energy transfer from the fundamental mode to the higher harmonics can be estimated from

$$\begin{aligned} \frac{\langle P_{nl} \rangle}{\rho_0 U_0^3 A} &= \frac{\sigma^2}{8M} \left(\frac{\hat{u}_{ac}}{U_0} \right)^2 \\ &= \frac{\pi^2 (\gamma + 1)^2}{32} M \left(\frac{\hat{u}_{ac}}{U_0} \right)^4 \end{aligned} \quad (6.11)$$

which is usually negligible compared to the viscous losses at least for $\hat{u}_{ac}/U_0 < 0.4$, but it is the main acoustic energy loss for $\hat{u}_{ac}/U_0 = \mathcal{O}(1)$.

6.5 PREDICTION OF EQUILIBRIUM AMPLITUDE

In a pipe system with negligible losses due to radiation of acoustic energy the equilibrium amplitude of the acoustic resonance can be determined from a balance of the ideally net production of acoustic energy and the net loss of acoustic energy due to friction, heat conduction and radiation. The losses of acoustic energy due to friction and heat conduction increase with the square of the amplitude, see equation (6.3), while the losses due to the energy transfer to higher harmonics and subsequent radiation of the energy contained in the even harmonics increase with the acoustic amplitude to the fourth power, see equation (6.11).

For moderate acoustic amplitudes the source strength increases linearly with the amplitude, i.e. $\langle P \rangle / \rho_0 U_0^3 A = S_0 (\hat{u}_{ac}/U_0)$ with S_0 the constant of proportionality which depends on the geometry and the direction of the mean and that of the acoustic velocity field. In this case nonlinear losses are negligible and the equilibrium amplitude of acoustic pulsations can be determined from

$$\hat{p}_{ac} = \rho U_0^2 \left(\frac{2S_0}{\alpha_0 L_{tot}} \right) \quad (6.12)$$

where L_{tot} is the total length of the part of resonator in which the acoustic field is present. For a single T-junction with a resonant acoustic velocity field across the downstream edge it follows from figure 6.3 that $S_0 = 0.04 \pm 0.005$ for $Sr = 0.4$, valid for $\hat{u}_{ac}/U_0 < 0.4$, while for a cross junction a value follows of $S_0 = 0.04 \pm 0.005$, also for $Sr = 0.4$, here valid for $\hat{u}_{ac}/U_0 < 0.3$ (see figure 6.7).

The damping coefficient α_0 depends on the frequency and the pipe geometry as given by equation (6.2). Therefore the amplitude of the pulsation increases linearly with increasing pipe width and quadratically with increasing mean flow and decreases with increasing side branch length. For high amplitudes, when $\hat{u}_{ac}/U_0 > 0.4$, equation (6.12) is not valid anymore and the equilibrium amplitude must be obtained from equating the numerically obtained source strength (see figure 6.3 and figure 6.7) with the net energy losses by friction, heat conduction and nonlinear effects.

For a double T-junction geometry with tandem branches the source strength is equal to zero for a critical amplitude $(\hat{u}_{ac}/U_0)_c \approx 0.65$, see figure 6.5. Close to this maximally attainable acoustic amplitude, the amplitude is more or less constant, i.e. close to $(\hat{u}_{ac}/U_0)_c$ and therefore the pressure amplitude varies according to

$$\hat{p}_{ac} = \rho_0 c_0 U_0 \left(\frac{\hat{u}_{ac}}{U_0} \right)_c \quad (6.13)$$

which is independent of the length of the side branch and of the frequency.

6.6 EXPERIMENTS

6.6.1 Introduction

An estimate of the source strength at moderate amplitudes was obtained by Bruggeman (1987) for a pipe system with square pipes consisting of a main pipe with a single closed side branch. The main pipe ends in a plenum chamber. By measuring the reflection coefficient of the plenum chamber by the two-microphone method Bruggeman (1987) estimated the energy losses caused by radiation. Bruggeman (1987) assumed that for this specific geometry energy losses due to friction and heat conduction are negligible compared to the radiation losses. Bruggeman estimated the net source strength in the linear regime to be represented by the slope $S_0 = 0.04 \pm 0.01$, which agrees reasonably with the value predicted by the two-vortex method.

Ziada & Bühlmann (1992) studied resonances in a geometry with a main pipe of diameter $D_0 = 0.090$ m and co-axial circular branches of various length with diameter $D = 0.050$ m. Since in this geometry the radiation losses into the main pipe are presumably negligible for the resonance frequencies of the pipe system at low frequencies $kD \ll 1$, which is valid for $f < 600$ Hz, the net source strength can be determined from the total losses by visco-thermal damping. The maximum amplitude observed by Ziada & Bühlmann (1992) is $\hat{u}_{ac}/U_0 \approx 0.3$ which is still in the linear regime of the net acoustic source strength. The slope of the net energy source strength measured by Ziada & Bühlmann is $S_0 = 0.04 \pm 0.01$ which is close to the predicted source strength for a cross junction by the numerical simulation by the vortex-blob method.

It is uncertain whether an aeroacoustic source in a circular pipe is equally effective compared to an aeroacoustic source in a square pipe. A small difference between the source strength in square and circular pipes has been observed by Bruggeman (1987) for the case of a double tandem side branch system.

In the next section an investigation is described into the characteristics of a pipe system with co-axial branches both with square and with circular pipe segments. This study is aimed at validating the results of Ziada & Bühlmann (1992) as well as validating the results of the present numerical prediction of the equilibrium amplitude.

6.6.2 Influence of pipe geometry on pulsation amplitude

Pipes with circular cross-section

Since in practice circular pipes are used for the transport of gas the aero-acoustic behavior of a pipe system with circular pipes and two closed side branches has been studied experimentally. Experiments performed for single and double side branch setups with pipes of circular cross-section have been described by Bruggeman (1987). The present study involving circular pipes is limited to the cross-junction geometry shown in figure 6.1a, with two closed co-axial side branches opposite to each other.

For the experiment we utilize the setup used for the experiments on the aero-acoustic behavior of an open pipe end, described in section 5.2. The main pipe with a circular cross-section has a diameter $D_0 = 0.030$ m and a pipe wall thickness $d_0 = 0.005$ m. The closed side branch has a diameter $D = 0.025$ m and the same wall thickness. The length of the side branches can be varied continuously by a piston. With the experimental setup it is also possible to perform experiments under conditions at high ambient pressure p_0 (up to 15 bar) which will increase the Reynolds number and therefore decrease the visco-thermal energy losses in the pipe system. The present experiments have been performed at room temperature.

The amplitude of the acoustic pressure field is measured at the end of the closed side branches, i.e. at a pressure maximum of the standing pressure wave, by using acceleration-compensated piëzo-electrical transducers (type PCB 117) mounted flush in the wall of the piston.

Since the cross-junction is positioned at a distance more than 150 times the pipe diameter from the entrance of the pipe the mean flow has a fully developed turbulent velocity profile which can be described by

$$\frac{U(r)}{U_{max}} = \left(1 - \frac{2r}{D_0}\right)^{\frac{1}{n}} \quad (6.14)$$

where the value of n depends on the Reynolds number and can be found in Schlichting (1968). For the present experiments the Reynolds number $Re = U_{max}D_0/\nu$ is of the order of 10^5 and $n \approx 7$. The momentum thickness θ of the boundary layer of the turbulent flow is $\theta = n\left(\frac{1.5}{n+1} - \frac{1}{n+2} - \frac{1}{2n+1}\right)D_0$. The experiments have been performed for four different values of the side branch length and for a mean velocity amplitude varying between 0 and 200 m/s. The magnitude of the average main velocity is obtained from a volume flux measurement far upstream of the cross-junction (accuracy $\pm 1\%$). In the determination

of the mean velocity ambient temperature and pressure variations have been taken into account (see chapter 5).

The amplitude of the acoustic pressure are presented in figure 6.8 for a side branch length of 0.200 m and 0.397 m. Acoustic resonance is observed at certain ranges of the mean flow velocity. In such a range the frequency locks into a fixed value which corresponds with the resonance frequency of the acoustic resonator or with an uneven multiple of the fundamental frequency. For the frequencies at which resonance occurs the Strouhal number varies between 0.3 and 0.5 for the first and between 0.9 and 1.0 for the second hydrodynamic mode of instability of the shear layer.

Using linear stability analysis Michalke (1965) showed that for an infinite free shear layer with finite thickness the maximum amplification of initial disturbances of frequency f occurs for $f\theta/U_0 \approx 0.02$, while no amplification of the disturbances is expected for $f\theta/U_0 > 0.04$. In the present experiment with a fully developed turbulent pipe flow the momentum thickness $\theta \approx 0.07D$ we obtain a maximum amplification for $Sr = fD/U_0 = 0.3$.

For a Strouhal number of $Sr \approx 0.45$ the convection of the vortex sheet generated at the upstream edge of the cross junction within *one* period of the acoustic field is about equal to the diameter of the side branch (since $0.45 U_0 T \approx D$). At the higher value of the Strouhal number at which resonance occurs, $Sr \approx 0.90$, the distance of convection during *two* periods fits with the side branch diameter. The third hydrodynamic mode of instability of the shear layer $Sr \approx 1.35$ is not observed at atmospheric pressure, since the large shear layer thickness prevents an amplification of an instability for this mode.

For an initially thinner shear layer an acoustic resonance in this unstable hydrodynamic mode of the shear layer has been observed by Bruggeman (1987) and also in the present experimental setup at high ambient pressure.

For short side branches ($L/D < 10$) the amplitude of the acoustic fluctuations are at maximum for the first mode of resonance as predicted by equation (6.12). Furthermore, the Strouhal number is found to decrease with an increasing pulsation amplitude. This suggests that the convection velocity of disturbances in the shear layer decreases with increasing acoustic amplitude.

The pressure amplitude obtained for the first mode in a cross-junction geometry with various lengths of the side branch is presented in figure 6.9. The amplitude of the resonances is much larger than the values obtained by Ziada & Bühlmann (1992), since the side branch length is much smaller in our experiment and visco-thermal losses are much smaller. Ziada & Bühlmann (1992) suggested that the pulsation amplitude attains a maximum value of $\hat{p}_{ac}/\rho_0 c_0 U_0 = \hat{u}_{ac}/U_0 \approx 0.4$ for a sharp-edged cross-junction. At atmospheric pressure we obtain a maximum amplitude of $\hat{p}_{ac}/\rho_0 c_0 U_0 \approx 0.80$ for a side branch length of 0.100 m. This high-amplitude behavior was also found by Hirschberg *et al.* (1989) for a single side branch and the main pipe terminated by a horn.

The acoustic energy losses by friction and heat conduction, given by equation (6.3), obtained for a cross-junction geometry with circular side branches are shown in figure 6.10. The present experimental data agree with the experimental data obtained by Ziada & Bühlmann for a similar setup with circular pipe segments of a larger diameter.

For moderate acoustic amplitude $\hat{u}_{ac}/U_0 < 0.4$ the experimental data agree with the

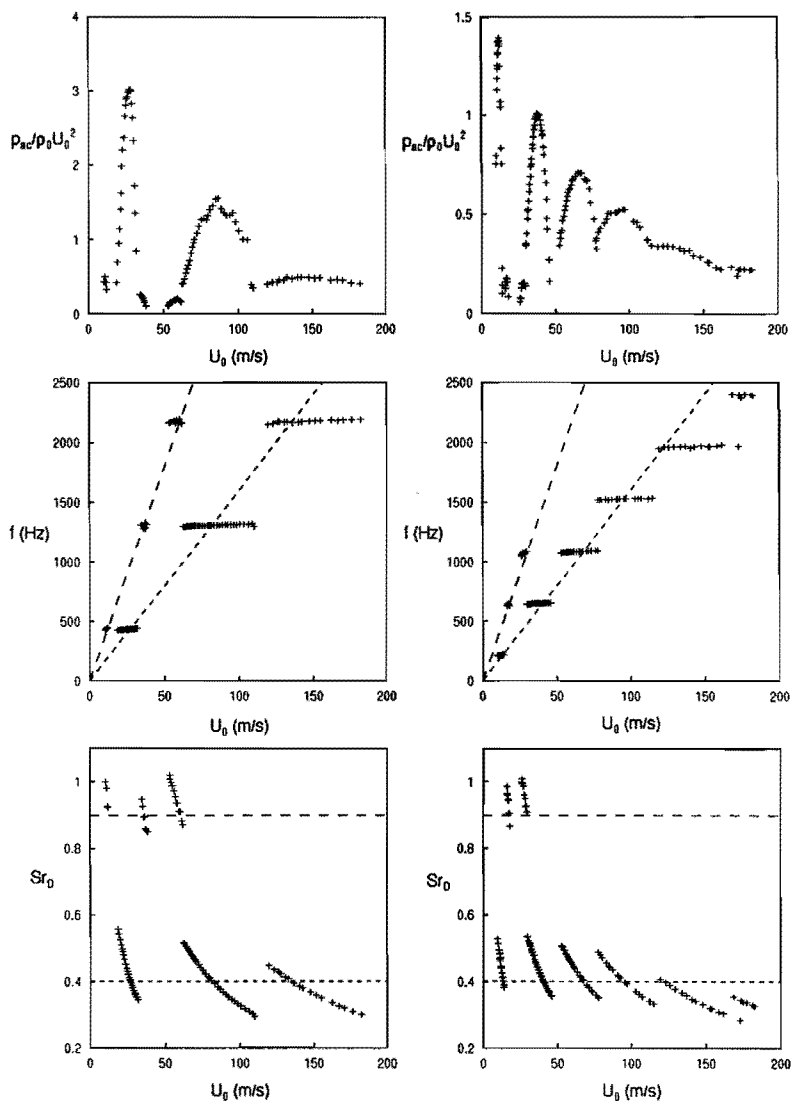


FIGURE 6.8: Flow-acoustic coupling measured in a pipe system with two co-axial closed circular side branches with sharp edges at atmospheric pressure $p_0 = 1$ bar (see figure 6.1a). (a) $L_1 = L_2 = 0.200$ m (b) $L_1 = L_2 = 0.397$ m (1) amplitude of the acoustic pressure (2) frequency (3) Strouhal number fD/U_0 , (---) constant Strouhal number $Sr_D = 0.9$, (-.-.-) constant Strouhal number $Sr_D = 0.4$

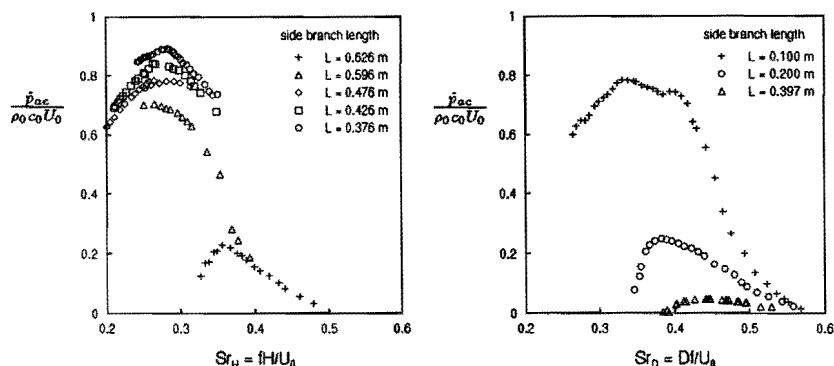


FIGURE 6.9: Dependence of side branch length $L_1 = L_2$ on the amplitude of the acoustic pulsations measured in a pipe system with two closed coaxial side branches at atmospheric pressure $p_0 = 1$ bar, see figure 6.1a. (a) square pipes, $L_3 = 0.075$ m (b) circular pipes, $L_3 = 2$ m

results of the vortex-blob method. For higher amplitudes, a strong deviation is observed from the predicted net energy source. The deviation is caused by the losses of acoustic energy from the fundamental mode towards higher harmonics due to nonlinear effects. An estimate of this additional energy loss given by equation (6.11) is included in figure (6.10). It is clear that the losses due to nonlinear effects can explain the difference between the calculated net source strength and the measured visco-thermal losses.

When the ambient pressure is increased the mean density increases and as a result the kinematic viscosity decreases. In this way the influence of visco-thermal losses on the amplitude of the acoustic oscillations can be studied. In figure 6.11 results are presented for a cross-junction geometry with circular pipe segments with side branch length $L = 0.200$ m and 0.397 m. The ambient pressure has been varied from 1 bar up to 15 bar. Both for $L = 0.200$ m and 0.397 m the amplitude of the resonating acoustic field increases due to decreasing visco-thermal losses. When for $L = 0.397$ m the ambient pressure is increased from 6 up to 11 bar, suddenly the amplitude of the acoustic field increases strongly. This is due to the nonlinear increase of the source strength in the region $\hat{u}_{ac} > 0.4$, see figure 6.10.

Pipes with square cross-section

The influence of the geometry and the direction of the mean flow on the amplitude of the resonant acoustic field is studied with the experimental setup used for the visualization study described in chapter 4. In the setup, shown in figure 4.9, square aluminum pipe segments were used, with pipe width $H = 0.06$ m. The mean flow of air is provided by a high pressure supply. The mean flow velocity is computed from the measured pressure

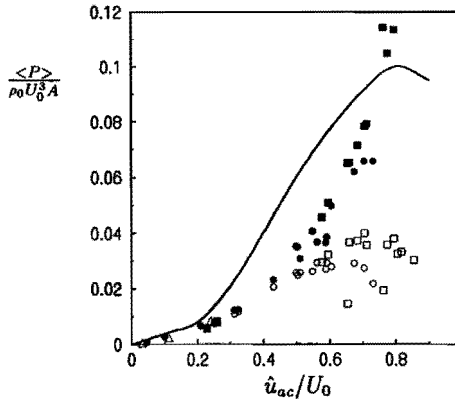


FIGURE 6.10: Acoustic energy balance for a cross-junction at different amplitudes of the acoustic velocity field. (—) maximum value of the net acoustic source strength predicted by the vortex-blob method (o) visco-thermal losses estimated from measurements for circular pipes ($D = 0.025$ m) (□) visco-thermal losses estimated from measurements for square pipes ($H = 0.06$). (Δ) visco-thermal losses estimated from measurements by Ziada & Bühlmann (1992) for circular pipes ($D = 0.050$ m) Filled markers represent the estimated total losses, given by the visco-thermal losses and the losses of the fundamental mode due to nonlinear wave steepening, given by equation (6.11).

difference between the plenum chamber and the main pipe by using the Bernoulli equation. In figure 6.9a the amplitude of the acoustic pressure as obtained for the cross-junction geometry (see figure 6.1a) with sharp edges is presented for various lengths of the side branch. Data are presented for the fundamental mode of the oscillation only.

For a increasing side branch length L , the amplitude of the resonant oscillations decreases from a value of about 0.9 to a value of about 0.2 due to the energy losses by visco-thermal damping increasing with increasing L . In the process also the Strouhal number at which the amplitude of the resonant oscillation is at maximum increases slightly with increasing L , i.e. from 0.35 to 0.45. Note that the maximum amplitude observed for the cross-junction with sharp edges is much larger than the maximum amplitude found for the double T-junction. In a double T-junction the energy losses are higher because of more losses by friction and heat conduction, additional acoustic energy losses due to the interaction of the acoustic field with the turbulent mean flow and also the difference between the net source strength in a cross junction (see figure 6.7) and a double T-junction (see figure 6.5).

For a pipe system with co-axial side branches the maximum amplitude observed for square pipes is comparable with the maximum amplitude obtained for a pipe system with circular cross-section. Furthermore, for the largest value of the side branch length the

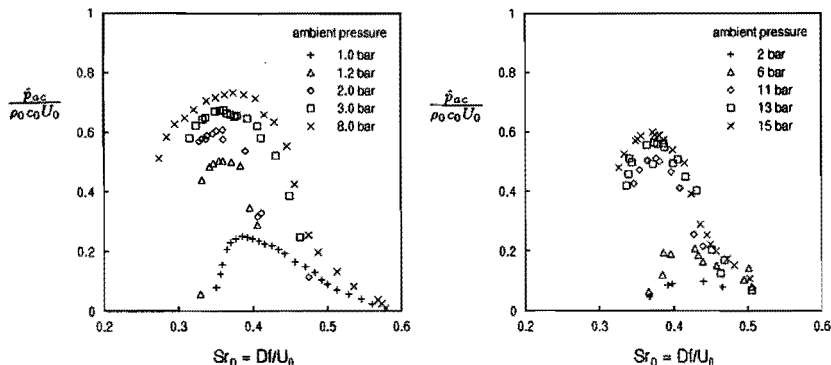


FIGURE 6.11: Influence of ambient pressure on the amplitude of the acoustic resonance in a pipe system with circular pipe segments and two co-axial closed side branches with sharp edges.

(a) $L_1 = L_2 = 0.200$ m (b) $L_1 = L_2 = 0.397$ m

amplitude of the second mode is higher than the amplitude of the fundamental mode. This phenomenon was also observed by Ziada & Bühlmann (1992) for a cross junction with long circular pipe segments with diameter $D = 0.051$ m and with side branch length $L_1 = L_2 = 0.61, 1.0$ and 2.0 m.

The acoustic energy losses due to visco-thermal action determined for the geometry with co-axial branches is included in figure 6.10. For moderate acoustic amplitudes the data obtained for the cross-junction with circular pipes are in agreement with the data for square pipes. For high acoustic amplitudes the viscous losses are somewhat lower for the circular pipes than for the square pipes. To maintain the resonant oscillations the net aeroacoustic source strength should balance the losses. Figure 6.10 shows that the visco-thermal losses are for moderate acoustic amplitudes qualitatively in agreement with the net aeroacoustic source strength predicted by the vortex-blob method. The difference in the high-amplitude range is caused by the additional energy loss due to nonlinear effects.

6.6.3 Influence of rounding the edges on pulsation amplitude

For a single and for a double side branch geometry Bruggeman (1987) observed a strong influence of the radius of curvature of the edges of the junction on the amplitude of the acoustic resonance. In the present study the influence of rounding the edges is here studied systematically for the double T-junction geometry shown in figure 6.1d with square pipe segments. In figure 6.12 the results are presented of the effect of changing one of the four edges of the T-junction. For one T-junction the radius of curvature R of the edges have been changed from $R/H = 0$ to values of $R/H = 0.1$ and $R/H = 0.2$, while the other T-junction had rounded edges with $R/H = 0.1$.

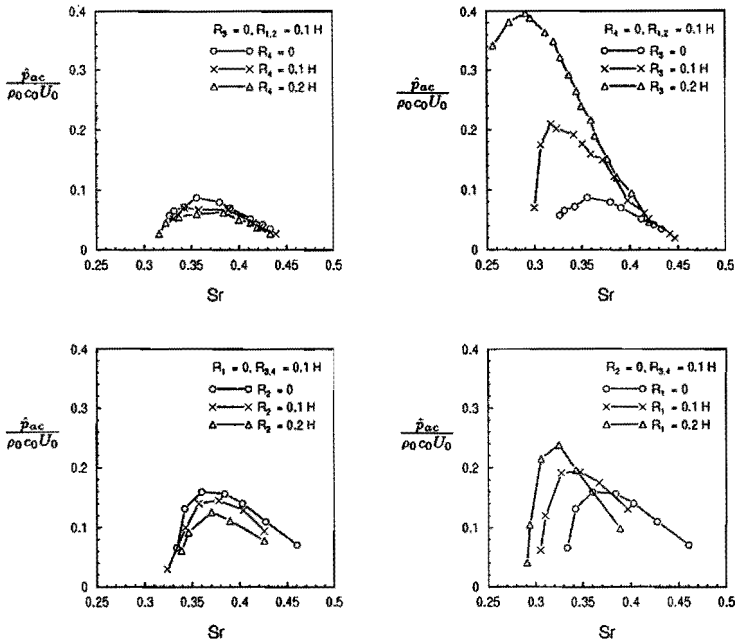


FIGURE 6.12: Effect of rounding the edges of the T-junction on the amplitude of the acoustic resonances in a pipe system with square pipes and two closed side branches in tandem. (see figure 6.1d) with $L_1 = 0.580$ m, $L_2 = 1.260$ m, $L_3 = 0.543$ m, $L_4 = 0.462$ m, $f \approx 140$ Hz. (a) downstream edge second T-junction (b) upstream edge second T-junction (c) downstream edge first T-junction (d) upstream edge first T-junction

From figure 6.12 it is clear that rounding the upstream edge increases the amplitude of acoustic resonance, while rounding the downstream edge decreases the acoustic amplitude, but only slightly. The effect is the strongest for the upstream edge of the second T-junction and for the downstream edge of the first T-junction. This is because the acoustic velocity is at maximum at precisely these edges and changing the radius of curvature of these edges has the strongest influence on the absorption or production near these edges (see also figure 6.4).

Clearly not only the maximum amplitude increases but simultaneously the Strouhal number at which the maximum amplitude resonance occurs decreases. This observed effect of rounding the edges can be explained in terms of a change in the source strength when the local geometry is changed. The source strength is given by equation (6.1). During the first half period of the acoustic field the vortex formation takes place near the upstream edge and acoustic energy is transferred to kinetic energy of the vortex. After half a period

of the acoustic field, when the acoustic velocity changes sign, acoustic energy is produced by the interaction of the just generated vorticity field with the acoustic field.

It is expected that rounding the upstream edge of the T-junction will affect the vorticity generation and the absorption of acoustic energy is will decrease so that the net energy source strength increases. The opposite will occur when the radius of curvature of the downstream edge is increased. This effect is indeed observed in the experiments, presented in figure 6.12. The stronger influence of rounding the edge at which the local acoustic amplitude is maximum is in agreement with the computed source strength at these edges, e.g. see figure 6.4.

The amplitude of the acoustic resonance in the cross-junction geometry is also strongly influenced by rounding the edges. For the cross-junction geometry with co-axial square branches the influence of edge rounding is presented in figure 6.13. Increasing the radius

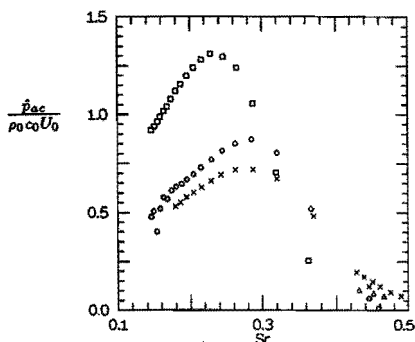


FIGURE 6.13: Influence of radius of curvature of the edges on the amplitude of the acoustic resonance in a pipe system with two co-axial square side branches (see figure 6.1a) with $L_1 = L_2 = 0.610$ m, $L_3 = 0.075$ m. (x) sharp edges $R/H = 0$ (o) edge radius of curvature $R/H = 0.1$ (□) $R/H = 0.2$ (Δ) with spoilers at upstream edges of length $l/H = 0.1$

of all the edges from zero to $R/H = 0.1$ increases the maximum amplitude by approximately 20 %, further increasing the radius of curvature to $R/H = 0.20$ yields a maximum amplitude of $\hat{p}_{ac}/\rho_0 c_0 U_0 \approx 1.3$, almost twice the value observed for sharp edges! This amplitude of the acoustic pressure yields an amplitude of the acoustic velocity field which is larger than the mean flow velocity U_0 .

For this resonance condition $Sr = 0.23$ and $\hat{u}_{ac}/U_0 = 1.3$ obtained for a side branch length of $L = 0.61$ m the flow has been visualized without injecting CO_2 at the upstream edges of the cross-junction. The flow visualization presented in figure 6.14 shows a weak shock wave which each half period is formed in the side branches due to nonlinear steepening of the acoustic waves. The density variations associated with this weak shock allow a visualization of the flow by a schlieren method.

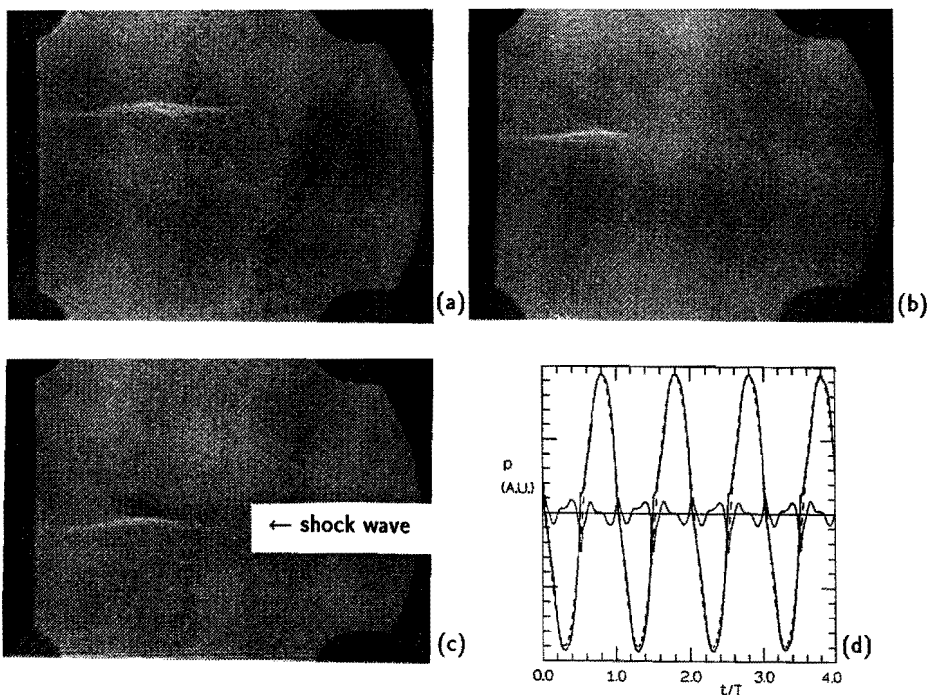


FIGURE 6.14: Flow visualization of shock wave formation in a cross-junction geometry with rounded edges ($R/H = 0.2$) using a schlieren method. $L_1 = L_2 = 0.61$ m, $L_3 = 0.040$ m, $f = 135$ Hz and $p_0 = 1$ bar. Figure (a) - (c) are at subsequent stages of the shock passing the cross-junction. In figure (d) the pressure signal measured at the end of the closed side branch is shown.

Under these flow conditions the amplitude of the acoustic pressure is approximately 20% of the ambient pressure ($p_0 \approx 1$ bar) and hence $M_{ac} = \hat{u}_{ac}/c_0 \approx 0.14$. The value of σ defined by equation (6.7) is approximately 0.5 assuming a simple wave traveling a distance twice the length of the side branch. This explains the formation of a weak shock. These measurements show that nonlinear effects are indeed important for high acoustic amplitudes with $\hat{u}_{ac}/U_0 = \mathcal{O}(1)$ which cannot be neglected in the theoretical analysis and the numerical simulation.

When the shock wave reaches the intersection it is directed by the mean flow towards the main pipe where it collides with the downstream edge. After the collision reflected circular waves are observed in the junction after which a new shock wave emerges from the opposite side branch.

The pressure measured at the end of the closed side branch is also presented in figure 6.14. The pressure signal differs strongly from a single-mode harmonic signal and a

weak shock can be observed.

Bruggeman (1987), in his study on flow-induced pulsations in a pipe system with a double T-junction, suggested to prevent pulsations by introducing so-called spoilers at the upstream edges of the T-junction. If these spoilers are also introduced at the upstream edges of the cross-junction geometry with rounded edges (with $R/H = 0.2$, while the spoilers were straight and had a length $l/H = 0.1$), the amplitude of the pulsations could be reduced by a factor of 10 compared to the amplitude found in the cross-junction with rounded edges without spoilers (see figure 6.13).

6.7 CONCLUSIONS

The strength of the aero-acoustic sound source due to flow-induced pulsations has been obtained from the numerical solutions for the periodic flow in a cross-junction and in a T-junction. During the first half period of the acoustic field, when a new vortex structure is formed at the upstream edges, acoustic energy is transferred into kinetic energy of the mean flow. During the next half period the vortex structure transfers kinetic energy of the mean flow back into acoustic energy. If during the second half period the vortex structure is close to the downstream edge of the pipe junction the net strength of the acoustic energy source can become positive. This explains why flow-acoustic coupling can only be observed at specific values of the mean flow Strouhal number.

Up to moderate amplitudes of the acoustic field ($\hat{u}_{ac}/U_0 < 0.3$) the source strength averaged over a period of the acoustic field, i.e. the net source strength, increases linearly with the amplitude of the acoustic field. For higher amplitudes a maximum value of the net source strength is obtained. For an amplitude of the acoustic field ($\hat{u}_{ac}/U_0 \geq 0.9$), at a given value of the Strouhal number, the source strength decreases slightly.

In a double T-junction geometry the net source strength is obtained by adding the contributions of the upstream and that of the downstream T-junction. For this geometry the net source strength becomes zero at a critical amplitude $(\hat{u}_{ac}/U_0)_c \approx 0.65$. This critical value is the maximum amplitude which ideally can be obtained in a pipe system with sharp-edged tandem branches. This predicted maximum value of the amplitude of the acoustic field can only be obtained if losses due to friction and radiation are negligible.

From the numerical simulations it is observed that for the cross-junction the net source strength is larger than that in a double T-junction geometry. As a result higher amplitude resonances can be expected for a pipe geometry with two closed side branched positioned co-axially opposite to each other on the main pipe.

For a pipe system with two closed co-axial side branches the acoustic energy losses due to visco-thermal effects have been determined experimentally. For resonant conditions at moderate acoustic amplitude ($\hat{u}_{ac}/U_0 < 0.4$) both for pipes with square and circular cross-section the acoustic energy losses due to viscous and thermal effects are reasonably close to the net source strength predicted by the vortex-blob method.

For resonant conditions at high acoustic amplitude the predicted source strength is much larger than the estimated energy loss through visco-thermal losses. The difference is due to energy losses through nonlinear effects: at high amplitudes the acoustic waves are distorted during propagation and energy is transferred from the fundamental mode

to higher harmonics. The even higher harmonics are efficiently radiated into the main pipe, while the uneven harmonics correspond to the higher modes of the resonator and the energy contained in these modes is accumulated in the pipe system.

The source strength is strongly influenced by the direction of the mean and the acoustic velocity field as well as the radius of curvature of the edges of the junctions. For rounded upstream edges the net source strength is increased since the initial acoustic energy absorption is decreased. However, for rounded downstream edges the net source strength is decreased since the acoustic energy production is decreased.

In a cross-junction geometry with rounded edges amplitudes of the acoustic velocity field larger than the amplitude of the mean flow field have been measured, i.e. $\hat{u}_{ac}/U_0 \approx 1.3$. At this amplitude with acoustic Mach number $M_{ac} \approx 0.14$ weak shock waves have been observed. If upstream edges are effectively sharpened by introducing spoilers the pulsation amplitude can be reduced by a factor of ten.

REFERENCES

- BALDWIN R.M. & SIMMONS H.R. (1986) Flow-induced vibration in safety relief valves. *J. Pressure Vessel Techn.* **108**, 267 - 272.
- BRUGGEMAN J.C. (1987) Flow induced pulsations in pipe systems. PhD thesis Eindhoven University of Technology
- BRUGGEMAN J.C., HIRSCHBERG A., DONGEN M.E.H. VAN, WIJNANDS A.P.J. & GORTER J. (1989) Flow-induced pulsations in gas transport systems: analysis of the influence of closed side branches. *J. Fluids Eng.* **111**, 484 - 491.
- BRUGGEMAN J.C., HIRSCHBERG A., DONGEN M.E.H. VAN, WIJNANDS A.P.J. & GORTER J. (1991) Self-sustained aero-acoustic pulsations in gas transport systems: experimental study of the influence of closed side branches. *J. Sound & Vibr.* **150** 3, 371 - 393.
- HIRSCHBERG A., BRUGGEMAN J.C., WIJNANDS A.P.J. & SMITS N. (1989) the 'whistler nozzle' and horn as aeroacoustic sound sources in pipe systems. *Acustica* **68**, 157 - 160.
- HOWE M.S. (1975) Contributions to the theory of aerodynamic sound, with application to excess jet noise and the theory of the flute. *J. Fluid Mech.* **71** 4, 625 - 673.
- INGARD U. & SINGHAL V.K. 1976 Flow excitation and coupling of acoustic modes of a side-branch gravity in a duct. *J. Acoust. Soc. Am.* **60** 5, 1213 - 1215.
- JUNGOWSKI W.M., BOTROS K.K. & STUDZINSKI W. (1989) Cylindrical side-branch as tone generator. *J. Sound & Vibr.* **131** 2, 265 - 285.
- MICHALKE A. (1965) On spatially growing disturbances in an inviscid shear layer. *J. Fluid Mech.* **23** 3, 521 - 544.
- NELSON P.A., HALLIWELL N.A. & DOAK P.E. (1983) Fluid dynamics of a flow-excited resonance, part II: Flow acoustic interaction. *J. Sound & Vibr.* **91** 3, 375 - 402.
- PIERCE A.D. (1989) Acoustics, an introduction to its physical principles and applications. McGraw-Hill Book Company.
- POWELL A. (1964) Theory of vortex sound. *J. Acoust. Soc. Am.* **36** 1, 177 - 195.
- SCHLICHTING H. (1987) Boundary-layer theory. 7th edition McGraw-Hill Book Company
- TJEDEMAN, H. (1975) On the propagation of sound in cylindrical tubes. *J. Sound & Vibr.* **39** 1, 1 - 33, also as NLR Report MP 74004 U.
- ZIADA S. & BÜHLMANN E.T. (1992) Self-excited resonances of two side-branches in close proximity. *J. Fluids & Structures* **6**, 583 - 601.

Summary and conclusions

7.1 NUMERICAL SIMULATION OF UNSTEADY INTERNAL FLOW

In the present study results of computational methods used to describe the unsteady, high-Reynolds-number, low-Mach-number flow within pipes with closed side branches have been compared with results of flow visualization and Laser Doppler velocity measurements. The second-order panel method, developed at National Aerospace Laboratory (NLR) by Hoeijmakers & Vaatstra (1983) and described extensively by Hoeijmakers (1989) for the simulation of the vortex wake roll-up as occurs behind an aircraft has been adapted such that it can handle interior flows and has been extended to include vorticity generation at sharp edges through a Kutta condition. The rigid-wall boundary conditions are incorporated by using a Schwarz-Christoffel mapping in which the physical flow domain is transformed into the half-plane in computational space. This adaptations allow the method to be used for unsteady two-dimensional internal flow problems with flow separation at sharp edges. Results of the method have been compared with results of a vortex-blob method in combination with a first-order boundary element method, developed by Piva *et al.* (1992).

On the basis of results of these methods simplified methods have been developed which compute the trajectory of the center of vorticity and the evolution of the circulation of the shear layer fairly well but do not give the details on the distribution of vorticity. Concentrating all vorticity contained in the shear layer into a single point vortex results in a so-called single-vortex method. This method, amongst others developed by Brown & Michael (1954) and used by Howe (1975), overestimates the amount of vorticity generated. The trajectory of the center of vorticity is reasonably predicted by the method provided that certain conditions are imposed on the system consisting of the point vortex and the so-called feeding sheet connecting the point vortex to the edge.

By improving the single-vortex method on the aspect of vorticity generation a so-called two-vortex and a so-called single-panel method are obtained which gives a fair prediction of the trajectory of the center of vorticity and the evolution of the circulation of the vortical flow region. This holds as long as the distance of the center of vorticity to the edge where the vortex system is generated is of the same order as or smaller than the characteristic length scale of the problem (in internal flow problems usually the channel width). In addition the method requires empirical information on the moment of formation of a new vortex structure.

Results of different methods applied to starting flows are discussed and compared in chapter 3. The cases considered are: the self-similar starting flow past a wedge (section 3.2); the impulsively started flow in a pipe with a T-junction (section 3.3); and the impulsively started flow out of a nozzle (section 3.4).

In the prediction of the periodic flow in internal configurations additional difficulties appear. The first problem is the periodic formation of vortical structures. The frequency of the initialization of a new vortex structure is determined by the frequency of the imposed periodic outer flow. However, as also has been observed in experimental studies, it appears that there can be a phase shift between the periodic outer flow and the periodic generation of new vortex structures. This phase shift depends on the acoustic amplitude \hat{u}_{ac}/U_0 . The phase shift is predicted by the vortex-sheet and by the vortex-blob method, since these methods can describe the Kelvin-Helmholtz instability of the vortex sheet, which signals the formation of a vortex structure.

In the single-vortex, two-vortex and single-panel method the instant in the cycles when of a new vortex structure is formed is an external parameter which has to be obtained empirically or theoretically from more elaborate methods. Test cases are discussed in section 4.4 and 4.5, namely the periodic flow in a pipe with a T-junction and a pipe with a cross-junction, respectively. An example where the moment of formation of a new vortex structure can be determined a priori is discussed in section 4.2. It concerns the vortex formation in the periodic flow out of a sharp-edged nozzle with zero mean flow. Without a mean flow component or when the acoustic amplitude is high ($\hat{u}_{ac}/U_0 \approx 1$), vorticity of opposite sign is generated during each period. In that case, the formation of a new vortex structure starts at the moment the newly generated vorticity changes sign.

A second difficulty in numerically simulating periodic flows is that vorticity has to be annihilated after a number of periods following the period it has been generated, this in order to limit to computation time and the extent of the computational region. Physically this annihilation corresponds to the merging of vortices with vorticity of opposite sign or with boundary layers as a result of (turbulent) diffusion but none of these effects is included within the potential-flow models employed. Usually vorticity is annihilated or removed from the computational domain if it has been convected far away from the region of interest, so that it doesn't influence the generation and convection of vorticity in the source region. The problem is avoided by limiting the number of periods the numerical simulation is carried on.

7.2 INTERACTION OF A VORTICITY FIELD WITH AN ACOUSTIC FIELD

In the presence of an acoustic field an unsteady vorticity field can transfer acoustic energy into kinetic energy of the vortical flow field and the other way around. In general a vortex structure is formed during the half-period the acoustic flow field is directed downstream around the sharp edge where the flow separates. During this half-period of the acoustic velocity field acoustic energy is transferred to kinetic energy of the vortical flow. During the next half-period the vortical structure can transfer kinetic energy back into acoustic energy.

In general the net production of acoustic energy is negative, so that the flow field vorticity causes damping of the acoustic field. For example, for the periodic acoustic flow around a sharp-edged nozzle the periodic vortex formation process causes an absorption of acoustic energy. This has been found by measurements described in section 5.4. The net acoustic energy absorption, obtained from the simulation of the periodic flow in section 4.2

using the vortex sound theory by Howe (1975), is discussed by Peters & Hirschberg (1993).

If during the second half period of the acoustic oscillation part of the vortex system is close to a boundary, for example a sharp edge, the amount of acoustic energy produced during the second part of the acoustic field can exceed the initial absorption. In that case the interaction between the flow-field vorticity and the acoustic velocity field is an aero-acoustic source of sound. An example of this sound generating phenomenon is described in chapter 6. In a pipe system with two closed side branches, either in tandem (double T-junction) or positioned opposite to each other (cross-junction), the vortex structures formed periodically near the upstream edges interact with the downstream edges. For a certain range of values of the mean flow Strouhal number based on the resonance frequency of the resonator a net production of acoustic energy can lead to a self-sustained pulsation in which the vortex formation frequency is imposed by the resonating acoustic field.

7.3 LOSS MECHANISMS OF ACOUSTIC ENERGY

The Strouhal number at which acoustic resonances can occur in a pipe system with closed side branches can be predicted accurately, see for example Stokes *et al.* (1986) and Bruggerman (1987). However, a prediction of the equilibrium amplitude of the periodic acoustic field requires an accurate knowledge on the strength of the aero-acoustic source on one hand and the mechanisms imparting losses in acoustic energy on the other hand. If an acoustic field is resonating in part of a pipe system with closed side branches acoustic energy is lost by radiation into other parts of the pipe system or by radiation out of the pipe system through wall vibrations. Furthermore, the acoustic waves are damped by viscous dissipation and thermal conduction, the so-called visco-thermal effects. Finally, at higher acoustic amplitudes, due to nonlinear effects the acoustic waves steepen and acoustic energy of the fundamental mode is transferred to higher modes, which can cause a significant damping of the fundamental mode of the acoustic standing wave in a pipe system. Even shock waves are observed in a cross-junction at very high amplitudes.

For low-frequency waves the radiation losses at open pipe ends can be measured by a so-called two-microphone method. With this method the reflection of acoustic waves is obtained if the damping of these waves inside the pipe system is known. In the presence of a (turbulent) mean flow the damping of acoustic waves is not accurately known. Several theoretical results, varying from empirical (Ingard & Singhal (1974)) to highly elaborate (Howe (1979, 1984)) do not succeed in predicting the measured data within 20%. Other theoretical results are only valid in a specific range of frequencies and Mach numbers (Ronneberger (1975)). In the present study the two-microphone method has been extended to a multi-microphone method which enables the measurement of both the reflection coefficient and the wave numbers in up- and downstream direction.

The imaginary part of the wave number is the damping coefficient. A simple theoretical analysis indicates that accounting for the delay in the response of turbulence to shear waves generated at the wall by the acoustic field is essential to accurately predict the viscous contribution to the damping coefficient.

The multi-microphone method is described in section 5.2 and the results for the damping and reflection coefficients are presented in section 5.3 and 5.4. The present experiments

validate the theories of Munt (1990), Cargill (1982) and Rienstra (1981) on the influence of a low Mach number mean flow on the reflection of plane acoustic waves at an unflanged pipe end. The present experimental data on the damping coefficients agree with data obtained by Ronneberger & Ahrens (1977), but are obtained for a wider range of frequencies and Mach numbers (see also Peters *et al.* (1993)). Quantitative information is provided on the way the reflection coefficient for an open pipe exit without a mean flow depends on the amplitude. These latter measurements confirm results of Disselhorst & van Wijngaarden (1980).

7.4 PREDICTION OF EQUILIBRIUM AMPLITUDE OF ACOUSTIC OSCILLATION

In order to predict the equilibrium amplitude of flow-induced pulsations in a pipe system with two closed side branches with sharp-edged junctions the strength of the aero-acoustic source has been determined in section 6.2. For moderate acoustic amplitude ($\hat{u}_{ac}/U_0 \ll 1$) the net source strength increases linearly with the acoustic amplitude. For a larger amplitude, the net source strength increases more rapidly until a maximum source strength is reached at acoustic amplitudes of about one ($\hat{u}_{ac}/U_0 = \mathcal{O}(1)$).

For a cross-junction geometry the maximum is obtained for $\hat{u}_{ac}/U_0 \approx 0.8$, while for a double T-junction geometry this maximum is obtained at a lower value, i.e. $\hat{u}_{ac}/U_0 \approx 0.4$. For a still higher value of the amplitude of the acoustic field the net source strength can even become negative. This yields the highest amplitude which can be obtained in such a pipe system if acoustic energy losses are negligible. This maximum is found to be $\hat{u}_{ac}/U_0 \approx 0.65$ for a double T-junction geometry for T-junctions with sharp edges.

However, if the geometry of the edges of the junctions is changed, the net source strength can be strongly influenced. This effect is described both theoretically and experimentally in section 6.5. Increasing the radius of curvature of the upstream edges of the junction decreases the acoustic energy absorption while increasing the radius of curvature of the downstream edges decreases the acoustic energy production. In order to decrease the strength of the aero-acoustic source, and as a result the amplitude of the acoustic pulsations, the upstream edges should be sharp while the downstream edges should be rounded. An enhanced acoustic energy absorption can be obtained if so-called spoilers are introduced at the upstream edges (see Bruggeman (1987)).

The acoustic energy losses due to visco-thermal effects in a pipe system with two co-axial closed side branches are for moderate acoustic amplitudes $\hat{u}_{ac}/U_0 < 0.3$ in agreement with the source strength predicted by the computational methods for simulating the periodic vorticity generation and convection in the source regions.

For high acoustic amplitudes \hat{u}_{ac}/U_0 visco-thermal losses are only responsible for a part of the total energy losses. The other part can be explained by a transfer of acoustic energy from the fundamental mode to higher harmonics by nonlinear effects. This indicates that we are now able to predict the maximum equilibrium amplitude of pulsations in resonator, formed by a pipe system with closed side branches, connected to the main pipe by sharp-edged junctions.

REFERENCES

- BROWN C.E. & MICHAEL W.H. (1954) Effect of leading-edge separation on the lift of a delta wing. *J. Aero. Sci.* **21**, 690 - 694.
- BRUGGEMAN J.C. (1987) Flow induced pulsations in pipe systems. PhD thesis Eindhoven University of Technology
- BRUGGEMAN J.C., HIRSCHBERG A., DONGEN M.E.H. VAN, WIJNANDS A.P.J. & GORTER J. (1989) Flow induced pulsations in gas transport systems: analysis of the influence of closed side branches. *J. Fluids Eng.* **111**, 484 - 491.
- CARGILL A.M. (1982) Low frequency acoustic radiation from a jet pipe - a second order theory. *J. Sound & Vibr.* **83** 3, 339 - 354.
- DISSELHORST J.H.M. & WIJNGAARDEN L. VAN (1980) Flow in the exit of open pipes during acoustic resonance. *J. Fluid Mech.* **99** 2, 293 - 319.
- HOEIJMAKERS H.W.M. & VAATSTRA W. (1983) A higher order panel method applied to vortex sheet roll-up. *A.I.A.A. Journal* **21** 4, 516 - 523.
- HOEIJMAKERS H.W.M. (1989) Computational aerodynamics of ordered vortex flows. PhD thesis Delft University of Technology, also NLR Report TR 88088 U.
- HOWE M.S. (1975) Contributions to the theory of aerodynamic sound, with application to excess jet noise and the theory of the flute. *J. Fluid Mech.* **71** 4, 625 - 673.
- HOWE M.S. (1979) The interaction of sound with low mach number wall turbulence, with application to sound propagation in turbulent pipe flow. *J. Fluid Mech.* **94** 4, 729 - 744.
- HOWE M.S. (1984) On the absorption of sound by turbulence and other hydrodynamic flows. *I.M.A. J. Appl. Math.* **32**, 187 - 209.
- MUNT R.M. (1990) Acoustic transmission properties of a jet pipe with subsonic jet flow: 1. The cold jet reflection coefficient. *J. Sound & Vibr.* **142** 3, 413 - 436.
- PETERS M.C.A.M. & HIRSCHBERG A. (1993) Acoustically induced periodic vortex shedding at sharp-edged open channel ends: Simple vortex models. *J. Sound & Vibr.* **161** 2, 281 - 299.
- PETERS M.C.A.M., HIRSCHBERG A., REIJNEN A.J. & WIJNANDS A.P.J. (1993) Damping and reflection coefficient measurements for an open pipe at low Mach and low Helmholtz numbers. *J. Fluid Mech.*, in press.
- PIVA R., RICCARDI G. & IAFRATI A. (1992) University of Rome *La Sapienza*, private communication
- RIENSTRA S.W. (1981) On the acoustical implications of vortex shedding from an exhaust pipe. *J. Eng. for Ind.* **103**, 378 - 384.
- RONNEBERGER D. (1975) Genaue Messung der Schalldämpfung und der phasengeschwindigkeit in durchstromten Rohren im Hinblick auf die Weckselwirkung zwischen Schall und Turbulenz. *Habilitationsschrift Math.-Naturw. Fak. Univ. Göttingen*
- RONNEBERGER D. & AHRENS C.D. (1977) Wall shear stress caused by small amplitude perturbations of turbulent boundary-layer flow: an experimental investigation. *J. Fluid Mech.* **83** 3, 433 - 464.
- STOKES A.N. & WELSH M.C. (1986) Flow-resonant sound interaction in a duct containing a plate II: square leading edge. *J. Sound & Vibr.* **104** 1, 55 - 73.

Appendix A

GOVERNING EQUATIONS FOR AERO-ACOUSTIC SOURCES.

For the derivation of the equations describing the propagation of an acoustical disturbance in an arbitrary inviscid mean flow we will follow the general description given by Howe (1975). The equations found by Lighthill (1952, 1954) and Powell (1964) describing the aero-acoustic sources in a turbulent flow and the vortex sound mechanism in an isentropic flow, respectively, can be derived from the general description given by Howe (1975).

In a quiescent, inviscid and non-conducting medium the propagation of acoustic disturbances is described by a wave equation, in which the acoustic disturbances are expressed in terms of the acoustic pressure p or fluctuations of the density ρ , the time-dependent scalar velocity potential ϕ or its time-derivative, or the acoustic velocity \vec{u}_{ac} . This because the wave operator is linear. However, it will be shown that in the presence of a mean flow the equations describing the propagation of acoustical disturbances can be combined into a nonlinear operator, which acts upon a variable describing the acoustical disturbances. The most appropriate variable to describe the acoustic disturbances is found to be the specific total enthalpy H , which is defined as

$$H(\vec{x}, t) = h(\vec{x}, t) + \frac{1}{2}|\vec{v}(\vec{x}, t)|^2 \quad (\text{A-1})$$

with \vec{v} the total velocity and $h(\vec{x}, t)$ the enthalpy, which using the second law of thermodynamics can be written as

$$h = \int \frac{dp}{\rho} + \int T dS \quad (\text{A-2})$$

where p , ρ , T , and S are the pressure, density, temperature and entropy, respectively. In the derivation of the propagation operator for the stagnation enthalpy H , it will be assumed that the medium is inviscid, but the effect of heat conduction will be taken into account, so that the entropy may increase in time.

In absence of external mass sources and external forces the equations for the conservation of mass and momentum in an inviscid, compressible flow are given by

$$\frac{D\rho}{Dt} + \rho \nabla \cdot \vec{v} = 0 \quad (\text{A-3})$$

$$\rho \frac{D\vec{v}}{Dt} + \nabla p = \vec{0} \quad (\text{A-4})$$

where $D/Dt = \partial/\partial t + \vec{v} \cdot \nabla$ denotes the substantial derivative.

The momentum equation can be written in Crocco's form by using the vector identity

$(\vec{v} \cdot \nabla)\vec{v} = \vec{\omega} \times \vec{v} + \nabla(\frac{1}{2}|\vec{v}|^2)$, leading to

$$\frac{\partial \vec{v}}{\partial t} + \nabla H + \vec{L} = \vec{0} \quad (\text{A-5})$$

in which H is given by equation (A-1) and \vec{L} is the Lamb vector, defined as

$$\vec{L} = \vec{\omega} \times \vec{v} - T \nabla S \quad (\text{A-6})$$

The density ρ is in general a function of the pressure and the entropy, so that

$$\frac{D\rho}{Dt} = \left(\frac{\partial \rho}{\partial p}\right)_S \frac{Dp}{Dt} + \left(\frac{\partial \rho}{\partial S}\right)_p \frac{DS}{Dt} \quad (\text{A-7})$$

where $\left(\frac{\partial p}{\partial \rho}\right)_S = c^2$ defines the local speed of sound c .

Furthermore for an ideal gas

$$\begin{aligned} \left(\frac{\partial \rho}{\partial S}\right)_p &= \left(\frac{\partial \rho}{\partial T}\right)_p / \left(\frac{\partial S}{\partial T}\right)_p \\ &= -\frac{\rho}{c_p} \end{aligned} \quad (\text{A-8})$$

where $c_p = T \left(\frac{\partial S}{\partial T}\right)_p$ is the specific heat at constant pressure.

As a result, the continuity equation (A-3) can be written as

$$\frac{1}{\rho c^2} \frac{Dp}{Dt} + \nabla \cdot \vec{v} = \frac{1}{c_p} \frac{DS}{Dt} \quad (\text{A-9})$$

By taking the derivative with respect to time of this equation and subtracting the divergence of the momentum equation in Crocco's form (A-5) we find

$$\frac{\partial}{\partial t} \left(\frac{1}{\rho c^2} \frac{Dp}{Dt} \right) - \nabla^2 H = \nabla \cdot \vec{L} + \frac{\partial}{\partial t} \left(\frac{1}{c_p} \frac{DS}{Dt} \right) \quad (\text{A-10})$$

In order to obtain the propagation operator for H , equation (A-10) can be written in the form

$$\mathcal{L}H = \nabla \cdot \vec{L} + \frac{1}{c^2} \frac{D^2 H}{Dt^2} + \frac{1}{c^2} \frac{D\vec{v}}{Dt} \cdot \nabla H - \frac{\partial}{\partial t} \left(\frac{1}{\rho c^2} \frac{Dp}{Dt} \right) + \frac{\partial}{\partial t} \left(\frac{1}{c_p} \frac{DS}{Dt} \right) \quad (\text{A-11})$$

where

$$\mathcal{L} = \frac{1}{c^2} \frac{D^2}{Dt^2} + \frac{1}{c^2} \frac{D\vec{v}}{Dt} \cdot \nabla - \nabla^2 \quad (\text{A-12})$$

is the propagation operator for the stagnation enthalpy H .

The choice of \mathcal{L} has its origin in that the propagation of an acoustic disturbance in a quiescent isentropic medium with constant speed of sound is described by the linear wave operator

$$\mathcal{L}_0 = \frac{1}{c^2} \frac{\partial^2}{\partial t^2} - \nabla^2 \quad (\text{A-13})$$

Furthermore, introducing $\vec{v} = \nabla\varphi$, where $\varphi(\vec{x}, t) = \varphi_0(\vec{x}) + \varphi_1(\vec{x}, t)$ the propagation of an irrotational disturbance in an irrotational inviscid, non-conducting mean flow is given by

$$\left(\frac{1}{c^2} \frac{D^2}{Dt^2} + \frac{1}{c^2} \frac{D\vec{v}}{Dt} \cdot \nabla - \nabla^2 \right) \frac{\partial\varphi}{\partial t} = 0 \quad (\text{A-14})$$

This shows that both cases are described by the general propagation vector \mathcal{L} given by (A-12) for an arbitrary mean flow \vec{v} .

In order to simplify the right-hand side of equation (A-11) we use the momentum equation in Crocco's form (A-5) dotted into $\frac{1}{c^2} \frac{D\vec{v}}{Dt}$, to get

$$\frac{1}{c^2} \frac{D\vec{v}}{Dt} \cdot \nabla H = -\frac{1}{c^2} \frac{D\vec{v}}{Dt} \cdot \frac{\partial\vec{v}}{\partial t} - \frac{1}{c^2} \frac{D\vec{v}}{Dt} \cdot \vec{L} \quad (\text{A-15})$$

and the definition of the total enthalpy H equation (A-1), combined with the momentum equation (A-4) to get

$$\frac{1}{c^2} \frac{D^2 H}{Dt^2} = \frac{1}{c^2} \frac{D}{Dt} \left(\frac{1}{\rho} \frac{\partial p}{\partial t} \right) + \frac{1}{c^2} \frac{D}{Dt} \left(T \frac{DS}{Dt} \right) \quad (\text{A-16})$$

Furthermore, using the momentum equation (A-4) and the relation $\vec{v} \cdot \nabla = \frac{D}{Dt} - \frac{\partial}{\partial t}$ leads to

$$\begin{aligned} -\frac{1}{c^2} \frac{D\vec{v}}{Dt} \cdot \frac{\partial\vec{v}}{\partial t} &= \frac{1}{\rho c^2} \nabla p \cdot \frac{\partial\vec{v}}{\partial t} \\ &= \frac{1}{\rho c^2} \left(\frac{\partial}{\partial t} (\vec{v} \cdot \nabla p) - \vec{v} \cdot \nabla \left(\frac{\partial p}{\partial t} \right) \right) \\ &= \frac{1}{\rho c^2} \left(\frac{\partial}{\partial t} \left(\frac{Dp}{Dt} \right) - \frac{D}{Dt} \left(\frac{\partial p}{\partial t} \right) \right) \end{aligned} \quad (\text{A-17})$$

Substitution of equations (A-15), (A-16) and (A-17) into the general equation for H (A-11) results in

$$\begin{aligned} \mathcal{L}H &= \nabla \cdot \vec{L} - \frac{1}{c^2} \frac{D\vec{v}}{Dt} \cdot \vec{L} + \frac{1}{c^2} \frac{\partial p}{\partial t} \frac{D}{Dt} \left(\frac{1}{\rho} \right) \\ &\quad - \frac{Dp}{Dt} \frac{\partial}{\partial t} \left(\frac{1}{\rho c^2} \right) + \frac{1}{c^2} \frac{D}{Dt} \left(T \frac{DS}{Dt} \right) + \frac{\partial}{\partial t} \left(\frac{1}{c_p} \frac{DS}{Dt} \right) \end{aligned} \quad (\text{A-18})$$

where we have used that

$$\begin{aligned} \frac{1}{c^2} \frac{D}{Dt} \left(\frac{1}{\rho} \frac{\partial p}{\partial t} \right) &- \frac{1}{\rho c^2} \frac{D}{Dt} \left(\frac{\partial p}{\partial t} \right) + \frac{1}{\rho c^2} \frac{\partial}{\partial t} \left(\frac{Dp}{Dt} \right) - \frac{\partial}{\partial t} \left(\frac{1}{\rho c^2} \frac{Dp}{Dt} \right) \\ &= \frac{1}{c^2} \frac{\partial p}{\partial t} \frac{D}{Dt} \left(\frac{1}{\rho} \right) - \frac{Dp}{Dt} \frac{\partial}{\partial t} \left(\frac{1}{\rho c^2} \right) \end{aligned} \quad (\text{A-19})$$

A further simplification of the right-hand side of equation (A-18) can be obtained by using the relation $\gamma p = \rho c^2$ (for an ideal gas), so that

$$\begin{aligned} & \frac{1}{c^2} \frac{\partial p}{\partial t} \frac{D}{Dt} \left(\frac{1}{\rho} \right) - \frac{Dp}{Dt} \frac{\partial}{\partial t} \left(\frac{1}{\rho c^2} \right) \\ = & \frac{\partial p}{\partial t} \frac{D}{Dt} \left(\frac{1}{\rho c^2} \right) - \frac{Dp}{Dt} \frac{\partial}{\partial t} \left(\frac{1}{\rho c^2} \right) - \frac{1}{\rho} \frac{\partial p}{\partial t} \frac{D}{Dt} \left(\frac{1}{c^2} \right) \\ = & -\frac{1}{\rho} \frac{\partial p}{\partial t} \frac{D}{Dt} \left(\frac{1}{c^2} \right) \end{aligned} \quad (\text{A-20})$$

However, this term appears to be linear in the stagnation enthalpy H and should therefore be taken into the propagation operator \mathcal{L} . This can be understood by using the momentum equation (A-4) and the definition of the stagnation enthalpy H , equation (A-1).

$$\begin{aligned} -\frac{1}{\rho} \frac{\partial p}{\partial t} &= -\frac{1}{\rho} \frac{Dp}{Dt} + \frac{\vec{v}}{\rho} \cdot \nabla p \\ &= -\frac{1}{\rho} \frac{Dp}{Dt} - \vec{v} \cdot \frac{D\vec{v}}{Dt} \\ &= -\frac{DH}{Dt} + T \frac{DS}{Dt} \end{aligned} \quad (\text{A-21})$$

Combining equations (A-20) and (A-21) with the general equation (A-18) and combining the linear term in H into a new propagation operator \mathcal{L}^* , we find

$$\begin{aligned} \mathcal{L}^* H &= \nabla \cdot \vec{L} - \frac{1}{c^2} \frac{D\vec{v}}{Dt} \cdot \vec{L} \\ &+ T \frac{DS}{Dt} \frac{D}{Dt} \left(\frac{1}{c^2} \right) + \frac{1}{c^2} \frac{D}{Dt} \left(T \frac{DS}{Dt} \right) + \frac{\partial}{\partial t} \left(\frac{1}{c_p} \frac{DS}{Dt} \right) \end{aligned} \quad (\text{A-22})$$

with the modified propagation operator given by

$$\mathcal{L}^* = \frac{1}{c^2} \frac{D^2}{Dt^2} + \frac{D}{Dt} \left(\frac{1}{c^2} \right) \frac{D}{Dt} + \frac{1}{c^2} \frac{D\vec{v}}{Dt} \cdot \nabla - \nabla^2 \quad (\text{A-23})$$

which can be simplified to

$$\mathcal{L}^* = \frac{D}{Dt} \left(\frac{1}{c^2} \frac{D}{Dt} \right) + \frac{1}{c^2} \frac{D\vec{v}}{Dt} \cdot \nabla - \nabla^2 \quad (\text{A-24})$$

The term in the propagation operator \mathcal{L}^* which does not appear in \mathcal{L} given in equation (A-12) represents the variation of the speed of sound in time, which in its turn is a result of the entropy variations in time associated with heat conduction in the inviscid medium. Finally, the right-hand side of equation (A-22) can be simplified to arrive at the general equation for the description of the propagation of acoustic disturbances in terms of the stagnation enthalpy variable H in a heat-conducting, inviscid ideal medium, given by

$$\mathcal{L}^* H = \nabla \cdot \vec{L} - \frac{1}{c^2} \frac{D\vec{v}}{Dt} \cdot \vec{L} + \frac{D}{Dt} \left(\frac{T}{c^2} \frac{DS}{Dt} \right) + \frac{\partial}{\partial t} \left(\frac{1}{c_p} \frac{DS}{Dt} \right) \quad (\text{A-25})$$

For an inviscid medium the total energy can be obtained from

$$\frac{\partial}{\partial t}(\rho E) + \nabla \cdot (\rho \vec{v} H) = \rho T \frac{DS}{Dt} \quad (\text{A-26})$$

where $E = e + \frac{1}{2}|\vec{v}|^2$ is the total energy with $e = \int T dS - \int p \frac{d\phi}{\rho^2}$ is the internal energy.

Since we have made no further assumptions during the derivation of equation (A-25), this relation is exact for an inviscid, ideal gas. However, often it is useful to derive simplified equations from this relation, especially since the equation is in general nonlinear and therefore cannot be solved analytically. For example, for a non-conducting medium the flow is isentropic $\frac{DS}{Dt} = 0$, which will simplify the above expressions considerably. In the case of a homentropic medium $\nabla S = \vec{0}$ and the Lamb vector simplifies to the Powell vector $\vec{L} = \vec{\omega} \times \vec{v}$ (Powell 1964) while the speed of sound is constant $c = c_0$. For an homentropic flow, equation (A-25) simplifies to

$$\mathcal{L}^* H = \nabla \cdot \vec{L} - \frac{1}{c^2} \frac{D\vec{v}}{Dt} \cdot \vec{L} \quad (\text{A-27})$$

REFERENCES

- HOWE M.S. (1975) Contributions to the theory of aerodynamic sound, with application to excess jet noise and the theory of the flute. *J. Fluid Mech.* **71** 4, 625 - 673.
- LIGHTHILL M.J. (1952) On sound generated aerodynamically I: General theory. *Proc. Roy. Soc. Lond. A* **211**, 564 - 587.
- LIGHTHILL M.J. (1954) On sound generated aerodynamically II: Turbulence as a source of sound. *Proc. Roy. Soc. Lond. A* **222**, 1 - 32.
- POWELL A. (1964) Theory of vortex sound. *J. Acoust. Soc. Am.* **36** 1, 177 - 195.

Appendix B

SINGLE VORTEX MODEL OF THE STARTING FLOW PAST A WEDGE.

Consider the two-dimensional starting flow around a wedge of infinite extent. Assume that one potential flow component rounds the edge, while the other component flows symmetrically towards the edge. Due to the flow rounding the wedge the velocity at the edge of the wedge becomes infinite. In real flows the velocity remains finite at the edge due to the action of viscosity resulting in flow separation and generation of vorticity at the edge. At high Reynolds numbers the vorticity remains concentrated in a thin layer, which in the potential-flow model is assumed to be infinitesimally thin, i.e. a vortex sheet. In the potential-flow model viscosity is neglected and flow separation is enforced by imposing a Kutta condition, requiring the velocity to be finite at the edge.

Due to its self-induced velocity field, the vortex sheet rolls up into a spiral-like vortex structure. In single-vortex methods it is assumed that the vorticity contained within the sheet may be concentrated into a single point vortex, at a position which is assumed to be close to the center of vorticity of the vortex sheet. Once the position of the point vortex z_v is known, the circulation Γ_v of the vortex can be obtained by imposing the Kutta condition. To satisfy the boundary condition on the solid surface for a given z_v and Γ_v a conformal mapping is employed which maps the space around the wedge onto the half-plane in the computational space. Imaging the vortex in the wall then exactly satisfies the boundary condition of zero normal velocity. Finally the position of the vortex is obtained by convecting the vortex with a velocity which depends on the specific method, i.e. considering the vortex as a *free* vortex or a vortex, *bounded* to the edge by a feeding sheet.

The transformation function from the physical plane, with complex coordinate $z = x + iy$ to the computational half-plane $\Re(\zeta) > 0$, with coordinate $\zeta = \xi + i\eta$, shown in figure B.1, is given by

$$\zeta = Dz^n \quad (\text{B-1})$$

where D is a constant, $n = \pi/(2\pi - \theta)$, with θ the interior angle of the wedge. For the sake of generality we assume a starting flow for both the symmetric and antisymmetric part of the mean potential flow given by the complex velocity potential

$$\Phi_0(\zeta) = -iA\zeta + B\zeta^2 \quad (\text{B-2})$$

where $A = at^\alpha$ and $B = bt^\beta$ with a and b real constants and t the time. The velocity potential at a point ζ in the computational plane due to the point vortex of strength Γ_v

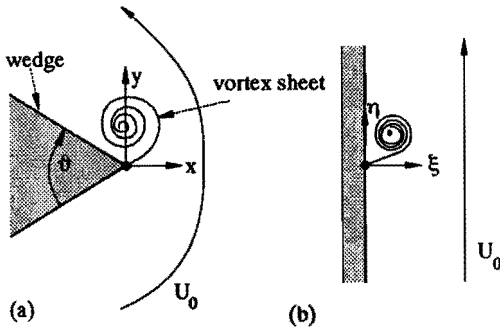


FIGURE B.1: Schwarz-Christoffel transformation of the region around a wedge into a semi-infinite plane. (a) physical plane $z = x + iy$ (b) computational plane $\zeta = \xi + i\eta$

at ζ_v , which satisfies the normal-velocity boundary condition is given by

$$\Phi_v(\zeta) = \frac{\Gamma_v}{2\pi i} \ln \left(\frac{\zeta - \zeta_v}{\zeta + \zeta_v^*} \right) \quad (\text{B-3})$$

where a star denotes the complex conjugate. The complex velocity potential is the sum of the velocity potential due to the attached flow and the velocity potential due to the point vortex.

$$\Phi(\zeta) = \Phi_0(\zeta) + \Phi_v(\zeta) \quad (\text{B-4})$$

The determination of the complex conjugate of the velocity at the position of the point vortex in the physical plane, written in ζ -coordinates, necessitates the use of the Routh correction (Clements (1973)), i.e.

$$\left. \frac{d\Phi}{dz} \right|_{z_v} = \lim_{\zeta \rightarrow \zeta_v} \left(\frac{d\Phi}{d\zeta} + \frac{i\Gamma_v}{2\pi(\zeta - \zeta_v)} \right) / \frac{dz}{d\zeta} + \frac{i\Gamma_v}{4\pi} \frac{d^2z}{d\zeta^2} / \left(\frac{dz}{d\zeta} \right)^2 \quad (\text{B-5})$$

In the literature there has been some discussion about the appropriate velocity with which the point vortex is to be convected. For a *free* vortex the Helmholtz theorem indicates that the vortex convects with the local flow velocity. i.e.

$$\frac{dz_v}{dt} = \lim_{z \rightarrow z_v} \left(\frac{d\Phi}{dz} \right)^* \quad (\text{B-6})$$

However, Brown & Michael (1954) argued that a point vortex with a time-dependent circulation is not a *free* vortex since it is connected to the edge with a so-called feeding sheet along which the vorticity feeds into the vortex. This implies that there is a time-dependent jump in the velocity potential across the feeding sheet which is equivalent to a pressure

jump since the velocity is continuous. In order to have a force-free point vortex/feeding sheet system, one has to allow for a force on the point vortex which cancels the one on the feeding sheet. Therefore at the point vortex there has to be a resulting slip-velocity which yields a Magnus force. The velocity required at the vortex is given by

$$\frac{dz_v}{dt} = \lim_{z \rightarrow z_v} \left(\frac{d\Phi}{dz} \right)^* - \frac{z_v}{\Gamma_v} \frac{d\Gamma_v}{dt} \quad (\text{B-7})$$

However, if we require that the aero-acoustic source strength associated with the additional forces in the point vortex/feeding sheet combination balance, the velocity at the point vortex has to be

$$\frac{dz_v}{dt} = \lim_{z \rightarrow z_v} \left(\frac{d\Phi}{dz} \right)^* - \left. \frac{\zeta_v}{\Gamma_v} \left(\frac{dz}{d\zeta} \right) \right|_{z_v} \frac{d\Gamma_v}{dt} \quad (\text{B-8})$$

which is derived in section 2.2.3.

In the following the similarity solutions for the three different methods will be described. The solution for a free-vortex method will be derived in detail, for the force-free and source-free method only the results will be given. Since the problem is self-similar, the point vortex convects along a line with an angle θ_v , independent of time. Writing $z_v(t) = r_v(t) e^{i\theta_v}$, we can assume that $r_v(t) = \hat{r}t^\gamma$.

The Kutta-Joukowski condition requires the velocity $\frac{dz}{dt}$ to be finite at the edge where the transformation is singular. This condition therefore requires that the singularity at the edge is eliminated by imposing equation (2.90), i.e. zero velocity in the computational plane. From the condition that the first derivative of the velocity potential $\Phi(\zeta)$ with respect to ζ at $\zeta = 0$ is zero, the circulation of the vortex can be related to its position as

$$\Gamma_v = \frac{\pi a D t^\alpha (\hat{r}t^\gamma)^n}{\cos n\theta_v} \quad (\text{B-9})$$

Substituting equation (B-9) into the expression for the velocity at the vortex position, given by equation (B-5), and using equation (B-6) we obtain for the free-vortex-method

$$\frac{\gamma \hat{r} t^{\gamma-1}}{nD} (\hat{r}t^\gamma)^{1-n} e^{-in\theta_v} = 2bt^\beta D (\hat{r}t^\gamma)^n e^{in\theta_v} + iat^\alpha \left(\frac{1}{2 \cos n\theta_v} \left[\frac{1}{2 \cos n\theta_v} + \frac{1-n}{2n} e^{-in\theta_v} \right] - 1 \right) \quad (\text{B-10})$$

The time-dependence of the term on the left is $t^{2\gamma-1-\gamma n}$, while the two terms on the right have time-dependence $t^{\beta+\gamma n}$ and t^α , respectively. Analytical solutions of this equation can be obtained for both the case that $0 < |a| \ll |b|$ and $|b| \ll |a|$. The value of $|b|$ can be zero in the second case. However, $|a|$ cannot be zero in the first case, since for $|a| = 0$ the flow is not singular at the edge flow separation does not occur. This follows directly from the circulation given by equation (B-9), which only depends on the value of a . For the two limiting cases we find for the power of time describing the increase of the distance of the vortex

$$\gamma = (1 + \alpha)/(2 - n) \quad \text{for } |b| \ll |a| \quad (\text{B-11})$$

$$\gamma = (1 + \beta)/(2 - 2n) \quad \text{for } 0 < |a| \ll |b| \quad (\text{B-12})$$

Consider first the case $|b| \ll |a|$, i.e. when the first term on the right of equation (B-10) is negligible compared to the second term. Since the time drops out, we obtain

$$\frac{\gamma}{nD} \hat{r}^{2-n} = -ia e^{in\theta_v} \left(1 - \frac{1}{4 \cos^2 n\theta_v} - \frac{1-n}{4n} \frac{e^{-in\theta_v}}{\cos n\theta_v} \right) \quad (\text{B-13})$$

where the left-hand side is real. For the imaginary part of this equation we find

$$\left(1 - \frac{1}{4 \cos^2 n\theta_v} \right) \cos n\theta_v - \left(\frac{1-n}{4n} \right) \frac{1}{\cos n\theta_v} = 0 \quad (\text{B-14})$$

and as a result

$$\theta_v = \frac{1}{n} \arccos \left(\frac{1}{2\sqrt{n}} \right). \quad (\text{B-15})$$

For the real part we obtain

$$\frac{\gamma}{nD} \hat{r}^{2-n} = a \sin n\theta_v \left(1 - \frac{1}{4 \cos^2 n\theta_v} \right) \quad (\text{B-16})$$

and by using the solution for θ_v and equation (B-11) we obtain

$$\hat{r}^{2-n} = \frac{aDn(1-n)(2-n)\sqrt{1-\frac{1}{4n}}}{1+\alpha} \quad (\text{B-17})$$

For the case that $0 < |a| \ll |b|$ the second term on the right-hand side of equation (B-10) can be neglected compared to the other terms and we find

$$\frac{\gamma}{nD} \hat{r}^{2-n} = 2bD \hat{r}^n e^{2in\theta_v} \quad (\text{B-18})$$

From the imaginary part of this equation we find

$$\sin 2n\theta_v = 0 \quad (\text{B-19})$$

which results into $\theta_v = 0$, so that apparently the vortex moves along the centerline of the wedge. From the real part of equation (B-18) we obtain from equation (B-18) by using equation (B-12)

$$\hat{r}^{2-2n} = \frac{4n(1-n)bD^2}{1+\beta} \quad (\text{B-20})$$

Summarizing, for the case $|b| \ll |a|$ we obtain

$$\begin{aligned} r_v &= \left(aDK_1 t^{\alpha+1} \right)^{\frac{1}{2-n}} \\ \theta_v &= \frac{1}{n} \arccos \frac{1}{2\sqrt{n}} \\ \Gamma_v &= 2\pi\sqrt{n}aDt^\alpha r^n \\ K_1 &= \frac{n(1-n)(2-n)(1-\frac{1}{4n})^{\frac{1}{2}}}{1+\alpha} \end{aligned} \quad (\text{B-21})$$

and for $0 < |a| \ll |b|$

$$\begin{aligned} r_v &= (bD^2 K_2 t^{1+\beta})^{\frac{1}{2-2n}} \\ \theta_v &= 0 \\ \Gamma_v &= \pi a D t^\alpha r^n \\ K_2 &= \frac{4n(1-n)}{1+\beta} \end{aligned} \quad (\text{B-22})$$

Also for the force-free method and the source-free method we can obtain analytic solutions for both of above case, if the velocity at the vortex position, given by equation (B-7) and (B-8), is rewritten as

$$\frac{d(z_v \Gamma_v)}{dt} = \Gamma_v \lim_{z \rightarrow z_v} \left(\frac{d\Phi}{dz} \right)^* \quad (\text{B-23})$$

$$\frac{d(\zeta_v \Gamma_v)}{dt} = \Gamma_v \lim_{z \rightarrow z_v} \left(\frac{d\Phi}{dz} \right)^* \left(\frac{d\zeta}{dz} \right) \quad (\text{B-24})$$

The analytical solutions for the *force-free* method with the point vortex/feeding sheet combination agree with equations (B-21, B-22) but with different constants K_1 and K_2 . With the velocity of the vortex determined by equation (B-23) we find

$$K_1 = \frac{n(1-n)(2-n)(1-\frac{1}{4n})^{\frac{1}{2}}}{3\alpha+n+1} \quad (\text{B-25})$$

$$K_2 = \frac{4n(1-n)}{(1+\beta)(n+1)+2\alpha(1-n)} \quad (\text{B-26})$$

and for the *source-free* method with the velocity determined by equation (B-24)

$$K_1 = \frac{n^2(1-n)(2-n)(1-\frac{1}{4n})^{\frac{1}{2}}}{2\alpha+\alpha n+2n} \quad (\text{B-27})$$

$$K_2 = \frac{4n^2(1-n)}{2n(1+\beta)+2\alpha(1-n)} \quad (\text{B-28})$$

For the case the velocity component that rounds the edge is dominant it follows that if $\alpha = -\frac{1}{2}n$ then the circulation of the vortex will be constant in time and the solution of the methods will be identical since the constant K_1 is equal. If the symmetrical component of the velocity is dominant the circulation will be constant in time if $\alpha = \frac{n(1+\beta)}{2n-2}$ and also in that case the three solutions are identical since the constants K_2 are equal.

REFERENCES

- BROWN C.E., MICHAEL W.H. (1954) Effect of leading-edge separation on the lift of a delta wing, *J. Aero. Sci.* **21**, 690 - 694.
- CLEMENTS R.R. (1973) An inviscid model of two-dimensional vortex shedding, *J. Fluid Mech.* **57** 2, 321 - 336.

SAMENVATTING

Stromingsgeïnduceerde pulsaties komen in de praktijk veel voor in leidingsystemen van de procesindustrie en zijn een constante bron van zorg vanwege de schade die ze kunnen veroorzaken aan het leidingnet. De resonanties ontstaan doordat de stroming loslaat aan scherpe hoeken en periodiek wervels vormt. Deze wervelafschudding koppelt hierbij met akoestische staande golven in het leidingnet. Het doel van het onderzoek is het voorspellen van de zelfgeïnduceerde pulsaties in diverse leidingconfiguraties.

De wervelafschudding is beschreven met behulp met diverse methoden gebaseerd op het potentiaal stromingsmodel, met als doel het verschijnsel met een zo eenvoudig mogelijke rekenmethode te kunnen kwantificeren. De resultaten van de rekenmethoden zijn vergeleken met resultaten van stromingsvisualisatie van startende stromingen en van periodieke wervelafschudding aan schaalmodellen van een systeem met één of twee afgesloten zijtakken, generiek voor in de praktijk voorkomende situaties waar resonantie kan optreden.

Met behulp van de rekenmethoden is de maximale resonantieamplitude bepaald, die in een pijpsysteem met twee even lange, afgesloten zijtakken kan ontstaan als de verliezen door uitstraling van geluid, wrijving en niet-lineaire golfverschijnselen zijn te verwaarlozen.

In het geval dat de verbindingstukken tussen hoofdleiding en de twee zijtakken scherpe hoeken hebben zal the tijdsafhankelijke flux in de zijtak nooit sterker zijn dan 65% van de gemiddelde flux in de hoofdleiding als de zijtakken achter elkaar staan. Als de zijtakken echter tegenover elkaar staan kan de amplitude van de tijdsafhankelijke flux gelijk aan de tijdsgemiddelde flux in de hoofdleiding worden.

De verliezen van akoestische energie door uitstraling en wrijving worden sterk beïnvloed door de (turbulente) tijdsgemiddelde stroming in het leidingsysteem. Door de meting van de reflectie coefficient van de akoestische energie en de demping van akoestische golven in een rechte pijp met diverse pipeinden zijn deze verliezen gekwantiseerd.

De rekenmethoden worden in het tijdsdomein, voor een gegeven Strouhal getal en gegeven amplitude van het akoestisch veld, toegepast op de impulsief startende stroming in een aantal generieke configuraties. Na verloop van tijd is de invloed van het opstarten van de stroming verdwenen en wordt de oplossing periodiek. De over een periode gemiddelde productie en absorptie van akoestische energie kan dan worden bepaald en daarmee de netto akoestische bronsterkte van de pulsatie onder verliesvrije condities.

Uit een balans tussen de productie van akoestische energie door de interactie van de wervelstructuren met het akoestisch veld aan een kant en de schatting van het verlies van akoestische energie door viskeuze effecten en uitstraling aan de andere kant kan de evenwichtsamplitude worden bepaald waarin het systeem resonanceert. Inzicht in de factoren die van invloed zijn op de bronsterkte en de verliezen van akoestische energie geeft aan hoe de resonanties kunnen worden voorkomen of worden gedempt.

NAWOORD

Hoewel alleen mijn naam op de kaft van dit boekje staat is de inhoud van dit proefschrift natuurlijk een voortbrengsel van een grote groep mensen die ik hier wil bedanken voor hun bijdrage. Al deze mensen vormen tesamen een gezellige vakgroep, een vereiste omgeving om productief onderzoek te kunnen verrichten. Ik had het geluk vier jaar deel uit te mogen maken van de vakgroep Transportfysica van de faculteit Technische Natuurkunde aan de Technische Universiteit Eindhoven. Aan velen in deze groep, en in het bijzonder de sectie Gasdynamica/Aeroakoestiek, ben ik dank verschuldigd.

Allereerst natuurlijk Mico Hirschberg, hij zorgde voor een constante stroom van ideeën, die op willekeurige momenten van de dag opkwamen en bediscussieerd werden. Het spuien van deze ideeën heeft misschien een hoge telefoonrekening opgeleverd, maar heeft tevens gezorgd voor een goede stimulans en voor blijvend enthousiasme voor het onderzoek. Helaas hebben we in de beperkte tijd van vier jaar maar een gedeelte ten uitvoer kunnen brengen. Door jouw betrokkenheid bij de experimenten heb ik veel van de resultaten van hoofdstuk 5 te danken. Soms leek het wel alsof jij het was die zou promoveren! Mico, ik zal je missen als energieke motor, als sturende leider, als stimulerend gaspedaal en als noodzakelijke rem om niet uit de bocht te vliegen en vooral als 'back-up' om op terug te vallen.

Daarnaast ben ik Harry Hoeijmakers bijzonder veel dank verschuldigd voor zijn hulp bij het numerieke gedeelte van mijn onderzoek. Harry, jij hebt ervoor gewaakt dat de numerieke beschrijving van de stroming met een zelfde nauwkeurigheid is gedaan als de experimenten. Door de vele discussies over de resultaten tot in de kleinste details zijn veel nieuwe ideeën ontstaan. Zo heb ik goede herinneringen aan onze discussie over de kromming van een wervellaag aan een scherpe hoek. Ondanks dat ik je gelijk heb moeten geven, heeft het me wel een stelling opgeleverd. Hoewel aeroakoestiek niet direct jouw vakgebied is, heb je enorm veel energie gestoken in de beschrijving van de werveldynamica. Ik ben je hiervoor dankbaar en tevens voor het zeer kritisch lezen van het manuscript waarvoor je zelfs nog enkele dagen van je vakantie hebt opgeofferd.

Bram Wijnands, mijn kamergenoot, heeft ervoor gezorgd dat alle experimenten met *Deutsche Gründlichkeit* uitgevoerd werden. Hij was steeds het juiste aanspreekpunt als er weer eens een numerieke simulatie in overeenstemming was met het experiment,... of als dat weer eens niet zo was. Bram, door jou heb ik me steeds gerealiseerd dat aeroakoestiek naast de productie van 140 dB herrie in een pijpleiding systeem ook een aantrekkelijke kant heeft in de vorm van muziek bij blaasinstrumenten.

Ook de overige leden van de vakgroep ben ik erkentelijk voor hun bijdrage aan het onderzoek. Met name wil ik nog bedanken: Rini van Dongen voor het meedenken over theoretische problemen, Eep van Voorthuizen voor zijn technische assistentie en Pierre Kriesels voor het verrichten van veel van de metingen gepresenteerd in hoofdstuk 6 en de discussies over de vergelijking met de numerieke simulaties.

Het onderzoek zou in vier jaar nooit zo ver gekomen zijn zonder de inzet van veel studenten. De afstudeerders Erik van den Bogaard, Rob Bastiaans en Floris Huijsmans zorgden voor de basis van de numerieke simulatie en de experimenten. Guido ter Horst en

Johan van de Konijnenberg hebben daarna de meeste reflectiecoëfficiënt metingen verricht. Antwan Reijnen ben ik een sigaar schuldig vanwege zijn zeer nauwkeurige metingen van de demping, weergegeven in hoofdstuk 5, terwijl Werner Mahu veel energie heeft gestoken in de numerieke simulatie. Werner, jij hebt voor mij bewezen dat het niet alleen belangrijk is een nauwkeurige numerieke simulatie van de stroming te kunnen maken, maar dat het nog belangrijker is deze resultaten op een aantrekkelijke manier te presenteren! Leonie Schoenmakers tenslotte heeft door visualisatie van de startende stroming in een T-stuk een vergelijking met de numerieke simulatie mogelijk gemaakt.

Bij alle experimenten en numerieke simulaties waren ook veel stagiaires betrokken. Ate van Steenberg, Leo Steeghs, Stefan Opdebeek, Joost de Vries, Jitze-Jan de Vries, Rard de Leeuw, Karel Burm, Anton den Boer, Cees-Jan Hogendoorn, Erik van Ballegooijen, Carlo Lagrouw, Armand Jongen, André Linssen, Maurice Bindels, Oscar van Schijndel, Olivier Schneider, Peter Hogendoorn en Ferry Tabor ben ik dankbaar voor hun bijdrage aan het project.

Echter ook van buiten de vakgroep Transportfysica heb ik steun gehad. Van de faculteit Wiskunde ben ik René van Hassel en Sjoerd Rienstra bijzonder dankbaar.

Aan Ruth Gruijters dank ik veel van de illustraties in dit proefschrift.

Tijdens mijn verblijf in Italië aan de Universiteit van Rome, 'La Sapienza' heb ik in een prettige sfeer samengewerkt met Prof. Renzo Piva, Enrico de Bernardis, Giorgio Riccardi en in het bijzonder Alessandro Iafrazi. De zogenaamde *vortex-blob* methode dank ik aan deze samenwerking.

Tenslotte ben ik mijn promotor prof. Gerrit Vossers dankbaar voor het initiëren van het project, en het op de achtergrond in goede banen leiden van het onderzoek en tevens de overige leden van de promotiecommissie, prof. H.W.M. Hoeijmakers (2^e promotor), dr. A. Hirschberg (co-promotor), prof. D. Ronneberger (Dtl.), prof. R. Piva (It.), prof. A.A. van Steenhoven en prof. R.J. Zwaan voor hun suggesties ter verbetering van het manuscript.

Promoveren eindigt altijd in een periode waarin andere activiteiten tijdelijk op een zijspoor worden gezet. Iedereen die ik hiermee tekort heb gedaan wil ik bedanken voor hun begrip hiervoor. Het werk is af, het wordt tijd om te voorkomen dat de zijsporen dwaalsporen worden.

CURRICULUM VITAE

René Peters werd op 17 september 1966 geboren in Loon op Zand als zoon van schoenfabrikant Jan Peters en Riet Peters-Spee. Op het Dr. Mollercollege in Waalwijk haalde hij in 1984 het diploma Gymnasium β . Hierna startte hij de studie Technische Natuurkunde aan de Technische Universiteit te Eindhoven. Met zijn afstudeerwerk verricht in de vakgroep Transportfysica, sectie windenergie onder begeleiding van Dr. G.A.M. van Kuik en Dr. A. Hirschberg rondde hij deze studie cum laude af in februari 1989. Tijdens zijn studie vervulde hij een studentassistentchap by de vakgroep Fysische Technische Informatica.

Op 1 april 1989 kwam hij in dienst van de Stichting Fundamenteel Onderzoek der Materie (FOM) als Onderzoeker In Opleiding (OIO) en deed in Eindhoven, in de sectie Gasdynamica/Aeroakoestiek van de vakgroep Transportfysica, faculteit Technische Natuurkunde, onderzoek aan 'Het modelleren van aeroakoestische bronnen in interne stromingen' (FOM project ETN 71.1403). Dit onderzoek, onder leiding van prof. G. Vossers en prof. H.W.M. Hoeijmakers en begeleiding van dr. A. Hirschberg resulteerde in dit proefschrift.

Per 1 oktober 1993 treedt hij in dienst bij het Koninklijke/Shell Exploratie en Productie Laboratorium (KSEPL) in Rijswijk ZH als Associate Research Physicist.

STELLINGEN

BEHORENDE BIJ HET PROEFSCHRIFT

AEROACOUSTIC SOURCES IN INTERNAL FLOWS

M.C.A.M. PETERS

3 SEPTEMBER 1993

I De eindcorrectie δ van een open pijp einde met straal a daalt in aanwezigheid van hoofdstroming van de waarde zonder hoofdstroming naar $\delta/a = 0.20 \pm 0.02$ zowel voor een scherp als voor een dikwandig pijp einde. Dit wijst erop dat in aanwezigheid van stroming het singulier gedrag van de stroming nabij de scherpe rand van het pijp einde geen invloed heeft op de eindcorrectie.

Dit proefschrift, hoofdstuk 5

S.W. RIENSTRA, *J. Sound & Vibr.* **86** 1983, 539

II Bij een loslatende, startende stroming om een scherpe hoek verlaat de schuiflaag de hoek tangentieel. Desondanks is de kromming van deze laag nabij de hoek oneindig.

Dit proefschrift, hoofdstuk 3

III De demping van akoestische golven in een turbulente pijp stroming kan voor lage frequenties worden beschreven door een quasi-stationaire theory. In de quasi-stationaire limiet, waarin de demping wordt gerelateerd aan de frictiecoëfficiënt voor een turbulente pijp stroming, wordt geen rekening gehouden met warmtegeleiding en derhalve is de theory niet algemeen geldig voor een gas. Voor een consequente toepassing van deze theorie zou dan ook de isotherme geluidssnelheid gebruikt moeten worden.

Dit proefschrift, hoofdstuk 5

U. INGARD & V.K. SINGHAL, *J. Acoust. Soc. Am.* **55** 1974, 535

IV Om de werking van een eindige puntkracht in een stromingsveld gedurende een eindige tijd te beschrijven gebruikt Sparenberg een lineaire theorie waarin een massabron en een massaput op afstand met elkaar verbonden zijn door een oneindig dunne jet stroming. Om aan massabehoud te kunnen voldoen moet deze jet een oneindige snelheid hebben. Deze oplossing is echter fysisch niet relevant omdat dit een oneindige impulsstroom tot gevolg heeft.

J.A. SPARENBERG, *Elements of hydrodynamic propulsion*. 1984

V Het nut van lineaire theorie hangt af van de gekozen referentie ten opzichte waarover wordt gelineariseerd.

B.J. BAYLY & S.A. ORZAG, *Ann. Rev. Fluid Mech.* **20** 1988, 359

VI In 1889 publiceerde Froude een theorie waarmee hij het maximale vermogen bepaalde wat door een actuatorschijf in kinetische energie kan worden omgezet. In deze theorie is het singulier gedrag van de stroming nabij de rand van de schijf niet nauwkeurig beschreven. De resultaten van Lee & Greenberg die een significante toename van het vermogen voorspellen op grond van een specifieke beschrijving van het singulier gedrag bij de randen zijn echter het gevolg van het introduceren van een randkracht in hun theorie en het ten onrechte identificeren van de druk minima als de randen van de actuatorschijf in hun experimenten. Afwijkingen van de Froude limiet zijn derhalve nog niet bewezen.

J.H.W. LEE & M.D. GREENBERG, *J. Fluid Mech.* **145** 1984, 287

M.C.A.M. PETERS, *afstudeerverslag T.U. Eindhoven nr. R-982-A*, 1989

G.A.M. VAN KUIK, *proefschrift T.U. Eindhoven* 1991

VII De wet die regelt dat lokale omroepen een deel van hun inkomsten via ether-reclame zonder tegenprestatie moeten afstaan aan de regionale pers is in strijd met het concurrentieprincipe.

VIII De teloorgang van de schoenindustrie in de Langstraat is naast de concurrentie van lage-lonen landen mede te wijten aan een gebrek aan opvolging in deze veelal traditionele familiebedrijven.

IX Voor een optimale floaterservice bij volleybal is de positie van het ventiel van de bal van ondergeschikt belang. Het niet spinnen van de bal is belangrijker, omdat in dat geval een Von Kármán wervelstraat kan ontstaan achter de bal.
W. QING-DING *et al.*, *Fluid. Dyn. Res.* **3** 1988, 231

X Uit milieuoogpunt is het verstandiger de volgorde: 1. koffie inschenken, 2. melk en suiker toevoegen om te keren, zodat het plastic roerstaafje kan worden uitgespaard.